Doctoral Dissertation
Doctoral Program in Electrical, Electronics and Communications Engineering
(38^{th}cycle)

Modeling and Design of a Railgun-Driven Actuator for Ultrafast LVDC Circuit Breakers

Fermín Gómez de León

******

Supervisors:
Prof. Maurizio Repetto
Dr. Ara Bissal

Politecnico di Torino
March 9, 2026

Declaration

I hereby declare that, the contents and organization of this dissertation constitute my own original work and does not compromise in any way the rights of third parties, including those relating to the security of personal data.

Fermín GdL

Fermín Gómez de León
Nuremberg, March 9, 2026

Acknowledgements

First of all, I would like to express my deepest gratitude to my industrial supervisor, Dr. Ara Bissal, for his invaluable technical guidance, constant encouragement, and unwavering support throughout this work. I am particularly thankful for his trust, his patience, and for always pushing me beyond my limits to bring out the best in me.

I would also like to sincerely thank Prof. Maurizio Repetto, whose exceptional academic guidance and theoretical perspective have been fundamental to the development of this research. His flexibility and openness greatly facilitated the collaboration between Huawei Nuremberg Research Center and Politecnico di Torino, ensuring that this industrial PhD program could progress smoothly and effectively.

My sincere appreciation extends to my colleagues Waqas Ali and Kedar Joshi, whose technical support, teamwork, and friendship made every challenge more rewarding. Working as part of such a dedicated and talented team has been an honor. I have learned that with a truly committed group of people, any goal can be achieved.

I am also grateful to Huawei Nuremberg Research Center for providing the financial and technical resources that made this project possible — from laboratory equipment and experimental facilities to conference participation and professional development opportunities.

I wish to thank Politecnico di Torino and its Doctoral School for providing a stimulating academic environment and for their continuous support of industrial research collaborations. The institutional commitment to fostering innovation between academia and industry has been essential for the success of this PhD journey.

Finally, I owe my deepest gratitude to my family for their unconditional support from afar — not only during this demanding process but throughout my entire life. Their love, patience, and encouragement have been the foundation that allowed me to pursue this path. Without them, I would not be who I am today.

Abstract

Low-voltage direct current (LVDC) distribution systems are increasingly adopted in applications such as electric vehicle charging infrastructure, data centers, and DC microgrids. However, the absence of natural current zero crossings and the typically low inductance of LVDC networks make fault current interruption particularly challenging, requiring protection devices capable of operating on a sub-millisecond timescale. While solid-state and hybrid circuit breakers offer fast response, they suffer from high losses, limited galvanic isolation, and unfavorable failure modes. Mechanical circuit breakers remain the most robust and efficient solution, but their performance is fundamentally constrained by the speed of the contact actuation mechanism.

This thesis investigates the modeling and design of a railgun-driven electromagnetic actuator for ultrafast mechanical LVDC circuit breakers. The proposed actuation concept leverages the extremely low inductance and high force density of railgun systems to achieve very high acceleration and contact separation speeds. A hierarchical modeling framework is developed, ranging from analytical formulations to quasistatic and fully transient multiphysics simulations, enabling an in-depth analysis of electromagnetic forces, mechanical dynamics, thermal effects, and friction phenomena. In parallel, a dedicated pulse-power electric drive is designed to supply the railgun actuator, capable of delivering peak currents exceeding 165 kA within 22 µs.

System-level simulations are used to assess breaker performance under realistic LVDC fault conditions and to quantify the impact of system inductance and actuator dynamics on current interruption. The results demonstrate that higher actuation speeds lead to faster current extinction, lower peak fault currents, and significantly reduced energy dissipation in the breaker. Experimental validation of the railgun actuator confirms excellent agreement with the proposed models, achieving a con-

tact displacement of 15 mm in 300 µs and peak velocities above 100 m/s. When integrated into a system-level protection scenario, the measured actuator dynamics enable current interruption within 420 µs to 700 µs for system inductances between 10 µH and 100 µH.

The achieved performance significantly exceeds that of state-of-the-art single-use protection devices such as pyrofuses and provides a markedly faster response than Thomson-coil–based actuators commonly employed in ultrafast circuit breakers. The results demonstrate that railgun-based actuation constitutes a viable and high-performance solution for next-generation ultrafast mechanical LVDC circuit breakers, bridging the gap between conventional mechanical and solid-state protection technologies.

Publications

Journal Publications

- Fermín Gómez de León, Ara Bissal, Maurizio Repetto, and Fabio Freschi "A Novel Railgun-Based Actuation System for Ultrafast DC Circuit Breakers in EV Fast-Charging Applications" *World Electric Vehicle Journal*, 16(9)-514, September 2025.

Conference Publications

- Fermín Gómez de León, Kedar Joshi, Ara Bissal, Waqas Ali, and Maurizio Repetto "Utilization of a Snubber Capacitor in a 1 kV Flyback Converter to Optimize the Charging of a Capacitor Bank" *IECON 2023-49th Annual Conference of the IEEE Industrial Electronics Society*, pages 1–6, September 2023, ISSN: 2577-1647.
- Fermín Gómez de León, Maurizio Repetto, and Ara Bissal "A Novel Railgun Simulation Model Based on a Quasistatic Study" *XXVIII Symposium Electromagnetic Phenomena in Nonlinear Circuits (EPNC 2024)*, May 2025.
- Fermín Gómez de León, Ara Bissal, Maurizio Repetto, and Fabio Freschi "Comparison of Multiphysics 3-D Transient and Quasistatic Models for Railgun Simulations" *Computation of Electromagnetic Fields (COMPUMAG)*, Accepted, not published.

Patents

- Ara Bissal, Kedar Joshi, Waqas Ali, Fermín Gómez de León, and Jürgen Kuglmeier “CIRCUIT BREAKER WITH ROTOR AND STATOR”, Patent Number: WO2025223646A1, October 2025.
- Ara Bissal, and Fermín Gómez de León “ULTRA-FAST BREAKER”, Patent Number: WO2025223667A1, October 2025.

Contents

List of Figures

List of Tables

List of Symbols and Acronyms

Symbols

V_s	Source voltage	(V)
R_s	System resistance	(Ω)
L_s	System inductance	(H)
R_l	Load resistance	(Ω)
L_l	Load inductance	(H)
i	Current	(A)
v_{arc}	Arc voltage across the breaker contacts	(V)
t	Time	(s)
k	Arc voltage gradient constant	(V/m)
E_s	Magnetic energy stored in the system inductance	(J)
E_b	Energy dissipated in the circuit breaker during interruption	(J)
C	Capacitance of the pulse-power capacitor bank	(F)
C_{cr}	Critical capacitance for critically damped response	(F)
C_{max}	Maximum admissible capacitance from peak-time constraint	(F)
C_{min}	Minimum capacitance imposed by peak-current constraint	(F)
V_0	Initial capacitor-bank voltage	(V)
i_p	Peak discharge current	(A)
t_p	Time to current peak	(s)
L_{tot}	Total loop inductance of the electric drive	(H)
R_{tot}	Total series resistance of the electric drive	(Ω)
$L_{stray,1}$	Stray inductance between capacitor bank and diode	(H)
$L_{stray,2}$	Stray inductance between diode and load	(H)
$R_{stray,1}$	Stray resistance between capacitor bank and diode	(Ω)
$R_{stray,2}$	Stray resistance between diode and load	(Ω)

α	Damping factor of the electric drive	(1/s)
ω_0	Undamped natural angular frequency	(rad/s)
ω_d	Damped natural angular frequency	(rad/s)
$s_{1,2}$	Characteristic roots of the electric drive	(1/s)
v_F	Forward voltage of the freewheeling diode	(V)
v_T	On-state voltage of the thyristor	(V)
$\mathrm{V}_\mathrm{T0,D}$	Diode threshold voltage	(V)
$\mathrm{V}_\mathrm{T0,T}$	Thyristor threshold voltage	(V)
i_F	Forward current of the diode	(A)
i_T	On-state current of the thyristor	(A)
$\mathrm{r}_\mathrm{t,D}$	Diode slope resistance	(Ω)
$\mathrm{r}_\mathrm{t,T}$	Thyristor slope resistance	(Ω)
$\mathrm{L}_\mathrm{stray}$	Total stray inductance of the drive layout	(H)
$\mathrm{R}_\mathrm{stray}$	Total stray resistance of the drive layout	(Ω)
f	Frequency	(Hz)
Z	Complex impedance	(Ω)
f_0	Resonance frequency	(Hz)
i_1	Flyback primary current	(A)
i_1p	Peak primary current	(A)
i_2	Flyback secondary current	(A)
i_2p	Peak secondary current	(A)
V_in	Input voltage of the auxiliary power supply	(V)
v_out	Output voltage of the flyback converter	(V)
L_m	Magnetizing inductance of the flyback transformer	(H)
L_lk	Leakage inductance of the flyback transformer	(H)
C_oss	MOSFET output capacitance	(F)
C_D	Primary-side damping/snubber capacitor	(F)
v_DS	MOSFET drain–source voltage	(V)
v_DSp	Peak drain–source voltage	(V)
$f_\mathrm{0,toff}$	Turn-off resonance frequency	(Hz)
$f_\mathrm{0,dm}$	Demagnetization resonance frequency	(Hz)
v_valley	Minimum drain–source voltage valley	(V)
E_m	Magnetic energy stored in the flyback magnetic core	(J)
$E_\mathrm{Llk,max}$	Maximum leakage-inductance energy	(J)
$P_\mathrm{in,max}$	Maximum input power	(W)

$P_{\text{out,max}}$	Maximum output power	(W)
η	Efficiency	(%)
$f_{\text{s,max}}$	Maximum switching frequency	(Hz)
N_1	Number of primary turns	(−)
N_2	Number of secondary turns	(−)
N_{ZCD}	Number of ZCD auxiliary winding turns	(−)
N_{aux}	Number of auxiliary winding turns	(−)
A_{e}	Effective magnetic core cross-sectional area	(m^2)
Φ_{max}	Peak magnetic flux	(Wb)
B_{max}	Peak magnetic flux density	(T)
R_{sn}	Snubber resistance	(Ω)
C_{sn}	Snubber capacitance	(F)
v_{clamp}	Snubber clamp voltage	(V)
v_{Csn}	Snubber capacitor voltage	(V)
$\mathrm{R}_{\text{sense}}$	Current-sense resistance	(Ω)
$v_{\text{CS,th}}$	Current-sense threshold voltage	(V)
$E_{\text{in,1}}$	Input energy during charging interval	(J)
$E_{\text{out,1}}$	Energy stored in the output capacitor	(J)
$\mathbf{J}$	Current density	($\mathrm{A/m^2}$)
$\mathbf{B}$	Magnetic flux density	(T)
$\mathbf{F}$	Electromagnetic force	(N)
V	Volume over which the Lorentz force is integrated	(m^3)
R	Railgun electrical resistance	(Ω)
R_{a}	Armature electrical resistance	(Ω)
R'	Rail resistance gradient	(Ω/m)
L	Railgun inductance	(H)
L_{a}	Armature inductance	(H)
L'	Inductance gradient	(H/m)
y	Armature position along the rail	(m)
$\dot{y}$	Armature velocity	(m/s)
$\ddot{y}$	Armature acceleration	($\mathrm{m/s^2}$)
λ	Magnetic flux linkage	(Wb)
E_{mag}	Magnetic energy	(J)
E'_{mag}	Magnetic co-energy	(J)
F_y	Electromagnetic force on the armature along the y-direction	(N)

F_a	Electromagnetic force acting on the armature	(N)
$\mathrm{m_a}$	Armature mass	(kg)
$\mathbf{A}$	Magnetic vector potential	(T m)
$\mathbf{H}$	Magnetic field intensity	(A/m)
μ	Magnetic permeability	(H/m)
σ	Electrical conductivity	(S/m)
$\mathbf{E}$	Electric field	(V/m)
$\mathbf{v}$	Conductor velocity	(m/s)
ρ	Mass density	($\mathrm{kg/m^3}$)
$\mathrm{C_p}$	Specific heat capacity at constant pressure	(J/(kg K))
T	Temperature	(K)
$\mathbf{q}$	Heat flux	($\mathrm{W/m^2}$)
k	Thermal conductivity	(W/(m K))
$F_{x,\mathrm{a}}$	Transverse electromagnetic force acting on the armature	(N)
$F_{x,\mathrm{r}}$	Transverse electromagnetic force acting on the rails	(N)
F_f	Friction force	(N)
μ	Coefficient of friction	(−)
N	Normal contact force at the rail–armature interface	(N)
F_sp	Spring preload force	(N)
k	Spring stiffness	(N/m)
Δx	Spring compression	(m)
F_eq	Equivalent driving force acting on the armature	(N)

Acronyms

LVDC	Low-Voltage Direct Current
DC	Direct Current
AC	Alternating Current
LC	Inductor–Capacitor (resonant) circuit
MOV	Metal-Oxide Varistor
HVDC	High-Voltage Direct Current
VSC	Voltage-Source Converter
SSCB	Solid-State Circuit Breaker
IGBT	Insulated-Gate Bipolar Transistor

MOSFET	Metal–Oxide–Semiconductor Field-Effect Transistor
SCR	Silicon-Controlled Rectifier
IGCT	Integrated Gate-Commutated Thyristor
WBG	Wide-Bandgap (semiconductors)
SiC	Silicon Carbide
GaN	Gallium Nitride
HEMT	High-Electron-Mobility Transistor
RC	Resistor–Capacitor (snubber) network
RCD	Resistor–Capacitor–Diode (snubber) network
TVS	Transient Voltage Suppression (diode)
ZVC	Zero-Voltage Commutation
ZVS	Zero-Voltage Switching
ZCC	Zero-Current Commutation
HCB	Hybrid Circuit Breaker
FEM	Finite-Element Method
APS	Auxiliary Power Supply
BEV	Battery Electric Vehicle
ESL	Equivalent Series Inductance
ESR	Equivalent Series Resistance
FR4	Flame Retardant 4 (glass-reinforced epoxy laminate)
GD	Gate Driver (output pin of the controller)
KVL	Kirchhoff's Voltage Law
LCR	Inductor–Capacitor–Resistor (circuit)
QR	Quasi-Resonant
UPS	Uninterruptible Power Supply
ZCD	Zero-Current Detection
ALE	Arbitrary Lagrangian–Eulerian
ht	Heat Transfer (COMSOL physics interface)
mef	Magnetic and Electric Fields (COMSOL physics interface)
mf	Magnetic Fields (COMSOL physics interface)
PDE	Partial Differential Equation

Chapter 1

Introduction

The first chapter provides an overview of the research framework and goals. It begins by discussing the motivation and background that led to this study, followed by a review of the state of the art in circuit breaker technologies. The chapter concludes with the definition of the main objectives and the scope of the thesis, together with a brief outline of its organization.

1.1 Motivation and Background

According to the European Low Voltage Directive (2014/35/EU), low-voltage direct current (LVDC) systems are defined as electrical systems operating at voltages up to 1500 V. Within this voltage range, LVDC distribution is emerging as a promising solution to improve efficiency and simplify the integration of renewable and distributed energy resources.

Building upon this trend, the adoption of LVDC power distribution systems has expanded across several emerging applications, including electric vehicle charging infrastructure, renewable energy integration, data centers, and direct current (DC) microgrids [1–3]. The shift toward DC architectures is driven by the growing prevalence of inherently DC-based sources and loads—such as photovoltaic panels and battery storage systems—and by the increasing demand for higher efficiency in power conversion. Compared to conventional alternating current (AC) systems, DC distribution offers several advantages, including the elimination of reactive power, the absence of frequency synchronization requirements, reduced conversion stages, lower transmission losses, and simplified interconnection of distributed energy resources [4–7]. These benefits translate into improved overall system efficiency, reduced equipment size, lower cost, and better performance, particularly in applications where bidirectional power flow and fast dynamic response are required.

Despite these advantages, the widespread deployment of LVDC systems is still limited by the lack of reliable and standardized protection [8, 9]. In particular, the ability to interrupt fault currents safely and rapidly remains one of the major technological challenges [10–12]. Fast current interruption is essential to limit the energy dissipated during a fault, prevents damage to semiconductor devices and cables, and ensures system stability and safety. Moreover, the inherently low inductivity of DC grids leads to a very high rate of rise of short-circuit currents, which can reach destructive values within a few hundred microseconds if not properly cleared, further emphasizing the need for ultra-fast interruption [12, 13].

The fundamental difficulty in interrupting DC currents arises from the absence of natural current zero-crossings, which in AC systems facilitate arc extinction and allow smooth contact separation [14, 15]. In a DC network, once an arc is established between separating contacts, the current can continue to flow steadily and maintain the plasma channel unless the circuit breaker actively forces it to zero through an external mechanism. Achieving this condition requires either the generation of a sufficiently high counter-voltage to reverse the current or the implementation of auxiliary circuits designed to divert, limit, or absorb the fault current. Moreover, DC arcs are characterized by greater thermal stability, higher energy density, and longer persistence than their AC counterparts [16]. These combined factors make DC interruption particularly challenging. Consequently, DC circuit breakers continue to represent a major research focus aimed at ensuring safe, reliable, and resilient operation of emerging LVDC power distribution systems.

1.2 State of the Art in DC Fault Protection Devices

Depending on their operating principle and topology, circuit breakers can be broadly classified into mechanical, solid-state, and hybrid types [17]. Each technology exhibits distinct advantages and drawbacks in terms of interruption speed, losses, cost, and reliability.

1.2.1 Mechanical Circuit Breakers

In mechanical DC circuit breakers, two main interruption approaches are commonly employed. The first relies on current injection to create an artificial current zero, typically using an LC oscillation circuit connected in parallel with the mechanical switch. When a fault occurs, the pre-charged capacitor is discharged, driving an opposing current through the switch. This injected current cancels the fault current, producing a zero-current crossing that enables arc-free contact separation. To ensure interruption under all conditions, the peak injected current must be at least equal to the prospective fault current. In addition, its rate of rise must exceed that of the fault current so that the current zero occurs before the fault current reaches its prospective value, thereby limiting the peak short-circuit current. During contact opening, the current commutates to the energy absorption branch—typically a metal-oxide varistor (MOV)—where the stored energy is dissipated. The topology of this approach is illustrated in Fig. 1.1.

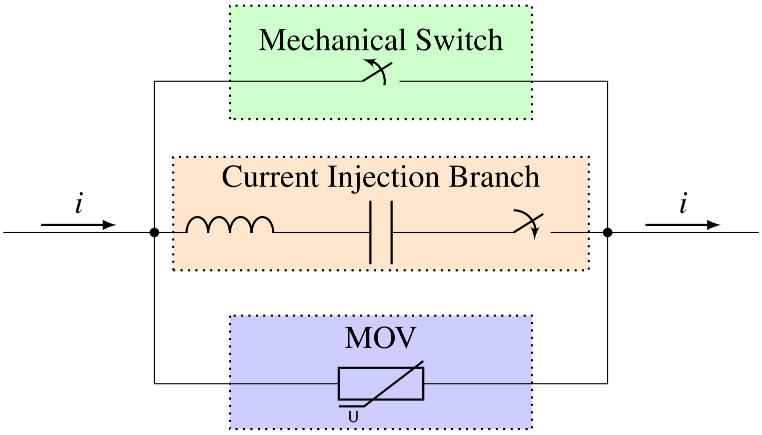

Fig. 1.1 Topology of a mechanical breaker with current injection.

The current injection principle for high-voltage direct current (HVDC) circuit breakers was first introduced in [18], establishing the basis for generating an artificial current zero through the discharge of a pre-charged LC circuit. It was later implemented in practical HVDC breakers employing current injection [19]. A recent study reports the realization of a mechanical HVDC breaker using the same approach in a voltage-source converter (VSC) HVDC system [20]. Subsequent research enhanced interruption process by shaping the current near zero crossing [21] and optimizing the injection topology to extend operating range and reduce component stress [22].

In contrast to the current-injection method, the second approach used in mechanical DC circuit breakers relies on arc formation between the contacts to interrupt the current, rather than generating an artificial current zero. The key to achieving interruption in this approach is to increase the impedance of the electric arc. A higher arc impedance results in a larger arc voltage, which leads to faster current extinction, improved interruption efficiency, and reduced energy dissipation in the contacts. As a result, the overall breaker can be made more compact, and contact degradation is significantly reduced.

One common way to increase the arc impedance is to use splitter plates, often in combination with a magnetic field that drives the arc into the plates through the Lorentz force. As the contacts separate and the arc forms, the magnetic field pushes the plasma column sideways into the splitter stack, where it is divided into several smaller arc segments. The splitter plates not only elongate the arc but also act as heat sinks, absorbing a significant portion of the thermal energy and thereby cooling the plasma. This combined effect increases the arc voltage and accelerates its extinction. Figure 1.2 shows a circuit breaker with arc deflection and splitter plates.

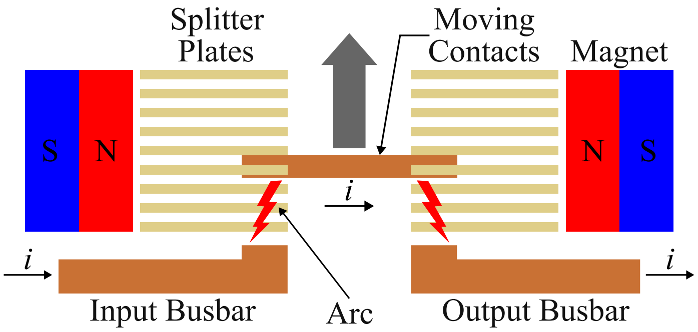

Fig. 1.2 Mechanical circuit breaker with magnetic arc deflection and splitter plates [23].

Another way to increase the overall arc voltage is to use three- or four-pole AC breakers with their poles wired in series [24], which raises the effective arc voltage and improves the breaking performance, albeit at the expense of larger size and higher cost. This configuration, illustrated in Fig. 1.3, distributes the arc across multiple contact gaps, increasing the total arc length and facilitating faster current interruption. Despite their relatively slow operation, these breakers remain attractive due to their simplicity, high reliability, and negligible conduction losses during normal operation.

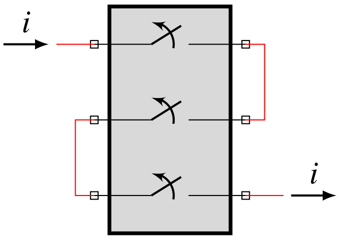

Fig. 1.3 Three-pole circuit breaker with poles wired in series.

In practical mechanical DC circuit breakers that operate without current injection, it is common to combine several arc-management techniques to achieve reliable interruption. Splitter plates, magnetic arc deflection, and the series arrangement of poles are often used together to increase the arc impedance, elongate its path, and accelerate cooling. In addition, an energy absorption branch—typically implemented with a MOV [23]—is frequently included so that part of the stored energy is dissipated in the MOV rather than entirely in the arc. This approach reduces contact erosion and extends the breaker's lifetime; however, careful design is required to ensure proper current commutation to the energy absorption branch once the contacts separate.

The actuator that drives the moving contact plays a crucial role in the overall performance of a mechanical DC circuit breaker, as it directly influences the elongation of the electric arc and, consequently, its impedance. A faster and larger contact displacement increases the arc length, raises its voltage, and promotes quicker current extinction. Therefore, the use of ultrafast actuators is essential to achieve rapid contact separation and to limit the fault current at the earliest possible stage. Among the available technologies, piezoelectric and electromagnetic actuators are the most prominent solutions for high-speed mechanical motion [25]. Piezoelectric actuators provide high energy efficiency, precise displacement control, and excellent repeatability; however, their maximum stroke is typically below 2 mm [26]. In contrast, electromagnetic actuators—particularly the Thomson coil design—can achieve displacements of up to 30 mm and contact velocities around $30\,\mathrm{m/s}$ [27–29], making them highly suitable for fast switching and high-voltage isolation in DC circuit breaker applications.

Mechanical DC circuit breakers offer advantages for low- and medium-voltage applications. Their operation is based on direct mechanical contact separation, providing a structurally simple and efficient solution. During normal operation, current flows through metallic contacts, resulting in very low conduction losses. When open, they ensure galvanic isolation and complete physical disconnection—an important safety requirement. They require no complex cooling or control electronics, simplifying integration and maintenance. However, limited switching speed and contact degradation due to arcing increase energy dissipation and fault-clearing times compared to solid-state or hybrid breakers.

1.2.2 Solid-State Circuit Breakers

Solid-state circuit breakers (SSCBs) have emerged as a promising alternative to conventional mechanical circuit breakers for protection in DC power systems [30–32]. Their main advantage lies in the use of semiconductor devices as switching elements, which enables microsecond-level interruption and arc-free operation due to the absence of moving parts.

The performance of a solid-state circuit breaker is largely determined by the characteristics of its semiconductor device, which define its voltage blocking capability, current handling capacity, switching speed, and power losses. SSCBs typically employ silicon-based devices such as insulated-gate bipolar transistors (IGBTs), metal–oxide–semiconductor field-effect transistors (MOSFETs), silicon-controlled rectifiers (SCRs), and integrated gate-commutated thyristors (IGCTs). In recent years, wide-bandgap (WBG) semiconductors, SiC MOSFETs and GaN high-electron-mobility transistors (HEMTs), have attracted increasing attention owing to their superior switching performance, lower conduction and switching losses, and improved thermal properties.

Among the available semiconductor technologies for SSCBs, Si MOSFETs are commonly employed in applications below 1 kV due to their fast switching speed and low conduction losses, although their limited voltage rating restricts use at higher voltages [33, 34]. In a similar range, GaN HEMTs offer even faster switching and lower losses, making them suitable for compact, high-efficiency SSCBs, though their blocking voltage is typically limited to 600–650 V [35]. SiC MOSFETs extend the voltage capability of Si devices, providing blocking voltages up to 3.3 kV [30], lower switching losses, and improved thermal performance due to higher thermal conductivity and allowable junction temperatures, making them attractive for low- and medium-voltage SSCBs [36]. At higher voltage and power levels, IGBTs operate in the 1–10 kV range [37], while IGCTs [38] and SCRs [39] can exceed 10 kV, offering high current capability and surge robustness at the expense of higher conduction losses and slower response times. It should be noted that SCRs are semi-controlled devices that can only be turned off when the anode–cathode current reaches zero; therefore, in DC applications they typically require additional commutation circuitry to force a current zero for turn-off.

During current interruption, the energy stored in the line or load inductance must be dissipated or redirected to prevent overvoltage stress on the semiconductor device. To achieve this, SSCBs integrate a voltage clamping or energy absorption branch, which ensures safe current decay and protects the main switch from overvoltage transients. Several clamping techniques are used depending on the voltage and energy level of the application.

MOVs provide a nonlinear voltage-dependent impedance, remaining insulating under normal conditions and becoming conductive when the voltage exceeds their clamping level. They can absorb large energy surges and are widely used in medium- and high-energy SSCBs [38]. Once the fault current decays to zero, the MOV returns to its high-impedance state, completing interruption. RC or RCD snubbers—consisting of a resistor-capacitor network, with the RCD variant including a diode for unidirectional energy discharge—provide controlled energy dissipation by storing transient energy in a capacitor and dissipating it through a resistor, limiting the voltage derivative across the semiconductor, making them suitable for low- to medium-power SSCBs [30, 31]. Transient voltage suppression (TVS) diodes rely on avalanche conduction to clamp fast, low-energy voltage spikes [40]. Although their energy-handling capability is limited, they offer extremely fast response, making them effective for auxiliary protection. Each clamping method represents a trade-off between response speed, energy absorption, and cost: MOVs are preferred for robustness and simplicity, while snubbers and TVS diodes are used where transient shaping and precision are required.

The overall configuration of an SSCB depends on how the semiconductor switch, clamping branch, and auxiliary components are connected. The main topologies are classified as fully controlled and semi-controlled. Fully controlled topologies use actively driven devices such as IGBTs, MOSFETs, or IGCTs for conduction and interruption, offering fast response but requiring complex gate control and limited by device current ratings. Semi-controlled topologies, typically based on SCRs, achieve commutation through auxiliary resonant circuits; they are simpler and efficient for high-current, medium-voltage applications but rely on external energy absorption circuits. In these configurations, a current injection branch, usually an LC network, generates a reverse current that forces the SCR below its holding current. Figure 1.4 illustrates representative SSCB implementations for both topologies.

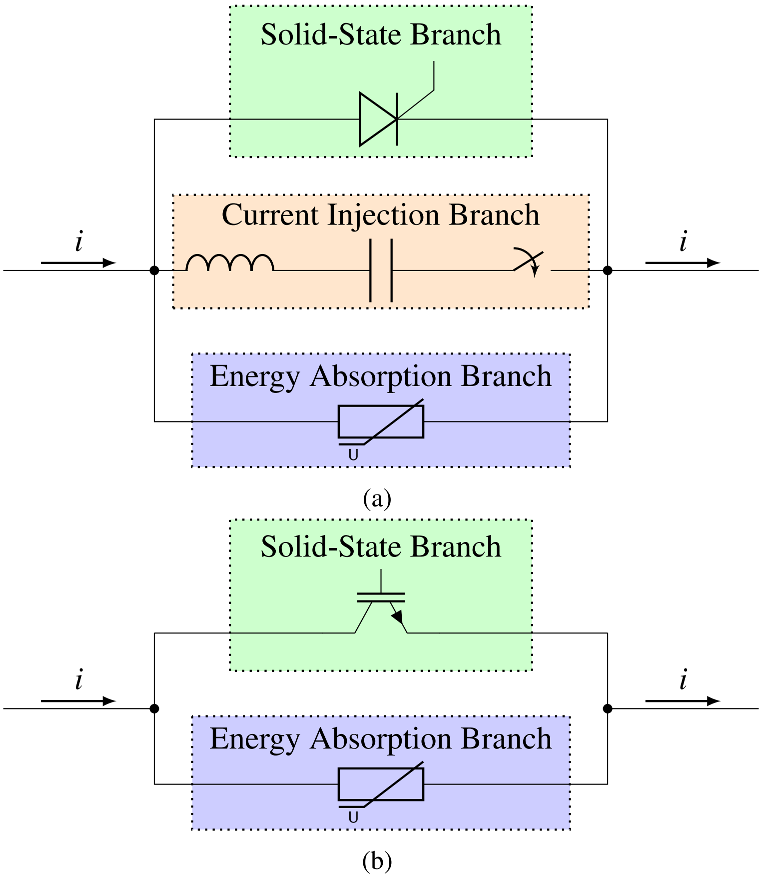

(a)

(b)

Fig. 1.4 Solid-state circuit breaker topologies: (a) semi-controlled topology using an SCR, an LC resonant current-injection branch, and a MOV for energy absorption; (b) fully-controlled topology using an IGBT with a MOV in the clamping branch.

SSCBs enable ultrafast, arc-free fault interruption, providing high speed, silent operation, and easy coordination with control systems. Their main drawbacks are thermal management challenges, and cost, especially at high voltages and currents. They also lack galvanic isolation, and semiconductor failures often create short circuits, hindering fault clearance. Research focuses on wide-bandgap devices, improved energy absorption circuits, and hybrid designs. SSCBs are best suited for low- and medium-voltage DC grids, aerospace, marine, and fast-charging applications.

1.2.3 Hybrid Circuit Breakers

Hybrid circuit breakers (HCBs) combine mechanical and solid-state switching technologies to achieve fast, reliable, and arc-free current interruption while minimizing conduction losses during normal operation. They have emerged as a promising solution for low- and medium-voltage DC applications, where purely mechanical breakers are too slow and fully solid-state designs suffer from high on-state losses. By integrating the advantages of both technologies, HCBs offer an effective balance between speed, efficiency, and robustness, enabling fault interruption in tens to hundreds of microseconds.

An HCB consists of three main components [41]: a mechanical switch, a solid-state branch, and an optional auxiliary commutation circuit. The mechanical switch conducts during steady-state operation with minimal losses, while the solid-state branch—based on devices such as IGBTs, MOSFETs, or thyristors—operates only during fault interruption, enabling fast and arc-free current breaking. An energy absorption branch, typically a MOV or a snubber, dissipates the energy stored in the line inductance after interruption. Figure 1.5 illustrates the topology of a hybrid circuit breaker. The semiconductor and energy-absorption technologies were discussed in the previous subsection; the following discussion focuses on the commutation mechanisms that govern hybrid breaker operation.

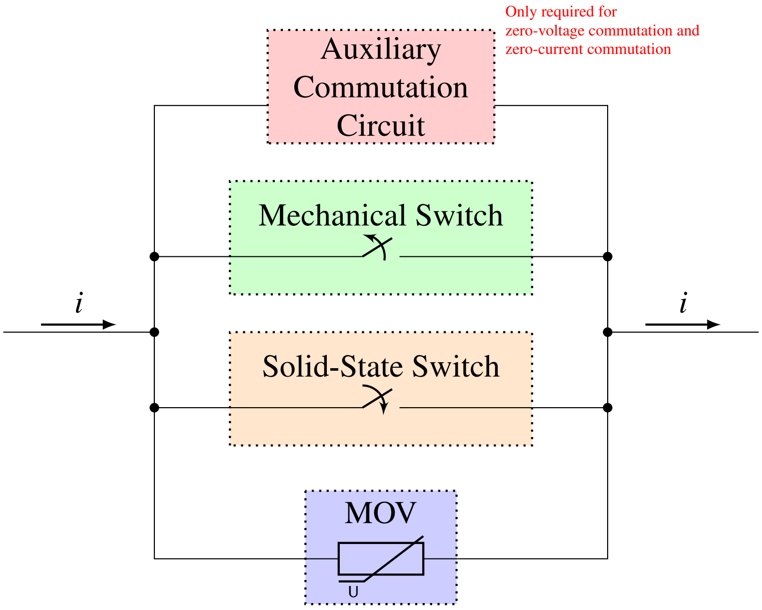

Fig. 1.5 Topology of a hybrid circuit breaker.

Depending on the way current is transferred between the mechanical and solid-state branches, different commutation methods are employed. The simplest approach relies on arc-based commutation, where, once a fault is detected, the solid-state switch is turned on and the mechanical switch begins to open. As the contacts separate, an arc forms and the voltage across it gradually increases. This rising arc voltage drives a progressive current transfer from the mechanical path to the solid-state branch, which eventually carries the entire fault current. In this configuration, the arc voltage itself acts as the driving force for commutation, allowing fault current transfer without auxiliary circuitry. Although this approach is relatively simple, it still involves arcing and contact erosion, which limit the breaker's lifetime and make it less suitable for applications requiring frequent operation. A practical demonstration of this concept is presented in [42], where a test setup validates the current transfer mechanism through arc-assisted commutation.

A more controlled technique is the zero-voltage commutation (ZVC) method. In this approach, an auxiliary circuit—typically implemented as an LC branch or snubber network—limits and shapes the voltage across the mechanical switch during the commutation phase [41]. By keeping the contact voltage close to zero, ZVC prevents premature arcing and reduces the electrical stress on the contacts. Once the current has fully transferred to the solid-state branch, the mechanical switch opens under near-zero-voltage conditions, achieving arc-free operation and extending the lifetime of the mechanical component. In [43], a practical implementation of the ZVS concept is demonstrated using a snubber-based voltage clamping circuit.

The zero-current commutation (ZCC) method takes the concept further by ensuring that the current through the mechanical switch becomes zero before contact separation. This is achieved using an auxiliary LC resonant circuit that generates a reverse current to cancel the forward current in the mechanical path. When the net current approaches zero, the mechanical contacts open without arcing. In [44], a hybrid circuit breaker implementing the ZCC method is presented, experimentally demonstrating arc-free operation through resonant current injection.

1.2.4 Non-Reclosing Protective Devices

Pyrofuses and current-limiting fuses have emerged as alternatives for DC fault protection, particularly in low-voltage systems where cost, conduction losses, and simplicity are critical. Unlike semiconductor-based schemes, pyrofuse solutions use a pyrotechnically actuated mechanical disconnect to provide rapid conductor separation. This approach ensures galvanic isolation, compact design, and negligible on-state losses, making it suitable for applications where single-use protection and reduced complexity are acceptable trade-offs.

A fuse interrupts faults by melting its conductive element when current exceeds a threshold. The melting creates an arc inside the sand-filled body, whose voltage rise limits the fault current and dissipates inductive energy. Melting time depends on the ratio between short-circuit current and nominal rating—higher currents result in faster melting and shorter clearing times, whereas moderate overcurrents require longer interruption. Consequently, a fuse alone is often insufficient in DC applications, as it may not clear low overcurrents within an acceptable time.

To overcome these limitations, a pyrofuse (also called pyroswitch) is integrated in the protection branch. It consists of a low-resistance copper link mechanically severed by a small pyrotechnic actuator when triggered. Upon activation, an explosive charge drives a cutter or piston that breaks the conductor, achieving complete electrical isolation within a few hundred microseconds. Although the pyrofuse opens extremely fast, it cannot absorb significant energy or interrupt large fault currents directly; therefore, it must be combined with a fuse that first limits or extinguishes the current. Figure 1.6 shows a schematic of the fuse structure and pyrofuse assembly.

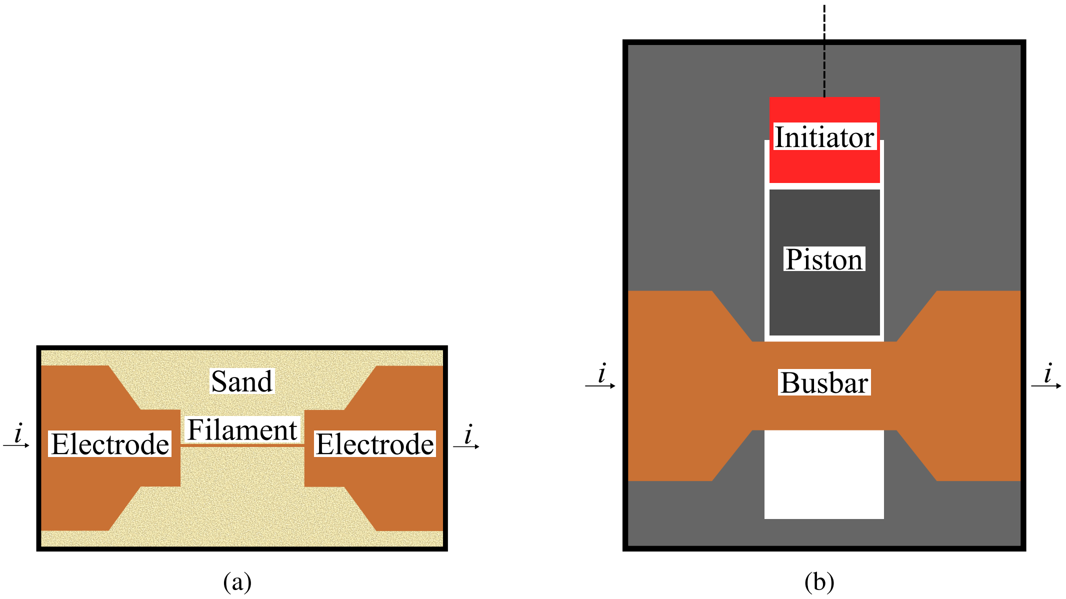

(a) (b)

Fig. 1.6 Structure of (a) fuse and (b) pyrofuse.

Two control strategies are typically used to coordinate the operation of the fuse and pyrofuse: passive and active triggering [45]. In the passive-triggered topology, shown in Fig. 1.7, the pyrofuse is activated by the voltage developed across a triggering fuse. Under normal conditions, the voltage drop across the fuse is negligible, and no current flows through the pyrofuse initiator. When a fault occurs, the fuse melts and an arc forms, causing its voltage to rise to several hundred volts—enough to drive current through the initiator and ignite the pyrotechnic charge. The triggering fuse must limit the current before the pyrofuse opens; if it melts too quickly, the remaining current may still be too high, risking incomplete interruption or mechanical failure of the pyrofuse.

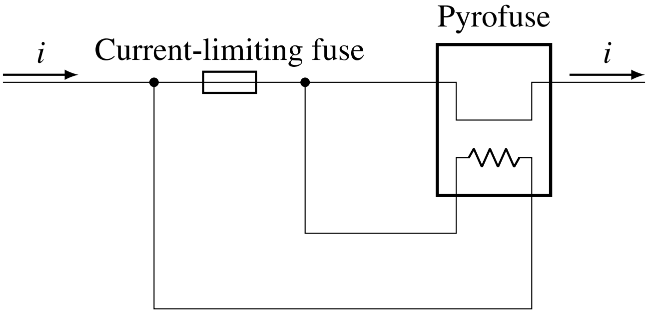

Fig. 1.7 Passive-triggered pyrofuse-based hybrid circuit breaker.

In contrast, active-triggered architectures employ a control circuit and semiconductor switch to detect the fuse's melting state and command the pyrofuse at the optimal instant, as illustrated in Fig. 1.8. This active coordination prevents premature triggering and guarantees that the pyrofuse operates only when the current has decreased to a safe level. Such designs achieve higher reliability and repeatability but require additional sensors and control electronics. An example of this approach is demonstrated in [45].

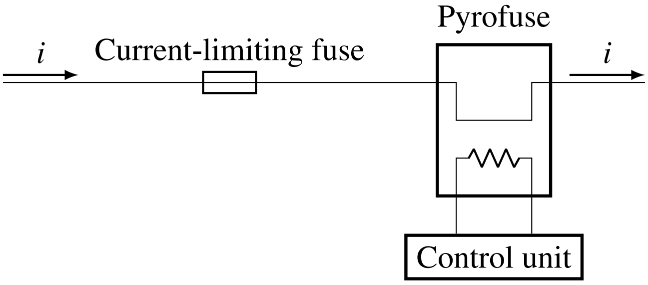

Fig. 1.8 Active-triggered pyrofuse-based hybrid circuit breaker.

A further improvement can be achieved by connecting an additional fuse in parallel with the pyrofuse, as proposed in [46]. This topology, illustrated in Fig. 1.9, allows the current to flow entirely through the pyrofuse branch under normal operation. When a fault occurs, the pyrofuse is triggered, and its rapid mechanical opening produces a transient voltage that commutates the current into the parallel fuse. Once the current flows through the fuse, an internal arc is formed whose voltage rises above the system voltage, forcing the current to decrease and dissipate the stored inductive energy. For this scheme to operate reliably, the fuse parameters must be carefully chosen. The current rating should be relatively low so that the fuse melts quickly—fast melting results in faster interruption. The voltage rating should be high because the arc voltage is directly proportional to the fuse's voltage class. In practice, a high-voltage, low-current-rated current-limiting fuse provides the best performance.

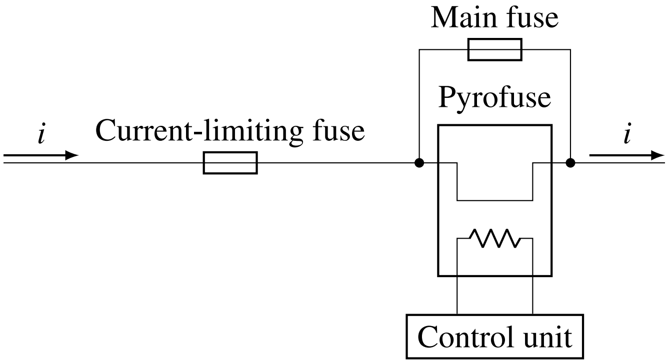

Fig. 1.9 Pyrofuse-based hybrid circuit breaker with a parallel fuse for enhanced energy dissipation and faster fault interruption.

Pyrofuses are particularly well suited for applications that demand ultrafast fault interruption and complete galvanic isolation, while accepting single-use protection. They are especially attractive in DC systems that can provide very high prospective short-circuit currents, where the fault current can rise extremely fast and must be cleared within a few hundred microseconds to avoid severe damage. Typical examples include battery protection in electric vehicles and energy storage systems, as well as aerospace, automotive, and other safety-critical DC networks, where compactness, reliability, and clean disconnection are essential. In these environments, conventional mechanical breakers are often too slow, while fully solid-state solutions may be penalized by high cost and continuous conduction losses.

Pyrofuses offer galvanic isolation, compact design, and low cost. When properly coordinated with a current-limiting fuse, they enable rapid fault interruption, though not as fast as their solid-state counterparts. Their main drawbacks are the single-use nature of the pyrotechnic element and the need for accurate fuse–pyrofuse coordination. Overall, the two approaches are complementary: solid-state designs prioritize speed and control, while pyrofuse-based solutions emphasize simplicity, isolation, and cost efficiency.

1.2.5 Summary and Discussion

Mechanical DC breakers are valued for their simplicity, robustness, low cost, and negligible conduction losses during normal operation. Once open, they provide complete galvanic isolation, ensuring full electrical separation. However, their performance is limited by the physics of electric arcs. The absence of natural current zero crossings in DC systems results in longer interruption times and higher contact erosion. Although techniques such as splitter plates, magnetic arc deflection, series pole wiring, and MOV energy absorption can improve interruption capability, they also increase system size and design complexity. Current mechanical breakers cannot achieve the sub-millisecond interruption times demanded by modern LVDC systems.

Solid-state breakers offer the fastest and most controllable interruption, typically in the microsecond range, since they have no moving parts and operate without arcing. They are silent, precise, and easy to integrate into control and monitoring systems. Their main limitations are continuous conduction losses caused by the voltage drop across semiconductor devices, the need for complex cooling and protection systems, and the lack of galvanic isolation. Semiconductor failures usually result in short circuits, which can prevent fault clearance. Overall, SSCBs are best suited for applications where speed and control outweigh cost and efficiency concerns.

Hybrid breakers combine the low conduction losses of mechanical contacts with the fast interruption capability of solid-state switches. The current flows through the mechanical path under normal operation, while the semiconductor branch handles current only during fault interruption, providing arc-free operation. However, these breakers are more complex and costly, as they require auxiliary commutation circuits (for zero-voltage or zero-current commutation). They also lack galvanic isolation because the semiconductor branch remains electrically connected even after interruption. Despite these challenges, hybrid SSCBs are widely regarded as one of the most practical solutions for achieving both efficiency and fast response in LV and MV DC systems.

Pyrofuses offer very low on-state losses, compactness, and complete galvanic isolation after operation. The pyrofuse rapidly severs the conductor when triggered, but since it cannot absorb significant fault energy, it must be combined with a current-limiting fuse. The coordination between the fuse and pyrofuse is crucial to ensure that the current is sufficiently reduced before the pyrofuse operates. Parallel-fuse topologies enhance energy dissipation and reduce current stress but require careful selection of a high-voltage, low-current-rated fuse to achieve the desired arc voltage and commutation performance. Although slower than solid-state-based designs—with typical interruption times of 1–5 ms—pyrofuse hybrids are inexpensive, reliable, and fast enough for most low-voltage DC systems.

Mechanical breakers remain the simplest and most efficient in terms of losses but are inherently slow. Solid-state breakers deliver unmatched speed and controllability but at high cost, higher losses, and no galvanic isolation. Hybrid designs with semiconductor branches balance these trade-offs by combining speed and efficiency, while pyrofuses emphasize low cost, compactness, and isolation, though they are single-use and require precise coordination. In short, each technology occupies a different niche: mechanical for robustness and isolation, solid-state for ultrafast protection, semiconductor-hybrids for performance balance, and pyrofuses for cost-sensitive, compact DC systems.

1.3 Objectives and Scope of the Thesis

The main objective of this thesis is to demonstrate the feasibility of a railgun-based actuator for single-use, ultra-fast current interruption in LVDC protection systems. The study also aims to show that this technology can surpass the speed, energy-limiting capability, and overall performance of conventional single-use protection devices, including current-limiting fuses and hybrid breakers based on pyrofuses.

To achieve this, a hierarchy of models, with different levels of fidelity and computational cost, is developed. The first level consists of an analytical model that provides a simplified yet insightful representation of the actuator's electromechanical behavior, allowing fast design iterations and scalability studies. The second level corresponds to a quasi-static model, which incorporates the main nonlinearities and spatial effects while maintaining moderate computational requirements. The third level is a transient multiphysics finite-element method (FEM) model, which couples electromagnetic, motional, and thermal physics to capture the detailed dynamic behavior of the system with high accuracy. The comparison among these models allows the evaluation of their validity range and the establishment of a balance between computational efficiency and predictive capability.

In parallel, the thesis also aims to design and develop a pulse-power electric drive capable of supplying the energy required to operate the railgun actuator. The drive must deliver peak currents exceeding 150 kA with a pulse peak time shorter than 25 µs, ensuring sufficient electromagnetic force to accelerate the armature and open the contacts. A dedicated charging unit is designed to charge the capacitor bank of the drive safely and efficiently.

The scope of the thesis is therefore limited to the modeling, design, and experimental validation of the railgun actuator and its associated pulse-power drive. The development of a complete DC circuit breaker prototype lies beyond the present work and is identified as future research.

1.4 Thesis Outline

The thesis is organized into five main chapters:

Chapter 1: This chapter introduces the motivation and background of the research, reviews the current state of the art in DC circuit breaker technologies, and defines the objectives and scope of the thesis.

Chapter 2: It focuses on the system integration of the proposed ultrafast circuit breaker. It describes the overall system architecture, the interaction between the main subsystems, and the design considerations required to integrate the actuator, the drive, and the mechanical interrupter into a unified protection device.

Chapter 3: In this chapter the design and implementation of the electric drive supplying the railgun actuator is presented. It details the requirements, component selection, and modeling of the pulse-power stage, including capacitor and switch technologies. The chapter also describes the experimental validation of the drive and the development of the capacitor bank charging unit.

Chapter 4: This chapter is dedicated to the railgun actuator. It first reviews the state of the art and operating principles of railgun-based systems, then introduces the modeling approach at three levels of fidelity: analytical, quasi-static, and transient multiphysics. The chapter concludes with the experimental validation of the actuator and an analysis of the influence of the spring-loading and rail–armature contact mechanisms on the overall performance.

Chapter 5: This chapter concludes the thesis by summarizing the main findings and outlining potential directions for future research in this field.

Chapter 2

System-Level Performance of the Railgun-Based Ultrafast Circuit Breaker

Chapter 2 presents a system-level evaluation of the proposed railgun-based ultrafast circuit breaker. The objective of this model is to assess the potential of a railgun-based breaker, considering an average contact speed of $100\,\mathrm{m/second}$, a realistic value for railgun actuation. After introducing the simplified fault model, the chapter analyzes the performance under different system inductances. The results are compared against pyrofuses, the closest single-use benchmark. A comparison with a Thomson coil actuator, the state of the art in ultrafast breakers, concludes the chapter.

2.1 System Description

Figure 2.1 shows the overall system configuration, and the corresponding parameters are listed in Table 2.1. These values are representative of typical LVDC systems such as EV charging stations, photovoltaic power plants, and data centers. The source is modeled as an ideal voltage supply $\mathrm{V_s}$, representing the output capacitors of a power converter, a battery, or a DC bus. Although modeled as ideal with infinite current capability, the actual short-circuit current is limited by the stray resistance of the capacitors or the battery's internal resistance. The transmission line, including cables and interconnections, is characterized by series resistance $\mathrm{R_s}$ and inductance

L_s, while the load is modeled as a series branch composed of R_l and L_l. The nominal voltage and current are 800 V and 800 A, corresponding to 640 kW. During a fault, the breaker trips when the current exceeds 1200 A (1.5 times nominal). A similar fault model was used in [47].

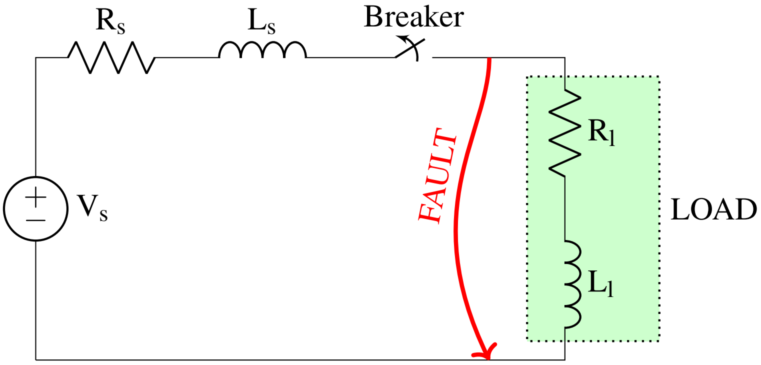

Fig. 2.1 System-level fault model used for the analysis.

Table 2.1 System electrical parameters.

Parameter	**Value**
V_s	800 V
R_s	25 mΩ
L_s	10–100 µH
R_l	1 Ω
L_l	10 µH

The simulations are performed in the Simulink environment. In this model, the mechanical circuit breaker is represented by an ideal switch in series with a controlled voltage source. The ideal switch captures the contact-opening action, while the controlled source reproduces the arc voltage developing across the breaker once separation begins. The arc voltage is defined by the following expression:

$$v_{\mathrm{arc}} = 2\,\mathrm{k}\,\dot{y}_{\mathrm{avg}}\,t, \tag{2.1}$$

where v_{arc} denotes the arc voltage, $\dot{y}_{\mathrm{avg}}$ the average opening speed of the contacts, t the elapsed time since arc initiation, and k a constant linking the arc voltage to the arc length. Experimental observations in [48] indicate that arc gradients can reach approximately 85 V/mm. To maintain a conservative modelling assumption, this work adopts a reduced value of 50 V/mm. For a maximum contact travel of 15 mm, the resulting peak arc voltage is therefore 1500 V. The factor of two reflects the presence of arcs developing on both contact surfaces, as illustrated in Fig. 2.2. Once the current naturally reaches zero, the ideal circuit breaker opens, completing the interruption sequence.

Figure 2.2 depicts the operating principle of the railgun-based mechanical circuit breaker. Under normal conditions, current flows through the busbars and the closed contact set. When a fault is detected, the railgun is triggered and the armature accelerates, driving the contact system open and initiating an arc. The armature is linked to the contact assembly through an electrical insulator, which preserves galvanic isolation between the main current path and the railgun. As the armature travels along its stroke, the contact gap continues to increase until full separation is achieved. Additional insulating elements are installed beneath the busbars to avoid any unintended short circuit across the contact gap once the armature reaches its final position.

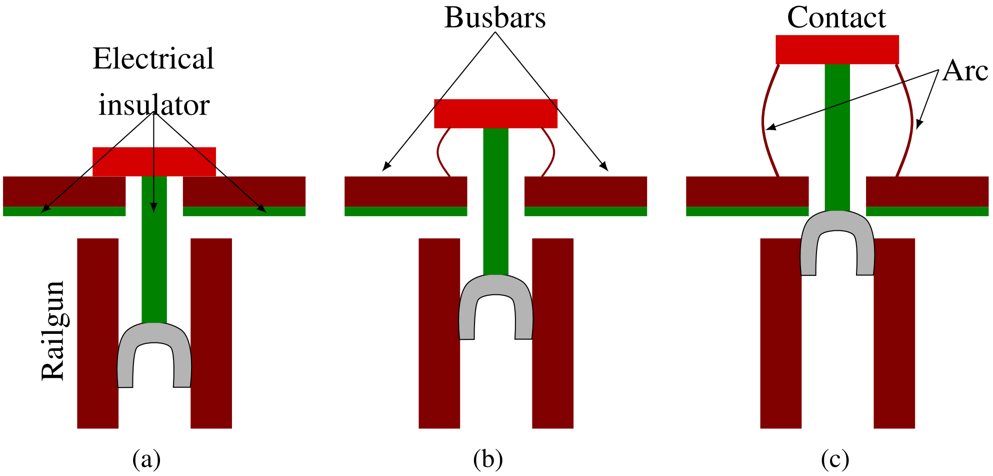

(a) (b) (c)

Fig. 2.2 Railgun-based mechanical circuit breaker at successive stages of operation: (a) nominal conduction with closed contacts; (b) contact separation with the armature mid-stroke; (c) full opening with the armature at the end of its travel.

Figure 2.3 illustrates the prospective short-circuit current for different values of system inductance when a fault occurs directly across the load at $t = 2\,\mathrm{ms}$.

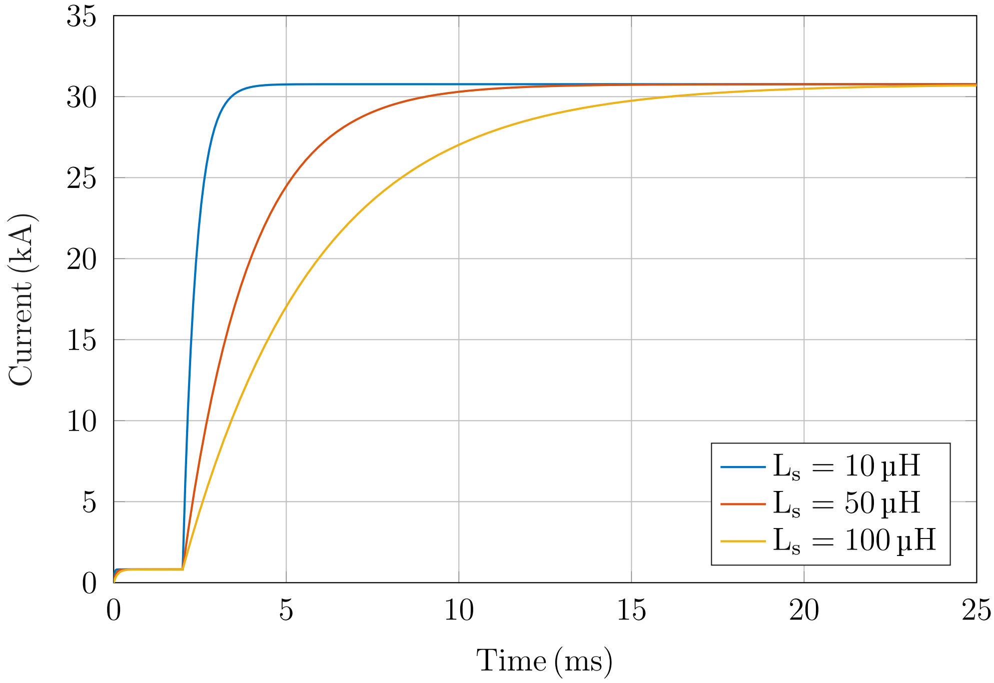

Fig. 2.3 Prospective short-circuit current for system inductances of 10 µH, 50 µH, and 100 µH.

2.2 Influence of the System Inductance on the Current Interruption Process

The system inductance plays a decisive role in the dynamics of fault interruption. When a short circuit occurs, the evolution of the current is governed by the basic relation

$$\frac{\mathrm{d}i}{\mathrm{d}t} = \frac{V_s}{L_s}. \tag{2.2}$$

Figure 2.3 shows that lower inductance values result in a significantly steeper current rise. In practical terms, this means that for low-inductance systems—typical of compact LVDC architectures—the fault current reaches high values within only a few microseconds. Such rapid current escalation places extreme requirements on the breaker, which must initiate contact separation and develop sufficient arc voltage before the current becomes uncontrollable.

Conversely, while low inductance leads to higher $\mathrm{d}i/\mathrm{d}t$, it also facilitates current reduction once the breaker generates a counter-voltage during the interruption process. When the arc voltage v_{arc} exceeds the source voltage $\mathrm{V_s}$, the current derivative becomes negative and the current begins to decrease according to

$$\frac{\mathrm{d}i}{\mathrm{d}t} = \frac{\mathrm{V_s} - v_{\mathrm{arc}}}{\mathrm{L_s}}. \tag{2.3}$$

With a small system inductance, the slope of this decay is steep, allowing the current to be forced toward zero very quickly—provided that the breaker is capable of generating a sufficiently high arc voltage in a very short time during the interruption process.

In contrast, higher system inductance reduces the initial rate of rise of the short-circuit current but increases the amount of magnetic energy stored in the loop. The instantaneous magnetic energy stored in the system E_{s} is given by the following expression:

$$E_{\mathrm{s}} = \frac{1}{2}\mathrm{L_s}\, i^2. \tag{2.4}$$

Thus, although the current grows more slowly for larger inductances, the amount of energy that must be absorbed during interruption may become greater. The higher the energy to be dissipated, the lower the efficiency of the interruption process and the larger and more robust the breaker must be to effectively withstand the associated thermal and mechanical stresses.

Overall, the system inductance introduces two opposing effects: low inductances lead to an extremely fast current rise but allow for rapid current suppression once the arc voltage is established, whereas high inductances yield slower fault dynamics but may require more energy to be dissipated during the interruption process, increasing the stress on the breaker.

For the three inductance values considered in this study, Table 2.2 summarizes the initial $\mathrm{d}i/\mathrm{d}t$ and the magnetic energy stored in the system before the fault occurs $E_{\mathrm{s}}(t_0)$.

Table 2.2 Initial $\mathrm{d}i/\mathrm{d}t$ and stored magnetic energy for different system inductances.

$\mathrm{L_s}$ [μH]	$\mathrm{d}i/\mathrm{d}t$ [A/μs]	$E_{\mathrm{s}}(t_0)$ [J]
10	80	3.2
50	16	16
100	8	32

Figure 2.4 illustrates the current interruption process for the three inductance values considered. As previously discussed, the lowest-inductance case ($L_s = 10\,\mu H$) exhibits the fastest current rise, reaching a peak of 5.9 kA within 130 µs; nevertheless, the proposed breaker clears the fault in only 300 µs. For a medium inductance of 50 µH, the peak current is significantly reduced to 2.3 kA, and full interruption is achieved in approximately 520 µs. Finally, in the high-inductance case ($L_s = 100\,\mu H$), the peak current is limited to 1.8 kA, with complete current extinction occurring within 620 µs.

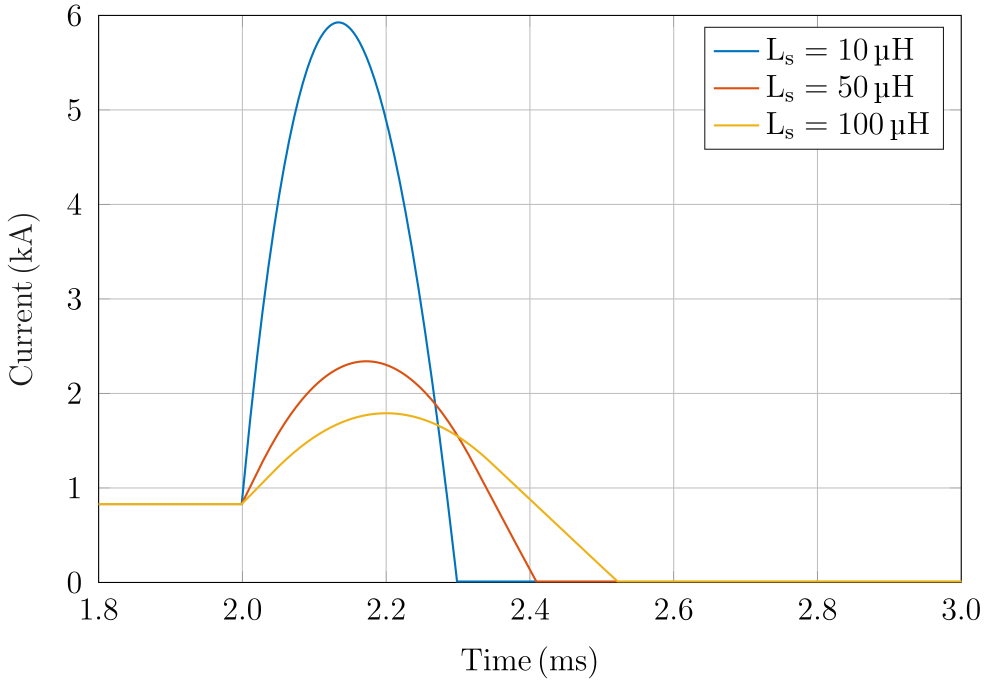

Fig. 2.4 Current interruption for system inductances of 10 µH, 50 µH, and 100 µH.

These results demonstrate that the railgun-based breaker consistently achieves sub-millisecond interruption across a wide range of inductances, outperforming state-of-the-art single-use protection devices. For comparison, the Autoliv PSS-5 pyrofuse provides interruption times of up to 1 ms for $L_s = 25\,\mu H$ at a nominal rating of 500 A and 1000 V [49]. Eaton's EBPS100F40A device reaches interruption times of up to 2 ms for $L_s = 20\,\mu H$ at 400 A and 1000 V [50]. Similarly, the Mersen XP series offers interruption times around 1 ms for 800 A, 1000 V, $L_s = 10\,\mu H$ [51]. In all cases, the proposed railgun-based breaker provides substantially faster interruption while handling significantly higher currents.

The energy dissipated in the breaker, E_b, during the interruption process is also evaluated. This quantity is obtained by integrating the instantaneous power across the breaker contacts, as expressed by

$$E_\mathrm{b} = \int v_\mathrm{arc}\, i \, \mathrm{d}t. \tag{2.5}$$

Figure 2.5 shows the resulting dissipated energy for the different inductance values considered in this study. Although the stored energy in the system is lowest for the 10 µH case—and the interruption time is also the shortest—the dissipated energy is the highest. This occurs because the very low inductance causes an extremely rapid current rise, which in turn produces a high instantaneous arc power and therefore a greater total energy dissipation in the breaker during the entire interruption process. It is also noteworthy that, despite the lower peak current observed in the 100 µH case, the dissipated energy is nearly equal to that of the 50 µH case. This is explained by the longer interruption time associated with higher inductance systems, which compensates for the reduced peak current and ultimately leads to comparable overall energy absorption in the breaker, even though the fault dynamics evolve noticeably more slowly.

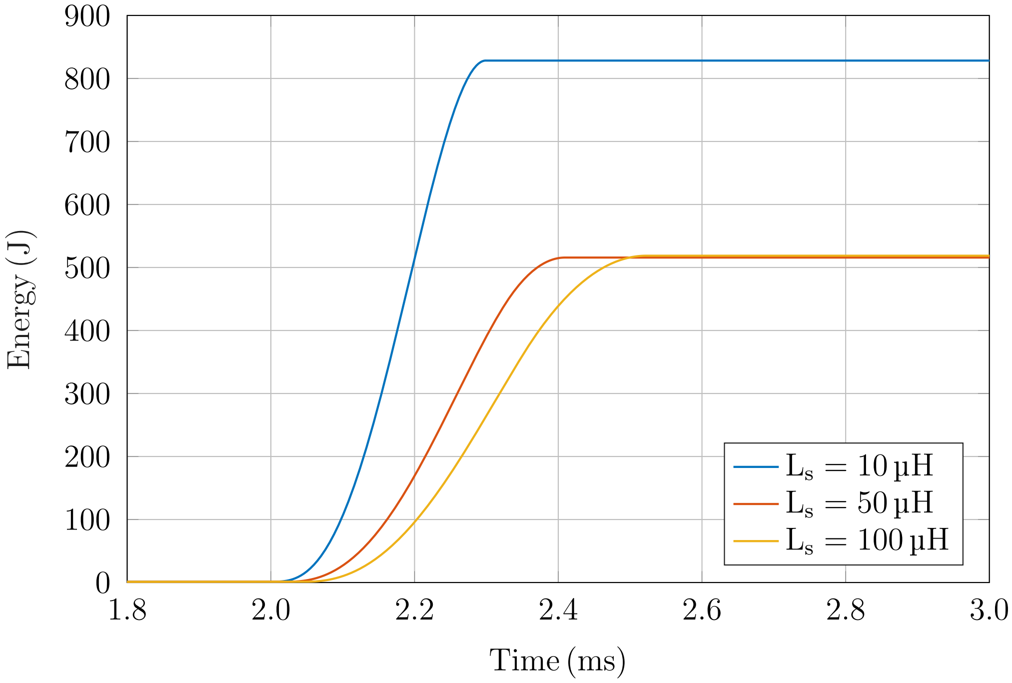

Fig. 2.5 Energy dissipated in the breaker for system inductances of 10 µH, 50 µH, and 100 µH.

2.3 Railgun vs. Thomson Coil Actuation: Impact on the Current Interruption Process

As shown in (2.3), the arc voltage strongly influences the interruption time, as it determines how quickly the current is forced to zero. A higher arc voltage results in a larger negative $\mathrm{d}i/\mathrm{d}t$, accelerating current decay. Equation (2.1) further indicates that arc voltage is proportional to actuator speed: faster contact separation produces higher arc voltage. Actuators capable of higher speeds are therefore more suitable for ultrafast interruption, since they establish larger arc voltages earlier and reduce clearing time.

The Thomson coil is widely regarded as the state-of-the-art electromagnetic actuator for ultrafast DC circuit breakers due to its simplicity and ability to generate large repulsive forces. It operates by discharging a high-current pulse through a flat spiral coil, producing a rapidly varying magnetic field. This field induces eddy currents in a nearby conductive armature (usually an aluminum or copper disk), and the interaction between the induced eddy currents and the resulting magnetic field produces a repulsive Lorentz force that accelerates the movable contact, enabling ultrafast separation. Figure 2.6 illustrates a basic configuration. A fundamental limitation, however, is its relatively high initial inductance, typically around 1 µH, compared to the proposed railgun, which exhibits an inductance below 100 nH. This difference is critical because inductance directly constrains current rise. Since the electromagnetic force is proportional to the square of the current, lower inductance enables faster current buildup and greater initial acceleration.

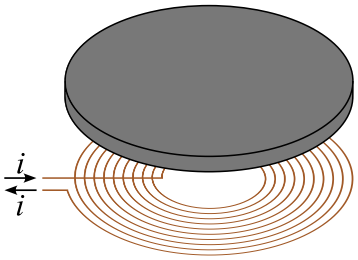

Fig. 2.6 Basic sketch of the Thomson coil actuator.

Reported Thomson coil actuators in the literature exhibit a wide range of achievable velocities, but all remain within the sub-100-m/s domain. In [52], the armature travels 35 mm in 1 ms, corresponding to an average speed of about 35 m/s. The modeling study in [53] reports terminal velocities up to 75 m/s, the closest to the railgun performance, although requiring around 2.5 ms to reach this value. Faster acceleration is observed in [29], showing 23 m/s in 500 µs, while [54] achieves 34 m/s in only 300 µs, representing the best trade-off between speed and reaction time. Experimental work in [55] reports 22 m/s in 1.5 ms, and [56] shows 25 m/s from a 25 mm stroke in 1 ms. Collectively, these data indicate that a Thomson coil can realistically reach an average speed of about 30 m/s within the first 300 µs, providing a practical benchmark for comparison with the railgun-based actuator.

Figure 2.7 shows the arc voltage generated by both actuation mechanisms for a system inductance of 10 µH. In the case of the railgun actuator, the arc voltage rises rapidly and reaches nearly 1.5 kV within approximately 300 µs, whereas the Thomson coil-based actuator achieves only about 1200 V and requires close to 800 µs to reach this value. This difference is fully consistent with the discussion presented earlier: higher actuator speeds lead to faster contact separation, which in turn produces a larger arc voltage in the early stages of the interruption process. The superior acceleration capability of the railgun therefore translates directly into a higher and more rapidly established arc voltage, enabling a substantially faster current extinction compared to the Thomson coil.

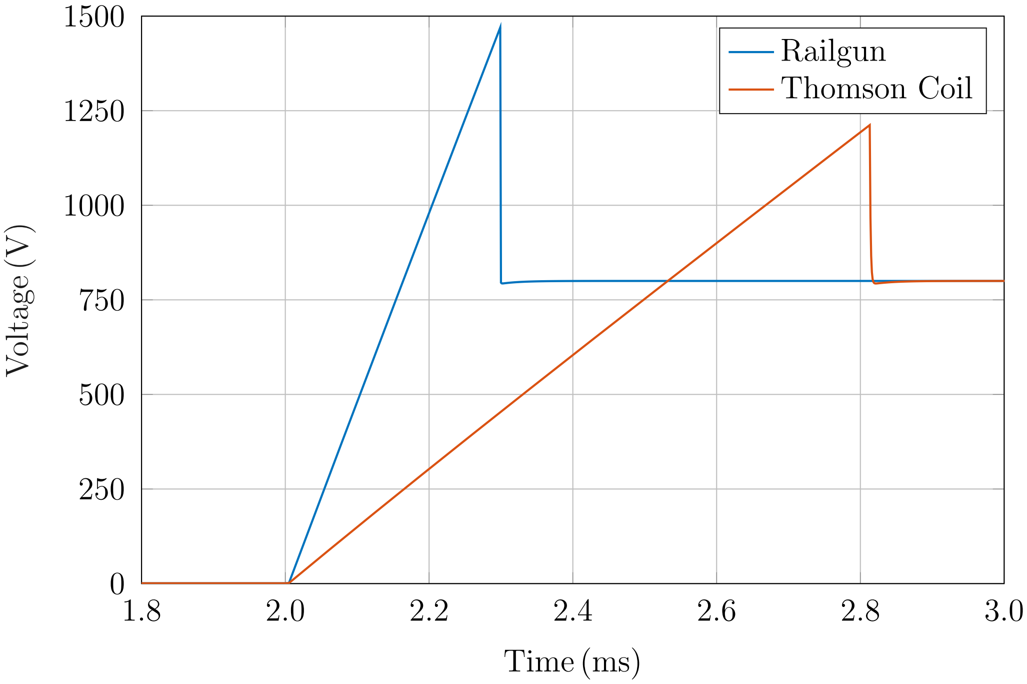

Fig. 2.7 Arc voltage obtained with the railgun actuator and the Thomson coil actuator.

Figure 2.8 illustrates how the higher arc voltage generated by the railgun-based actuator leads to a more effective current interruption compared to the Thomson coil-based breaker. With the railgun, the fault current remains below 6 kA and is fully interrupted within roughly 300 µs. In contrast, the Thomson coil produces a weaker, slower-rising arc voltage, allowing the current to reach nearly 12 kA and persist for more than 800 µs. These results demonstrate that the faster actuator speed of the railgun enables earlier arc-voltage buildup, accelerating current extinction and reducing system stress.

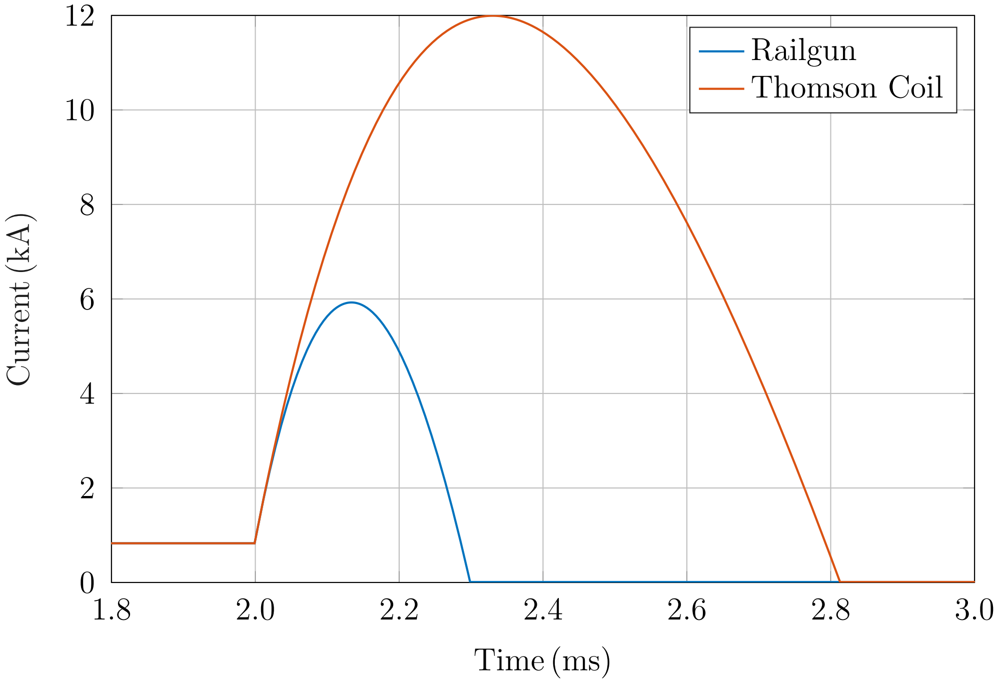

Fig. 2.8 Current interruption process using the railgun and Thomson coil actuators.

The advantages of the railgun-based actuator are also reflected in the energy dissipated during the interruption process. As shown in Fig.2.9, the breaker equipped with the railgun dissipates approximately 900 J during the fault-clearing sequence, whereas the Thomson coil-based breaker dissipates nearly 3.6 kJ. This represents a fourfold increase in dissipation for the Thomson coil. The substantially lower energy in the railgun case is a direct consequence of its faster current extinction and higher arc voltage, which reduce both the magnitude and the duration of the fault current. In contrast, the slower response of the Thomson coil results in a higher peak current and a much longer interruption time, significantly increasing the total energy that must be absorbed by the breaker. A more efficient interruption process not only lowers the thermal and mechanical stress on the components but also reduces degradation of the contact system and arc chamber, ultimately enabling more compact, robust, and longer-lasting breaker designs.

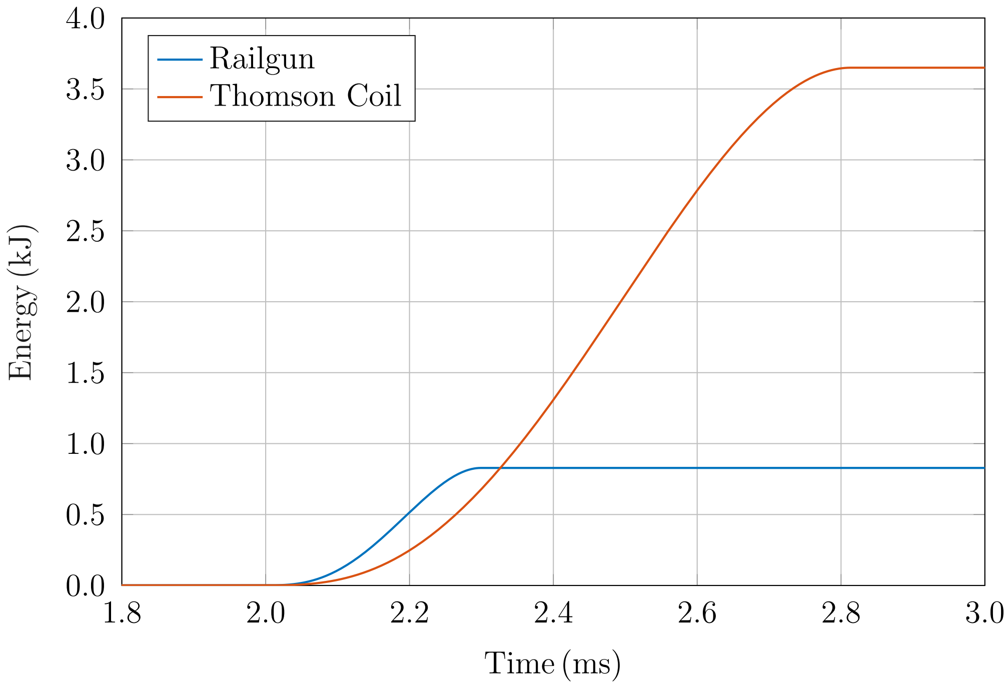

Fig. 2.9 Energy dissipated during the interruption process using the railgun and Thomson coil actuators.

2.4 Summary and Conclusions

This chapter has examined the system-level performance of the proposed railgun-based ultrafast circuit breaker in a simplified LVDC fault scenario, providing a comprehensive evaluation of its interruption capabilities under realistic operating conditions. The analysis first highlighted the crucial influence of the system inductance in shaping both the short-circuit current evolution and the amount of energy that must ultimately be dissipated during the interruption process. Low-inductance systems—typical of compact, cable-dominated LVDC architectures—exhibit extremely fast current rise, placing stringent demands on the breaker. However, once a sufficiently high arc voltage is established, these same low-inductance systems also enable very rapid current suppression. Conversely, higher inductances slow down the initial fault dynamics but significantly increase the stored magnetic energy, thereby imposing greater thermal and mechanical stress on the breaker. The parametric study for $L_s = 10\,\mu H$, $L_s = 50\,\mu H$, and $L_s = 100\,\mu H$ demonstrated that the proposed railgun-based breaker consistently achieves sub-millisecond fault clearing across all cases, while providing effective current limitation and maintaining robustness against a wide range of fault severities.

A comparison with state-of-the-art pyrofuse-based single-use protection devices further quantified the performance benefits of the railgun approach. Commercial pyrofuses such as the Autoliv PSS-5, the Eaton EBPS100F40A, and the Mersen XP series typically exhibit clearing times between 1 ms and 2 ms under comparable voltage, current, and inductance conditions. These devices therefore operate at least an order of magnitude slower than the railgun-based breaker, especially in low-inductance LVDC systems where ultrafast current escalation is most critical. The analysis in this chapter shows that the railgun-based design can interrupt significantly faster, while simultaneously limiting the peak currents and reducing the total interruption energy. As a result, the railgun-based solution offers a clearly superior protection envelope for emerging LVDC applications where high power density and ultrafast fault clearing are essential.

A detailed comparison between railgun and Thomson coil actuation mechanisms was then conducted to assess the role of actuator speed on the arc voltage, current extinction, and energy dissipation. For a representative system inductance of 10 µH, the railgun actuator generated an arc voltage approaching 1.5 kV within roughly 300 µs, while the Thomson coil required nearly 800 µs to reach only 1200 V. This disparity directly translated into markedly different interruption behaviors: the railgun-based breaker limited the fault current to below 6 kA and cleared the fault in around 300 µs, whereas the Thomson-coil-based breaker allowed the current to reach almost 12 kA and needed more than 800 µs to interrupt. Energy dissipation results further reinforced this trend: the railgun-based design absorbed approximately 900 J, compared to nearly 3.6 kJ for the Thomson coil—representing a fourfold reduction. This enhanced efficiency not only lowers thermal and mechanical stress on the breaker but also reduces erosion of the contacts and arc chamber, enabling more compact, durable, and reliable designs.

Overall, this chapter demonstrates that the railgun-based actuator provides substantial system-level advantages over both pyrofuse-based hybrids and Thomson-coil-based electromagnetic breakers. Its ability to generate higher arc voltages at much earlier stages of the fault, combined with faster current extinction and substantially lower interruption energy, positions the railgun-based breaker as a promising solution for next-generation LVDC protection systems requiring ultrafast, reliable, and compact single-use interruption capability.

Chapter 3

The Electric Drive

Chapter 3 focuses on the design and implementation of the electrical drive that powers the railgun-based actuator. The chapter begins by establishing the key electrical specifications for the pulse-power drive, followed by a systematic evaluation of suitable pulse-power topologies. It then presents the detailed design of the electric drive, with particular attention given to the minimization of stray inductance. The chapter concludes with the experimental validation of the drive and a summary of the main design insights.

3.1 Electric Drive Design

The operation of the proposed railgun-based actuator relies on the rapid delivery of a high-current pulse, which places stringent requirements on the electrical drive. To achieve the target armature acceleration and contact separation speed, the drive must supply a current waveform with a peak amplitude exceeding 100 kA and a rise time below approximately 25 μs. These values, derived from the actuator simulation presented in the next section, determine the minimum energy, voltage, and $\mathrm{d}i/\mathrm{d}t$ capability that the drive must provide.

Such requirements are met using the capacitor-discharge pulse-power architecture shown in Fig. 3.1. In this topology, the capacitor bank stores the energy required for the shot, and when the switching device is triggered, this energy is rapidly delivered to the railgun, generating the high-current pulse needed for acceleration. Once the diode becomes forward-biased, it freewheels the railgun current. It is important to note that the parasitic elements of the drive are not represented in the schematic of Fig. 3.1; these will be discussed in detail in the later sections of this chapter.

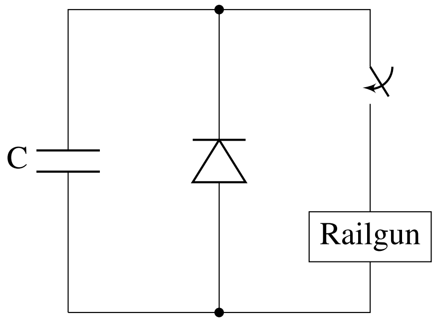

Fig. 3.1 Topology of the pulse-power electric drive used to supply the railgun-based actuator.

3.1.1 Capacitor Bank Design

A wide range of capacitor technologies is available, each tailored to specific electrical, thermal, and mechanical requirements. These technologies exhibit different trade-offs in terms of energy density, voltage rating, current capability, parasitic elements, lifetime, and reliability. Selecting an appropriate capacitor technology is therefore a critical step, as it directly affects the performance, efficiency, and robustness of the electric drive. This section reviews the main capacitor technologies commonly used in power electronics and high-energy systems, highlighting their advantages, limitations, and typical use cases.

Aluminium electrolytic capacitors offer very high volumetric energy density and are widely used in applications requiring bulk energy storage, such as DC-link filtering, UPS systems, and industrial drives. Their main advantages include low cost, high energy density, and availability in high-voltage configurations when used in series. However, electrolytic capacitors suffer from relatively high equivalent series resistance (ESR) and equivalent series inductance (ESL). The ESR limits the permissible peak current due to the associated thermal stress, while the ESL restricts the achievable $\mathrm{d}i/\mathrm{d}t$ by introducing an inductive impedance that slows the current rise. As a result, despite their large energy density, electrolytic capacitors are not appropriate for delivering the fast, high-amplitude pulses required by the railgun-based actuator.

Multilayer ceramic capacitors exhibit very low ESR and ESL, excellent high-frequency characteristics, and high reliability. These properties make them particularly well suited to high-frequency switching converters, resonant circuits, decoupling applications, and fast transient suppression. Nevertheless, their capacitance per volume is limited, especially at high voltage ratings, and they cannot store the energy levels required for large-scale pulse-power systems.

Supercapacitors provide extremely high capacitance values and excellent cycle life. However, their relatively low voltage rating per cell (typically 2.7–3.0 V), high ESR, and limited ability to supply high peak currents on short time scales make them unsuitable for delivering high-power microsecond pulses. Their energy must be released over longer time intervals, and large series stacks introduce balancing requirements and further increase in the ESR. For these reasons, supercapacitors are not a practical option for high-voltage, high-$\mathrm{d}i/\mathrm{d}t$ pulse-power drives.

Polypropylene film capacitors have become the preferred choice for modern pulsed-power applications. They combine low ESR and ESL with high peak current capability, excellent dielectric strength, and long operational lifetime. Their self-healing property enhances reliability by preventing catastrophic failure under localized dielectric breakdown. Film capacitors also offer high voltage ratings, stable capacitance over time and temperature, and very low dissipation factor, all of which are essential for delivering fast high-current pulses. Pulse-grade polypropylene capacitors are specifically designed for applications such as defibrillators, pulsed lasers, railguns, crowbar circuits, and high-power resonant converters. Considering these attributes, polypropylene film capacitors have been selected as the most suitable technology for the capacitor bank of the proposed electric drive.

In order to support the design of the drive, the pulse-power stage is represented by the lumped-parameter circuit shown in Fig. 3.2. The capacitor bank is modelled as an ideal capacitor C initially charged to V_0. The connection between the capacitor bank and the diode is represented by the stray inductance $\mathrm{L}_{\mathrm{stray},1}$ and the stray resistance $\mathrm{R}_{\mathrm{stray},1}$, which mainly capture the ESL and ESR associated with the capacitor and the conduction path from the capacitors to the diode. In a similar manner, the connection between the diode and the load is modelled by the stray inductance $\mathrm{L}_{\mathrm{stray},2}$ and the stray resistance $\mathrm{R}_{\mathrm{stray},2}$. The load is represented only by an equivalent inductance $\mathrm{L}_{\mathrm{load}}$. The load resistance is neglected, as it lies in the range of $10\,\mu\Omega$ to $20\,\mu\Omega$, which is negligible compared with $\mathrm{R}_{\mathrm{stray},1}$ as well as the internal on-state resistance of the diode and the thyristor. Since the impedance of the load is very low—on the order of only a few nanohenries—the dynamics of the circuit are predominantly governed by the stray inductances and resistances.

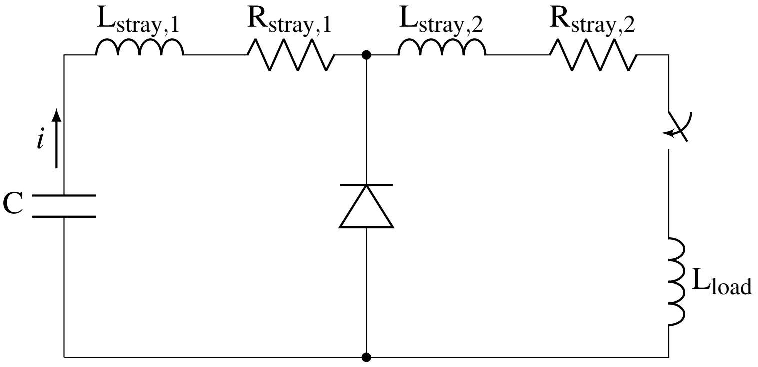

Fig. 3.2 Lumped-parameter representation of the pulse-power drive.

At the beginning of the discharge, the diode is reverse-biased and does not conduct, so the current flows exclusively through the capacitor bank, the stray elements, and the load. Under these conditions, the system behaves as an LCR circuit, where the total inductance L_{tot} is given by the sum of the individual inductances in the loop, i.e.,

$$L_{tot} = L_{stray,1} + L_{stray,2} + L_{tot}. \tag{3.1}$$

Similarly, the total series resistance R_{tot} is

$$R_{tot} = R_{stray,1} + R_{stray,2}. \tag{3.2}$$

The governing equation of the circuit during the initial discharge, when the diode is reverse-biased, is obtained by enforcing Kirchhoff's voltage law around the loop and is given by

$$L_{tot} \frac{di}{dt} + R_{tot} i + \frac{1}{C} \int_0^t i d\tau - V_0 = 0. \tag{3.3}$$

This expression combines the voltage drops across the total loop inductance, the total series resistance, and the capacitor voltage written in integral form. In order to obtain a standard differential equation, (3.3) is differentiated with respect to time. Using the fact that

$$\frac{di}{dt} \left(\int_0^t i d\tau \right) = i, \tag{3.4}$$

differentiation of (3.3) yields

$$\mathrm{L_{tot}}\,\frac{\mathrm{d}^2 i}{\mathrm{d}t} + \mathrm{R_{tot}}\,\frac{\mathrm{d}i}{\mathrm{d}t} + \frac{1}{\mathrm{C}}\,i = 0. \tag{3.5}$$

Equation 3.5 corresponds to the standard homogeneous second-order differential equation of a series LCR network. The initial conditions follow directly from the physical initial state of the circuit. Since the capacitor is initially charged to $\mathrm{V_0}$ and no current flows at $t = 0$,

$$i(0) = 0. \tag{3.6}$$

Evaluating 3.3 at $t = 0$, the integral term vanishes, leading to

$$\mathrm{L_{tot}}\,\frac{\mathrm{d}i}{\mathrm{d}t}(0) - \mathrm{V_0} = 0. \tag{3.7}$$

which yields

$$\frac{\mathrm{d}i}{\mathrm{d}t}(0) = \frac{\mathrm{V_0}}{\mathrm{L_{tot}}}. \tag{3.8}$$

The characteristic equation associated with (3.5) is

$$\mathrm{L_{tot}}\,s^2 + \mathrm{R_{tot}}\,s + \frac{1}{s}, \tag{3.9}$$

with solutions

$$s_{1,2} = \frac{-\mathrm{R_{tot}} \pm \sqrt{\mathrm{R_{tot}}^2 - 4\,\dfrac{\mathrm{L_{tot}}}{\mathrm{C}}}}{2\,\mathrm{L_{tot}}}. \tag{3.10}$$

Using the standard form of the solution to a second-order homogeneous differential equation and enforcing the initial conditions, the resulting expression for the current is

$$i = \frac{\mathrm{V_0}}{\mathrm{L_{tot}}\,(s_1 - s_2)}\left(\mathrm{e}^{s_1 t} - \mathrm{e}^{s_2 t}\right). \tag{3.11}$$

Equation 3.11 represents the general solution for the current and is valid in all damping regimes, with s_1 and s_2 taking real or complex values depending on the discriminant of the characteristic equation.

In the overdamped regime, the characteristic equation has a positive discriminant and yields two distinct real roots, resulting in a non-oscillatory transient formed by two exponentially decaying modes.

In the critically damped regime, the characteristic equation has a repeated root

$$s_{1,2} = -\frac{\mathrm{R_{tot}}}{2\,\mathrm{L_{tot}}}, \tag{3.12}$$

and the solution takes the standard form

$$i = \frac{\mathrm{V_0}}{\mathrm{L_{tot}}}\, t\, \mathrm{e}^{s_{1,2}t}. \tag{3.13}$$

This is the fastest non-oscillatory response achievable by the system.

When the system is underdamped, the roots of the characteristic equation are complex conjugates,

$$s_{1,2} = -\alpha \pm \mathrm{j}\,\omega_\mathrm{d}, \tag{3.14}$$

$$\alpha = \frac{\mathrm{R_{tot}}}{2\,\mathrm{L_{tot}}}, \tag{3.15}$$

$$\omega_\mathrm{d} = \sqrt{\omega_0^2 - \alpha^2}, \tag{3.16}$$

$$\omega_0 = \frac{1}{\sqrt{\mathrm{L_{tot}\,C}}}, \tag{3.17}$$

where α is the damping factor, ω_d is the damped natural frequency, and ω_0 is the undamped natural frequency. Substitution into (3.1) yields

$$i = \frac{\mathrm{V_0}}{\mathrm{L_{tot}}\,\omega_\mathrm{d}}\,\mathrm{e}^{-\alpha t}\,\sin(\omega_\mathrm{d} t)\,, \tag{3.18}$$

which corresponds to a sinusoidal waveform with exponentially decaying amplitude.

As a first approximation, the total resistance and inductance of the loop are assumed to be $2\,\mathrm{m\Omega}$ and $100\,\mathrm{nH}$, respectively. Under this assumption, the critical capacitance can be obtained by imposing a zero discriminant in the characteristic equation, i.e.,

$$\mathrm{C_{cr}} = \frac{4\,\mathrm{L_{tot}}}{\mathrm{R_{tot}}} = \frac{4 \cdot 100 \cdot 10^{-9}}{2 \cdot 10^{-3}} = 100\,\mathrm{mF}. \tag{3.19}$$

Figure 3.3 illustrates the system response for different values of the capacitance C. As expected from the analytical expressions, three distinct behaviours can be observed. For capacitance values over the critical value, the response is overdamped and exhibits a slow, non-oscillatory decay. When C is set to the critical value, the system becomes critically damped, producing the fastest non-oscillatory transient. For capacitance values below the critical threshold, the response becomes underdamped and shows a decaying oscillatory waveform.

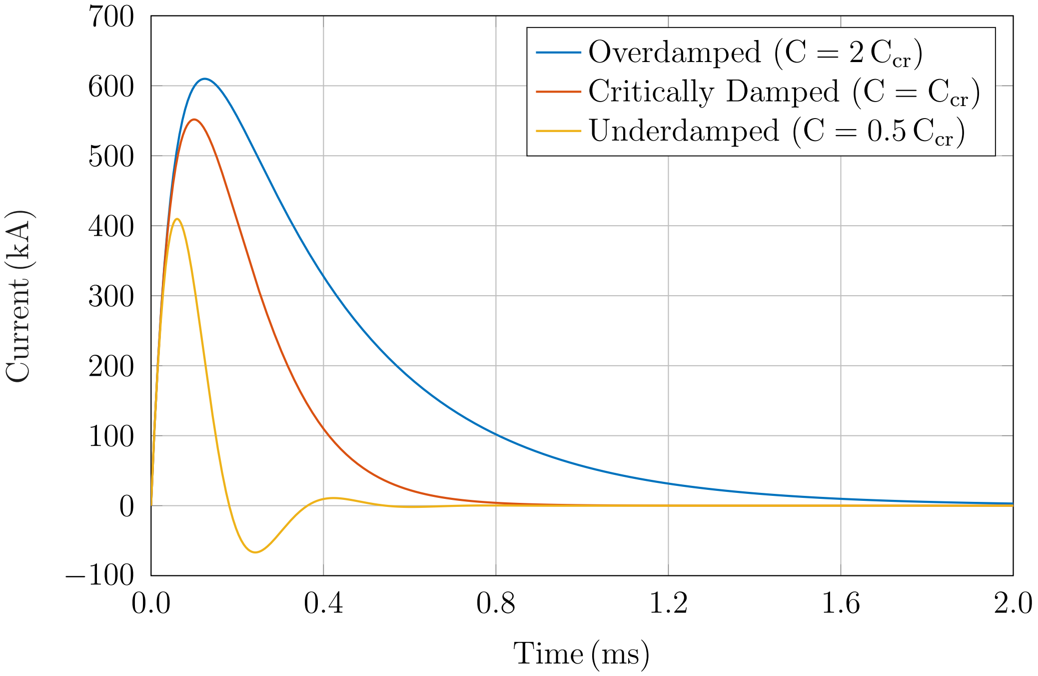

Fig. 3.3 Drive response for different capacitance values: $C = 2C_{cr}$, $C = C_{cr}$, and $C = 0.5C_{cr}$, illustrating the underdamped, critically damped, and overdamped regimes, respectively.

From Fig. 3.3, it is evident that the capacitance required to meet the drive specifications lies below the critical value, and the system therefore operates in the underdamped regime. Consequently, the expressions for an underdamped response are used for the sizing process. The time at which the first current maximum occurs t_p is obtained by imposing $\mathrm{d}i/\mathrm{d}t = 0$. Differention of i yields

$$\frac{\mathrm{d}i}{\mathrm{d}t} = \frac{V_0}{L_{tot}\,\omega_d}\,e^{-\alpha t}\,(\omega_d\cos(\omega_d t) - \alpha\sin(\omega_d t))\,. \tag{3.20}$$

Since the exponential term is always positive, the peak is determined by the condition

$$\omega_d\cos(\omega_d t) - \alpha\sin(\omega_d t) = 0. \tag{3.21}$$

Rearranging this expression gives

$$\tan(\omega_\mathrm{d} t) = \frac{\omega_\mathrm{d}}{\alpha}, \tag{3.22}$$

from which the time to the first peak t_p follows directly as

$$t_\mathrm{p} = \frac{1}{\omega_\mathrm{d}} \arctan\left(\frac{\omega_\mathrm{d}}{\alpha}\right). \tag{3.23}$$

This expression relates the peak time to the damping factor and the damped natural frequency and is used for the sizing of the capacitor bank in the underdamped regime.

In practical sizing calculations, it is often convenient to make use of a simplified approximation for the peak time. When the system is lightly damped, i.e., when $\alpha \ll \omega_0$, the ration ω_d/α becomes large and the argument of the arctangent approaches $\pi/2$. Under this condition, the peak time expression reduces to

$$t_\mathrm{p} \approx \frac{\pi}{2\,\omega_\mathrm{d}}, \tag{3.24}$$

which shows that the peak time is dominated by the damped natural frequency.

A further simplification can be obtained by assuming a lightly damped response, so that the damped natural frequency can be approximated by the undamped one, i.e., $\omega_\mathrm{d} \approx \omega_0$. Under this assumption, the peak-time expression reduces to

$$t_\mathrm{p} \approx \frac{\pi}{2\,\omega_0} = \frac{\pi}{2}\sqrt{\mathrm{L}_\mathrm{tot}\,\mathrm{C}}, \tag{3.25}$$

from which the capacitance can be explicitly expressed as a function of the total inductance and the desired peak time. Solving for C yields

$$\mathrm{C} \approx \frac{1}{\mathrm{L}_\mathrm{tot}} \left(\frac{2t_\mathrm{p}}{\pi}\right)^2 = \frac{4t_\mathrm{p}^2}{\pi^2\,\mathrm{L}_\mathrm{tot}}. \tag{3.26}$$

This relation provides a simple closed-form estimate of the required capacitance for a specified peak time and is used as a first sizing step for the capacitor bank.

Considering that the maximum allowable peak time is 25 µs, the upper bound on the capacitance C_max can be obtained directly from the approximate expression in

(3.26). Substituting $t_\mathrm{p} = 25\,\mu\mathrm{s}$ into this relation gives

$$\mathrm{C}_\mathrm{max} = \frac{4\,t_\mathrm{p}^2}{\pi^2\,\mathrm{L}_\mathrm{tot}} = 7.96\,\mathrm{mF}. \tag{3.27}$$

The peak-current requirement sets a lower bound on the capacitance of the bank, since a sufficiently large capacitance is necessary for the drive to deliver the specified peak current to the railgun. The first current maximum occurs at the time t_p, which is determined by the peak-time expression given in (3.23). Evaluating the underdamped current waveform at this instant yields

$$i_\mathrm{p} = \frac{\mathrm{V}_0}{\mathrm{L}_\mathrm{tot}\,\omega_\mathrm{d}}\,\mathrm{e}^{-\alpha t_\mathrm{p}}\,\sin\!\big(\omega_\mathrm{d}\,t_\mathrm{p}\big) \tag{3.28}$$

This exact expression does not provide a convenient closed-form dependency on the capacitance. However, under the lightly damped operating conditions of the drive, the following approximations can be adopted:

$$\omega_\mathrm{d} \approx \omega_0, \tag{3.29}$$

$$\sin\!\big(\omega_\mathrm{d}\,t_\mathrm{p}\big) \approx 1, \tag{3.30}$$

$$\mathrm{e}^{-\alpha t_\mathrm{p}} \approx 1. \tag{3.31}$$

Substituting these approximations into the exact expression for the peak current simplifies it to

$$i_\mathrm{p} \approx \frac{\mathrm{V}_0}{\sqrt{\dfrac{\mathrm{L}_\mathrm{tot}}{\mathrm{C}}}}, \tag{3.32}$$

which forms the basis for determining the minimum capacitance required by the peak-current constraint.

Rearranging (3.28), the capacitance can be expressed as a function of the desired peak current. Solving for C yields

$$\mathrm{C} \approx \frac{\mathrm{L}_\mathrm{tot}}{V_0^2}\,i_\mathrm{p}^2, \tag{3.33}$$

showing that the peak-current requirement directly defines the minimum admissible capacitance. This expression establishes a simple analytical link between the capacitor-bank size and the required drive performance: higher peak-current specifications translate into proportionally larger capacitor values. By imposing the design constraint $i_\mathrm{p} = 100\,\mathrm{kA}$, the lower bound of the capacitance $\mathrm{C_{min}}$ is therefore obtained as

$$\mathrm{C_{min}} = \frac{\mathrm{L_{tot}}}{V_0^2}\, i_\mathrm{p}^2 = 444\,\mu\mathrm{F}. \tag{3.34}$$

This result complements the upper limit derived from the peak-time requirement and fully defines the feasible design range of the capacitor bank.

Based on the capacitance range defined by the peak-time and peak-current requirements, together with the low-ESL and low-ESR constraints, a metallized polypropylene film capacitor was selected. The C44USGT6460M31K from the KEMET C44U-M series meets all electrical requirements of the pulse-power drive. Its main characteristics are summarised in Table 3.1.

Table 3.1 Main specifications of the selected capacitor (C44USGT6460M31K).

Parameter	**Value**
C	460 µF
$\mathrm{V_{NDC}}$	1500 V
ESL	40 nH
ESR	1.2 mΩ

The parameter $\mathrm{V_{NDC}}$ denotes the rated DC voltage of the capacitor.

Based on the electrical characteristics of the selected capacitor, the exact values of the peak time and peak current can now be determined:

$$\alpha = \frac{\mathrm{R_{tot}}}{2\,\mathrm{L_{tot}}} = 10^4\,1/\mathrm{s}, \tag{3.35}$$

$$\omega_0 = \frac{1}{\sqrt{\mathrm{L_{tot}\,C}}} = 1.47\cdot 10^5\mathrm{rad/s}, \tag{3.36}$$

$$\omega_\mathrm{d} = \sqrt{\omega_0^2 - \alpha^2} = 1.46\cdot 10^5\mathrm{rad/s}, \tag{3.37}$$

$$t_\mathrm{p} = \frac{1}{\omega_\mathrm{d}} \arctan\left(\frac{\omega_\mathrm{d}}{\alpha}\right) = 10.2\,\mu\mathrm{s}, \tag{3.38}$$

$$i_\mathrm{p} = \frac{\mathrm{V_0}}{\mathrm{L_{tot}}\,\omega_\mathrm{d}}\, \mathrm{e}^{-\alpha t_\mathrm{p}} \sin\left(\omega_\mathrm{d} t_\mathrm{p}\right) = 91.85\,\mathrm{kA}. \tag{3.39}$$

The selected capacitor bank satisfies the peak-time requirement, yielding $t_\mathrm{p} = 10.2\,\mu\mathrm{s}$, well below the design limit of 25 µs. However, the peak current reaches only 91.85 kA, which does not meet the 100 kA target. Two solutions can address this limitation. The first is to use the larger C44USGT6950M32K capacitor, rated at 950 µF, with 1.15 mΩ ESR and 80 nH ESL, while maintaining the 1.5 kV rating. The second option is to connect two C44USGT6460M31K units in parallel. This configuration provides 920 µF, approximately 600 µΩ ESR, and about 20 nH ESL. Due to the significantly reduced parasitic inductance and resistance, the parallel arrangement improves pulse performance and represents the most efficient solution. The expressions used to calculate the corresponding peak time and peak current for this configuration are given below:

$$\alpha = \frac{\mathrm{R_{tot}}}{2\,\mathrm{L_{tot}}} = 10^4\,1/\mathrm{s}, \tag{3.40}$$

$$\omega_0 = \frac{1}{\sqrt{\mathrm{L_{tot}}\,\mathrm{C}}} = 1.04 \cdot 10^5 \mathrm{rad/s}, \tag{3.41}$$

$$\omega_\mathrm{d} = \sqrt{\omega_0^2 - \alpha^2} = 1.04 \cdot 10^5 \mathrm{rad/s}, \tag{3.42}$$

$$t_\mathrm{p} = \frac{1}{\omega_\mathrm{d}} \arctan\left(\frac{\omega_\mathrm{d}}{\alpha}\right) = 14.2\,\mu\mathrm{s}, \tag{3.43}$$

$$i_\mathrm{p} = \frac{\mathrm{V_0}}{\mathrm{L_{tot}}\,\omega_\mathrm{d}}\, \mathrm{e}^{-\alpha t_\mathrm{p}} \sin\left(\omega_\mathrm{d} t_\mathrm{p}\right) = 124.82\,\mathrm{kA}. \tag{3.44}$$

As shown by the results obtained with the parallel configuration, the proposed capacitor bank fully satisfies the design criteria. The computed peak time is $t_\mathrm{p} = 14.2\,\mu\mathrm{s}$, which remains well below the required limit of 25 µs, while the corresponding peak current reaches 124.8 kA, exceeding the minimum specification of 100 kA. These values confirm that the selected capacitor arrangement provides the necessary performance margin for reliable operation of the pulse-power drive in the railgun actuator.

The drive design requires careful consideration of the maximum $\mathrm{d}v/\mathrm{d}t$ and peak current stresses on the capacitor bank. Metallized film capacitors are selected for their robustness under pulsed operation and intrinsic self-healing capability: localized dielectric breakdown causes the thin metallization to vaporize and isolate the defect, allowing continued operation. Exceeding 9 V/µs or 3900 A may accelerate capacitance degradation through increased self-healing events; however, such overstress does not lead to catastrophic failure. Since the proposed protection system is single-use, capacitance derating is not critical.

3.1.2 Switching Device Selection

High-current pulse-power applications typically rely on a limited set of switching technologies that can withstand extreme $\mathrm{d}i/\mathrm{d}t$ rates, large peak currents, and high transient voltages. Among the most widely used solutions are triggered spark-gap switches, SCRs, and their high-performance derivatives—the IGCTs.

A triggered spark-gap switch is a gas-discharge device in which the transition from insulating to conductive state is initiated in a controlled manner through an auxiliary triggering electrode. Under normal operating conditions the main electrodes remain separated by a non-conductive gas gap, sustaining the applied voltage without significant leakage. When a trigger pulse is applied, a localized discharge is first generated near the trigger pin. This localized ionization produces an initial population of free electrons and ions, which lowers the effective breakdown voltage in the vicinity of the trigger region. As these charge carriers multiply through impact ionization, the electrical field between the main electrodes becomes locally enhanced, leading to a rapid avalanche process and the formation of a conductive plasma channel across the main gap. Once established, this plasma column exhibits a very low dynamic resistance, allowing the switch to conduct extremely high peak currents with minimal voltage drop. Figure 3.4 illustrates a representative cross section of a triggered spark-gap switch, highlighting the main electrodes, trigger electrode, and discharge path.

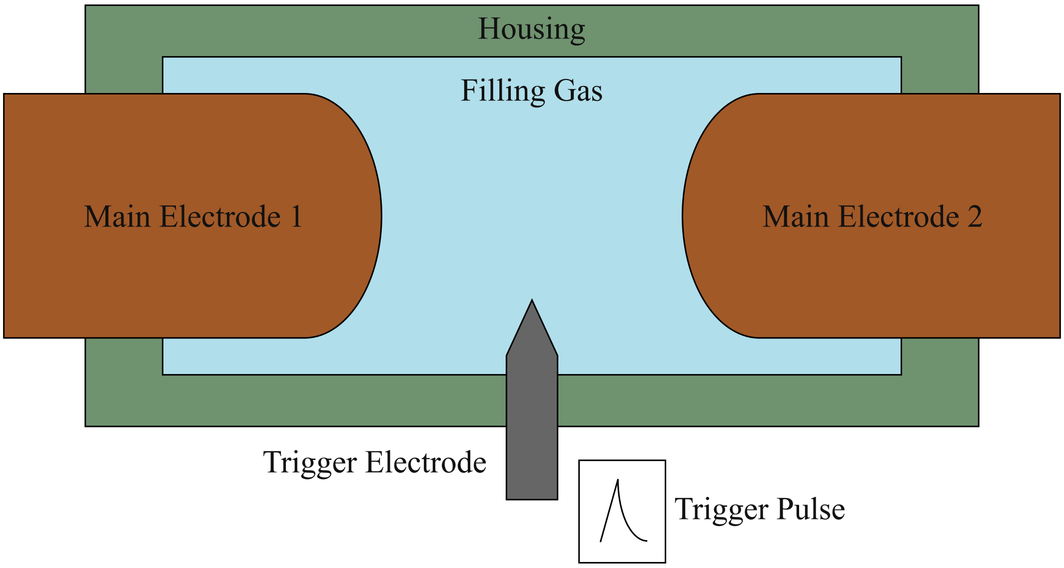

Fig. 3.4 Cross-sectional view of a triggered spark-gap.

The operation of a triggered spark gap is inherently affected by time jitter, defined as the statistical variation in the delay between the application of the trigger pulse and the formation of the main discharge. This jitter originates from the stochastic nature of the initial ionization processes within the filling gas: even under identical conditions, the number, spatial distribution, and energy of free electrons available at the moment of triggering fluctuate randomly. Consequently, the evolution from the localized trigger-initiated plasma to the full avalanche breakdown exhibits a non-deterministic delay. Experimental studies report that the trigger-pulse characteristics have a decisive influence on jitter performance. A higher trigger-pulse amplitude reduces the statistical-time lag by producing stronger local electric-field distortion and a larger initial density of seed electrons [57, 58], thereby improving reproducibility. Similarly, a steep trigger-pulse rise time (high $\mathrm{d}v/\mathrm{d}t$) accelerates the formation of the primary ionization region, shortening the formative-time lag and reducing overall jitter [57, 58]. The literature confirms that insufficient trigger amplitude or a slow-rising pulse can lead to incomplete pre-ionization, resulting in larger delay dispersion, misfires, or even self-breakdown of the gap at the working voltage. These effects have been experimentally characterized in several studies, which demonstrate that well-timed, high-voltage, fast-rising trigger pulses yield the lowest jitter and most reliable switching behavior in triggered spark-gap systems.

The filling gas plays a central role in determining the breakdown characteristics and switching performance of a triggered spark-gap switch. Its composition, pressure, and purity directly influence the statistical and formative time lags, the breakdown voltage, the arc conductivity, and the recovery behaviour of the device [59, 60]. Gases with high dielectric strength, such as SF_6 or high-pressure N_2, increase the self-breakdown voltage and reduce the probability of undesired pre-ionization, thereby improving hold-off capability. However, higher pressure also increases the statistical time lag unless sufficient trigger energy is provided. Conversely, gases with lower ionization potential support faster formation of initial electrons and typically yield lower jitter. The arc conductivity and voltage drop during conduction are also gas-dependent: heavier molecules tend to produce a higher arc voltage, while lighter gases support faster plasma expansion and lower conduction losses. In addition, the gas composition strongly affects the recovery time, i.e., the interval required after a discharge for the ionized plasma in the gap to recombine and diffuse sufficiently for the device to regain its full dielectric strength. Gases with slow deionization dynamics prolong this recovery process, thereby limiting the maximum achievable repetition rate. Overall, the choice of filling gas represents a trade-off between insulation strength, jitter performance, arc characteristics, and recovery speed, and must be matched to the specific requirements of the pulse-power application.

For the present application, the spark gap is not required to withstand high DC hold-off voltages, and the insulation margin is modest compared to systems operating at several tens of kilovolts. Consequently, there is no need to employ high-dielectric-strength gases such as SF_6 or pressurized N_2, which would unnecessarily increase the breakdown voltage and the statistical time lag. Instead, lighter gases offer clear advantages. In particular, H_2 provides very fast ionization kinetics, low ionization potential, and excellent arc conductivity, which collectively support reduced jitter, lower formative delays, and minimal conduction losses. Moreover, the recovery time of the switch is not a limiting factor for this application, since the actuator requires only a single discharge and does not operate at high repetition rates. These characteristics make H_2 a well-suited filling gas for a low-hold-off, high-current pulse-power switch, aligning the gas choice with the performance requirements of the proposed actuator drive.

The selection of electrode materials has a decisive impact on the performance, stability, and lifetime of triggered spark-gap switches. During conduction, the arc channel reaches extremely high temperatures, causing intense localized heating, erosion, and material vaporization at the electrode surfaces. Materials with a high melting point, high thermal stability, and strong resistance to arc erosion—commonly referred to as *refractory metals*—are therefore typically preferred. Refractory metals such as tungsten and molybdenum exhibit exceptionally high melting points and low vapor pressure at elevated temperatures, allowing them to withstand severe thermal and electrical stress while preserving a consistent gap geometry. Tungsten and tungsten–copper composites are particularly attractive due to their low erosion rate and favorable thermal properties. Copper or brass electrodes offer low arc voltage and excellent electrical conductivity but suffer from rapid erosion, making them less suitable for high-energy discharges. Stainless steel is sometimes used in low-cost or moderate-current spark gaps due to its mechanical robustness and ease of machining; however, it exhibits higher erosion and less stable emission behaviour compared to refractory metals. The electrode material also influences the onset of breakdown through its electronic properties [61, 62]. In particular, materials with a high work function emit fewer secondary electrons during triggering, reducing statistical fluctuations and improving breakdown reproducibility, which is especially critical in applications requiring low jitter and high switching reliability under repetitive operation.

Despite the suitability of triggered spark-gap switches for high-current pulse-power applications, this technology is ultimately not adopted in the present design. Most commercially available triggered spark gaps are engineered for high-voltage operation and exhibit minimum hold-off voltages far above the requirements of the proposed actuator drive. For example, the T-508 series from L3Harris operates in the 30–120 kV range, while the T-508A/AX versions are rated for 60–200 kV. Such voltage levels require large interelectrode spacing and correspondingly bulky mechanical structures, resulting in parasitic inductances on the order of 150 nH. Devices from the HOFSTRA Group exhibit similar constraints: the T-670 has a minimum operating voltage of approximately 18 kV, and the SW-50K also requires at least 10 kV to trigger reliably. Likewise, the GP-32B from Excelitas specifies minimum operating voltages around 20 kV. These intrinsically high-voltage designs are incompatible with the compact, ultra-low-inductance, sub-kilovolt requirements of the railgun actuator drive. In addition, most commercial triggered spark gaps fall under dual-use export regulations, significantly complicating procurement and limiting their feasibility for the intended single-shot application.

In contrast to triggered spark gaps, SCRs are widely available, commercially mature, and straightforward to procure, making them attractive candidates for high-current pulsed applications. Nevertheless, SCRs exhibit a significantly more limited $\mathrm{d}i/\mathrm{d}t$ capability compared with triggered spark gaps, whose plasma channel can sustain extremely fast current rise rates. The $\mathrm{d}i/\mathrm{d}t$ performance of an SCR is governed by its semiconductor turn-on dynamics, which impose intrinsic restrictions on how rapidly the device can transition into conduction. To understand the restrction of this limitation, it is therefore necessary to examine the internal structure and operating principle of the thyristor. This understanding will guide the selection of the most suitable thyristor technology for the pulse-power stage.

Figure 3.5(a) shows the basic silicon structure of the thyristor, composed of four alternating semiconductor layers arranged in an N^+–P–N^-–P^+ sequence. The N^+ diffusion forms the cathode emitter, providing a high concentration of electrons that are injected into the device once conduction begins. Adjacent to it lies the P-base region, which contains the gate contact and regulates the triggering process by controlling the initial carrier injection. The central N^- drift region is lightly doped and comparatively thick; its primary function is to sustain the forward and reverse blocking voltages by supporting the majority of the electric field when the device is in the off-state. The P^+ layer at the opposite end acts as the anode emitter, supplying holes during conduction. These four layers form three internal junctions: J_1 between P^+ and N^-, J_2 between N^- and P, and J_3 between P and N^+. The corresponding circuit symbol is shown in Fig. 3.5(b). When a positive voltage is applied from anode to cathode ($v_{AK} > 0$), junctions J_1 and J_3 are forward biased while J_2 remains reverse biased, placing the device in the forward-blocking state. Conversely, when $v_{AK} < 0$, junctions J_1 and J_3 become reverse biased and the device operates in the reverse-blocking state. In this reverse-biased condition, the thyristor cannot be turned on by the gate; gate triggering is only effective when the device is forward biased and J_2 is the sole reverse-biased junction. A thyristor exhibits a much higher forward-blocking capability than reverse-blocking capability because in the forward direction the voltage is supported by the lightly doped, thick N^- drift region, whereas in the reverse direction the blocking junction lies between heavily doped regions, which cannot sustain large depletion widths and therefore break down at lower voltages.

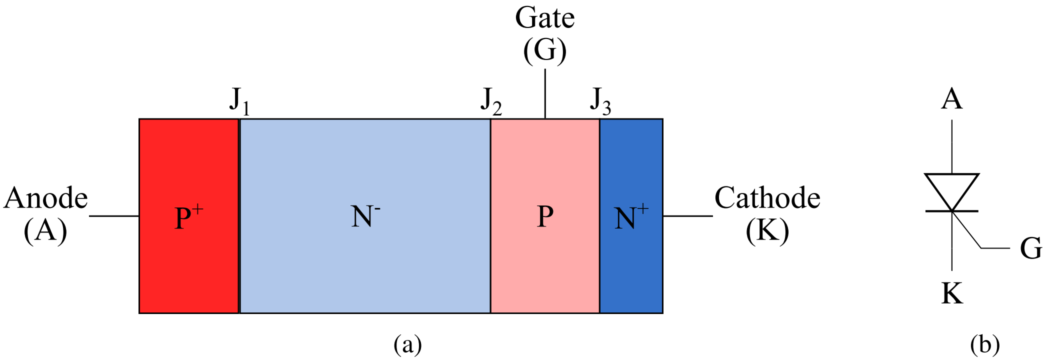

Fig. 3.5 Basic silicon structure of a thyristor (a) and its electrical symbol (b).

When the thyristor is forward biased, turn-on is initiated by injecting a positive gate current into the P-base region. This gate current introduces additional holes into the P region, raising the local hole concentration and thereby increasing the number of electrons that can diffuse from the N^+ cathode emitter into the P-base. These electrons are then attracted toward the N^- drift region, where the electric potential is higher due to the applied anode-to-cathode voltage. As a result, the net charge in the depletion region of J_2 is progressively neutralized, which reduces the reverse-bias barrier and collapses the depletion layer. The device turns on once the depletion region of J_2 is fully neutralized and the junction can no longer sustain reverse bias.

Figure 3.6 shows a detailed view of the thyristor silicon structure, including the semiconductor layers and their metallization. The gate metallization provides a low-impedance contact to the P-base, ensuring uniform hole injection during triggering. The cathode metallization, located above the N^+ emitter regions, collects the conduction current and distributes it across the N^+ emitter islands diffused into the P-base, improving current spreading and turn-on controllability. The anode metallization forms a low-resistance contact to the P^+ anode emitter, enabling uniform hole injection. Cathode shorts, implemented as local connections between the cathode metallization and the P-base, enhance dynamic robustness. During fast anode–cathode voltage transients, the displacement current

$$i = C_{J2}, \frac{\mathrm{d}v_{\mathrm{AK}}}{\mathrm{d}t}, \tag{3.45}$$

associated with the depletion capacitance of J_2 could otherwise inject carriers into its depletion region and reduce its reverse bias, triggering unintended turn-on. The cathode shorts divert this transient current under high $\mathrm{d}v/\mathrm{d}t$ conditions.

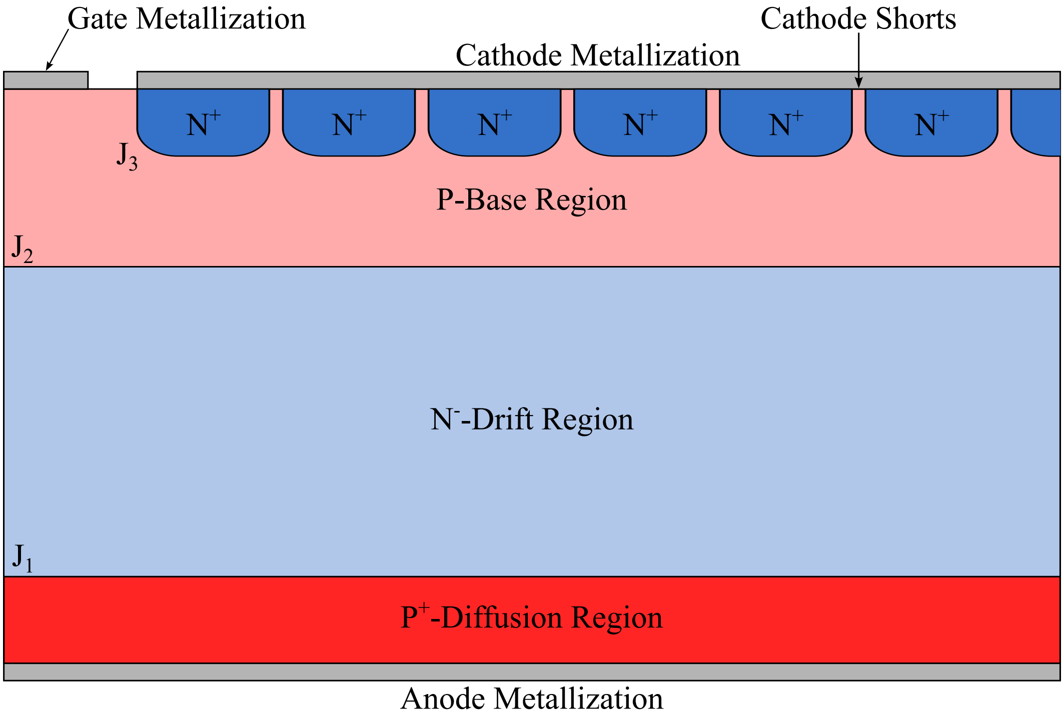

Fig. 3.6 Detailed view of the thyristor silicon structure.

Once the turn-on dynamics and internal structure of the thyristor are understood, the origin of the $\mathrm{d}i/\mathrm{d}t$ limitation becomes evident. At the start of triggering, hole injection from the gate into the P-base is highly localized and requires time to spread laterally across the emitter area. During this interval, only regions with sufficient hole concentration can sustain electron injection from the N^+ emitter, so conduction initiates in narrow localized zones. If the external circuit imposes a steep current rise, these zones experience excessive current density, leading to current crowding, local heating, and potentially device failure. This transient non-uniformity fundamentally limits the allowable turn-on $\mathrm{d}i/\mathrm{d}t$. Optimizing the gate metallization improves hole-spreading uniformity and enhances the achievable turn-on $\mathrm{d}i/\mathrm{d}t$. Figure 3.7 illustrates representative gate-layout geometries [63, 64].

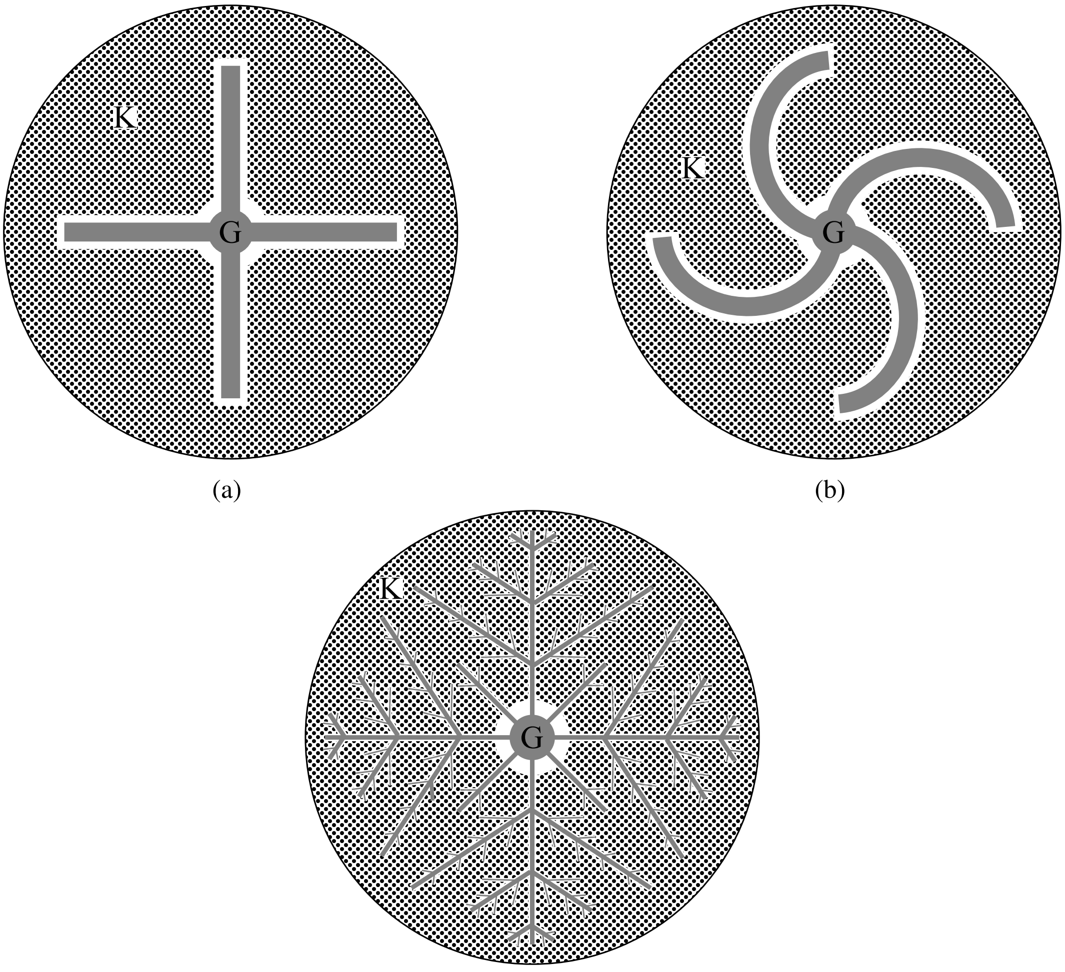

(a) (b)

(c)

Fig. 3.7 Examples of gate metallization layouts used in high-performance thyristors: (a) spoke-type gate structure, (b) involute gate geometry, and (c) distributed-gate design.

Among these alternatives, the distributed-gate configuration offers the highest achievable $\mathrm{d}i/\mathrm{d}t$ capability, as its extended gate periphery ensures the most uniform hole injection and the fastest lateral current spreading across the emitter area.

In addition to the internal device structure, the $\mathrm{d}i/\mathrm{d}t$ capability of a thyristor depends critically on the design of the gate-drive circuit. A rapid and spatially uniform turn-on requires both a sufficiently high gate-trigger current amplitude and a steep gate-current rise rate, ensuring strong and fast hole injection into the P-base region. If the gate drive is too weak or slow, the turn-on remains localized for a longer duration, reducing the effective $\mathrm{d}i/\mathrm{d}t$ capability and increasing the risk of current crowding. To guarantee a robust triggering process, the gate-drive topology shown in Fig. 3.8 has been implemented, providing a high-current, fast-rising gate pulse optimized for pulse-power operation.

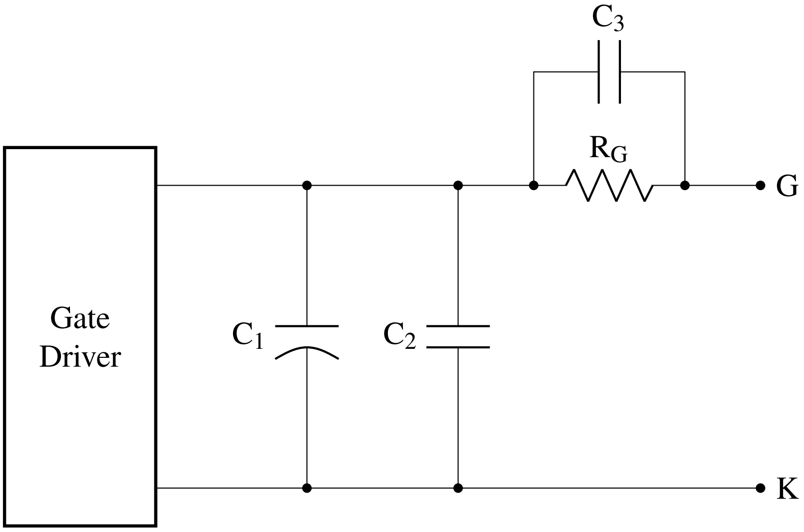

Fig. 3.8 Gate-drive circuit designed to provide high $\mathrm{d}i/\mathrm{d}t$ gate current during the thyristor turn-on.

In the gate-drive circuit of Fig. 3.8, capacitor C_1 is a high-value electrolytic capacitor whose purpose is to maintain a stiff DC voltage at the gate-driver output, ensuring that the gate circuit does not sag during the high-current pulse. Capacitor C_2 is a small ceramic capacitor placed in parallel with C_1; its low ESR and low ESL allow it to supply the fast high-frequency component of the gate current during the initial turn-on transient. Capacitor C_3 is connected in parallel with the gate resistor R_G and provides a low-impedance path during the rising edge of the gate current pulse, effectively bypassing R_G so that a high $\mathrm{d}i/\mathrm{d}t$ can be delivered to the gate. Once the transient is completed, C_3 charges, the bypass effect vanishes, and R_G determines the steady-state gate current, thereby protecting the gate driver IC. The selected parameters of the proposed gate-driver network are summarized in Table 3.2.

Table 3.2 Gate-driver component parameters for the proposed gate-driver circuit.

Parameter	**Value**
C_1	470 µF
C_2	22 µF
C_3	22 µF
R_G	3.3 Ω

In addition to the selection of the passive components, the stray inductance of the gate loop must be minimized, as any parasitic inductance reduces the effective $\mathrm{d}i/\mathrm{d}t$ delivered to the gate and can significantly slow down the triggering process. This requires short, low-inductance routing between the driver, the gate terminals, and the associated capacitors. Moreover, maximizing the gate-drive voltage is essential to increase the initial gate-current surge and improve turn-on uniformity. In the present design, a gate-drive voltage of 50 V is used, corresponding to the maximum allowable output of the 1ED3124MU12FXUMA1 gate-driver, ensuring the strongest possible gate excitation without exceeding the device's absolute ratings.

Based on the $\mathrm{d}i/\mathrm{d}t$ requirements of the pulse-power stage, a distributed-gate thyristor is selected. Devices employing this technology offer the highest turn-on $\mathrm{d}i/\mathrm{d}t$ capability among commercially available thyristors. In particular, the IXYS UK Westcode R5370EA22J satisfies the demand of the proposed actuator drive in terms of surch current, while providing exceptional $\mathrm{d}i/\mathrm{d}t$ performance. Table 3.3 summarizes the main characteristics of the selected device.

Table 3.3 Main electrical characteristics of the selected distributed-gate thyristor (IXYS UK Westcode R5370EA22J).

Parameter	**Value**
Maximum blocking voltage	1800 V
Peak surge current (1 ms pulse)	200 kA
Maximum $\mathrm{d}i/\mathrm{d}t$	1000 A/µs

IGCTs represent an evolution of conventional thyristors and offer even superior turn-on performance. An IGCT consists of a high-power thyristor monolithically integrated with an ultra-low-inductance gate unit capable of delivering very high gate-current amplitudes with extremely steep rise rates. During turn-on, the IGCT's gate drive floods the entire P-base with a nearly uniform and instantaneous carrier injection, forcing the device rapidly into a highly conductive, transistor-like state with minimal current filamentation. This results in exceptionally high permissible $\mathrm{d}i/\mathrm{d}t$ values and very low on-state voltage compared with standard or even distributed-gate thyristors. Despite these advantages, IGCT technology is not adopted in the present design. IGCTs require dedicated, high-performance gate units, have significantly higher device and driver costs, and are generally targeted at medium-voltage industrial applications. Incorporating such technology would substantially increase the complexity and cost of the actuator drive, rendering the overall system far less attractive for the intended application.

As shown in Section 3.1.2, the pulse-power stage exhibits an underdamped current response. In the absence of additional circuitry, the current through the thyristor would naturally reverse during the first oscillation cycle. Since a thyristor is a unidirectional device and cannot conduct negative current, such a reversal would force the device into reverse conduction and inevitably cause device failure. To prevent this, a freewheeling diode is connected across the capacitor bank. When the capacitor voltage reaches the negative value at which the diode becomes forward biased, the diode conducts and provides an alternative low-impedance path for the current, ensuring that the current through the thyristor remains strictly positive.

For the present application, a standard high-power rectifier diode is sufficient. The W108CED220 rectifier has therefore been selected; it provides a surge-current capability exceeding 200 kA for a 1 ms pulse and a blocking-voltage rating of 2200 V, comfortably meeting the requirements of the pulse-power drive.

3.1.3 Components Layout

A proper design of the pulse-power stage requires a clear understanding of how the parasitic elements introduced by the physical layout influence the dynamic behaviour of the railgun actuator. The impact of these parasitics is particularly significant because the circuit operates in two distinct stages:an initial phase, illustrated in

Fig. 3.9(a), during which the diode is reverse biased and the current flows exclusively through the thyristor and the railgun; followed by a second phase, shown in Fig. 3.9(b), in which the diode becomes forward biased and provides the freewheeling path for the current.

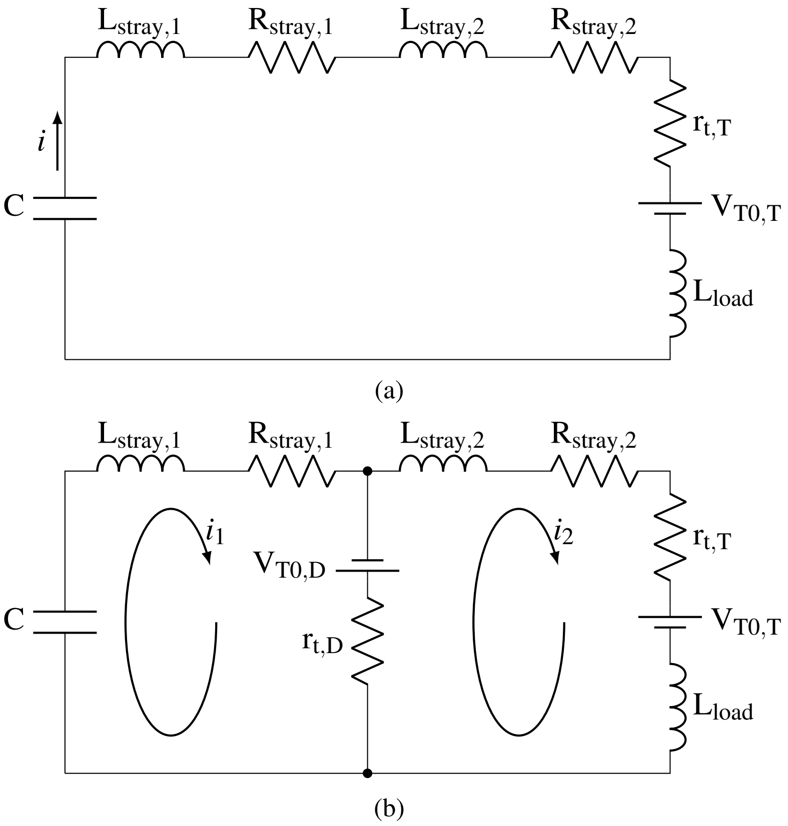

Fig. 3.9 Lumped-parameter model of the pulse-power drive: (a) diode reverse-biased during the initial current rise, and (b) diode forward-biased during the freewheeling phase.

During conduction, both the diode and the thyristor are represented using their standard piecewise–linear on-state models, consisting of a constant threshold voltage in series with a dynamic (slope) resistance. The forward voltage of the diode is expressed as

$$v_F = V_{T0,D} + i_F \, r_{t,D}, \tag{3.46}$$

where v_F is the diode forward voltage, $V_{T0,D}$ is the threshold voltage, i_F is the forward current, and $r_{t,D}$ is the diode slope resistance. Similarly, the thyristor on-state voltage is modelled as

$$v_T = V_{T0,T} + i_T \, r_{t,T}, \tag{3.47}$$

where v_T denotes the on-state voltage of the thyristor, $\mathrm{V}_{\mathrm{T0,T}}$ is the threshold voltage, i_T is the on-state current, and $\mathrm{r}_{\mathrm{t,T}}$ is the corresponding slope resistance.

It is important to emphasise that the parameters $\mathrm{r}_{\mathrm{t,T}}$ and $\mathrm{r}_{\mathrm{t,D}}$ represent the steady-state slope resistances of the thyristor and diode, respectively. During the first microseconds of conduction, however, both devices exhibit significantly higher transient on-state resistances due to incomplete carrier injection. For the selected components, the diode exhibits a steady-state resistance of 39 μΩ, while the thyristor reaches 71 μΩ; yet in the transient regime these values can temporarily rise to approximately 1–2 mΩ. This elevated resistance persists for roughly 10–20 μs in the thyristor and for less than 10 μs in the diode. Such transient behaviour has a pronounced impact on the resulting current waveform: it limits the achievable peak current during the initial rising interval and accelerates the current decay at the beginning of the freewheeling phase, thereby affecting both the delivered pulse energy and the overall performance of the drive.

When the diode is reverse biased, as shown in Fig. 3.9(a), the current path is confined to the capacitor bank, the stray elements, the thyristor, and the load inductance. In this interval, the parasitic elements $\mathrm{L}_{\mathrm{stray,1}}$, $\mathrm{R}_{\mathrm{stray,1}}$, $\mathrm{L}_{\mathrm{stray,2}}$, and $\mathrm{R}_{\mathrm{stray,2}}$ play a decisive role in shaping the current pulse. Their combined impedance limits both the peak current that the drive can deliver and the current rise time, directly affecting the acceleration capability of the railgun actuator. Minimising these parasitics is therefore essential, as any additional inductance slows the current transient and any added resistance reduces the effective energy transferred to the load.

Once the diode becomes forward biased, the operating condition transitions to the configuration shown in Fig. 3.9(b), where two distinct current loops are formed. The first loop, i_1, corresponds to the LCR path that includes the capacitor bank. At the instant the diode conducts, the capacitor voltage has nearly collapsed to zero, so the energy stored in this loop is almost entirely magnetic. The magnetic energy associated with $\mathrm{L}_{\mathrm{stray,1}}$ is dissipated in the diode and in $\mathrm{R}_{\mathrm{stray,1}}$, with none contributing to railgun acceleration. The second loop, i_2, is an LR path including $\mathrm{L}_{\mathrm{stray,2}}$ and the load. Although the magnetic field of $\mathrm{L}_{\mathrm{stray,2}}$ does not generate force in the armature, part of its stored energy is ultimately transferred to the railgun. In this chapter, the load is represented solely by an inductance because the drive output is short-circuited for characterization purposes.

Since the reduction of $L_{\mathrm{stray},1}$ is a primary design objective, several alternative configurations of the capacitor bank have been constructed and experimentally characterised. Figure 3.10 presents the three configurations considered—comprising four capacitors in parallel, two capacitors in parallel, and a single-capacitor arrangement.

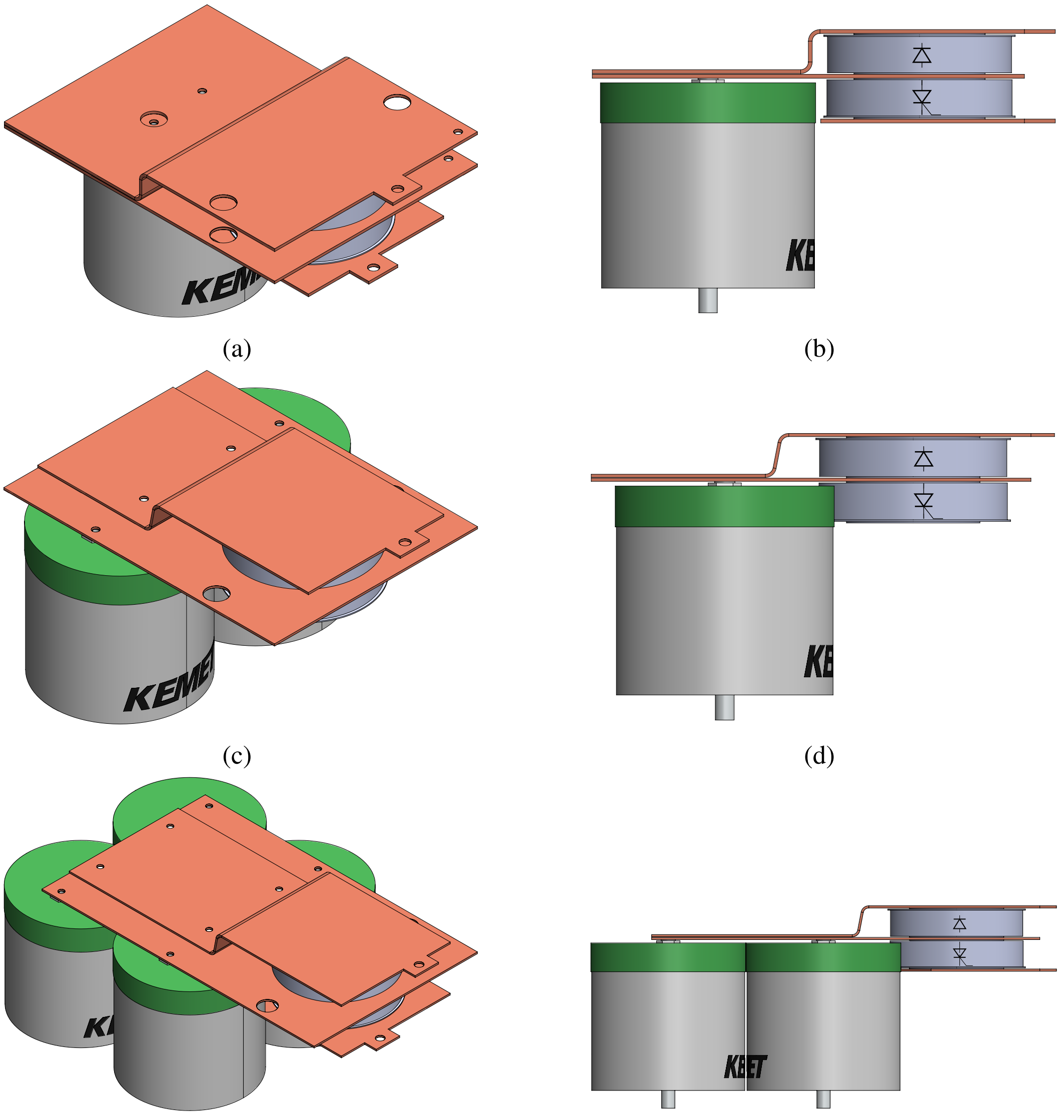

(a) (b)

(c) (d)

(e) (f)

Fig. 3.10 Different capacitor-bank drive configurations evaluated for stray-inductance reduction: (a) 1-capacitor drive isometric view, (b) 1-capacitor drive side view, (c) 2-capacitor drive isometric view, (d) 2-capacitor drive side view, (e) 4-capacitor drive isometric view, and (f) 4-capacitor drive side view.

$L_{\mathrm{stray,1}}$ arises from two main contributors: the ESL of the capacitors and the inductance of the current path from the capacitors to the freewheeling diode, denoted L_{CD}. The ESL component decreases when multiple capacitors are placed in parallel, since the effective inductance scales inversely with their number. L_{CD} is minimized by placing the capacitors as close as possible to the diode and by reducing the spacing between the positive and negative current-carrying plates. In the prototype, a 0.2 mm FR4 spacer tightly couples these plates, enhancing magnetic-field cancellation and lowering the loop inductance. However, a trade-off must be found: adding capacitors reduces ESL but forces some units farther from the diode, increasing L_{CD}. The optimal layout therefore balances these competing effects.

To characterize the influence of the different capacitor-bank layouts on the overall loop inductance, the Bode 100 impedance analyzer is used in shunt–thru configuration. Prior to the measurements, a complete open/short/load calibration is performed to ensure accurate low-impedance characterization. Direct measurement of $L_{\mathrm{stray,1}}$ alone is impractical because it would require placing the probe terminals precisely at the diode's electrical center, which is not feasible with the available mechanical access. However, $L_{\mathrm{stray,2}}$—the inductance between the diode and the output terminals—remains constant across all configurations because the physical distance and geometry of this segment are unchanged. Therefore, by measuring the total stray inductance seen from the drive terminals, variations in $L_{\mathrm{stray,1}}$ across different layouts can be inferred. The measurement setup is shown in Fig. 3.11.

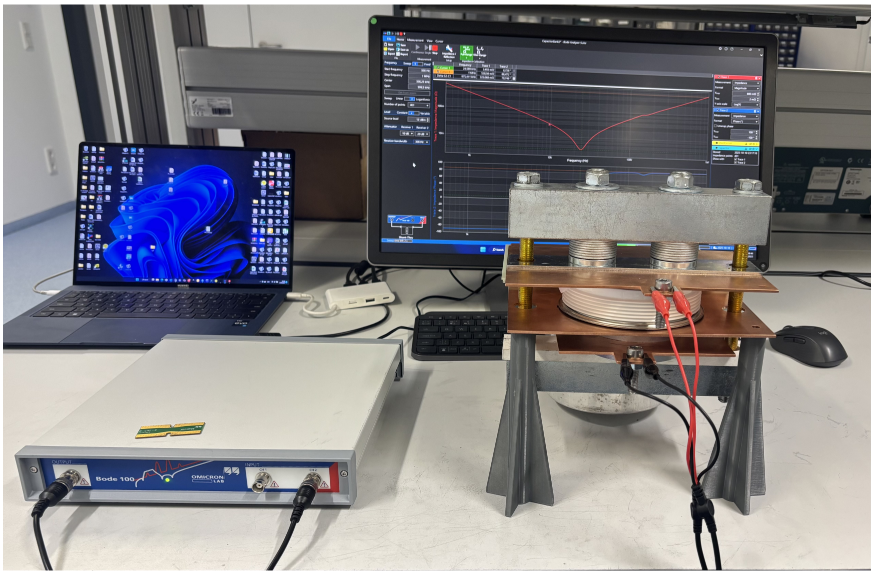

Fig. 3.11 Measurement setup for the electrical drive parasitics characterization.

A practical difficulty arises because the Bode 100 applies a small AC excitation. If this excitation forward-biases the freewheeling diode during either half-cycle, the measurement of the impedance becomes distorted. as the diode transitions into conduction and its nonlinear dynamic resistance masks the true inductive behavior. To prevent this, insulating paper was placed between the copper plates and both the diode anode and cathode, ensuring that the diode remains isolated from the circuit. This guarantees that the AC excitation flows only through the passive stray inductances and resistances of the layout.

Additionally, the thyristor must behave as a short circuit during the measurement so that the analyzer senses the complete current path. Since the real device cannot be kept continuously forward-biased under AC excitation, it was replaced during testing by a solid aluminum cylinder machined to match the dimensions of the thyristor package. This provides a stable, low-impedance conduction path that emulates the thyristor's on-state behavior for the purpose of inductance extraction.

Figure 3.12 presents the results obtained from the impedance characterization of the different drive configurations. For reference, a single capacitor has also been measured directly at its terminals to verify the consistency of the extracted parasitics with the manufacturer's specifications. This provides a baseline for assessing how the layout and the number of capacitors affect the overall stray inductance and resistance of the drive.

The total stray inductance $\mathrm{L}_{\mathrm{stray}}$ can be estimated from the impedance magnitude $|Z|$ in the frequency range f where the phase approaches 90°, that is, where the inductive behaviour dominates. In this region, the inductive reactance satisfies

$$\mathrm{L}_{\mathrm{stray}} \approx \frac{|Z|}{2\pi f}. \tag{3.48}$$

Similarly, the capacitance can be obtained from the frequency region where the impedance phase approaches -90°, corresponding to capacitive dominance. In that region,

$$\mathrm{C} \approx \frac{1}{2\pi f|Z|}. \tag{3.49}$$

The stray resistance $\mathrm{R}_{\mathrm{stray}}$ is evaluated at the resonance frequency f_0, where the reactive components cancel and the impedance becomes purely resistive. Thus,

$$\mathrm{R}_{\mathrm{stray}} \approx |Z|. \tag{3.50}$$

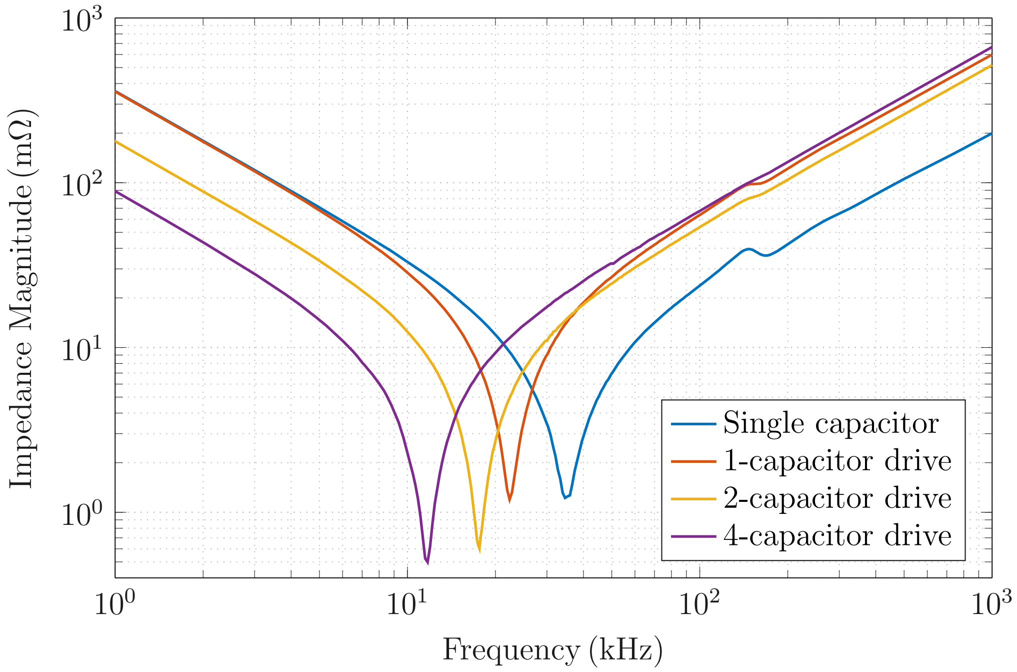

(a)

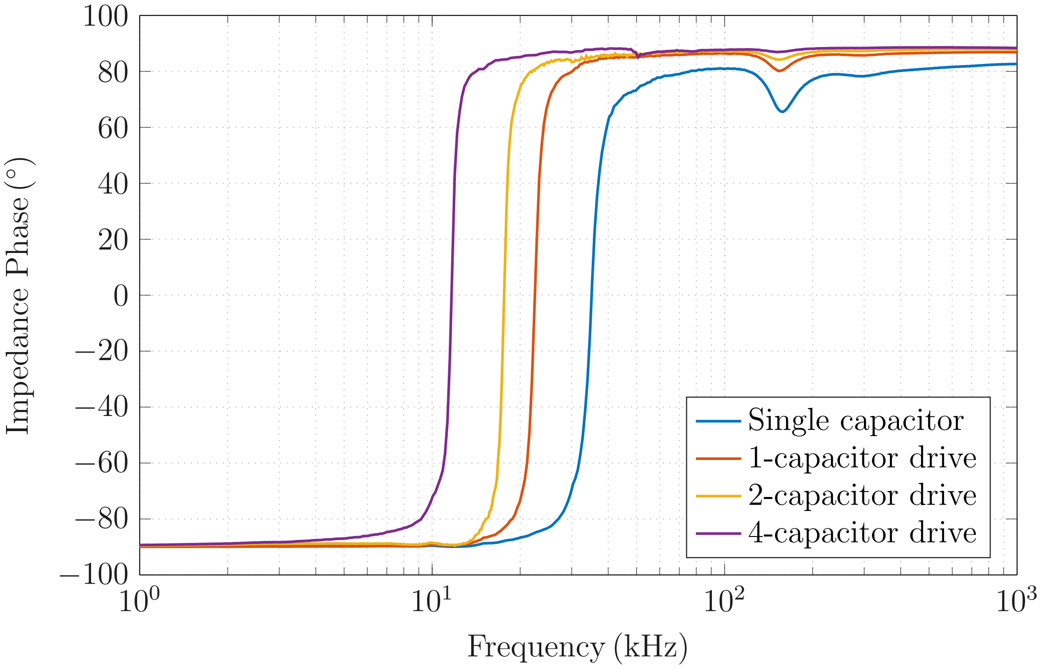

(b)

Fig. 3.12 Impedance magnitude and phase of the electric-drive parasitics for four configurations: single capacitor (terminal measurement), 1-capacitor drive, 2-capacitor drive, and 4-capacitor drive. Subfigure (a) shows the impedance magnitude, while subfigure (b) presents the impedance phase.

The characterization of the single capacitor provides a useful reference point to validate the measurement methodology. The extracted stray resistance is 1.18 mΩ, which agrees closely with the 1.2 mΩ value reported in the manufacturer's datasheet. The measured equivalent series inductance is 42.11 nH, also consistent with the specified 40 nH. The capacitance obtained from the low-frequency region of the impedance magnitude is 441.81 µF, slightly lower than the nominal 460 µF, but still within a reasonable tolerance for metallized polypropylene capacitors. Overall, the measured parameters exhibit very good agreement with the datasheet values, confirming the reliability of the experimental setup and extraction procedure.

Table 3.4 summarises the extracted values of L_{stray}, C, and R_{stray} for the 1-, 2-, and 4-capacitor drive configurations.

Table 3.4 Extracted parasitic parameters for the different capacitor-bank configurations.

Configuration	**C** [µF]	$\mathbf{L}_{\text{stray}}$ [nH]	$\mathbf{R}_{\text{stray}}$ [mΩ]
1-cap drive	444.03	106.67	1.18
2-cap drive	889.93	87.72	0.60
4-cap drive	1780.26	108.62	0.49

The characterization results show that the 2-capacitor configuration yields the lowest total stray inductance. When moving from one to two capacitors, the reduction in equivalent ESL more than compensates for the increase in current-path inductance L_{CD}, producing a net decrease in L_{stray}. In contrast, when increasing from two to four capacitors, the additional ESL reduction is too small to offset the larger L_{CD} caused by the greater spacing between devices, and the total stray inductance rises again. The results also indicate that the stray resistance is dominated by the capacitors' intrinsic ESR, since R_{stray} remains approximately equal to ESR/N_{p} for all configurations, where N_{p} is the number of parallel capacitors.

3.1.4 Design of the Charging Unit

Critical applications such as circuit breakers demand a high degree of robustness and must not rely on the external grid for their operation. Before the pulse-power stage can function, the DC link of the electric drive must be charged to its nominal voltage.

For this purpose, an auxiliary power supply (APS) is required. In safety-critical systems, the APS typically draws energy from a dedicated auxiliary battery and provides a controlled charging path for the capacitor bank, thereby ensuring full operational autonomy and guaranteeing that the breaker can operate reliably even in the complete absence of external power.

The capacitor bank must be charged to 1500 V, whereas the auxiliary battery provides only 48 V. Consequently, the APS must achieve a very high conversion ratio to bridge this substantial voltage difference and reliably energize the DC link. As discussed in [65], the conversion techniques capable of providing the highest step-up gain include voltage multipliers, switched-inductor structures, and magnetically coupled converters such as forward and flyback topologies. Among these, the flyback converter represents the simplest and most cost-effective solution, requiring only a minimal component count while still enabling very large boost ratios through appropriate transformer design and careful magnetic optimization for enhanced reliability.

Figure 3.13 shows the schematic of the flyback converter used as the auxiliary power supply. In the proposed design, the converter operates in quasi-resonant (QR) mode to minimize switching losses by turning on the MOSFET at or near the valley of the drain–source voltage, thereby achieving zero-voltage switching (ZVS) or near-ZVS.

During the MOSFET on-time, the secondary diodes ($\mathrm{D_1}$ and $\mathrm{D_2}$) are reverse biased, and the transformer magnetizing inductance $\mathrm{L_m}$ is linearly energized. The primary side current i_1 increases according to

$$i_1 = \frac{\mathrm{V_{in}}}{\mathrm{L_m}} t, \tag{3.51}$$

where $\mathrm{V_{in}}$ is the input voltage supplied by the auxiliary battery. The peak current i_{p1} can be expressed as

$$i_{\mathrm{1p}} = \frac{\mathrm{V_{in}}}{\mathrm{L_m}} t_{\mathrm{on}}, \tag{3.52}$$

where t_{on} denotes the MOSFET turn-on time. The stored magnetic energy E_{m} in the magnetic core

$$E_{\mathrm{m}} = \frac{1}{2} \mathrm{L_m} i_{\mathrm{1p}}^2 \tag{3.53}$$

is later transferred to the secondary once the MOSFET turns off.

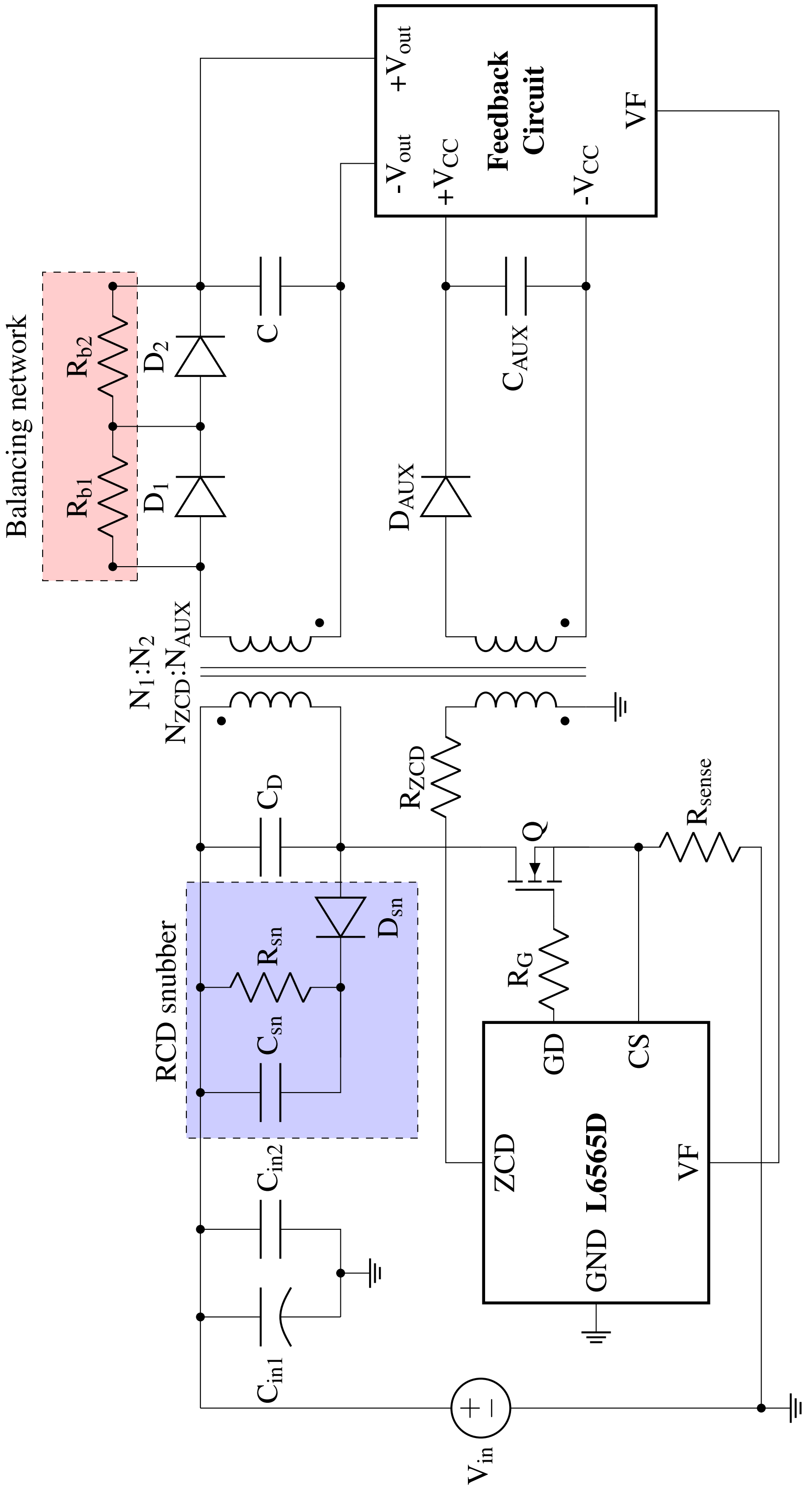

Fig. 3.13 Schematic of the flyback-based auxiliary power supply.

The voltages across D_1 and D_2, denoted v_{D1} and v_{D2}, are given by

$$v_{D1} + v_{D2} = v_{out} + \frac{N_2}{N_1} V_{in}, \tag{3.54}$$

where v_{out} is the output voltage, N_1 is the number of primary turns, and N_2 is the number of secondary turns. In this specific case, both the turns ratio and the output voltage are very high, which results in a reverse voltage that exceeds the blocking capability of a single diode. For this reason, two diodes are connected in series so that the reverse voltage is shared between them, thereby ensuring reliable operation without the need for a single ultra–high-voltage rectifier. In addition, a balancing network is connected in parallel to each diode to guarantee equal voltage sharing during operation.

When the MOSFET is turned off, the voltage in the secondary winding reverses and diodes D_1 and D_2 become forward biased. The MOSFET drain–source voltage v_{DS} then rises to

$$v_{DS} = V_{in} + \frac{N_1}{N_2} v_{out}. \tag{3.55}$$

However, the presence of the transformer leakage inductance L_{lk}, the MOSFET output capacitance C_{oss}, and the capacitor C_D connected across the primary winding prevents this transition from being abrupt. Instead, L_{lk} resonates with both C_{oss} and C_D, forming a transient resonant network:

$$f_{0,toff} = \frac{1}{2\pi\sqrt{L_{lk}\left(C_{oss} + C_D\right)}}, \tag{3.56}$$

where $f_{0,toff}$ denotes the natural resonant frequency of the leakage inductance–capacitance network that arises when the MOSFET is turned off.

An advantage of adding the capacitor C_D is reducing the turn-off resonance peak, thereby protecting the device. The peak drain–source voltage v_{DSp} is given by:

$$v_{DSp} = V_{in} + \frac{N_1}{N_2} v_{out} + i_{1p}\sqrt{\frac{L_{lk}}{\left(C_{oss} + C_D\right)}}. \tag{3.57}$$

However, the capacitor C_D alone is not sufficient to absorb all the energy stored in L_{lk}. Therefore, an RCD snubber, is required to safely dissipate this energy and further limit voltage stress on the MOSFET.

Besides limiting the resonance peak, the capacitor C_D also helps to reduce turn-off losses. By slowing down the rise of the drain–source voltage during the switching transition, the overlap between voltage and current is reduced. As a result, the instantaneous switching power is lower, and the overall switching losses decrease. The rise of the drain–source voltage can be expressed as

$$\frac{dv_{ds}}{dt} = \frac{i_{1p}}{C_{oss} + C_D} \tag{3.58}$$

Figure 3.14 shows the typical drain–source voltage waveform during the turn-off of the MOSFET, highlighting the resonant oscillation caused by L_{lk}, C_{oss}, and C_D as well as the moderated voltage rise due to C_D.

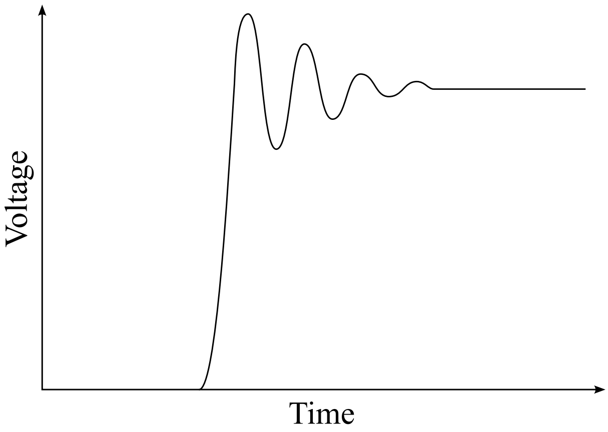

Fig. 3.14 Typical drain–source voltage waveform during MOSFET turn-off, showing the resonant behaviour and moderated rise due to C_D.

During the secondary conduction interval, the secondary side i_2 current decreases linearly as the stored energy is transferred to the output:

$$i_2 = i_{2p}\frac{N_1}{N_2} - \frac{v_{out}}{L_m\left(\frac{N_2}{N_1}\right)^2}t. \tag{3.59}$$

Once the magnetizing current falls to zero, the core is fully demagnetized and D_1 and D_2 turn off. At this instant, the converter enters a second resonant phase determined by L_m, C_{oss}, and C_D, with a resonant frequency

$$f_{0,dm} = \frac{1}{2\pi\sqrt{L_m\,(C_{oss}+C_D)}}, \tag{3.60}$$

where $f_{0,dm}$ denotes the natural frequency of the resonance associated with the magnetizing inductance and the capacitance network that arises once the magnetic core is fully demagnetized. In this state, the drain node oscillates freely around the input voltage, producing a sequence of voltage valleys. The minimum value of the oscillation v_{valley} is expressed as

$$v_{valley} = V_{in} - v_{out}\frac{N_1}{N_2}. \tag{3.61}$$

To guarantee true zero-voltage switching, the valley of the drain–source voltage must be sufficiently deep at the instant the MOSFET is turned on. This requires fulfilling the following condition:

$$v_{out}\frac{N_1}{N_2} >= V_{in}. \tag{3.62}$$

Figure 3.15 shows the typical drain–source voltage waveform observed once the magnetic core has been fully demagnetized, illustrating the free-running resonance that generates the characteristic sequence of voltage valleys exploited for quasi-resonant turn-on.

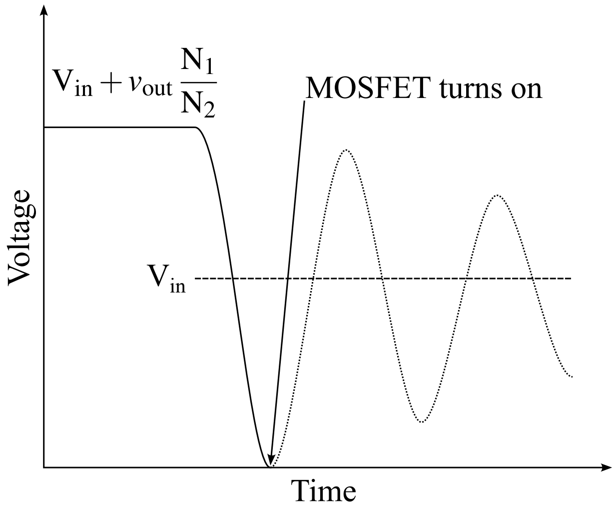

Fig. 3.15 Typical drain–source voltage waveform observed after complete core demagnetization, showing the free-running resonance and the sequence of voltage valleys exploited for quasi-resonant turn-on.

At the beginning of the charging process, the reflected voltage is very low, and as a consequence the MOSFET cannot achieve zero-voltage switching. Under these conditions, the drain–source voltage does not fall sufficiently before turn-on, and the energy stored in $\mathrm{C_D}$ and $\mathrm{C_{oss}}$ is fully dissipated in the MOSFET channel during each switching transition. This loss mechanism is quantified by

$$E_{\mathrm{off}} = \frac{1}{2}\,(\mathrm{C_D} + \mathrm{C_{oss}})\, v_{\mathrm{valley}}^2. \tag{3.63}$$

Therefore, a larger $\mathrm{C_D}$ directly increases switching losses in the early charging phase, negatively impacting efficiency until the reflected voltage becomes sufficiently high to enable ZVS operation. At the same time, $\mathrm{C_D}$ also helps to reduce turn-off losses by softening the drain–source voltage slope during the MOSFET turn-off. Thus, $\mathrm{C_D}$ has a dual and opposing influence on efficiency, and the optimal value is identified experimentally following the methodology presented in [66].

The zero–current detection (ZCD) required for quasi-resonant control is obtained using the auxiliary winding included in the transformer structure, as shown in Fig. 3.13. This winding provides a scaled replica of the voltage ringing that the controller can reliably detect. By monitoring this auxiliary signal, the controller identifies the instant at which the core is fully demagnetized and schedules the next MOSFET turn-on at the subsequent drain–source voltage valley, thereby enabling valley switching and ensuring high-efficiency quasi-resonant operation.

Once the operating principle of the quasi-resonant flyback has been established, the design process begins by specifying the maximum allowable primary peak current. This current limit is directly related to the maximum input power $P_{\mathrm{in,max}}$, which is obtained from the desired maximum output power $P_{\mathrm{out,max}}$ and the assumed converter efficiency η. For the present design, the target output power is 40 W and an efficiency of 90 % is assumed:

$$P_{\mathrm{in,max}} = \frac{P_{\mathrm{out,max}}}{\eta}, \tag{3.64}$$

$$P_{\mathrm{in,max}} = \mathrm{V_{in}}\, i_{1,\mathrm{avg,max}} = \mathrm{V_{in}}\, \frac{i_{1\mathrm{p,max}}\, D_{\mathrm{max}}}{2}. \tag{3.65}$$

Here, $i_{1,\mathrm{avg,max}}$ is the maximum cycle-average primary current, $i_{1\mathrm{p,max}}$ is the maximum admissible peak current, and $\mathrm{D_{max}}$ is the maximum duty cycle, set to 0.6 to prevent excessively short off-times that could overstress the MOSFET. Combining (3.64) and (3.65) yields

$$i_{1\mathrm{p,max}} = \frac{2\,P_{\mathrm{out,max}}}{\mathrm{V}_{\mathrm{in}}\,D_{\mathrm{max}}\,\eta} = 3.09\,\mathrm{A}. \tag{3.66}$$

Now that the maximum admissible primary peak current has been defined, the magnetizing inductance $\mathrm{L_m}$ of the flyback transformer can be determined from the linear current ramp during the MOSFET on-time. Using the relation

$$\mathrm{L_m} = \frac{\mathrm{V_{in}}}{i_{1\mathrm{p,max}}}\,t_{\mathrm{on}} = \frac{\mathrm{V_{in}}}{i_{1\mathrm{p,max}}}\,\frac{D_{\mathrm{max}}}{f_{\mathrm{s,max}}} = 93.31\,\mu\mathrm{H}, \tag{3.67}$$

the required magnetizing inductance is obtained for the chosen design parameters. According to the design guidelines provided in the STMicroelectronics Application Note AN1326 [67], quasi-resonant flyback converters of this class typically operate with a nominal switching-frequency range of 70–110 kHz. In the present design, a maximum switching frequency $f_{\mathrm{s,max}}$ of 100 kHz is selected, lying near the centre of the recommended interval and providing a suitable compromise between the transformer size, the efficiency, and the switching losses.

Once the magnetizing inductance and the maximum primary peak current are defined, the next step is to choose a suitable magnetic core. After an iterative evaluation of different core geometries and materials, the TDK/EPCOS ferrite core B66311G0170X187 (material N87) is selected. Using the manufacturer-specified inductance factor $\mathrm{A_L}$, the required number of primary turns is obtained from

$$\mathrm{N_1} = \sqrt{\frac{\mathrm{L_m}}{\mathrm{A_L}}} = 25.86 \approx 26. \tag{3.68}$$

With the selected number of turns, the peak magnetic flux Φ_{max} is

$$\Phi_{\mathrm{max}} = \frac{\mathrm{L_m}\,i_{1\mathrm{p,max}}}{\mathrm{N_1}} = 11.19\,\mu\mathrm{Wb}, \tag{3.69}$$

and the corresponding peak flux density B_{max} follows as

$$B_{\mathrm{max}} = \frac{\Phi_{\mathrm{max}}}{\mathrm{A_e}} = 349\,\mathrm{mT}, \tag{3.70}$$

where $\mathrm{A_e}$ is the effective area of the magnetic core. The resulting flux density remains well below the saturation limit of the N87 material at the operating frequency (approximately 490 mT at 25 °C), thereby confirming the suitability of the selected core.

The number of secondary turns N_2 is chosen to ensure that the quasi-resonant flyback operates under zero-voltage switching during most of the charging interval. To satisfy the condition established in (3.62), the transformer is designed such that ZVS is already achieved once the output voltage exceeds 350 V. In this way, ZVS is available throughout the major portion of the charge cycle, significantly reducing MOSFET turn-on losses and improving the overall efficiency. Enforcing this requirement with the selected primary turns ($N_1 = 26$), the number of secondary turns is set to $N_1 = 200$.

According to (3.55), the maximum steady-state drain–source voltage expected during the MOSFET Q turn-off transition is approximately 243 V. However, the leakage-inductance resonance that occurs at turn-off can generate significantly higher transient voltage peaks, which must be safely absorbed by the semiconductor switch and the RCD snubber circuit. For this reason, the Infineon IPN60R600P7SATMA1 MOSFET is selected. This device provides a 600 V voltage rating and a continuous drain current capability of 6 A, ensuring ample margin under all operating conditions. According to the manufacturer's recommendations, the same gate resistor R_G value should be used for both turn-on and turn-off operation. The datasheet specifies a value of 10 Ω, and this value is therefore adopted for the present design. Although a MOSFET with lower ratings could theoretically suffice, component cost optimisation of the charging unit is not a design objective in this research work, and the selected device offers robust performance and reliable operation.

The design of the RCD snubber follows a systematic procedure to ensure that the leakage-inductance energy is safely dissipated while limiting the drain–source voltage overshoot during the MOSFET turn-off transition. The maximum energy stored in the transformer leakage inductance $E_{\mathrm{Llk,max}}$ at the moment of the turn-off is first estimated as

$$E_{\mathrm{Llk,max}} = \frac{1}{2}\,\mathrm{L_{lk}}\,i^2_{\mathrm{1p,max}} = 8.98\,\mu\mathrm{J}. \tag{3.71}$$

For flyback transformers with tightly coupled windings, the leakage inductance typically lies in the range of 1–3 % of the magnetizing inductance. In this design, a leakage inductance of $\mathrm{L_{lk}} = 0.02\,\mathrm{L_m}$ is assumed, corresponding to $\mathrm{L_{lk}} = 1.89\,\mu\mathrm{H}$ for $\mathrm{L_m} = 94.30\,\mu\mathrm{H}$.

When the drain–source voltage exceeds the clamp level v_{clamp}, the snubber diode $\mathrm{D_{sn}}$ becomes forward biased and diverts the leakage-inductance current into the RCD network. The clamp voltage is defined by

$$v_{\mathrm{clamp}} = \mathrm{V_{in}} + v_{\mathrm{Csn}}, \tag{3.72}$$

where v_{Csn} is the voltage across the snubber capacitor $\mathrm{C_{sn}}$. It is important to note that v_{Csn} is not constant: at the beginning of the charging process, $v_{\mathrm{Csn}} = 0$, and during each switching cycle it increases as leakage energy is redirected into the snubber until stabilising at its steady-state maximum value $v_{\mathrm{Csn,max}}$.

In this design, the maximum clamp voltage is set to $v_{\mathrm{clamp,max}} = 500\,\mathrm{V}$, which corresponds to a maximum snubber-capacitor voltage of $v_{\mathrm{Csn,max}} = 257\,\mathrm{V}$. Following the methodology of Fairchild Application Note AN4147 [68], the snubber resistance $\mathrm{R_{sn}}$ is dimensioned as

$$\mathrm{R_{sn}} = \frac{v^2_{\mathrm{Csn,max}}}{P_{\mathrm{sn}}} = \frac{v_{\mathrm{Csn,max}}\left(v_{\mathrm{Csn,max}} - \frac{\mathrm{N_1}}{\mathrm{N_2}}\, v_{\mathrm{out,max}}\right)}{E_{\mathrm{L_{lk}},\mathrm{max}}\, f_{\mathrm{s,max}}} = 17.7\,\mathrm{k\Omega} \approx 18\,\mathrm{k\Omega}, \tag{3.73}$$

where $v_{\mathrm{out,max}}$ is the maximum output voltage.

Once $\mathrm{R_{sn}}$ is fixed, the snubber capacitance $\mathrm{C_{sn}}$ is obtained from the allowable ripple of the snubber voltage. According to [68], the ripple is

$$\Delta v_{\mathrm{Csn}} = \frac{v_{\mathrm{Csn}}}{\mathrm{R_{sn}}\,\mathrm{C_{sn}}\, f_{\mathrm{s}}}, \tag{3.74}$$

and in this design it is limited to 5 % of $v_{\mathrm{Csn,max}}$. Solving (3.74) for $\mathrm{C_{sn}}$ yields

$$\mathrm{C_{sn}} = \frac{v_{\mathrm{Csn,max}}}{\Delta V_{\mathrm{sn}}\,\mathrm{R_{sn}}\, f_{\mathrm{s}}} = 11.1\,\mathrm{nF} \approx 11\,\mathrm{nF}. \tag{3.75}$$

The snubber diode must combine fast switching behaviour with a sufficient reverse-voltage rating to operate safely at the selected clamp level. For this reason, a fast-recovery or ultrafast diode with a blocking-voltage rating equal to or greater than that of the MOSFET is required. The AES2JF-HF device from Comchip Technology is selected, providing a repetitive peak reverse voltage of 600 V, a continuous forward-current rating of 2 A, and a peak forward current of 50 A, which is sufficient to accommodate the short leakage-energy pulses in the snubber branch.

Furthermore, as a Schottky device, it exhibits negligible reverse-recovery current, thereby avoiding additional stress on the MOSFET and reducing switching losses in the RCD clamp.

According to (3.54), the maximum reverse voltage across the series-connected secondary rectifier diodes is approximately 1.9 kV under nominal operating conditions. To provide sufficient margin for switching-induced ringing, two STTH112U ultrafast diodes from STMicroelectronics are connected in series. Each device features a repetitive peak reverse-voltage rating of 1200 V, resulting in a combined blocking capability of 2400 V, which comfortably exceeds the estimated 1900 V requirement. The continuous forward-current rating of each diode is 2 A, which is adequate given that the peak secondary current $i_{2\mathrm{p}}$ satisfies

$$i_{2\mathrm{p}} = i_{1\mathrm{p}} \frac{\mathrm{N}_1}{\mathrm{N}_2} = 0.4\,\mathrm{mA}. \tag{3.76}$$

This ensures that both the voltage- and current-stress specifications of the secondary diodes are safely met.

To ensure proper static and dynamic voltage sharing between the series-connected rectifier diodes, a balancing network is typically required. Static voltage sharing is achieved by connecting the balancing resistors R_{b1} and R_{b2} in parallel with each diode. For a string of N_{S} identical devices with repetitive peak reverse voltage $\mathrm{V}_{\mathrm{RRM}}$, blocking a maximum total reverse voltage v_{M}, the balancing resistor can be dimensioned according to the STMicroelectronics Application Note AN443 [69]

$$\mathrm{R}_{\mathrm{b1}} = \mathrm{R}_{\mathrm{b2}} < \frac{\mathrm{N}_{\mathrm{S}}\,\mathrm{V}_{\mathrm{RRM}} - v_{\mathrm{M}}}{(\mathrm{N}_{\mathrm{S}} - 1)\,\mathrm{I}_{\mathrm{R}}} = 10\,\mathrm{M}\Omega, \tag{3.77}$$

where I_{R} is the maximum reverse leakage current of a single diode at $\mathrm{V}_{\mathrm{RRM}}$ and the specified junction temperature. In this design, the total reverse voltage is $v_{\mathrm{M}} = 1900\,\mathrm{V}$ and the selected diode exhibits a worst-case leakage current of $\mathrm{I}_{\mathrm{R}} = 50\,\mu\mathrm{A}$. These values ensure that the resistor current dominates the leakage-current dispersion, thereby equalising the DC voltage distribution across the series string.

In contrast, dynamic voltage sharing normally requires additional capacitors in parallel with each diode to compensate for reverse-recovery mismatches. However, in the present flyback converter operating in quasi-resonant mode, the secondary current decays smoothly to zero over several microseconds, and the peak secondary current is relatively low. Consequently, the current slew rate $\mathrm{d}i/\mathrm{d}t$ at turn-off is very small, the associated reverse-recovery charge is negligible, and both diodes effectively cease conduction at nearly the same instant. Under these soft-switching conditions, dynamic voltage imbalance is minimal and no additional balancing capacitors are required; only the resistive network is sufficient to ensure adequate voltage sharing.

The control of the flyback converter is implemented using the L6565D quasi-resonant controller from STMicroelectronics, which integrates both the control logic and the MOSFET gate driver. The device drives the primary switch Q through the GD pin and regulates the operation of the converter by monitoring the primary current via the current-sense pin CS and the output voltage through the feedback pin FB. In addition, the controller features a feedforward input that measures the input voltage and automatically adjusts the maximum peak current as a function of the mains level, thereby improving line regulation and ensuring safe operation across the input range. The device also includes a zero-crossing detection ZCD pin, which, using the voltage information from the ZCD winding, detects the drain–source voltage valleys following the transformer demagnetisation interval. This allows the controller to initiate each turn-on at the valley point, ensuring quasi-resonant operation and significantly reducing the switching losses of the primary MOSFET.

The L6565D monitors the primary current through the voltage developed across the sense resistor $\mathrm{R}_{\text{sense}}$. If the voltage at the CS pin exceeds the internal threshold $v_{\text{CS,th}}$ (0.74 V), the controller immediately turns off the MOSFET to prevent the primary current from rising further. The sense resistor is therefore dimensioned according to

$$\mathrm{R}_{\text{sense}} = \frac{v_{\text{CS,th}}}{i_{\text{1p,max}}} = 0.24\,\mathrm{m}\Omega \approx 0.25\,\mathrm{m}\Omega. \tag{3.78}$$

The auxiliary winding dedicated to zero-current detection generates the voltage applied to the ZCD pin, which is internally clamped between 5.2 V and 0.65 V. Let N_{ZCD} denote the number of turns of this winding. When the MOSFET is on, the auxiliary voltage is proportional to the input voltage and given by

$$v_{\text{ZCD,on}} = -\mathrm{V}_{\text{in}}\frac{\mathrm{N}_{\text{ZCD}}}{\mathrm{N}_1}. \tag{3.79}$$

Conversely, during the MOSFET off-time, the polarity reverses and the auxiliary voltage reflects the output voltage as

$$v_{\mathrm{ZCD,off}} = v_{\mathrm{out}} \frac{\mathrm{N_{ZCD}}}{\mathrm{N_2}}. \tag{3.80}$$

Selecting $\mathrm{N_{ZCD}} = 4$ results in a reflected voltage of approximately 7 V during the on-time and about -30 V during the off-time. Since both values exceed the ZCD pin clamp levels, a series resistor $\mathrm{R_{ZCD}}$ is required to limit the current flowing into the internal clamping network. Design guidelines recommend choosing $\mathrm{R_{ZCD}}$ in the range of 100–150 kΩ [67]. In this work, a value of $\mathrm{R_{ZCD}} = 150\,\mathrm{k\Omega}$ is adopted to ensure safe pin-current levels while maintaining reliable zero-crossing detection.

The voltage-feedback circuitry requires a local supply rail, which is obtained from the non-regulated auxiliary output of the flyback transformer. This auxiliary supply is designed to provide approximately 15 V when $v_{\mathrm{out}} = 1500\,\mathrm{V}$. Let $\mathrm{N_{aux}}$ denote the number of turns in the auxiliary winding. Since the auxiliary voltage is proportional to the output voltage, the turns ratio is selected according to

$$\mathrm{N_{aux}} = \frac{v_{\mathrm{out,max}}}{\mathrm{N_2}}, \tag{3.81}$$

ensuring that the auxiliary winding delivers the required 15 V when the output voltage reaches its maximum value.

With the values of $\mathrm{N_1}$, $\mathrm{N_2}$, $\mathrm{N_{ZCD}}$, $\mathrm{N_{aux}}$ and the magnetic core defined, the complete transformer structure is fully specified (see Fig. 3.16).

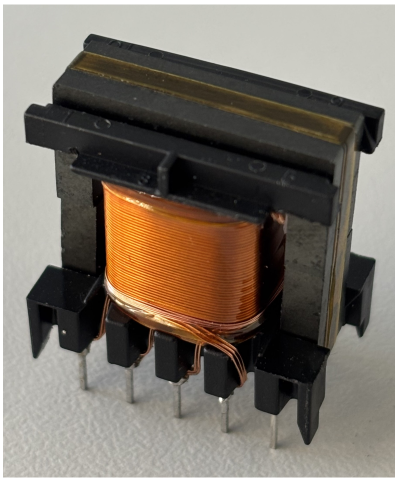

Fig. 3.16 Prototype of the designed flyback transformer.

The auxiliary winding is rectified by a Schottky diode SK34SMA from Diotec Semiconductor, featuring a reverse-voltage rating of 40 V and a continuous forward-current capability of 3 A. The rectified auxiliary voltage is filtered by a 47 µF, 35 V electrolytic capacitor.

The detailed design of the feedback and voltage-regulation circuitry is beyond the scope of this work; instead, the implementation recommended in the STMicroelectronics Application Note AN1326 has been adopted as a reference design [67].

The auxiliary battery cannot deliver the high-frequency current demanded by the flyback converter, particularly during the rapid switching transitions of the primary MOSFET. To maintain a stable input voltage under these dynamic conditions, a bulk decoupling capacitor C_{in1} of 47 µF (electrolytic) is placed across the input terminals to support the low-frequency energy requirement. In addition, a 22 µF ceramic capacitor C_{in2} is connected in parallel to provide the high-frequency current components associated with the switching action. The combination of C_{in1} and C_{in2} ensures a low-impedance input path over the entire frequency range, preventing voltage droop and reducing electromagnetic interference.

The complete prototype of the capacitor-charging unit, integrating the quasi-resonant flyback converter, and control circuitry, is shown in Fig. 3.17. This implementation reflects the final design described in this chapter and has been used for the experimental validation.

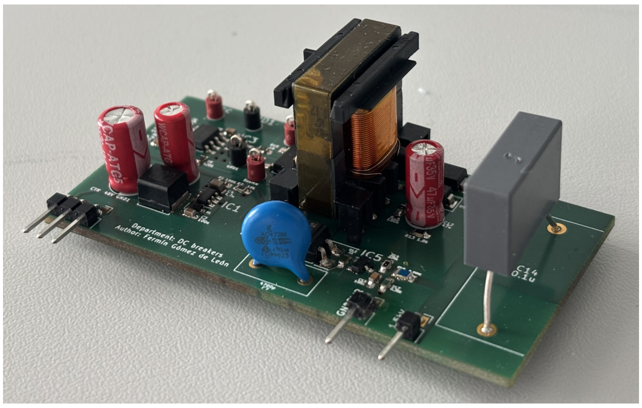

Fig. 3.17 Prototype of the complete capacitor-charging unit implementing the quasi-resonant flyback converter and associated control circuitry.

3.2 Experimental Validation

This chapter presents the experimental validation of the proposed system. First, the charging unit is verified using a dummy capacitor bank composed of four 680 µF capacitors connected in series, resulting in an effective capacitance of approximately 170 µF. Then, the complete electric drive is experimentally evaluated to confirm its overall behavior and its consistency with the design specifications. All measurements have been acquired using a Tektronix DPO 7104C oscilloscope.

The only design parameter that remains undefined is the primary-side damping/snubber capacitor $\mathrm{C_D}$, whose value is determined experimentally. This capacitor modifies the drain–source voltage transient of the MOSFET during turn-off by adding capacitive current and reducing the slope $\mathrm{d}v/\mathrm{d}t$. As a result, the device experiences lower turn-off losses, since the overlap between voltage and current during the switching transition is reduced. However, this beneficial effect comes at the cost of an increased energy that must be discharged from $\mathrm{C_D}$ at each turn-on. If ZVS is achieved, the stored energy in $\mathrm{C_D}$ is mostly recovered through the resonant transition, and the turn-on losses remain low. Conversely, if ZVS is not consistently maintained, the MOSFET turns on with a residual drain–source voltage, forcing the device to dissipate the energy stored in $\mathrm{C_D}$ at every switching cycle. In this case, increasing $\mathrm{C_D}$ significantly raises the turn-on losses.

Therefore, $\mathrm{C_D}$ introduces a trade-off between reduced turn-off losses and potentially increased turn-on losses. The optimal $\mathrm{C_D}$ is selected experimentally by evaluating the overall charging efficiency of the converter:

$$\eta = \frac{E_{\mathrm{out},1}}{E_{\mathrm{in},1}} 100, \tag{3.82}$$

where $E_{\mathrm{in},1}$ is the total input energy delivered to the converter during the interval $[t_0, t_1]$, and $E_{\mathrm{out},1}$ is the final energy stored in the load capacitor.

The input energy is computed as

$$E_{\mathrm{in},1} = \int_{t_0}^{t_1} \mathrm{V_{in}}\, i_{\mathrm{in}}\, \mathrm{d}t, \tag{3.83}$$

and the output energy is obtained from the capacitor voltage at the end of the charge:

$$E_{\mathrm{out},1} = \frac{1}{2}\mathrm{C}_{\mathrm{out}}\, v_{\mathrm{out},1}^2, \tag{3.84}$$

where $v_{\mathrm{out},1}$ is the output capacitor voltage measured at the end of the charging interval t_1.

The input voltage is measured using the Tektronix TA042 differential probe, the input current with the Tektronix TCP0150 current probe, and the output voltage with the Pico TA044 differential probe.

Figure 3.18 [66] shows the obtained efficiency results. It can be observed that increasing $\mathrm{C_D}$ initially improves the charging efficiency, as the reduction of turn-off losses dominates. The peak efficiency of 91.4 % is achieved with $\mathrm{C_D} = 680\,\mathrm{pF}$. Beyond this value, the efficiency decreases because the additional turn-on losses outweigh the reduction of turn-off losses.

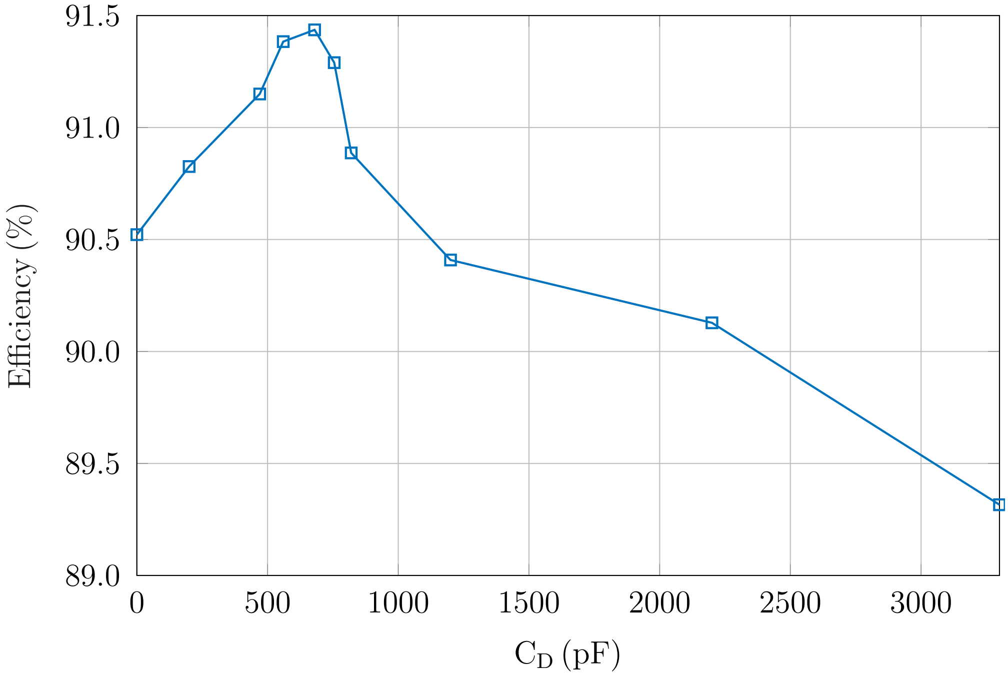

Fig. 3.18 Measured charging efficiency as a function of the primary-side damping/snubber capacitor $\mathrm{C_D}$.

Figure 3.19 shows the voltage charging profile of the capacitor bank. The bank is charged to approximately 1.5 kV in about 7 s, with a final measured value of 1470 V.

This deviation corresponds to an error of only 2 % and is attributed to the tolerance of the resistor divider used in the feedback circuit to sense the output voltage. Since the control loop relies on the scaled measurement provided by this divider, any mismatch in the resistor values directly results in a proportional error in the estimated output voltage.

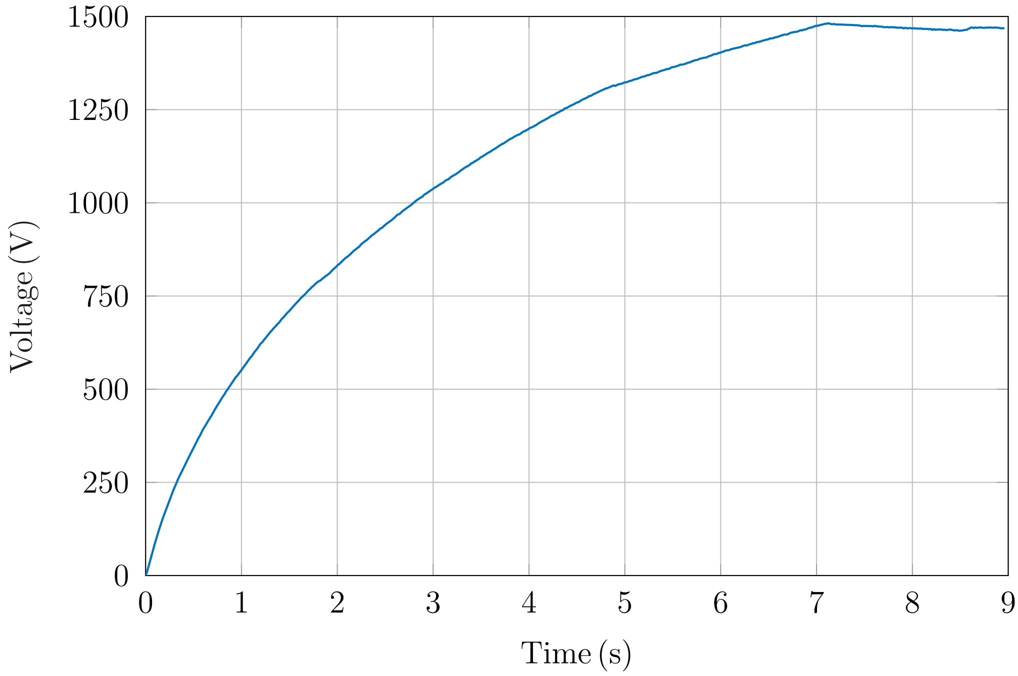

Fig. 3.19 Measured charging voltage profile of the capacitor bank.

Figure 3.2 shows the primary-side current at $v_{\mathrm{out}} = 750\,\mathrm{V}$. The current is not measured directly; instead, the voltage across the sense resistor $\mathrm{R}_{\mathrm{sense}}$ is acquired using the Rohde & Schwarz RT-ZD02 differential probe. The instantaneous current is then obtained by dividing the measured voltage by the known value of the sense resistor. As expected, the primary current increases linearly, reaching a peak value of approximately 2.95 A, which corresponds to the maximum current defined in the design stage. The linearity of this current ramp confirms that the magnetic core remains unsaturated throughout the conduction interval.

In addition, when the MOSFET is turned off, a small negative spike appears in the measured current waveform. This behaviour originates from the topology of the gate-drive circuit. Since the gate driver is not isolated, it applies the gate voltage with respect to ground rather than with respect to the source terminal, which is the conventional configuration. Although the voltage drop across the sense resistor is small and does not affect the switching operation, the gate current flows through the sense resistor on its return path to the driver. As a consequence, the measured signal corresponds to the superposition of the primary current i_1 and the transient gate current. During turn-off, this gate current briefly reverses direction, producing the observed negative spike in the reconstructed primary-current waveform.

Figure 3.20 also shows that the linear current ramp begins from a negative value of approximately -1 A. This behaviour originates from the resonance between the magnetizing inductance $\mathrm{L_m}$ and the total capacitance $(\mathrm{C_D}+\mathrm{C_{oss}})$. Once the magnetic core is fully demagnetized, the voltage across $\mathrm{C_D}$ and $\mathrm{C_{oss}}$ begins to oscillate, and a corresponding resonant current flows through the transformer. If the voltage amplitude of this resonance is sufficiently large such that $v_{\mathrm{out}}/\mathrm{N_2} > \mathrm{V_{in}}$, the MOSFET body diode becomes forward-biased, thereby clamping the resonance. At this point, the voltage applied to the transformer collapses to $\mathrm{V_{in}}$, and the primary current begins to rise linearly. As soon as the current becomes positive , conduction naturally commutes from the body diode to the MOSFET N-channel.

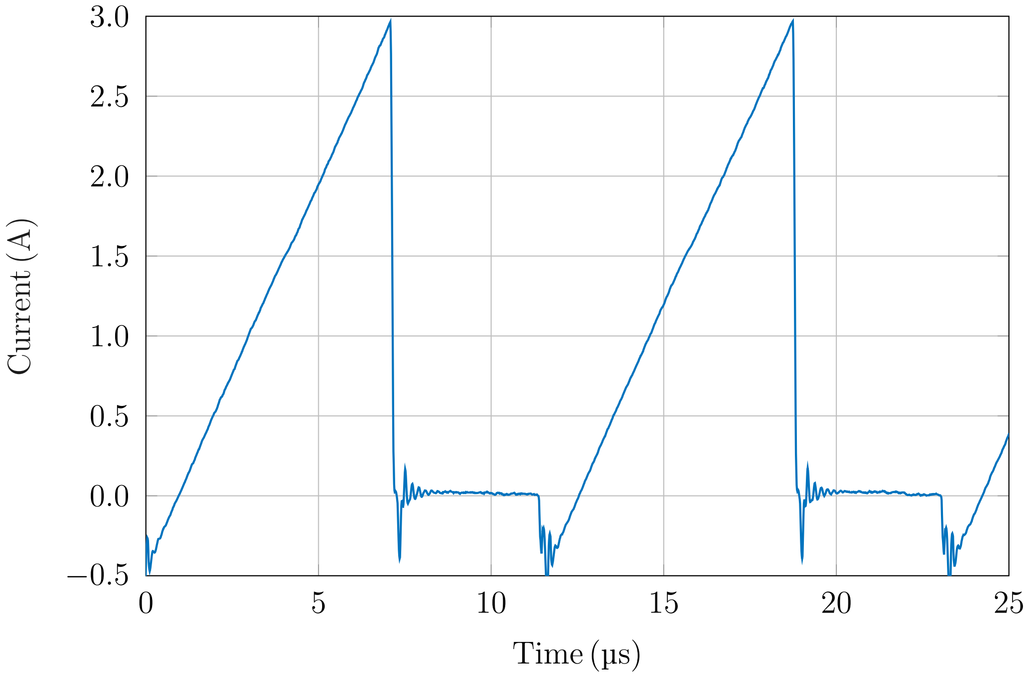

Fig. 3.20 Measured primary-side current waveform at $v_{\mathrm{out}} = 750\,\mathrm{V}$.

Figure 3.21 shows the measured drain–source voltage at $v_{\text{out}} = 750\,\text{V}$. The resonance between the leakage inductance L_{lk} and the total capacitance $(C_D + C_{\text{oss}})$ is highly damped, and the peak voltage reaches only 158 V, corresponding to an overshoot of approximately $9\,\%$. This performance is achieved through a careful transformer construction: the windings are tightly wound, and the primary and secondary are interleaved to minimize L_{lk}. In addition, the capacitor C_D contributes to limiting the voltage peak. It can also be observed that the drain–source voltage naturally transitions to zero when the magnetic core is fully demagnetized, indicating that ZVS is achieved.

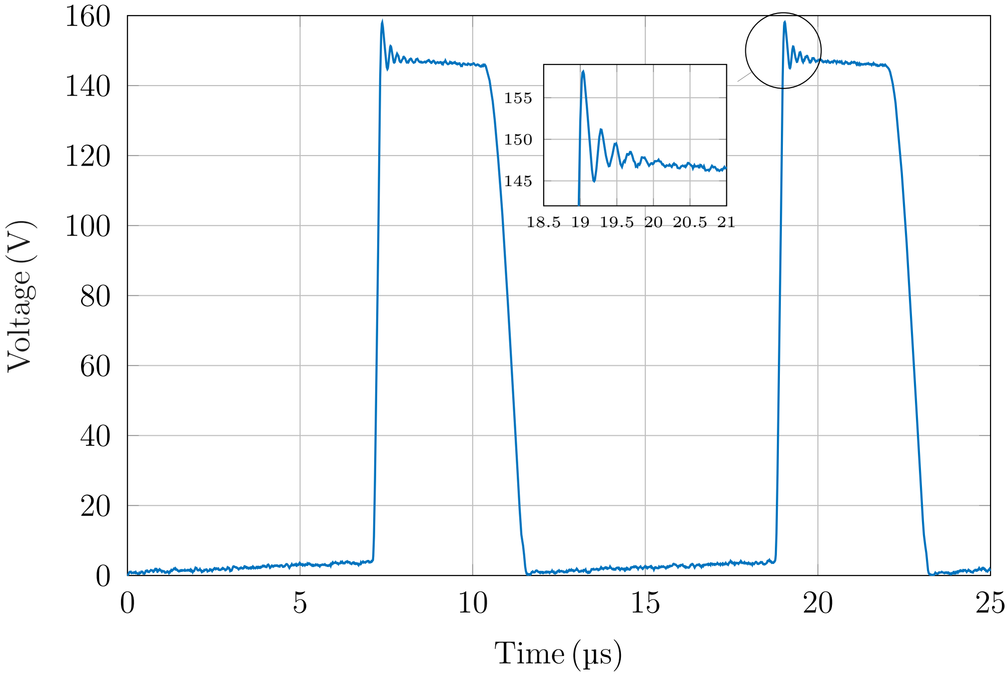

Fig. 3.21 Measured drain–source voltage waveform at $v_{\text{out}} = 750\,\text{V}$.

Once the charging unit design has been experimentally verified, the complete electric drive is evaluated. The analysis is carried out for three configurations: the 1-capacitor drive, the 2-capacitor drive, and the 4-capacitor drive, allowing a direct comparison of the dynamic behaviour and discharge performance as the available energy increases. Figure 3.22 shows the experimental test setup. As illustrated in the figure, the output terminals of the drive have been intentionally short-circuited in order to reproduce the worst-case load condition and to assess the maximum current capability of the system. The discharge current is measured using the PEM CWT 1500R current probe.

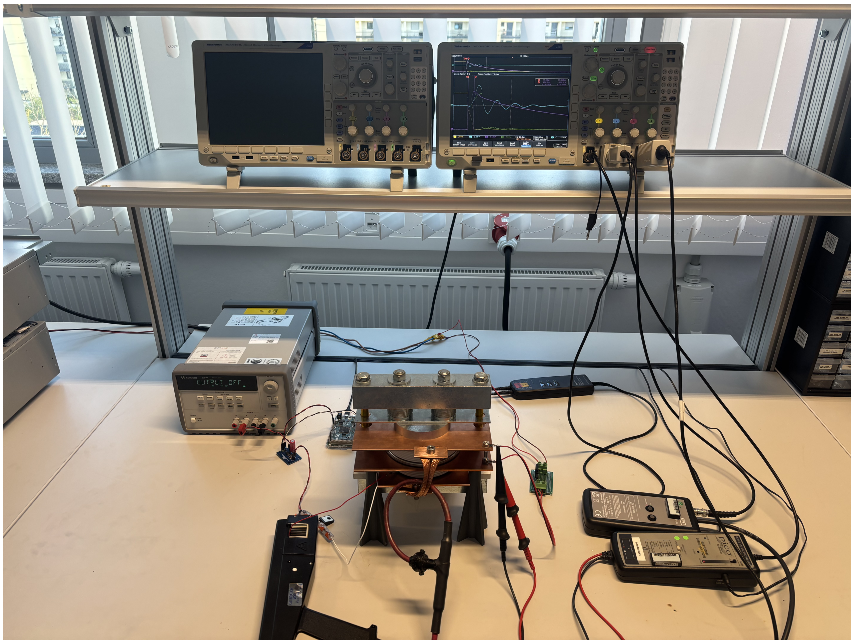

Fig. 3.22 Experimental setup used for the validation of the complete electric drive.

Figure 3.24 shows the discharge current for the three drive configurations. For the 1-capacitor bank drive, a peak current of approximately 80 kA is obtained, which is in good agreement with the rough estimation from the design stage (91.85 kA). In the 2-capacitor configuration, the peak current reaches 110 kA, again consistent with the expected value of 124 kA. This configuration meets the design requirement of delivering a peak current of at least 100 kA. Finally, the 4-capacitor drive produces a peak current of approximately 165 kA.

Figure 3.23 presents a zoomed view of the discharge current for the three configurations. The 1-capacitor drive reaches its peak current at approximately 10.5 µs, in close agreement with the design prediction of 10.2 µs. The 2-capacitor drive reaches the peak current at 16.5 µs, also consistent with the calculated value of 14.2 µs. Finally, the 4-capacitor configuration reaches its maximum current at 22.1 µs. Since all configurations share similar stray inductances, the results clearly show that increasing the total capacitance reduces the natural frequency of the discharge circuit, thereby increasing the peak-current time. It is also important to note that all configurations satisfy the design requirement of achieving the peak current within 25 µs.

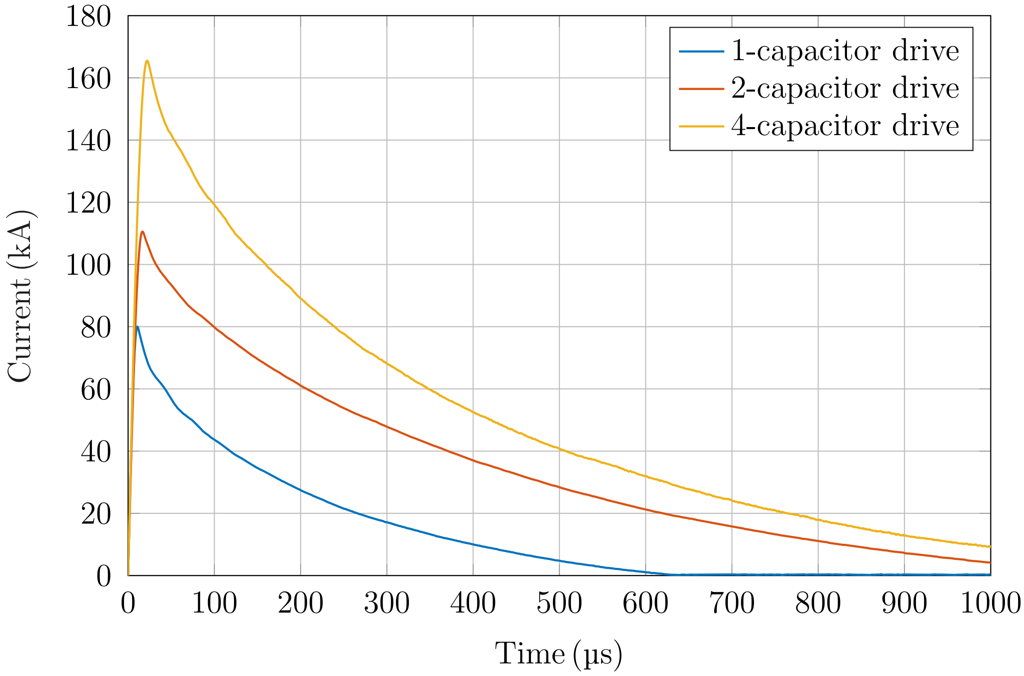

Fig. 3.23 Measured discharge current for the 1-, 2-, and 4-capacitor drive configurations under short-circuit conditions.

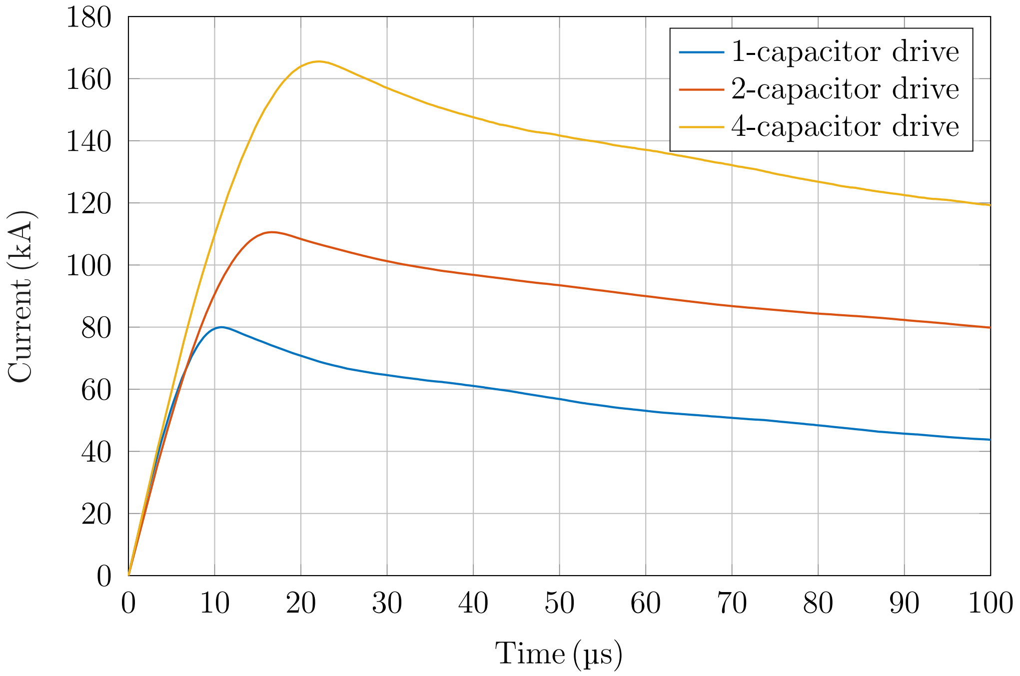

Fig. 3.24 Zoomed view of the measured discharge current during the first 100 µs for the 1-, 2-, and 4-capacitor drive configurations.

Figure 3.25 shows the calculated current slew rate during the first 100 µs. All configurations exhibit peak di/dt values between 10 kA/µs and 12 kA/µs, far exceeding the 1 kA/µs datasheet limit and confirming the robustness of both the thyristor and the freewheel diode under such demanding pulse-power conditions. ‘

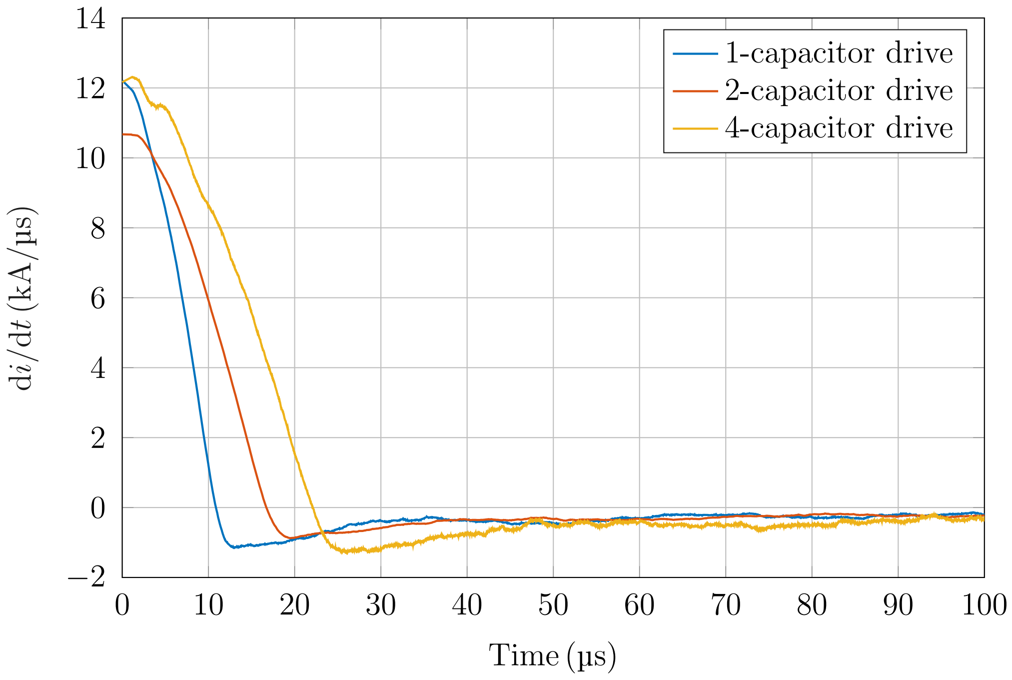

Fig. 3.25 Current slew rate di/dt during the first 100 µs for the 1-, 2-, and 4-capacitor drive configurations.

Table 3.5 summarizes the main experimental results obtained for the three drive configurations, including the peak current, the peak-current instant, and the maximum current slew rate di/dt. These values provide a clear comparison of the dynamic behaviour of the 1-, 2-, and 4-capacitor drives.

Table 3.5 Extracted current metrics for the different capacitor-bank configurations.

Configuration	**Peak current** [kA]	**Peak time** [µs]	**Maximum slew rate** [kA/µs]
1-capacitor drive	80	10.5	12.2
2-capacitor drive	110	16.5	10.7
4-capacitor drive	165	22.1	12.3

3.3 Summary and Conclusions

This chapter has presented the experimental validation of both the charging unit and the complete electric drive. The characterization of the quasi-resonant flyback stage confirmed the correct operation of the converter and provided the experimental determination of the primary-side damping capacitor C_D. By analysing the charging efficiency as a function of C_D, an optimal value of 680 pF was identified, achieving a peak efficiency of 91.44 % during the charging process. The waveform measurements showed a linear primary-current ramp, confirming that the magnetic core does not saturate, and demonstrated well-damped drain–source voltage transitions with a limited overshoot of only 9 %. The converter also achieved zero-voltage switching under the selected operating conditions. These results verify that the converter design satisfies the intended performance targets while ensuring safe switching behaviour of the MOSFET.

The complete electric drive was subsequently evaluated for three energy-storage configurations: 1-capacitor, 2-capacitor, and 4-capacitor bank arrangements. Peak discharge currents of 80 kA, 110 kA, and 165 kA were obtained, respectively, all in close agreement with the predictions from the design phase. The corresponding peak-current times (10.5 µs, 16.5 µs, and 22.1 µs) also matched the expected values, confirming that increasing the total capacitance reduces the natural frequency of the discharge circuit and consequently increases the time to reach the peak current. All three configurations fulfil the design requirement of reaching the peak current within 25 µs.

The extracted parasitic parameters further showed that the 2-capacitor configuration provides the lowest total stray inductance, as the reduction in equivalent ESL outweighs the increase in current-path inductance L_{CD}. In contrast, moving to four capacitors increases L_{stray} due to the larger physical spacing of the capacitor modules. The measured stray resistance remained close to ESR/N_p for all configurations, indicating that the capacitors' intrinsic ESR dominates the total resistive behaviour.

Finally, the di/dt analysis showed maximum slew rates between 10 kA/µs and 12 kA/µs for all configurations, far exceeding the 1 kA/µs limit indicated in the semiconductor datasheets. Despite this, both the thyristor and the freewheel diode operated reliably, demonstrating their robustness under extreme pulse-power stress conditions.

Overall, the experimental results confirm that the charging unit, the power stage, and the semiconductor devices all operate within the required performance envelope. The measured data validate the design methodology and demonstrate that the proposed electric drive architecture is capable of delivering the current levels, response times, and robustness necessary for the railgun-based actuation system in ultrafast DC circuit breakers.

Chapter 4

The Railgun

Chapter 4 focuses on the actuator. It begins with a review of the railgun and its main topologies, followed by the modelling framework comprising an analytical model, a quasi-static formulation, and a transient multiphysics model. The chapter concludes with the experimental validation of the actuator and a summary of the main findings.

4.1 State of the Art

During the last decades, research on electromagnetic railguns has intensified, driven by their role in military systems [70–73] and their potential for suborbital and orbital space-launch applications [74–76]. In parallel, several railgun topologies have been explored to improve current injection, reduce losses, and enhance acceleration performance. This section outlines the basic railgun operating principle and reviews the most relevant topological variations reported in the literature.

The operating principle of the railgun is based on the Lorentz force generated by the interaction between a high pulsed current and the magnetic field established in the armature. When a current density $\mathbf{J}$ flows through the conductive armature, the resulting electromagnetic force is given by

$$\mathbf{F} = \int \mathbf{J} \times \mathbf{B} \, \mathrm{d}V, \tag{4.1}$$

where $\mathbf{B}$ denotes the magnetic flux density. This force accelerates the armature along the rails. A sketch of the basic railgun geometry is shown in Fig. 4.1.

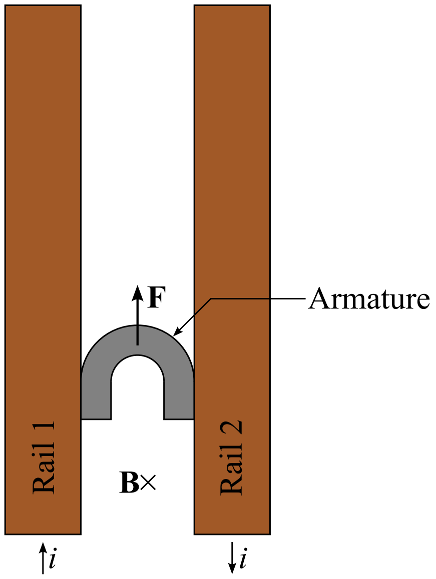

Fig. 4.1 Sketch of the basic railgun actuator configuration.

The performance of a railgun can be improved by increasing the magnetic coupling between the current path and the armature, i.e., the fraction of magnetic flux that effectively links the armature and contributes to the Lorentz force. Among the geometries proposed in the literature, the most common configuration is the planar-series railgun [77–79]. Figure 4.2 illustrates this configuration.

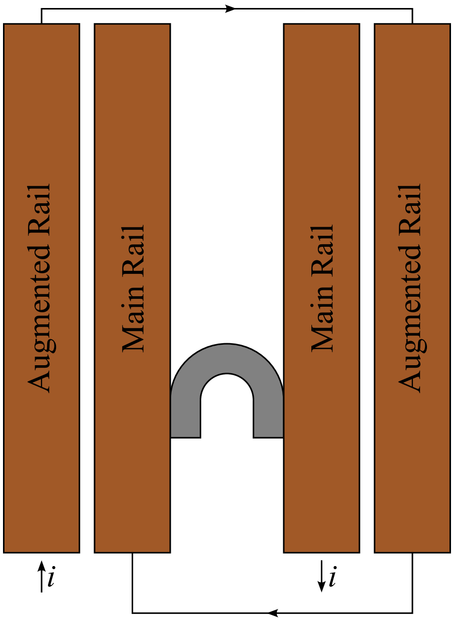

Fig. 4.2 Sketch of the planar-series railgun configuration.

The series planar augmented railgun achieves better magnetic coupling because the augmentation rails strengthen, confine, and better distribute the magnetic flux linking the armature, leading to a more effective Lorentz force.

One limitation of the series-planar augmented railgun is the increase in total inductance caused by the added augmentation rails and their electrical connections. As a result, the current requires more time to rise, slowing the electromagnetic response of the actuator. Furthermore, because the augmentation rails are connected at the muzzle, the current must travel along the full rail length before returning. This produces a magnetic field component toward the muzzle that does not link effectively with the armature, generating flux that does not contribute to force production.

Another widely adopted topology is the stacked-series railgun [80–82], consisting of two railgun stages connected in series and physically stacked on top of each other. This vertical arrangement, creates a more favorable magnetic field distribution and results in a stronger coupling to the armature compared to the planar-series configuration. A further advantage is that the return current does not travel to the muzzle before closing the circuit, avoiding unnecessary inductance and preventing magnetic flux components that do not contribute to force generation. As shown in [83], the stacked-series railgun can achieve efficiencies up to five times higher than the planar configuration. A sketch of this topology is presented in Fig. 4.3.

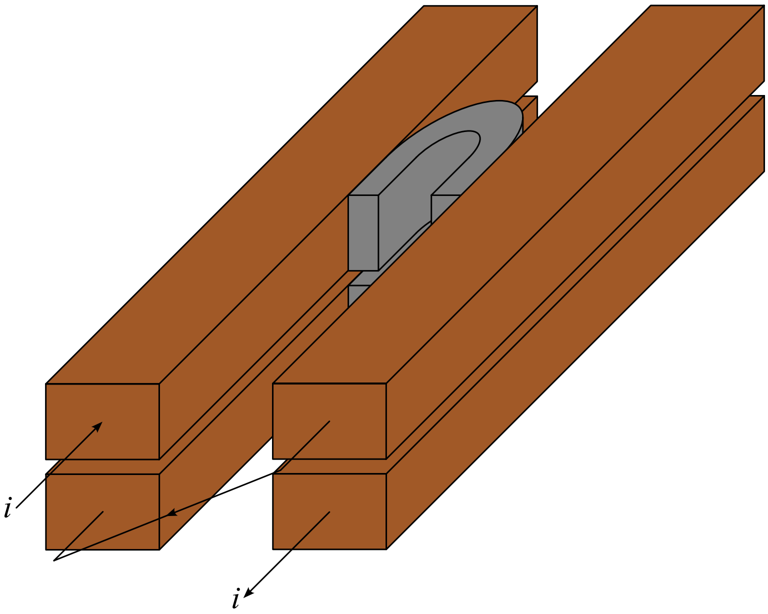

Fig. 4.3 Sketch of the stacked-series railgun configuration.

Another common configuration is the multipole railgun, with the quadrupole arrangement being the most widely adopted variant (Fig. 4.4). This topology consists of two railgun pairs connected in parallel, forming a symmetric four-rail structure. By distributing the total current across multiple rail–armature interfaces, the quadrupole configuration reduces bore erosion and mechanical stress. Railguns are also affected by the proximity effect: currents in the rails and armature generate time-varying magnetic fields that interact with adjacent conductors, inducing electromotive forces that cause non-uniform current distribution and current crowding within the conductor cross-section. In quadrupole configurations, the symmetric geometry improves magnetic field distribution and mitigates these effects, reducing current crowding and associated losses. These characteristics make the quadrupole topology particularly suitable for high-current applications, and extensive research on this configuration has been reported in [84–87].

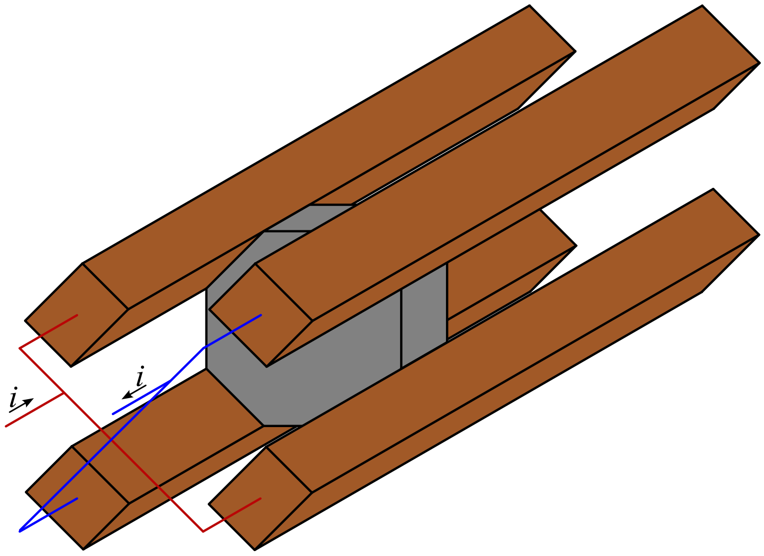

Fig. 4.4 Sketch of the quadrupole railgun configuration.

For simplicity, this work focuses on the basic railgun configuration.

4.2 Modeling

This chapter presents the modeling framework used to characterize the electromagnetic, mechanical, and thermal behaviour of the railgun actuator. The analysis begins with an analytical model that establishes the fundamental relationships between the current and the armature acceleration. This is followed by a quasi-static FEM formulation that resolves the spatial distribution of magnetic fields and current density under steady excitation, enabling accurate estimation of the resulting electromagnetic force and its dependence on geometry. Finally, a fully transient three-dimensional multiphysics model is introduced to capture the dynamic evolution of the electromagnetic field, the rail–armature interaction, current distribution, material heating, and armature motion under realistic drive conditions. Collectively, these models provide a progressively refined description of railgun behaviour and form the basis for a comprehensive performance assessment of the proposed ultra-fast actuator.

Figure 4.5 shows the railgun prototype used as the basis for the modeling work. Owing to the proximity effect, the current is forced to flow preferentially along the inner side of the loop, which corresponds to the slender rail section. For this reason, only this thin, electrically active rail segment is represented in the FEM model, while the remaining rail structure is omitted because it does not significantly influence the electromagnetic behaviour in the system under the considered operating conditions.

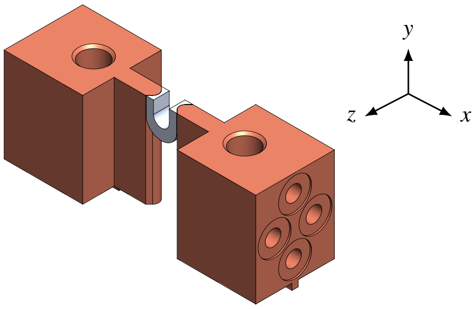

Fig. 4.5 Railgun prototype.

4.2.1 Analytical Model

The analytical model is widely used in railgun research [88–91] as a first-order representation of the electromagnetic behaviour of the launcher. It provides closed-form expressions relating the drive current, electromagnetic force, and resulting armature acceleration, offering valuable physical insight with minimal computational effort and comparatively simple implementation. However, it cannot resolve spatial variations in current density, magnetic field distribution, Lorentz force along the rail–armature interface, or temperature rise due to Joule heating. These limitations motivate the development of more detailed numerical models, presented in the subsequent sections.

A railgun can be analytically represented as a lumped electrical system consisting of a position-dependent resistance R and a position-dependent inductance L. Both quantities vary with the armature position y, which is measured from the breech toward the muzzle along the armature's direction of motion in the y-axis. The resistance is expressed as

$$R = \mathrm{R_a} + \mathrm{R}' y, \tag{4.2}$$

where $\mathrm{R_a}$ is the armature resistance and R' is the rail resistance gradient

$$\mathrm{R}' = \frac{\mathrm{d}R}{\mathrm{d}y}. \tag{4.3}$$

Similarly, the inductance is written as

$$L = \mathrm{L_a} + \mathrm{L}' y, \tag{4.4}$$

where $\mathrm{L_a}$ is the armature inductance and L' is the inductance gradient of the launcher

$$\mathrm{L}' = \frac{\mathrm{d}L}{\mathrm{d}y}. \tag{4.5}$$

The thermal dependence of the rail resistance is neglected, so the variation of R and L arises solely from the increasing electrical path length as the armature advances. The rail separation is assumed constant along the bore, and this simplified representation forms the basis of the analytical model used to describe the electromechanical behaviour of the launcher.

The total flux linkage λ associated with the rail–armature system is

$$\lambda = Li, \tag{4.6}$$

which increases as the armature moves forward. Differentiation of the flux linkage with respect to time yields

$$\frac{\mathrm{d}\lambda}{\mathrm{d}t} = L\frac{\mathrm{d}i}{\mathrm{d}t} + i\frac{\mathrm{d}L}{\mathrm{d}t}. \tag{4.7}$$

Combining (4.5) and (4.3), the time derivative of the flux linkage becomes

$$\frac{\mathrm{d}\lambda}{\mathrm{d}t} = L\frac{\mathrm{d}i}{\mathrm{d}t} + i\frac{\mathrm{d}(\mathrm{L_a} + y\mathrm{L}')}{\mathrm{d}t}. \tag{4.8}$$

Since $\mathrm{L_a}$ is constant and L' does not vary with the position, the second term reduces to

$$\frac{\mathrm{d}(\mathrm{L_a} + y\mathrm{L}')}{\mathrm{d}t} = \mathrm{L}'\dot{y}, \tag{4.9}$$

where $\dot{y}$ denotes the armature speed. Thus, the expression for the rate of change of the flux linkage simplifies to

$$\frac{\mathrm{d}\lambda}{\mathrm{d}t} = L\frac{\mathrm{d}i}{\mathrm{d}t} + i\mathrm{L}'\dot{y}. \tag{4.10}$$

The second term, $i\mathrm{L}'\dot{y}$, is commonly referred to as the motional electromotive force (e_{mot}), as it represents the voltage induced by the armature motion. Including this contribution together with the resistive voltage drop, the breech voltage of the railgun becomes

$$v = L\frac{\mathrm{d}i}{\mathrm{d}t} + i\mathrm{L}'\dot{y} + Ri. \tag{4.11}$$

The electromagnetic force acting on the armature can be derived from the generalized principle of energy conservation for electromechanical systems. In a lossless magnetic system, variations of the magnetic energy are balanced by the electrical energy supplied to the field and by the mechanical work performed by electromagnetic forces on all mechanical degrees of freedom. This balance can be expressed in differential form as [92]

$$\mathrm{d}E_{\mathrm{mag}} = \sum_{i=1}^{N} i_i\,\mathrm{d}\lambda_i - \sum_{j=1}^{M} F_j\,\mathrm{d}q_j, \tag{4.12}$$

where E_{mag} denotes the magnetic energy stored in the electromagnetic field. The quantities i_i and λ_i are the current and flux linkage associated with the i-th electrical terminal pair, where an electrical terminal is an interface through which electrical energy is supplied to or extracted from the magnetic field. The variable q_j denotes the j-th generalized mechanical coordinate, defined as an independent mechanical degree of freedom of the system. The electromagnetic generalized force conjugate to q_j is denoted by F_j, such that electromagnetic forces perform mechanical work through the associated displacement or deformation described by q_j.

The system under consideration comprises a single electrical terminal pair; therefore, $N = 1$. In addition to the armature, the current flowing in the rails possesses a component along the x-direction, which gives rise to electromagnetic forces acting on the rails in the y-direction. Depending on the mechanical arrangement of the rails, these forces may result either in rigid-body displacement, if the rails are free to move, or in elastic deformation, if the rails are mechanically constrained. For the sake of simplicity, the rails are here assumed to be infinitely rigid and perfectly clamped, such that no rail displacement or deformation is permitted. Under this assumption, only the armature motion is retained as an independent mechanical degree of freedom, and thus $M = 1$. Under these conditions, the generalized energy balance reduces to [93]

$$\mathrm{d}E_{\mathrm{mag}} = i\,\mathrm{d}\lambda - F_y\,\mathrm{d}y. \tag{4.13}$$

The magnetic energy E_{mag} is a state function of the electrical and mechanical variables of the system. Under the assumptions introduced above, it depends on the flux linkage λ and on the armature position y, and can therefore be written as $E_{\mathrm{mag}} = E_{\mathrm{mag}}(\lambda, y)$. The total differential of the magnetic energy is then given by

$$\mathrm{d}E_{\mathrm{mag}} = \left.\frac{\partial E_{\mathrm{mag}}}{\partial \lambda}\right|_{y} \mathrm{d}\lambda + \left.\frac{\partial E_{\mathrm{mag}}}{\partial y}\right|_{\lambda} \mathrm{d}y. \tag{4.14}$$

By equating this expression with the generalized energy balance previously derived for the single electrical terminal and single mechanical degree of freedom, the following relation is obtained:

$$\left.\frac{\partial E_{\mathrm{mag}}}{\partial \lambda}\right|_{y} \mathrm{d}\lambda + \left.\frac{\partial E_{\mathrm{mag}}}{\partial y}\right|_{\lambda} \mathrm{d}y = i\,\mathrm{d}\lambda - F_y\,\mathrm{d}y. \tag{4.15}$$

Since the differentials $\mathrm{d}\lambda$ and $\mathrm{d}y$ are independent, equality of the two expressions requires equality of the corresponding coefficients, yielding

$$i = \left.\frac{\partial E_{\mathrm{mag}}}{\partial \lambda}\right|_{y}, \tag{4.16}$$

$$F_y = -\left.\frac{\partial E_{\mathrm{mag}}}{\partial y}\right|_{\lambda}. \tag{4.17}$$

The latter expression provides the electromagnetic force acting on the armature as the partial derivative of the magnetic energy with respect to the mechanical coordinate, evaluated under the condition of constant flux linkage. This formulation is commonly referred to as the *energy form* of the electromagnetic force.

In practical actuation systems, the electrical excitation is typically imposed in terms of current rather than flux linkage. For this reason, it is convenient to reformulate the energy description of the system by introducing the magnetic co-energy E'_{mag}. The magnetic co-energy is defined as a function of the current and the mechanical coordinate through a Legendre transformation of the magnetic energy, according to

$$E'_{\mathrm{mag}}(i,y) = i\lambda - E_{\mathrm{mag}}(\lambda,y), \tag{4.18}$$

where the flux linkage λ is understood to be expressed as a function of the current i and the mechanical coordinate y.

Differentiating (4.18) yields

$$\mathrm{d}E'_{\mathrm{mag}} = \lambda\,\mathrm{d}i + i\,\mathrm{d}\lambda - \mathrm{d}E_{\mathrm{mag}}. \tag{4.19}$$

Substituting the energy balance for a single electrical terminal and a single mechanical coordinate, given by (4.13), into the differential expression of the magnetic co-energy leads to

$$E'_{\mathrm{mag}}(i,y) = i\lambda - (i\,\mathrm{d}\lambda - F_y\,\mathrm{d}y) = \lambda\,\mathrm{d}i + F_y\,\mathrm{d}y, \tag{4.20}$$

Since the magnetic co-energy is a state function of the independent variables i and y, its total differential can also be written as

$$\mathrm{d}E'_{\mathrm{mag}} = \left.\frac{\partial E'_{\mathrm{mag}}}{\partial i}\right|_y \mathrm{d}i + \left.\frac{\partial E'_{\mathrm{mag}}}{\partial y}\right|_i \mathrm{d}y. \tag{4.21}$$

By equating (4.20) and (4.21) and exploiting the independence of the differentials di and dy, the following relations are obtained:

$$\lambda = \left.\frac{\partial E'_{\mathrm{mag}}}{\partial i}\right|_y, \tag{4.22}$$

$$F_y = \left.\frac{\partial E'_{\mathrm{mag}}}{\partial y}\right|_i. \tag{4.23}$$

The latter expression provides the electromagnetic force acting on the armature under constant-current excitation and is commonly referred to as the *co-energy form* of the electromagnetic force.

For a linear magnetic system, magnetic saturation effects are neglected and the flux linkage is proportional to the current according to

$$\lambda = Li, \tag{4.24}$$

Under this assumption, the magnetic co-energy can be evaluated directly as

$$E'_{\mathrm{mag}}(i,y) = \int_0^i \lambda \, \mathrm{d}i' = \int_0^i L i' \, \mathrm{d}i' = \frac{1}{2} L i^2. \tag{4.25}$$

Substituting (4.25) into the co-energy-based force expression given in (4.23) yields the electromagnetic force acting on the armature as

$$F_y = \left. \frac{\partial E'_{\mathrm{mag}}}{\partial y} \right|_i = \frac{1}{2} i^2 \frac{\mathrm{d}L}{\mathrm{d}y}. \tag{4.26}$$

So the force acting on the armature is

$$F_{\mathrm{a}} = \frac{1}{2} i^2 \mathrm{L}'. \tag{4.27}$$

It is important to note that the force expression obtained in (4.26) is based on the simplifying assumption that only a single mechanical degree of freedom is considered. In particular, by assuming the rails to be infinitely rigid and perfectly clamped, all mechanical degrees of freedom associated with rail displacement or elastic deformation are neglected. Under this assumption, the electromagnetic force is assumed to act solely on the armature. In reality, electromagnetic forces also act on the rails, and the total electromagnetic force generated by the system is therefore distributed between the armature and the rails. As a result, the force predicted by (4.26) represents an upper bound for the electromagnetic force available for armature acceleration.

The armature dynamics follow directly from Newton's second law:

$$\mathrm{m_a} \ddot{y} = F_{\mathrm{a}}, \tag{4.28}$$

where $\mathrm{m_a}$ is the armature mass and $\ddot{y}$ denotes the armature acceleration. In this analytical model, frictional effects are neglected; therefore, the electromagnetic force is assumed to be the sole contributor to the armature acceleration along the y-direction. The armature speed $\dot{y}$ is obtained by time integration of the acceleration,

$$\dot{y} = \int_0^t \ddot{y}\,\mathrm{d}\tau, \tag{4.29}$$

while the armature position y follows from a second integration as

$$y = \int_0^t \dot{y}\,\mathrm{d}\tau, \tag{4.30}$$

Figure 4.6 shows the electro–mechanical equivalent circuit of the complete system, comprising the electric drive and the railgun actuator.

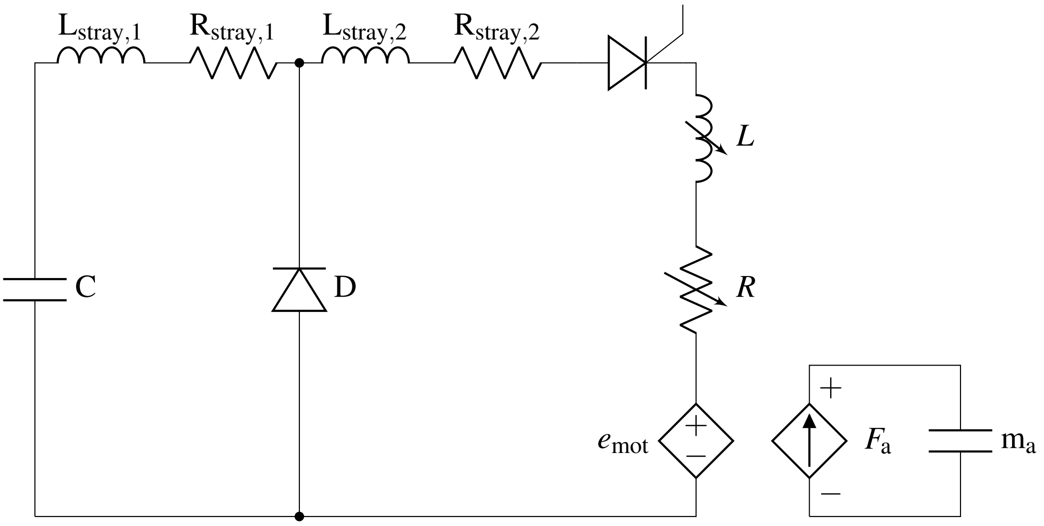

Fig. 4.6 Electro–mechanical equivalent circuit of the complete system, including the electric drive and the railgun actuator.

In the analytical formulation, the only unknowns required to characterize the railgun are the actuator inductance L and resistance R. Once these quantities are known, the coupled electrical and mechanical problem is fully determined. In this work, the position-dependent values of L and R are obtained using COMSOL Multiphysics 6.4 through a stationary study of the *Magnetic Fields (mf)* interface. In this formulation, the electric field is not solved explicitly; instead, a magnetoquasistatic approximation is employed, in which the magnetic vector potential $\mathbf{A}$ is the sole dependent variable.

The governing equations are given by the magnetoquasistatic form of Ampère's law,

$$\nabla \times \mathbf{H} = \mathbf{J}, \tag{4.31}$$

where **H** denotes the magnetic field intensity. The magnetic flux density is related to the magnetic field intensity by

$$\mathbf{B} = \mu \mathbf{H}, \tag{4.32}$$

where μ denotes the magnetic permeability of the material. The flux density can also be expressed in terms of the magnetic vector potential **A** as

$$\mathbf{B} = \nabla \times \mathbf{A}. \tag{4.33}$$

The total current density is described by

$$\mathbf{J} = \sigma \mathbf{E} + \mathbf{J}_\mathrm{e}, \tag{4.34}$$

where σ is the electrical conductivity of the material, $\mathbf{J}_\mathrm{e}$ an externally applied current density, and **E** the implied electric field associated with the coil excitation. Combining the above relations yields the curl–curl formulation solved for the magnetic vector potential,

$$\nabla \times \left(\frac{1}{\mu} \nabla \times \mathbf{A} \right) = \sigma \mathbf{E} + \mathbf{J}_\mathrm{e}. \tag{4.35}$$

Consistent with Maxwell's equations, the magnetic flux density must satisfy Gauss's law for magnetism,

$$\nabla \cdot \mathbf{B} = \nabla \cdot (\nabla \times \mathbf{A}) = 0, \tag{4.36}$$

which expresses the nonexistence of magnetic monopoles and ensures that magnetic field lines remain divergence-free.

In the present model, the railgun model is excited through a prescribed current. In the *Magnetic Fields* interface, a current excitation does not introduce an explicit volumetric current density. Instead, the specified current is imposed through a weak contribution in the finite-element formulation, which enforces the correct total current in the conductor without prescribing its spatial distribution. This approach allows the current density profile to be determined self-consistently from the solution of the magnetic vector potential, thereby capturing the effects of geometry-dependent phenomena such as proximity effect.

Figure 4.7 shows the geometry used in the FEM model. To reduce the computational cost, the geometric symmetries of the railgun prototype are exploited. Symmetry with respect to the *xy*- and *yz*-planes restricts the solution domain to one quarter of the full geometry. This reduction significantly decreases the number of degrees of freedom without altering the electromagnetic fields, as the imposed symmetry conditions reproduce the full-system behavior.

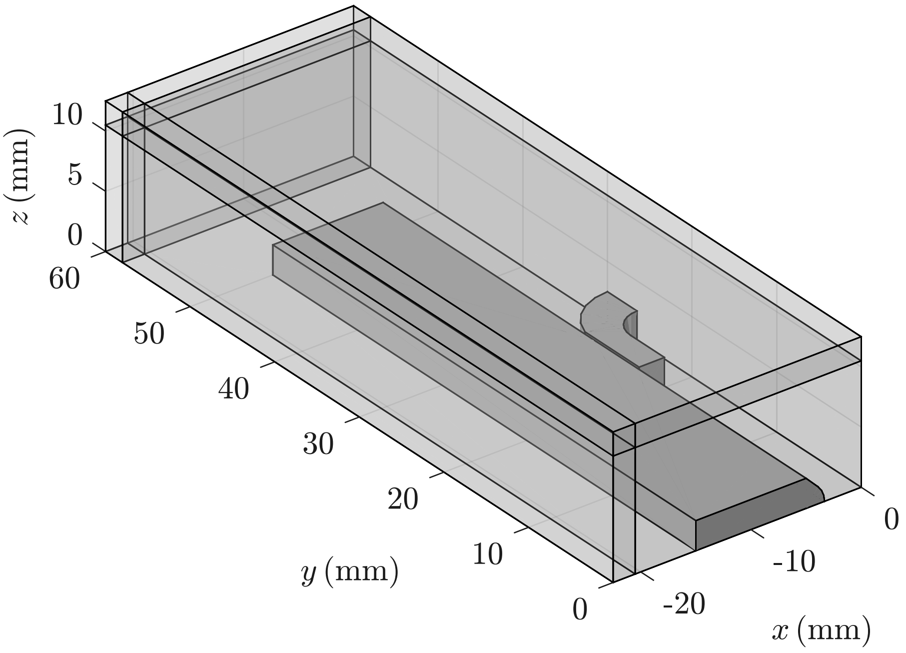

Fig. 4.7 Geometry used in the stationary FEM model.

The symmetry across the *yz*-plane is implemented using a perfect magnetic insulator boundary condition. This enforces zero normal magnetic flux, $\mathbf{n} \cdot \mathbf{B} = 0$. In the magnetic vector potential formulation, this condition is imposed as

$$\mathbf{n} \times \mathbf{A} = 0, \tag{4.37}$$

with $\mathbf{n} = \hat{x}$ defining the outward normal of the *yz*-plane.

Symmetry with respect to the *xy*-plane is enforced by applying a perfect magnetic conductor boundary condition. This constraint imposes a vanishing normal component of the magnetic vector potential on the boundary,

$$\mathbf{n} \cdot \mathbf{A} = 0, \tag{4.38}$$

with $\mathbf{n} = \hat{z}$ the outward normal. By forcing $\mathbf{A}$ to remain tangential to the plane and $\mathbf{B}$ to be perpendicular, this boundary condition emulates symmetry across the xy-plane.

On all remaining outer boundaries of the computational domain, a perfect magnetic insulation boundary condition is applied. This enforces zero normal magnetic flux, ensuring the magnetic field remains enclosed within the modeled region.

To obtain accurate electromagnetic results, the surrounding air domain must be sufficiently large for the magnetic field to decay before reaching the outer boundaries. Increasing the air region, however, raises the number of mesh elements and computational cost. COMSOL provides an efficient solution through the *infinite element domains* feature. A thin outer layer is added around the air region on all boundaries not lying on a symmetry plane (see Fig. 4.7) and assigned as an infinite element domain. This layer emulates an unbounded exterior space by applying a coordinate transformation that stretches the field toward infinity, enforcing correct magnetic-field decay without requiring a large volumetric air region. As a result, the computational domain is reduced without compromising solution accuracy.

The boundaries located in the xz-plane at $y = 0$ are assigned a magnetic insulation boundary condition. When the armature is positioned close to $y = 0$, the magnetic field lines are artificially constrained and cannot close naturally, but are truncated by the magnetic insulation boundary. This leads to an underestimation of the magnetic energy and, consequently, to artificially low inductance values. This effect is critical because, as the armature moves forward, the inductance increases not only due to the enlargement of the current loop, but also because the armature becomes progressively farther from the magnetic insulation boundary, allowing the magnetic field lines to close more realistically. As a result, the inductance gradient is overestimated at small armature positions, yielding nonphysical force values. To mitigate this artifact, the rails are modeled longer than their actual length and the armature initial position y_0 is sufficiently far from the magnetic insulation boundary.

Figures 4.8(a) and 4.8(b) illustrate the mesh used in the FEM model. Figure 4.8(a) shows the complete mesh, including the outer air region and the infinite element domains, which are meshed using a swept mesh. This is required because the infinite element formulation applies a coordinate stretching in the outward direction, and a swept mesh ensures a structured element distribution aligned with this mapping, maintaining a consistent topology for numerical stability. Figure 4.8(b) shows the mesh of the railgun geometry only, excluding the surrounding air region. The mesh in this part of the model is intentionally coarse, as the stationary study does not yield physically meaningful current- or magnetic-field distributions inside the conductors. The purpose of this simulation is to determine the position-dependent inductance and resistance, without requiring fine resolution of **J** and **B**.

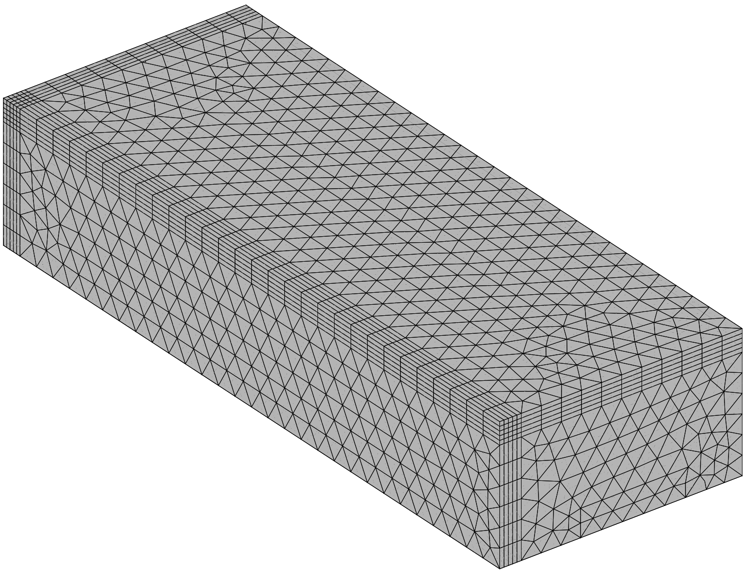

(a)

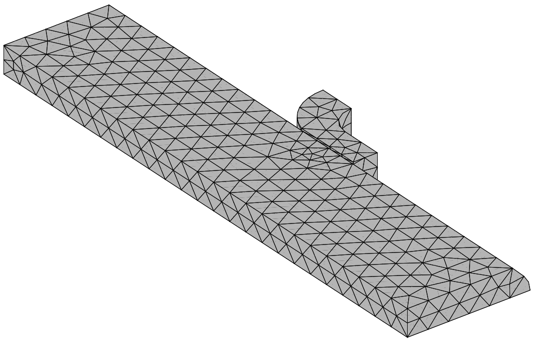

(b)

Fig. 4.8 Mesh used in the FEM model: (a) complete mesh; (b) railgun geometry only.

The mesh used in the FEM model, shown in Fig. 4.8, employs a minimum element size of 1 mm and a maximum size of 2 mm. During the mesh-refinement study, the minimum size was varied while the maximum size was fixed at twice this value. The inductance computed for different mesh configurations and armature positions ($y = \Delta y + y_0$) is reported in Fig. 4.9. Since the inductance is the quantity of interest, the mesh was considered acceptable once further refinement produced no significant change, with convergence reached at a minimum size of 1 mm.

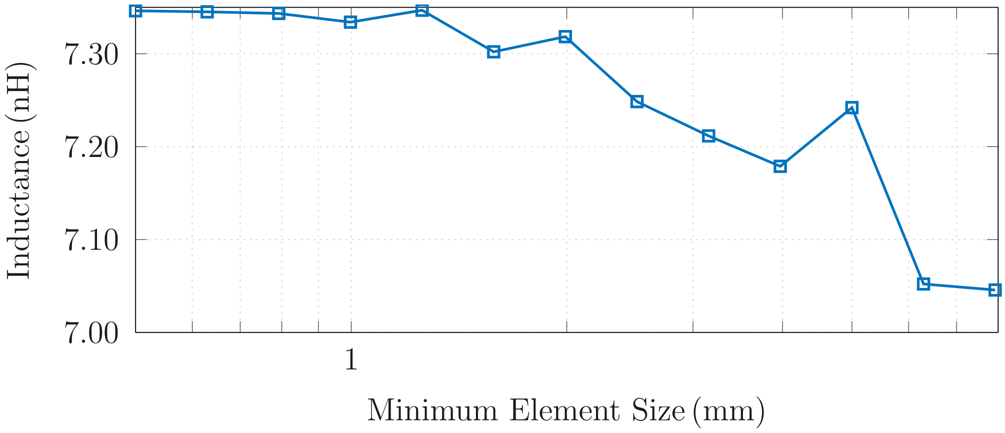

(a)

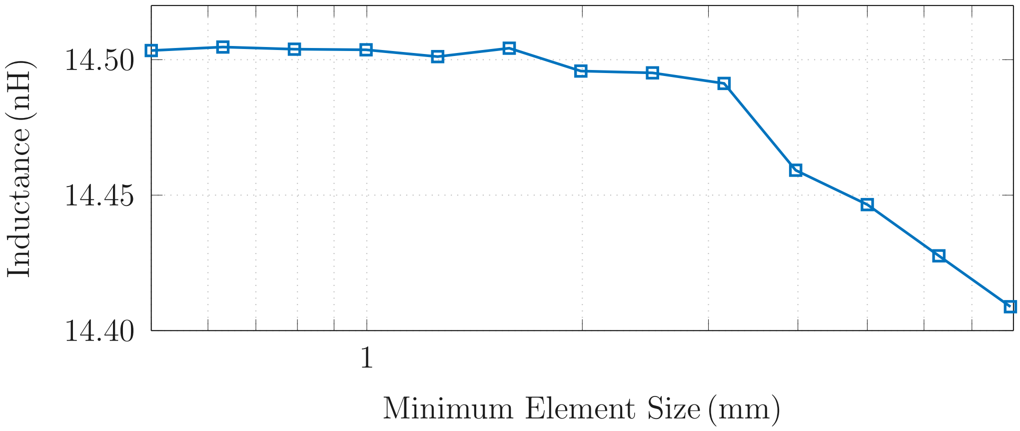

(b)

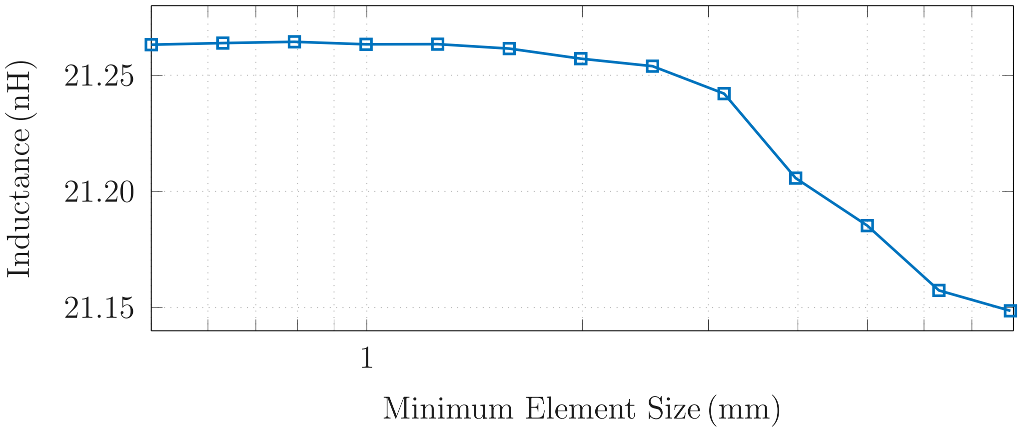

(c)

Fig. 4.9 Mesh-refinement study for the railgun model at three armature displacements: (a) $\Delta y = 0$, (b) $\Delta y = 10\,\text{mm}$, (c) and $\Delta y = 20\,\text{mm}$.

Figure 4.10 shows the railgun resistance as a function of the armature displacement, ranging from approximately 27 µΩ to 39 µΩ. As expected, the resistance increases linearly with the armature travel, reflecting the progressive extension of the current path along the rails. These values represent the purely geometric contribution to the DC resistance obtained from the stationary study. In practice, the actual rail resistance is higher. First, the proximity effect concentrates the current into a reduced effective cross-sectional area, thereby increasing the effective resistance. Second, the substantial power dissipation during operation leads to significant heating of the conductors, and the corresponding rise in temperature further increases the material resistivity. Neither of these phenomena is captured in the stationary model, and the results therefore represent a lower bound for the true railgun resistance during dynamic operation.

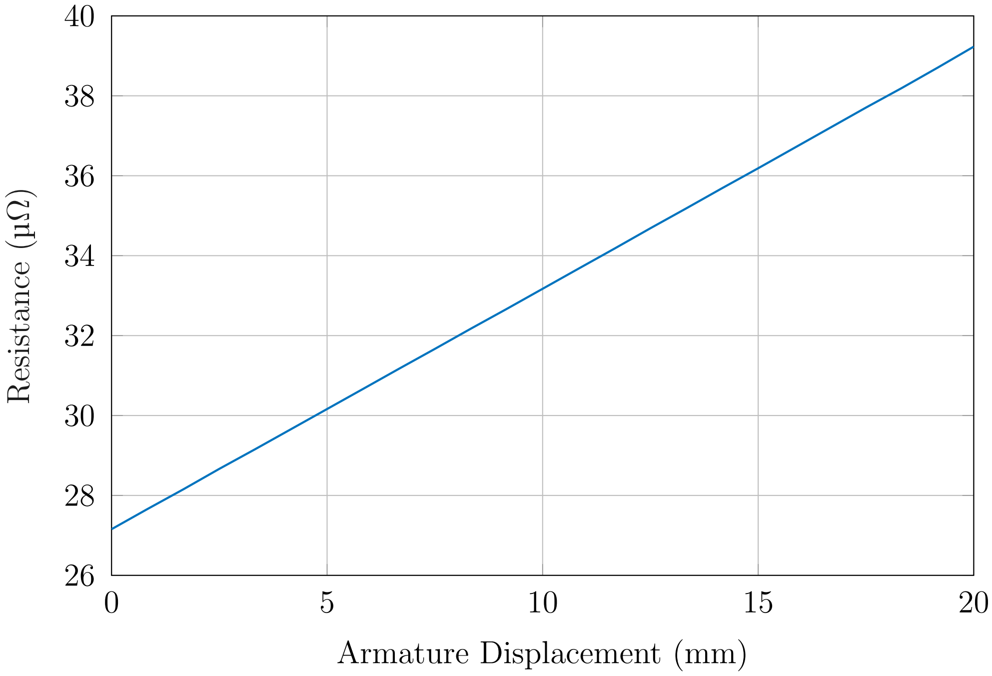

Fig. 4.10 Railgun resistance as a function of the armature displacement.

Figure 4.11 shows the railgun inductance as a function of the armature displacement, ranging from approximately 17 nH to 30 nH. These values are closer to those expected under realistic operating conditions, although the stationary study still tends to yield higher values. In an actual railgun pulse, the magnetic field distribution causes the current to crowd toward the inner rail edges, thereby reducing the effective length of the current loop. Because the inductance depends on the enclosed loop area, this current redistribution leads to a smaller effective inductance than the value predicted by the simplified stationary model. The results also confirm that the railgun actuator exhibits intrinsically low inductance, which is precisely the one of the characteristics sought for this ultra-fast actuation application.

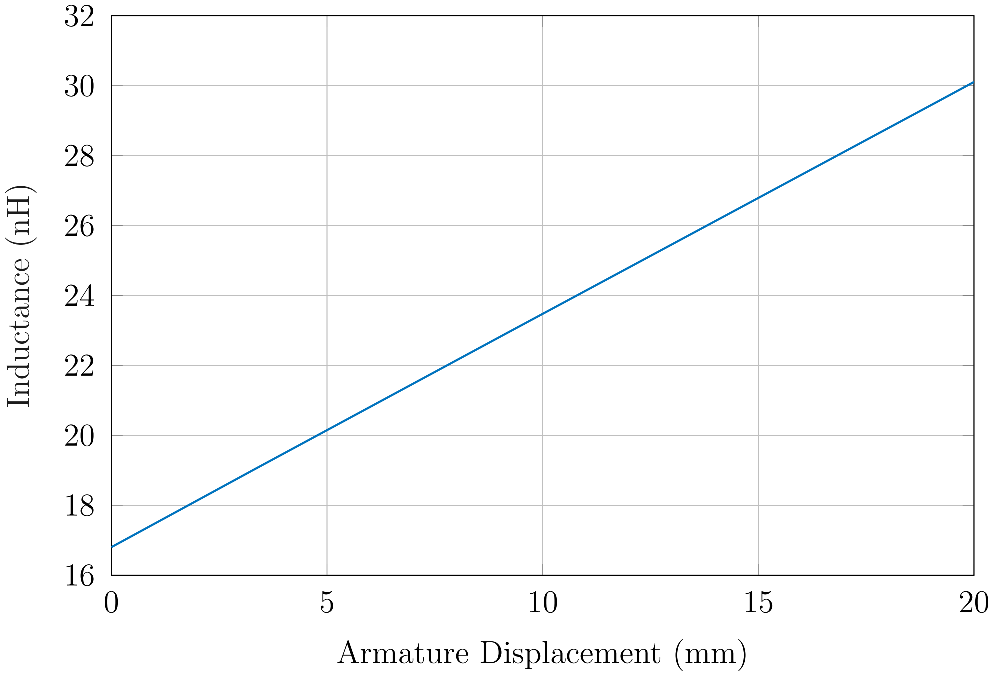

Fig. 4.11 Railgun inductance as a function of the armature displacement.

Since the armature is assigned an initial position of 15 mm, the railgun exhibits resistance and inductance values that are higher than the corresponding physical values. This results in a constant offset in both parameters. However, this offset is negligible when compared to the stray inductance and resistance of the electric drive, and therefore does not introduce any significant error in the overall system response or in the results of the present analysis.

Figure 4.12 shows the inductance gradient as a function of armature displacement. It can be observed that the inductance gradient is approximately 665 nH/m and remains nearly constant over the investigated range. The maximum deviation is about 1.5 %, indicating a weak dependence on displacement. This position independence confirms that assigning an initial armature offset effectively mitigates boundary-related artifacts and ensures a physically consistent inductance gradient.

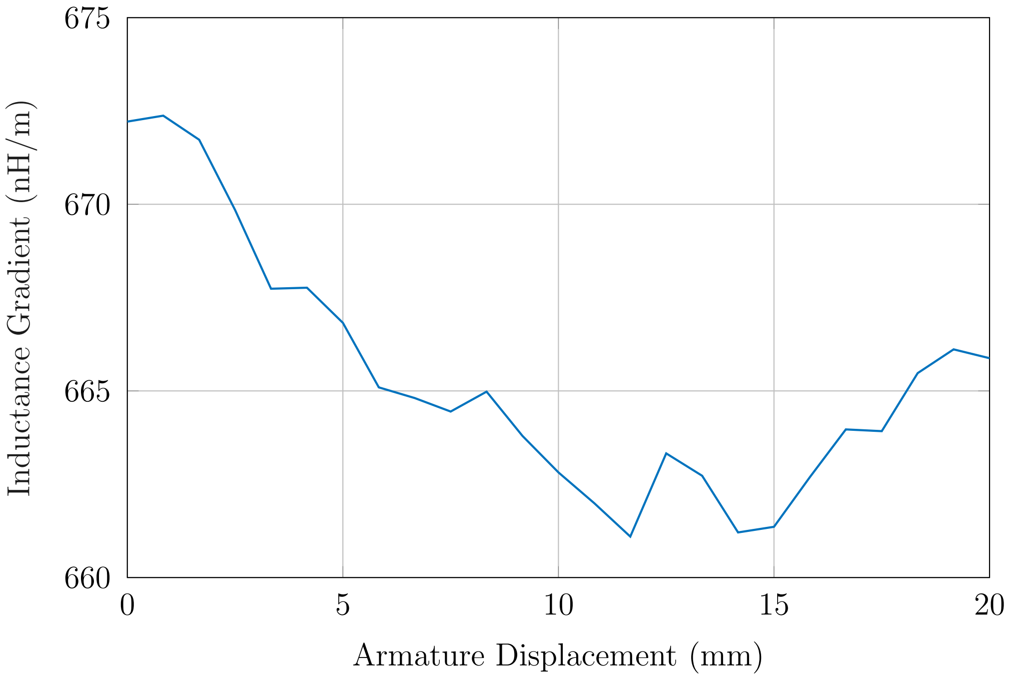

Fig. 4.12 Railgun inductance gradient as a function of the armature displacement.

Once the railgun resistance, inductance, and inductance gradient are known, the electro-mechanical equivalent circuit shown in Fig. 4.6 can in principle be solved directly. However, this approach is complicated by the behavior of the thyristor. According to manufacturer specialists, the device requires up to 70 μs to complete its turn-on process, during which it exhibits a high transient impedance on the order of 1–2 mΩ. This transient impedance is significantly larger than the railgun resistance and therefore dominates the initial current evolution, strongly shaping the current pulse and masking the intrinsic electrical response of the actuator. Accurately modeling both the magnitude and duration of this transient behavior lies outside the scope of the present work. For this reason, the system is instead represented by a prescribed current source driving the electromechanical subsystem consisting of the motional electromotive force and the mechanical dynamics. Figure 4.13(a) shows the simplified electromechanical model, while Fig. 4.13(b) presents the block diagram implemented in Simulink to solve the resulting coupled problem.

The applied current source corresponds to a measured current pulse obtained experimentally, shown in Fig. 4.14, and provides a realistic excitation for evaluating the actuator performance.

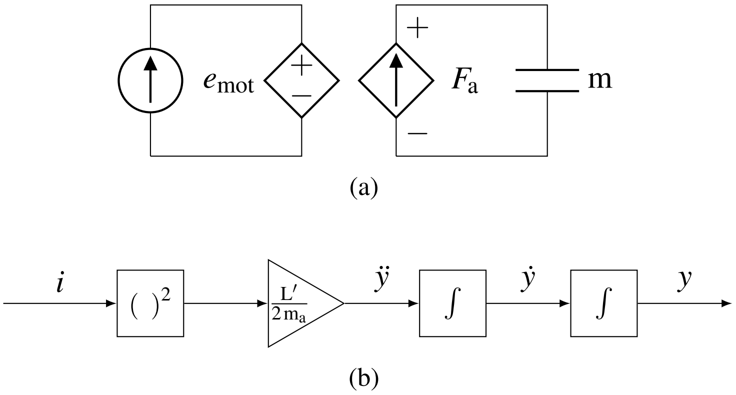

Fig. 4.13 (a) Simplified electro-mechanical equivalent circuit, and (b) block diagram used to solve the coupled electromechanical problem.

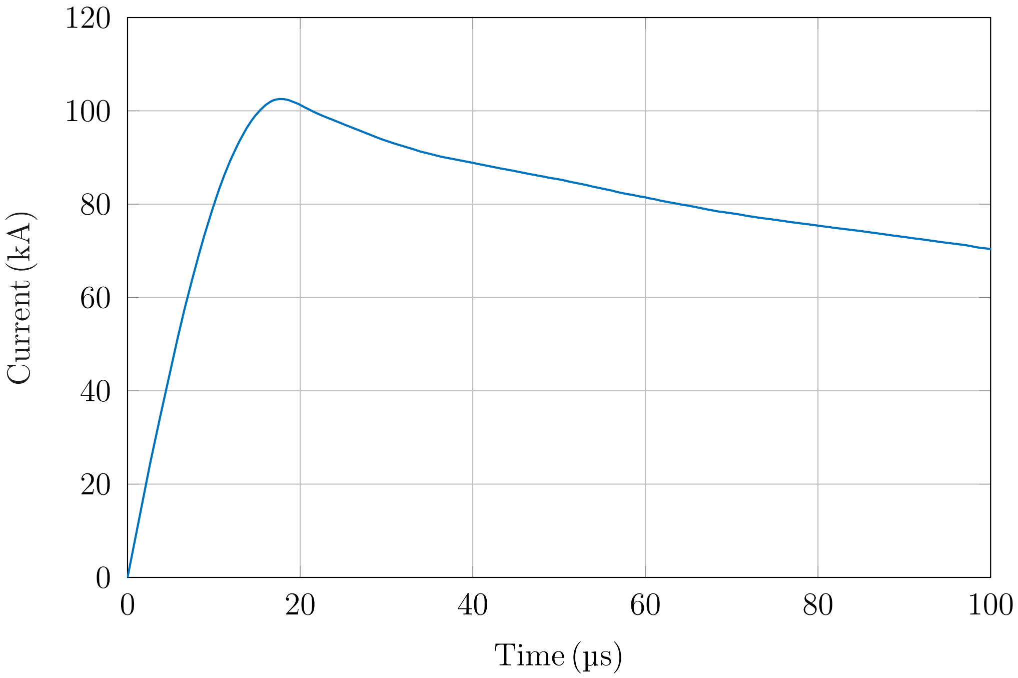

Fig. 4.14 Measured current pulse used as the excitation for the railgun model.

Figure 4.15 shows the electromagnetic force acting on the armature, obtained from the analytical model. The force rises sharply during the initial stage of the current pulse, reaching a peak of approximately 3.5 kN at around 17 µs. The resulting armature dynamics are shown in Figures 4.16 and 4.17, where the velocity reaches about 380 m/s and the displacement roughly 20 mm after 100 µs.

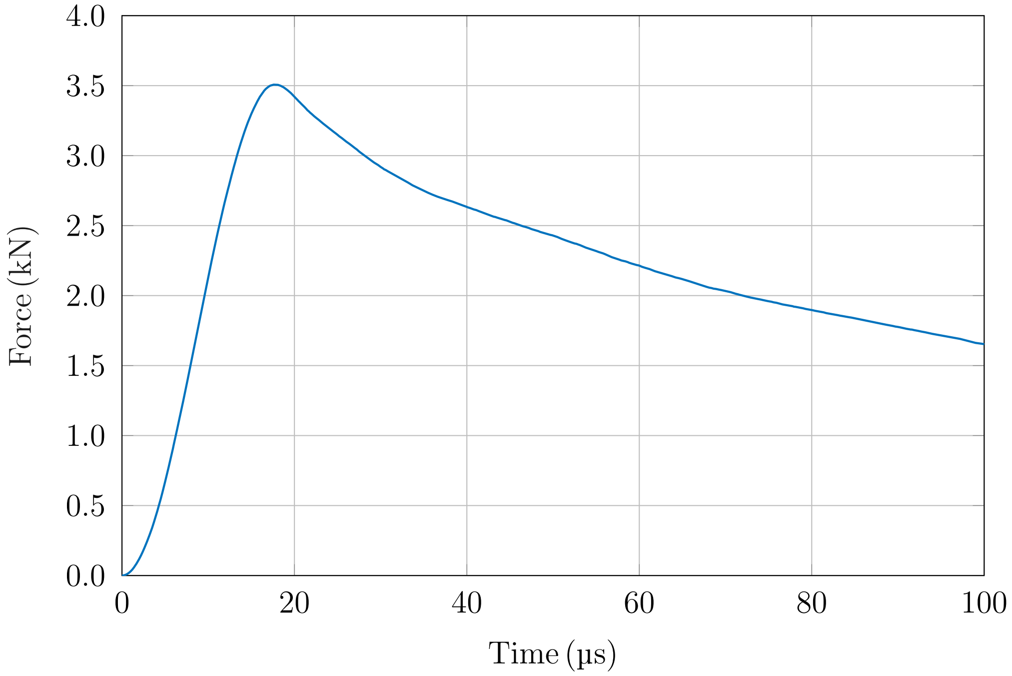

Fig. 4.15 Electromagnetic force acting on the armature computed using the analytical railgun model.

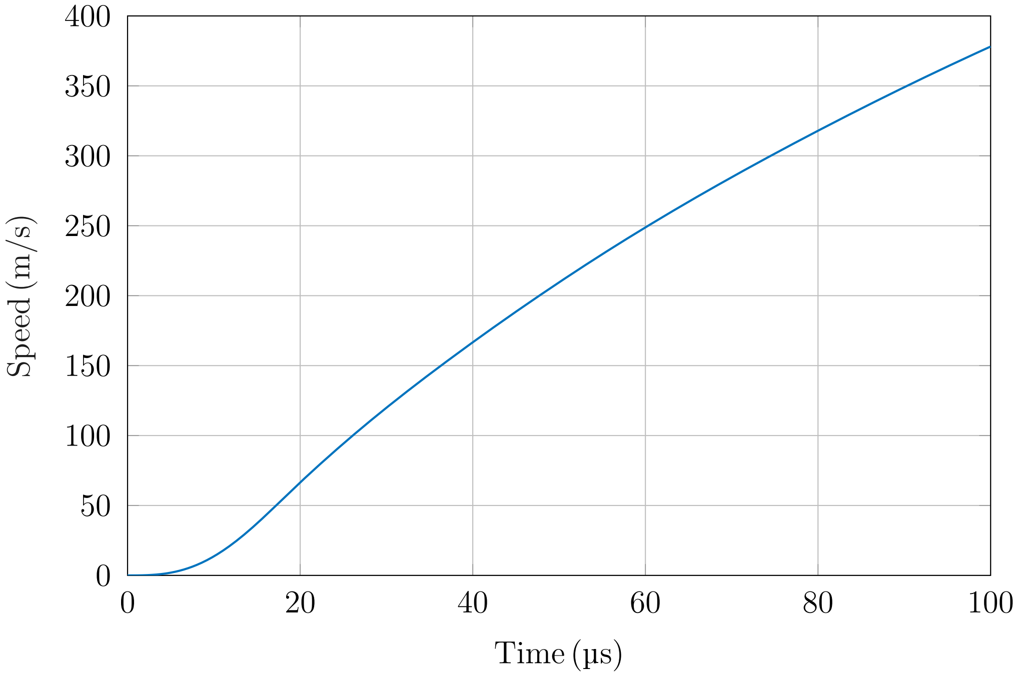

Fig. 4.16 Armature speed computed using the analytical railgun model.

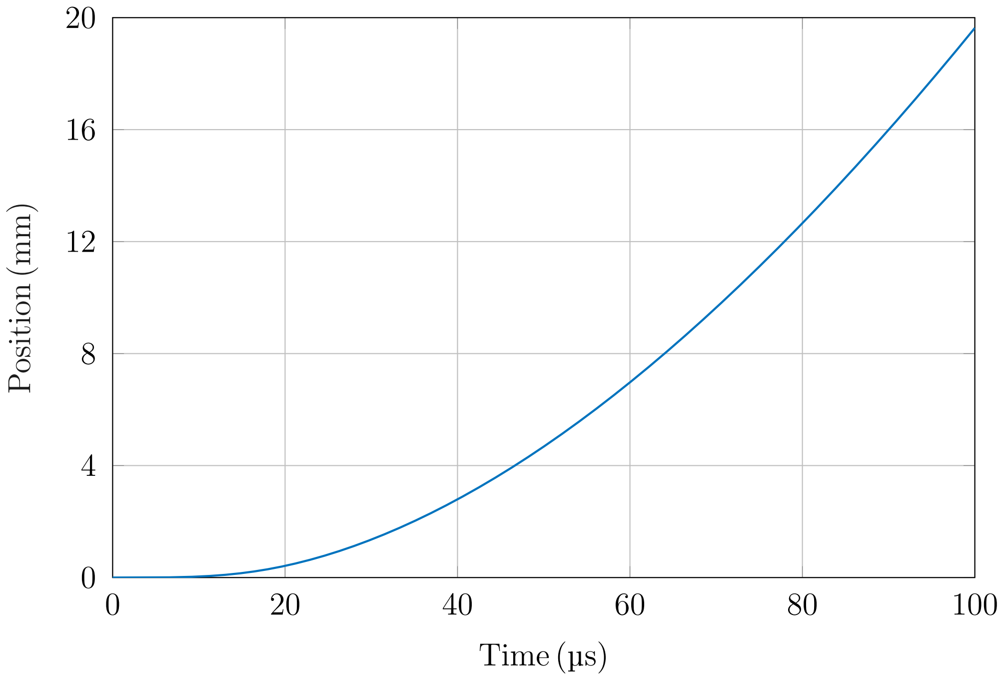

Fig. 4.17 Armature speed computed using the analytical railgun model.

Although these analytical results indicate exceptionally high acceleration and displacement, they represent an optimistic upper bound of the railgun performance. Friction is not included in the model, and its presence would significantly reduce the armature motion. In addition, the magnetic force is likely overestimated because the analytical formulation assumes that the entire force acting in the y-direction is applied to the armature, whereas in reality a portion of this force also acts on the rails.

4.2.2 Quasi-static Model

In the previous subsection, it was shown that evaluating the electromagnetic energy—and the associated force—solely through the inductance gradient leads to inaccurate results. This limitation arises from the simplifying assumptions inherent in the lumped-parameter formulation, which fail to fully capture the spatial distribution of the electromagnetic field and the resulting energy exchange within the railgun system. Consequently, a more rigorous modeling approach is required to correctly account for the electromagnetic energy and its coupling with the mechanical motion.

Following this observation, the methodology presented in [94] is adopted. The railgun is characterized by computing the electromagnetic force on the armature as a function of position and excitation current. A parametric sweep is performed in COMSOL Multiphysics, where the armature displacement Δy is varied from 0 mm to 20 mm and the current from 0 kA to 120 kA. Figure 4.18 shows the obtained results.

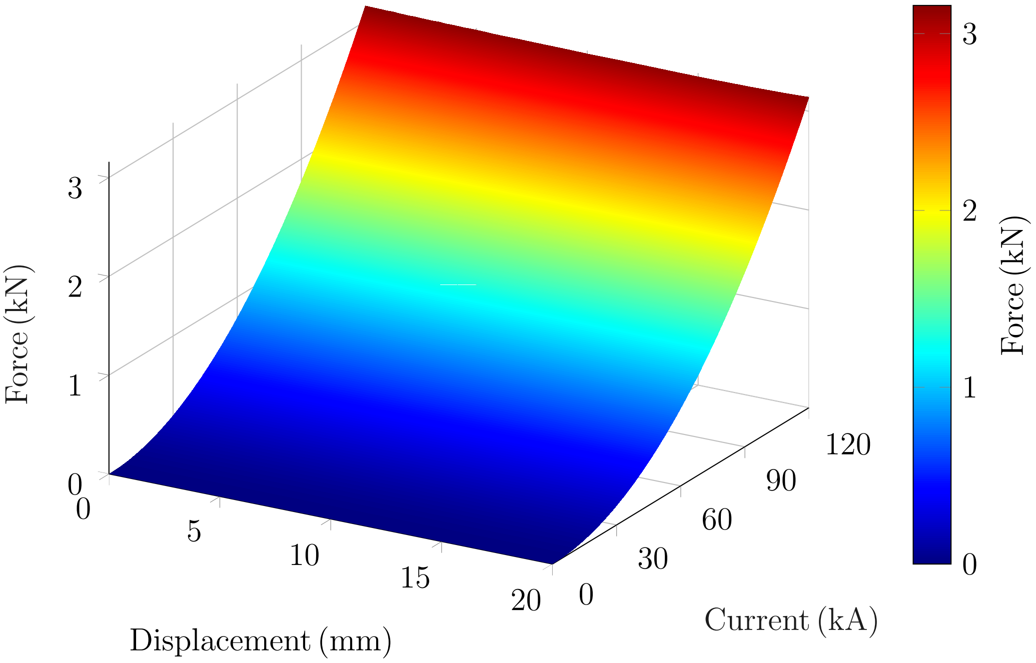

Fig. 4.18 Electromagnetic force acting on the armature as a function of armature position and excitation current, obtained from a parametric COMSOL simulation.

The overall system dynamics are simulated in Simulink. The implemented block diagram is shown in Fig. 4.19. The electromagnetic force results obtained from the COMSOL parametric study are incorporated into the Simulink model by means of a two-dimensional lookup table. This approach enables an efficient time-domain simulation of the coupled electromechanical system while retaining the accuracy of the FEM-based force computation.

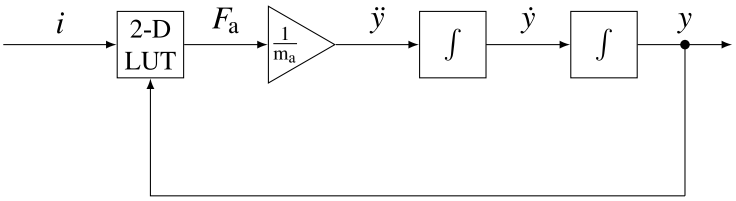

Fig. 4.19 Block diagram of the quasi-static model.

Figure 4.20 shows that the quasi-static model yields a peak electromagnetic force of 2.3 kN, approximately 35 % lower than the 3.5 kN predicted by the analytical model.

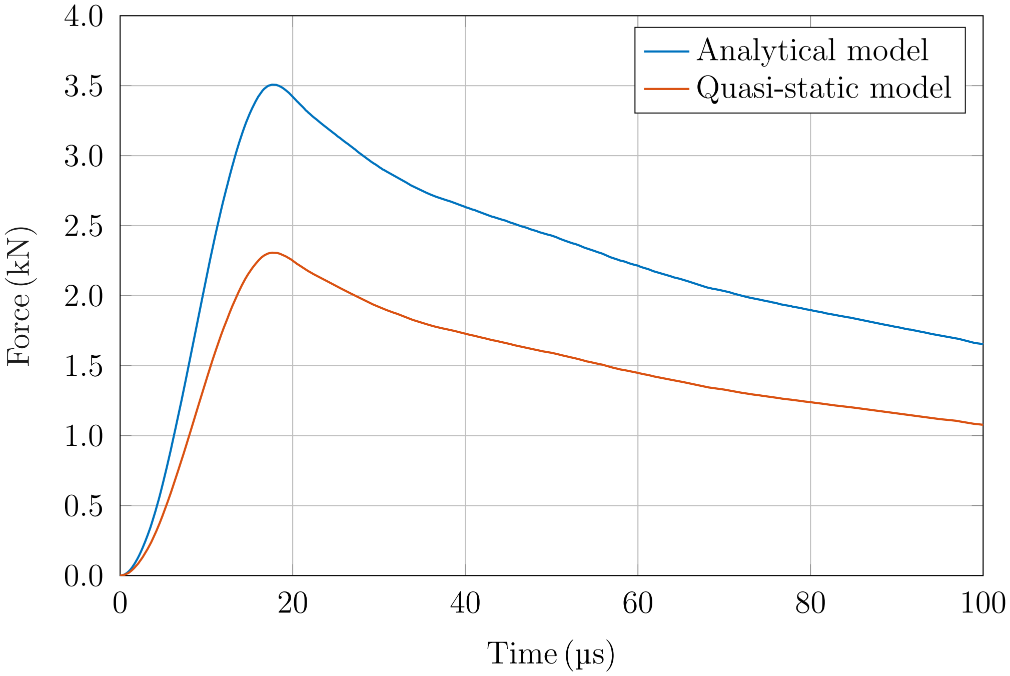

Fig. 4.20 Comparison of the electromagnetic force obtained from the analytical model and the quasi-static model.

The discrepancy observed in the electromagnetic force propagates to the dynamic response, as illustrated in Fig. 4.21, where the armature speed at 100 µs reaches about 250 m/s in the quasi-static model, compared with 380 m/s in the analytical model. This difference results in a significantly reduced acceleration of the armature over the considered time window. Similarly, Fig. 4.22 shows that the armature displacement at 100 µs is 13 mm for the quasi-static model, whereas the analytical model predicts approximately 20 mm.

The origin of this discrepancy lies in the force formulation of the analytical model, which assumes that the entire electromagnetic force component along the y-axis acts solely on the armature. In practice, a significant fraction of this force is distributed to the rails, reducing the effective force available to accelerate the armature. As a consequence, the analytical model overestimates the accelerating force and, consequently, the predicted armature dynamics.

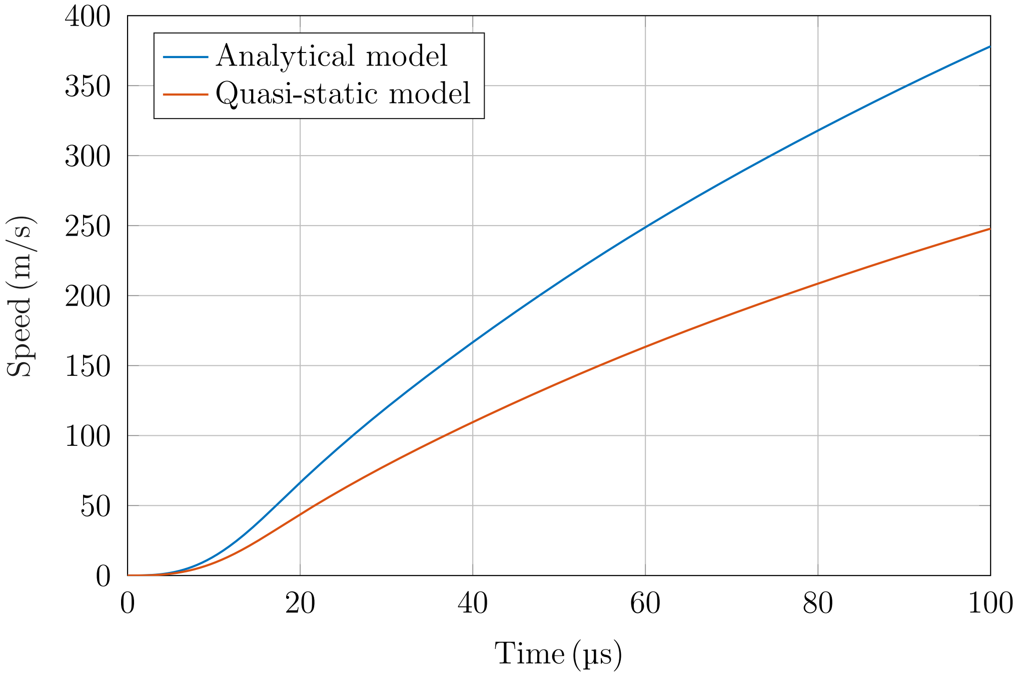

Fig. 4.21 Comparison of the armature speed obtained from the analytical model and the quasi-static model.

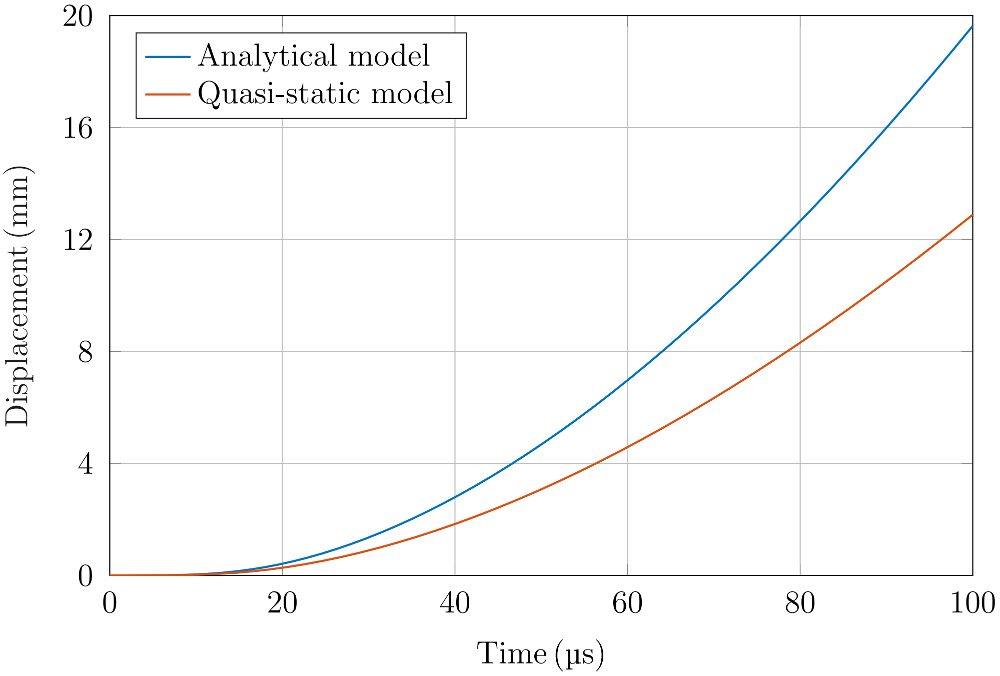

Fig. 4.22 Comparison of the armature displacement obtained from the analytical model and the quasi-static model.

Figure 4.23 shows the spatial distribution of the y-component of the electromagnetic force density obtained from the stationary study for an armature displacement of 5 mm and a current excitation of 80 kA. As anticipated, the results clearly indicate that the electromagnetic force is not solely applied to the armature, but is partly distributed to the rails. Under these operating conditions, the total electromagnetic force along the y-direction acting on the railgun amounts to 2132 N, of which 1396 N act on the armature and 736 N on the rails. Consequently, only about 65 % of the total force effectively contributes to accelerating the armature, which significantly deviates from the assumption adopted in the analytical model, where the entire force is assumed to act on the armature.

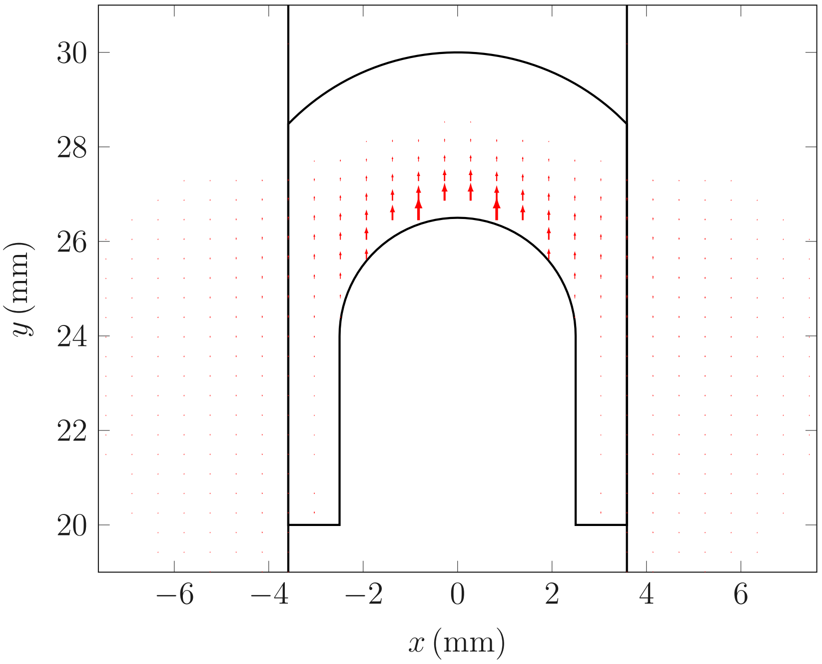

Fig. 4.23 Spatial distribution of the y-component of the electromagnetic force density F_y in the railgun, obtained from the stationary FEM model for an armature displacement of 5 mm and an excitation current of 80 kA.

Figure 4.24 compares the electromagnetic force obtained from the analytical model with the force computed using the quasi-static model, where the Lorentz force is integrated over both the armature and the rails and the resulting total force is applied to the armature. The two results exhibit a one-to-one correspondence, with no observable mismatch over the considered operating range. This agreement further confirms the analytical discussion presented in the previous subsection, namely that the analytical model inherently assumes that the total electromagnetic force generated in the system acts entirely on the armature.

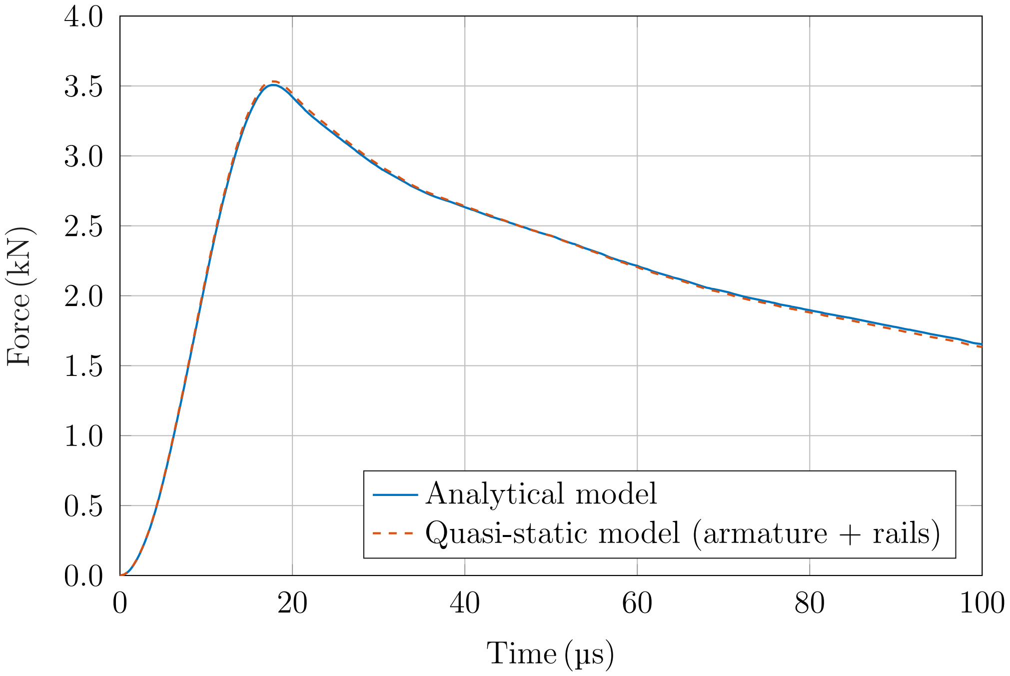

Fig. 4.24 Comparison between the analytical electromagnetic force and the total force obtained from the quasi-static FEM model by integrating the Lorentz force over the armature and rails.

4.2.3 Transient Model

Modeling three-dimensional electromagnetic problems with moving parts is an extremely complex task, as it requires the simultaneous treatment of field equations, material interfaces, and mechanical motion. A correct formulation therefore demands a clear understanding of the numerical framework employed by the simulation software. Within the finite-element method, the computational domain is first discretized into a set of mesh elements. Inside each element, the unknown field is approximated using predefined shape functions, and the choice of these functions represents a key modeling decision, as it determines the mathematical space in which the solution is sought and the physical continuity properties that are enforced.

In two-dimensional electromagnetic problems with translational invariance along the out-of-plane direction, the magnetic vector potential can be reduced to a single scalar component of the form

$$\mathbf{A} = A_z(x,y)\,\hat{\mathbf{z}}. \tag{4.39}$$

Under this assumption, the vector Maxwell equations collapse to a scalar Poisson-type equation for A_z. The resulting unknown must be continuous throughout the computational domain, and the problem becomes mathematically equivalent to a scalar field formulation. Consequently, the solution can be discretized using scalar nodal shape functions, which enforce pointwise continuity of the scalar unknown. In COMSOL terminology, this approach corresponds to the use of Lagrange elements.

In contrast, full three-dimensional electromagnetic problems involving multiple media require a fundamentally different treatment. Maxwell's equations in differential form are strictly valid at points within a continuous medium, where the material properties are well defined and differentiable. At interfaces between different materials, where material parameters are discontinuous, the differential formulation is no longer applicable. Instead, the electromagnetic behavior across such interfaces must be described using boundary conditions derived from the integral form of Maxwell's equations. These interface conditions are given by

$$\mathbf{n} \cdot (\mathbf{D}_2 - \mathbf{D}_1) = \rho_s, \tag{4.40}$$

$$\mathbf{n} \times (\mathbf{E}_2 - \mathbf{E}_1) = \mathbf{0}, \tag{4.41}$$

$$\mathbf{n} \cdot (\mathbf{B}_2 - \mathbf{B}_1) = 0, \tag{4.42}$$

$$\mathbf{n} \times (\mathbf{H}_2 - \mathbf{H}_1) = \mathbf{J}_s, \tag{4.43}$$

where $\mathbf{D}$ denotes the electric flux density, ρ_s and $\mathbf{J}_s$ are the surface charge and surface current densities, respectively, and the subscripts 1 and 2 refer to the electromagnetic field quantities evaluated in medium 1 and medium 2. Equations (4.41) and (4.42) enforce the continuity of the tangential component of the electric field and the normal component of the magnetic flux density, while (4.40) and (4.43) allow for discontinuities in the normal component of the electric flux density and the tangential component of the magnetic field.

These selective continuity conditions cannot be enforced correctly using nodal, scalar shape functions, as electromagnetic fields are inherently vectorial and their physical constraints apply to specific field components rather than to the field as a whole. As a result, three-dimensional electromagnetic problems must be formulated using vector-valued shape functions, with degrees of freedom associated with element edges rather than nodes. In COMSOL, this formulation is implemented through the use of curl-conforming (edge) elements, which naturally enforce tangential field continuity while allowing physically admissible discontinuities at material interfaces.

A more detailed discussion of the mathematical formulation and numerical implementation of Lagrange and curl-conforming finite elements, including their associated function spaces, continuity properties, and applicability to electromagnetic problems, can be found in [95]. The reference provides a comprehensive treatment of the theoretical background and practical implications of element selection in finite-element electromagnetic simulations.

Once the appropriate function space has been selected, the governing partial differential equations are reformulated in their weak (variational) form by multiplying them with suitable test functions and integrating over the computational domain. This weak formulation relaxes the differentiability requirements imposed on the solution and enables the numerical treatment of complex geometries and discontinuous material properties. The weak form is then discretized on each mesh element, yielding local system matrices that describe the electromagnetic behavior within individual elements. Finally, these local matrices are assembled into a global system of equations, which is solved numerically to obtain the electromagnetic field distribution throughout the domain.

For problems involving large geometric changes in the model, the Moving Mesh (ALE) approach—where ALE stands for Arbitrary Lagrangian–Eulerian—is often recommended. In this scenario, the motion is accommodated by letting the mesh of the moving domains slide relative to the surrounding fixed mesh. In order to ensure field continuity across the sliding interfaces, identity pair continuity boundary conditions must be introduced [96]. However, these continuity conditions are not compatible with electromagnetic formulations based on curl-conforming elements. In three-dimensional electromagnetic problems, where Maxwell's equations are solved using vector fields, selective continuity conditions must be satisfied at interfaces between different media, and full field continuity cannot be enforced. As a consequence, the identity pair approach cannot be applied in the present case.

An alternative strategy is proposed in [97], where mesh motion is avoided altogether. Instead of moving the mesh, a time-dependent conductivity distribution is defined in the region between the rails, such that the electrically conductive region follows the motion of the armature. While this approach circumvents mesh deformation and sliding interfaces, it requires a very fine mesh over the entire region between the rails in order to accurately resolve the current distribution throughout the simulation. As a result, the number of degrees of freedom becomes very large, leading to a significant increase in computational complexity and simulation time.

A different methodology based on a deformed geometry formulation is presented in [98]. In this approach, the mesh elements do not slide over one another but instead remain continuously connected. The motion is represented through a controlled deformation of the geometry, while periodic mesh deformation strategies are employed to prevent excessive mesh distortion and the formation of low-quality elements. This method preserves mesh conformity and avoids the incompatibility issues associated with sliding interfaces in curl-based electromagnetic formulations. In the present research study, the modeling strategy proposed in [98] is adopted.

Figure 4.25 illustrates the geometry used for the transient electromagnetic model. For clarity, the outer air domain is not shown. The gray region represents a portion of the rail that is not part of the deformed-geometry domains and therefore remains rigid throughout the simulation. As discussed previously, this auxiliary region artificially shifts the initial armature position to ensure sufficient distance from the magnetic insulation boundary. This domain does not correspond to any physical component and is introduced solely for numerical convenience. The height of this region is $\mathrm{H}/2$, its length is $\mathrm{y}_0 - \mathrm{y}_{00}$, and its width is W, where y_{00} denotes the initial armature position within the deformed geometry.

The yellow domains belong to the deformed-geometry regions and elongate according to the deformation field

$$\delta_1 = \Delta y \frac{Y_g - \mathrm{y}_0 + \mathrm{y}_{00}}{\mathrm{y}_{00}}. \tag{4.44}$$

Here, δ_1 denotes the local geometric deformation applied to the mesh, while Δy represents the instantaneous displacement of the armature. In COMSOL, Y_g is the global y-coordinate of a material point in the reference (undeformed) configuration. This expression defines a spatially varying deformation that is proportional to the armature displacement. Mesh elements located at $y = \mathrm{y}_0 - \mathrm{y}_{00}$, adjacent to the rigid gray region, experience zero deformation, whereas elements located at y_0 undergo the maximum deformation Δy.

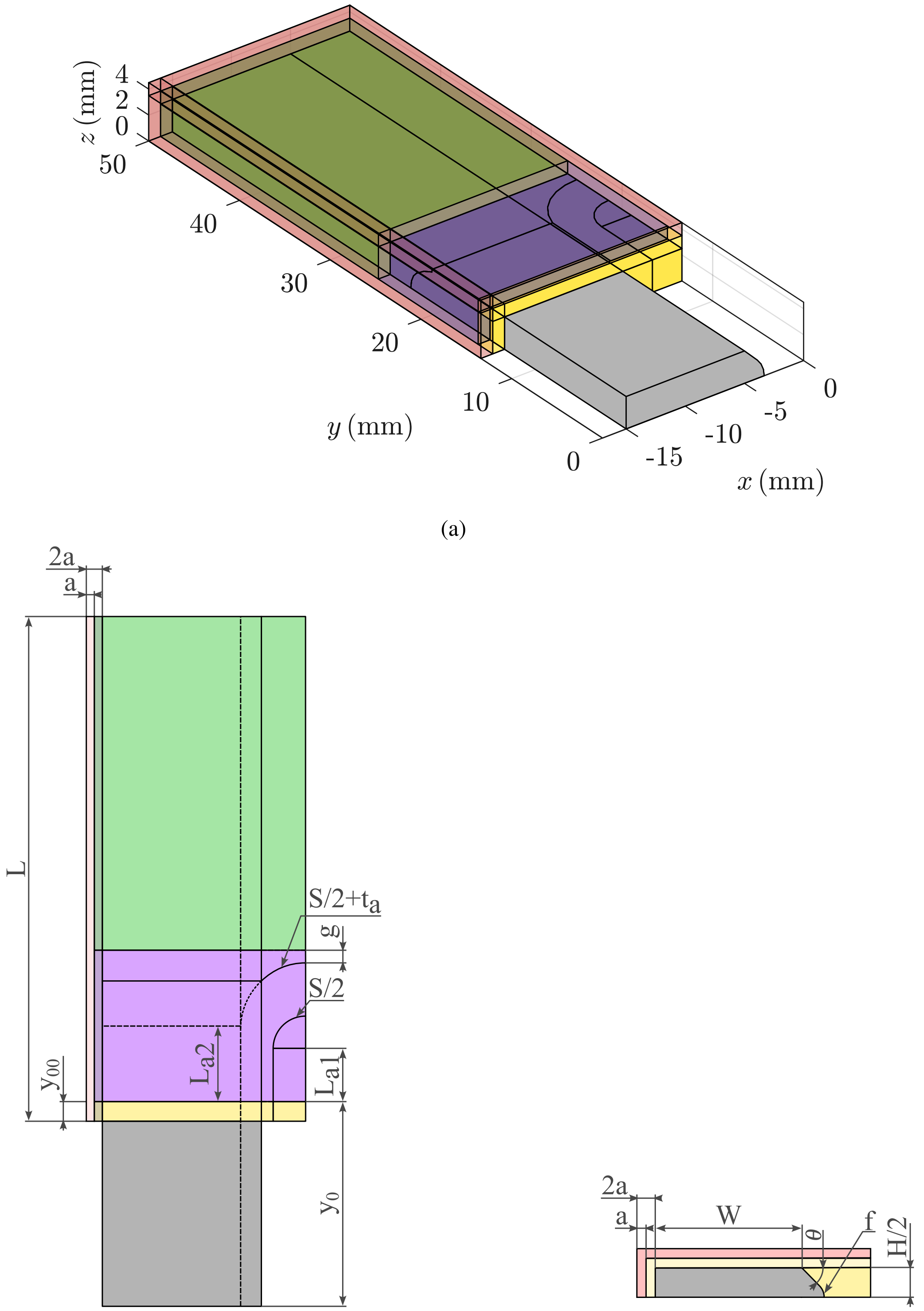

(a)

(b)

(c)

Fig. 4.25 Geometry of the transient model: (a) 3D view, (b) bottom view, and (c) front view.

The purple domains, unlike the yellow ones, do not undergo deformation. Instead, they experience a simple translation, where the mesh remains undeformed. This means that the geometry of these regions is shifted without altering the mesh elements, preserving their original shape.

The green domains contract according to the deformation δ_2

$$\delta_2 = -\Delta y \frac{Y_g - \mathrm{L}}{\mathrm{L} - \mathrm{L_{a2}} - \frac{\mathrm{S}}{2} - \mathrm{t_a} - \mathrm{g} - \mathrm{y_0}}. \tag{4.45}$$

Here, L denotes the rail length, $\mathrm{L_{a2}}$ and $\mathrm{L_{a1}}$ are the outer and inner armature lengths, respectively, S is the separation between the inner armature sides, $\mathrm{t_a}$ is the armature thickness, and a is the clearance between the armature tip and the green deforming domains. This clearance is introduced for meshing purposes to avoid narrow regions in the adjacent purple domain and the resulting low-quality mesh elements. The expression thus prescribes a spatially varying contraction of the green domains.

The yellow, purple, and green domains undergo prescribed deformations defined through analytical expressions. In contrast, the red domains are not assigned any deformation and are allowed to deform freely, with their mesh motion governed by the adjacent domains. As a result, they remain kinematically compatible with the surrounding geometry and follow the imposed motion without additional constraints, behaving as passively deformed regions.

Figure 4.25(c) shows the front view of the model geometry. This view highlights the rail height, equal to $\mathrm{H}/2$, the rail width W, and the inclination angle θ introduced to accommodate the armature geometry. In order to avoid sharp corners, a fillet of radius f is applied at this angled transition.

Figure 4.25 also shows that, within the prescribed-deformation regions, a non-conductive layer of thickness a surrounds the current-carrying domains, improving numerical stability after remeshing. These domains are discretized using a sweep mesh (except for the armature and its immediate surroundings), ensuring identical mesh topology before and after remeshing and promoting stable time integration. In contrast, the mesh in the free-deformation regions (red domains) is regenerated during remeshing, and the associated solution mapping can introduce numerical disturbances, to which current-carrying domains are particularly sensitive. The surrounding layer effectively mitigates these remeshing-induced perturbations, resulting in a more stable solution.

Figure 4.26 shows the side view of the rail, highlighting the edges that define the interface with the armature. The presence of these edges causes the rail cross-section within the purple domains to be non-sweepable, as the faces on opposite sides of the rail do not correspond geometrically. This issue can be resolved by subdividing the rail along these edges, as illustrated in Fig. 4.25. Through this subdivision, the original domain is partitioned into two geometrically compatible subdomains, each of which can be discretized using a sweep mesh.

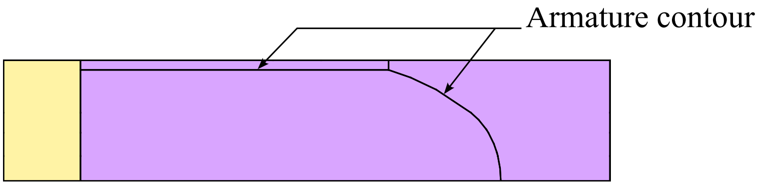

Fig. 4.26 Side view of the rail showing the edges at the interface with the armature.

Table 4.1 summarizes the numerical values of the geometrical parameters used to define the model geometry.

Table 4.1 Geometrical parameters of the transient electromagnetic model.

Parameter	**Value**
y_0	15 mm
y_{00}	1.6 mm
L	35 mm
W	10 mm
H	5 mm
θ	45°
f	2 mm
L_{a1}	4 mm
L_{a2}	5 mm
S	5 mm
a	1 mm
g	1 mm

Figure 4.27 shows that, wherever permitted by geometric constraints, the deformed-geometry regions are discretized using a sweep mesh. This approachyields a structured mesh in which the position of each element is controlled, thereby enabling a well-defined and repeatable remeshing process. As discussed previously, this significantly improves numerical stability during solution initialization after remeshing. Owing to the complex geometry of the armature, neither the armature itself nor its immediate surrounding domains can be meshed using a sweep method; instead, a free tetrahedral mesh is employed. This does not pose a difficulty, since these domains do not deform and their meshes can be copied unchanged into successive remeshed configurations, ensuring identical discretization. To preserve mesh consistency in the swept regions throughout the simulation, the number and spatial distribution of elements in the x-, y-, and z-directions are kept constant. The resulting trade-off is an initially over-refined mesh in the yellow domains and an over-refined mesh in the green domains toward the end of the simulation. Remeshing is therefore performed periodically based on a prescribed maximum allowable mesh element distortion.

Figure 4.27 also shows that diagonal edges are introduced in the hexahedral mesh elements of the swept rail domains. This choice is motivated by the linear discretization adopted for the governing equations of the system. With linear shape functions, the presence of a hybrid mesh in the current path—in particular at the interface between hexahedral- and tetrahedral-based elements—can lead to discontinuities in the computed current density. Two strategies can be used to avoid this issue: either employing higher-order (quadratic) shape functions, or eliminating the hybrid interface by subdividing the hexahedral elements through the insertion of diagonal edges. Both approaches were evaluated, and it was found that the latter provides better computational efficiency, despite resulting in a larger total number of mesh elements.

As illustrated in Fig. 4.27(a), the mesh on the inner sides of the rails and the armature is finer than on the outer sides. This refinement is introduced to accurately capture the initial current distribution, since proximity effect is particularly strong in this region. As the armature velocity increases, the velocity skin effect becomes more pronounced, causing the current to concentrate on the upper inner surface of the armature. For this reason, a locally finer mesh is also adopted in this area of the armature. It is noteworthy that, thanks to the previously described domain subdivision, the rails can be meshed using a sweep method, as shown in Fig. 4.27(a) and Fig. 4.27(c).

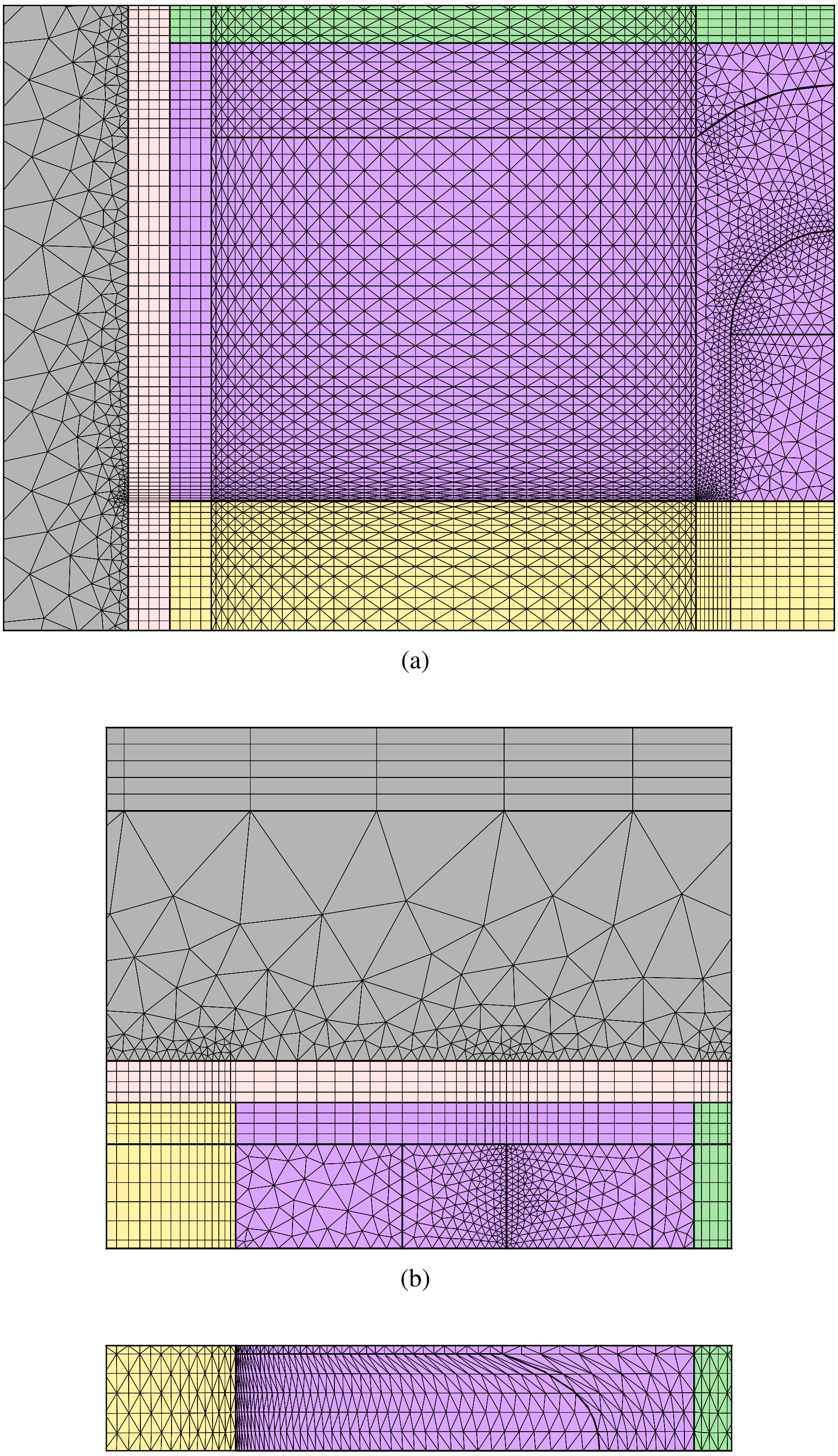

(a)

(b)

(c)

Fig. 4.27 Mesh of the transient model: (a) mesh on the *xy* symmetry plane, (b) mesh on the *yz* symmetryplane, and (c) side view of the rail mesh.

Equation (4.34) shows that the *Magnetic Fields* module does not account for the motional contribution in the calculation of the current distribution. This limitation is not acceptable in the present case, since the armature reaches very high velocities and its motion plays a crucial role in determining the current distribution. In contrast, the *Magnetic and Electric Fields (mef)* module explicitly includes the effects of conductor motion and is therefore more appropriate for accurately capturing the coupled electromagnetic–mechanical behavior of the system.

In this formulation, the electric field is expressed in terms of the electric scalar potential V and the magnetic vector potential $\mathbf{A}$ as

$$\mathbf{E} = -\nabla V - \frac{\partial \mathbf{A}}{\partial t}. \tag{4.46}$$

The current density in a moving conductor is described by the generalized Ohm's law

$$\mathbf{J} = \sigma \mathbf{E} + \sigma \mathbf{v} \times \mathbf{B} + \mathbf{J}_{\mathrm{e}}, \tag{4.47}$$

where $\mathbf{v}$ is the conductor velocity.

Ampère's law in its magnetoquasistatic form must also be satisfied,

$$\nabla \times \mathbf{H} = \mathbf{J}. \tag{4.48}$$

By defining the magnetic flux density $\mathbf{B}$ in terms of the magnetic vector potential $\mathbf{A}$,

$$\mathbf{B} = \nabla \times \mathbf{A}, \tag{4.49}$$

Gauss's law for magnetism,

$$\nabla \cdot \mathbf{B} = 0, \tag{4.50}$$

is implicitly fulfilled and therefore does not need to be enforced as an independent governing equation.

Current conservation can be derived directly from Ampère's law. Taking the divergence of Ampère's law in its magnetoquasistatic form yields

$$\nabla \cdot (\nabla \times \mathbf{H}) = \nabla \cdot \mathbf{J}. \tag{4.51}$$

By applying the vector identity

$$\nabla \cdot (\nabla \times \cdot) = 0, \tag{4.52}$$

it follows that

$$\nabla \cdot \mathbf{J} = 0. \tag{4.53}$$

This result is exact at the continuous level and expresses local current conservation. However, in a finite-element discretization, discrete differential operators do not preserve all continuous vector identities exactly, and in particular $\nabla \cdot (\nabla \times \cdot) = 0$ is not satisfied in a strict sense. For this reason, COMSOL explicitly enforces current conservation by imposing the condition from (4.53), ensuring numerical consistency and stability of the solution.

The electromagnetic fields are coupled to the material properties through linear constitutive equations:

$$\mathbf{B} = \mu \mathbf{H}, \tag{4.54}$$

$$\mathbf{D} = \varepsilon \mathbf{E}. \tag{4.55}$$

Here, **D** denotes the electric flux density, and ε is the electric permittivity of the medium.

In addition to the electromagnetic formulation, the *Heat Transfer (ht)* physics is also solved in the model in order to capture the transient thermal behavior of the system. The temperature field is governed by a transient energy balance equation that accounts for thermal inertia, heat transport due to material motion, conductive heat transfer, and internal heat generation associated with thermoelastic effects.

$$\rho \, \mathrm{C_p} \frac{\partial T}{\partial t} + \rho \, \mathrm{C_p} \, \mathbf{u} \cdot \nabla T + \nabla \cdot \mathbf{q} = Q + Q_{\mathrm{ted}}, \tag{4.56}$$

where ρ is the mass density, $\mathrm{C_p}$ the specific heat capacity, T the temperature, $\mathbf{u}$ the material velocity, $\mathbf{q}$ the heat flux, and Q_{ted} denotes the volumetric heat source associated with thermoelastic damping. Since the present model assumes rigid-body behavior and does not resolve elastic deformation or stress–strain dynamics, thermoelastic damping does not play a role in the simulation and does not contribute to the thermal response. The conductive heat flux is described by Fourier's law,

$$\mathbf{q} = -\mathrm{k}\nabla T, \tag{4.57}$$

with k being the thermal conductivity.

The electromagnetic and thermal problems are therefore fully coupled: the electromagnetic solution provides the heat sources for the thermal model, while the temperature field feeds back into the electromagnetic problem through temperature-dependent material properties, thus capturing self-heating effects and mutual interactions between both physical domains. In particular, the electrical conductivity of the conductors is modeled using a linearized temperature dependence,

$$\sigma(T) = \sigma_0 \left(1 - \alpha \left(T - T_0\right)\right), \tag{4.58}$$

where σ_0 is the electrical conductivity at the reference temperature T_0, and α is the temperature coefficient of resistivity.

Due to the extremely fast dynamics of the system, heat exchange with the surrounding air can be neglected over the short time scales considered. An adiabatic assumption is therefore adopted, allowing the thermal computation domain to be restricted to the railgun components only, without explicitly modeling the surrounding air. This simplification significantly reduces the computational cost while remaining physically justified for the time scales of interest and the high-power transient operation investigated. The adiabatic condition is enforced by prescribing zero normal heat flux on all exterior boundaries of the railgun,

$$-\mathbf{n} \cdot \mathbf{q} = 0, \tag{4.59}$$

where **n** denotes the outward-pointing unit normal vector to the boundary surface.

Although the total current is imposed in the simulation, this thermal dependence has a significant impact on the solution, as it modifies the current distribution within the conductors. The increase in electrical resistance in the inner portion of the current loop leads to a redistribution of the current toward regions of lower resistance, effectively pushing the current outward. As a result, the local current density in the regions most relevant for force generation is reduced, leading to a decrease in the electromagnetic force density $\mathbf{J} \times \mathbf{B}$.

Figure 4.28 presents a comparison of the results obtained from the analytical, quasi-static, and transient models. The transient model predicts a force evolution that lies between the analytical and quasi-static solutions, while remaining closer to the quasi-static response. In particular, the transient simulation yields a peak force of approximately 2.7 kN, compared to 2.3 kN for the quasi-static model and 3.5 kN for the analytical formulation.

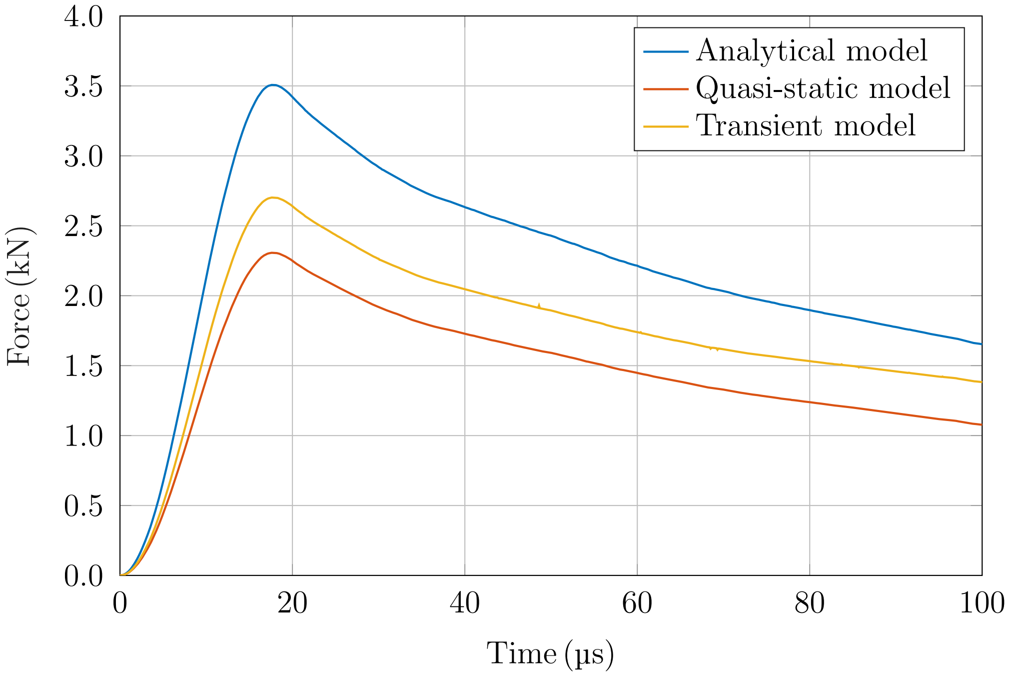

Fig. 4.28 Comparison of the electromagnetic force obtained from the analytical model, the quasi-static model, and the transient model.

Even though both the transient model and the quasi-static model are formulated using finite-element methods, their results exhibit noticeable differences in both magnitude and spatial distribution. These discrepancies arise primarily from the different distributions of magnetic flux density and current density obtained in the transient and the stationary studies. In both cases, the highest magnetic flux concentration is located at the inner faces of the armature tip (see Fig. 4.29). However, the current distribution differs significantly between the two approaches. In the stationary study, the current is distributed nearly uniformly across the conductor cross section (see Fig. 4.30(b)), neglecting local current crowding at sharp corners. By contrast, in the transient study the current density becomes strongly concentrated in regions of high magnetic flux density (see Fig. 4.30(a)). As a direct consequence, the resulting Lorentz force is increased in the transient model, as evidenced by the force comparison shown in Fig. 4.28.

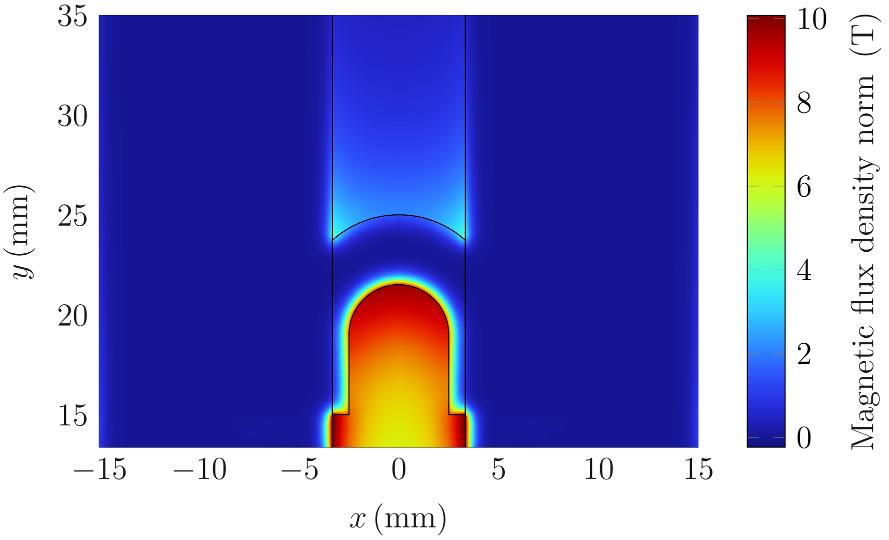

(a)

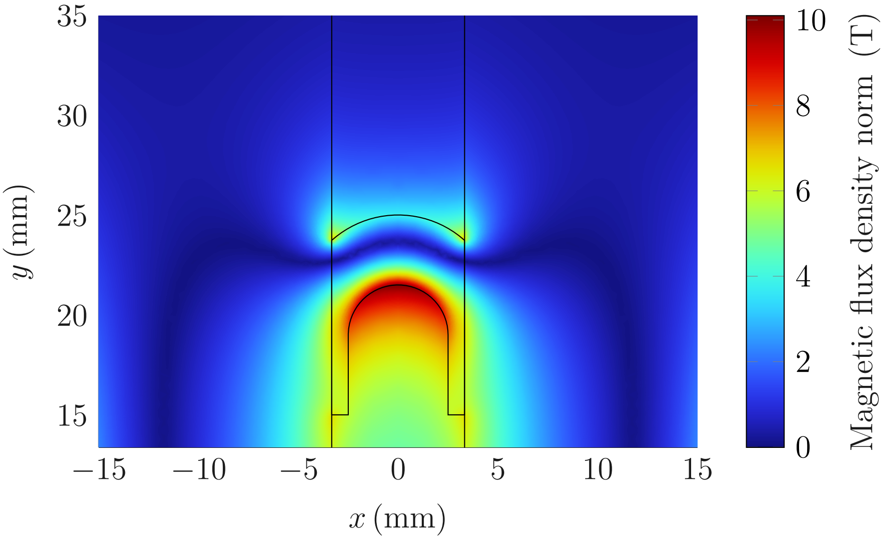

(b)

Fig. 4.29 Comparison of the the magnetic flux density norm in the railgun midplane. (a) Transient FEM model evaluated at $t = 10\,\mu\text{s}$. (b) Stationary FEM model evaluated for the same armature displacement and current as in the transient case at $t = 10\,\mu\text{s}$.

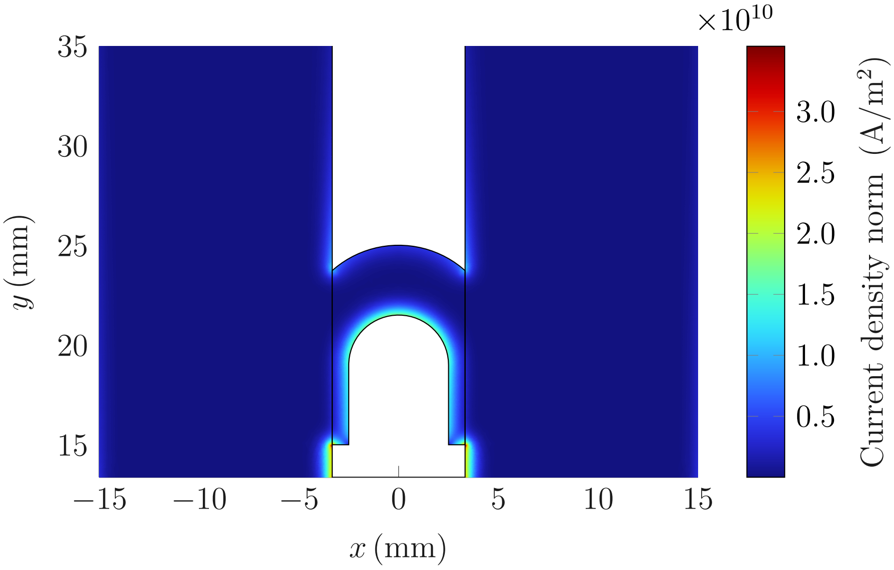

(a)

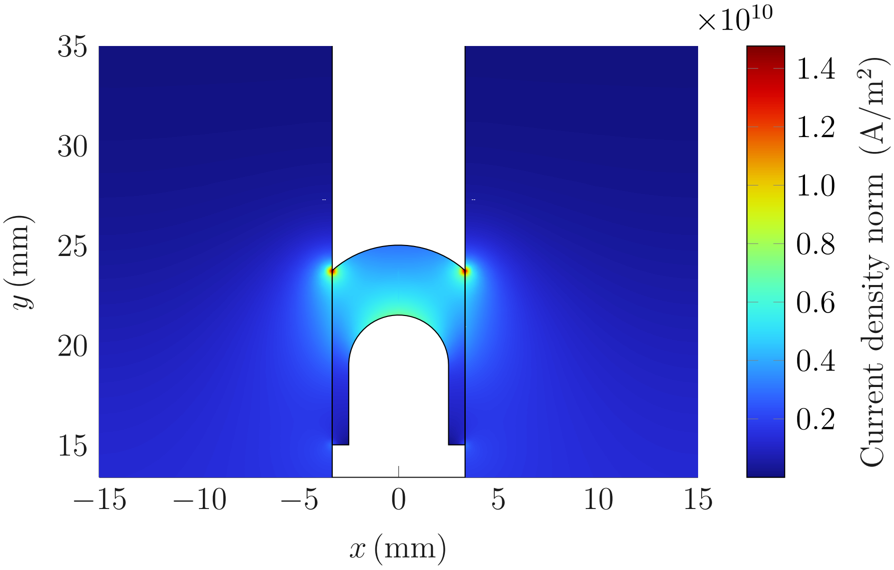

(b)

Fig. 4.30 Comparison of the the current density norm in the railgun midplane. (a) Transient FEM model evaluated at $t = 10\,\mu\text{s}$. (b) Stationary FEM model evaluated for the same armature displacement and current as in the transient case at $t = 10\,\mu\text{s}$.

At the initial stages, the current distribution is primarily governed by proximity effects, and the skin depth in both the rails and the armature is comparable. At this stage, the armature velocity remains low, and velocity-induced skin effects play a negligible role. As time progresses, the current diffuses into the rail conductors. However, as the armature velocity increases, the velocity skin effect becomes increasingly significant. Consequently, the current concentrates at the tip of the armature, on the inner faces. Figure 4.31 illustrates the current density norm at $t = 100\,\mu\text{s}$.

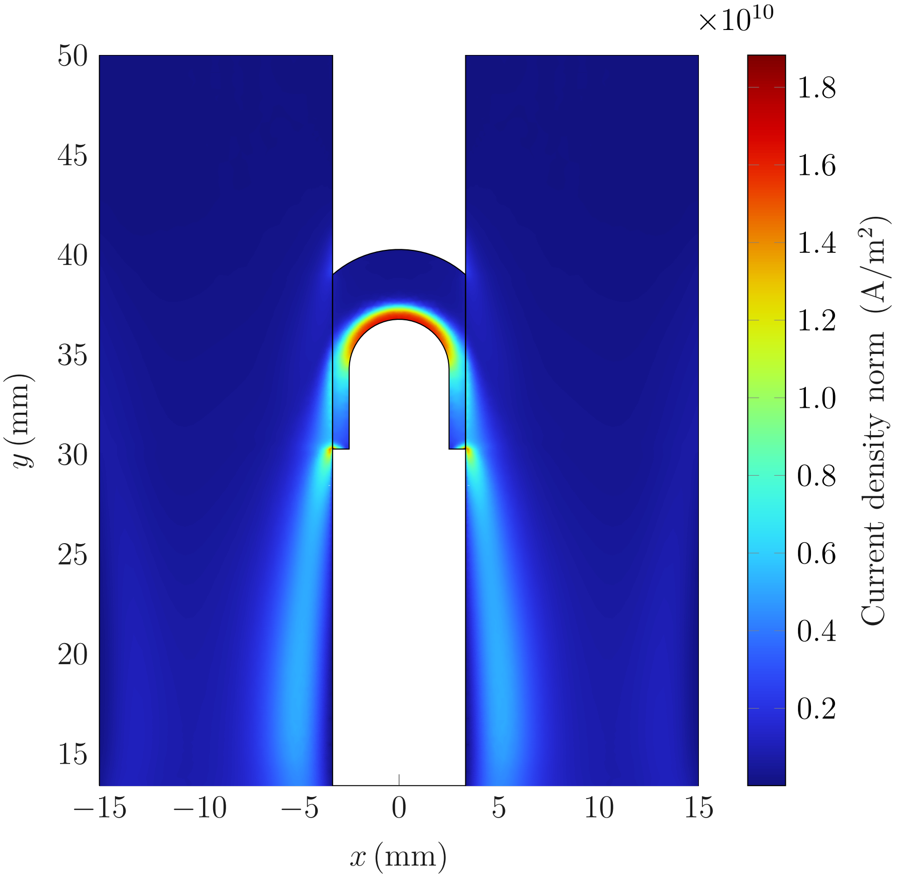

Fig. 4.31 Current density norm in the railgun midplane at $t = 100\,\mu\text{s}$.

From the computed electromagnetic force, the armature velocity and displacement are obtained by solving the mechanical equations of motion. Figure 4.32 compares the resulting armature speed predicted by the analytical, quasi-static FEM, and transient FEM models. At $t = 100\,\mu\text{s}$, the analytical model predicts an armature speed of approximately $380\,\text{m/s}$, whereas the quasi-static and transient models yield velocities of about $250\,\text{m/s}$ and $300\,\text{m/s}$, respectively. Figure 4.33 presents a corresponding comparison of the armature displacement. At $t = 100\,\mu\text{s}$, the analytical model predicts a displacement of approximately 20 mm, while the quasi-static and transient models result in displacements of about 13 mm and 15 mm, respectively.

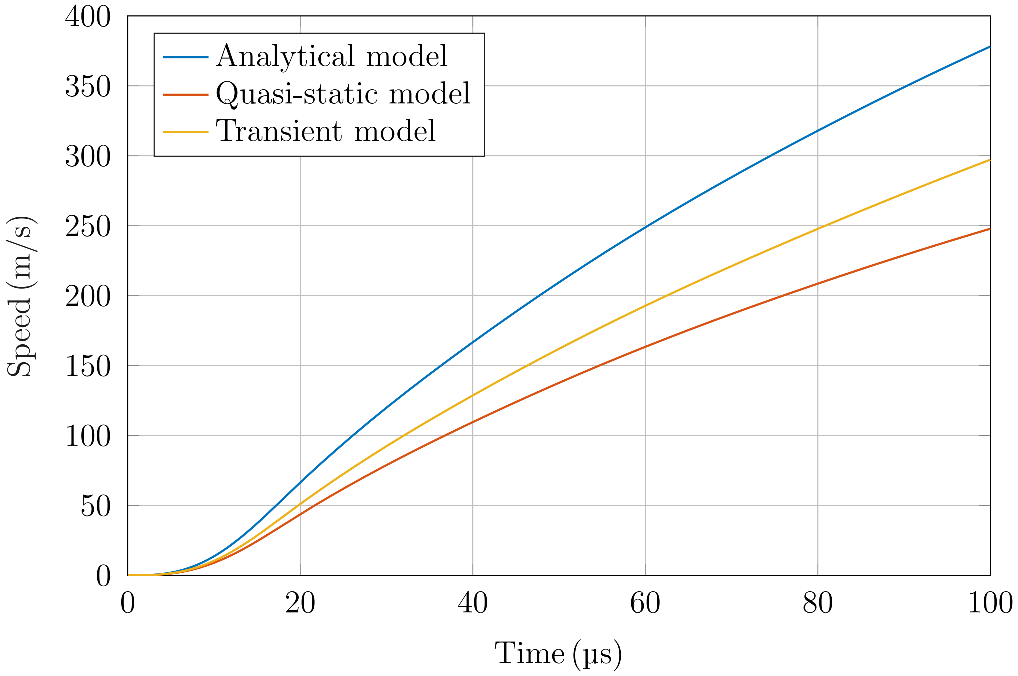

Fig. 4.32 Comparison of the armature speed obtained from the analytical model, the quasi-static model, and the transient model.

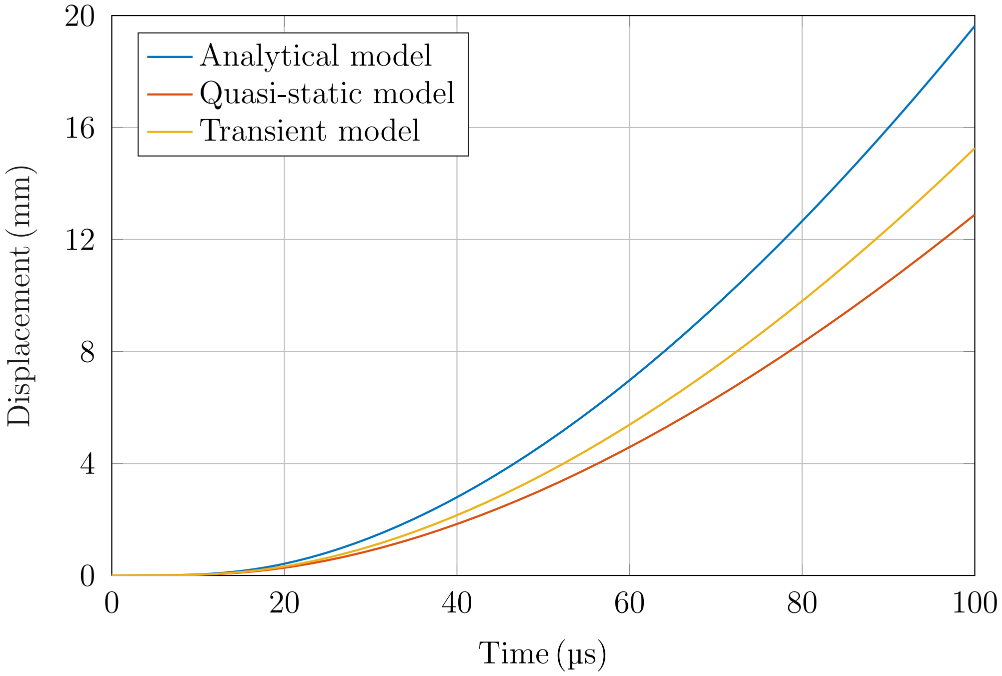

Fig. 4.33 Comparison of the armature displacement obtained from the analytical model, the quasi-static model, and the transient model.

Figure 4.35 presents the temporal evolution of the temperature at several evaluation points within the railgun. The locations of these points are defined in Fig. 4.34: P1 corresponds to the rail–armature interface at the midplane, P2 to the rail–armature interface at the armature top, P3 to the armature tip (inner face) at the midplane, and P4 to the armature tip (inner face) at the armature top. It can be observed that the temperatures at P3 and P4 are significantly higher than at the other locations, with the midplane exhibiting the highest values. As discussed previously, the velocity skin effect concentrates the current at the armature tip inner face, leading to localized Joule heating. Considering that the melting temperature of aluminum is approximately 933 K, these regions are expected to undergo melting during operation.

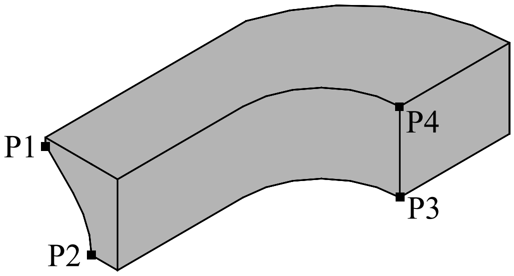

Fig. 4.34 Definition of the temperature evaluation points in the railgun.

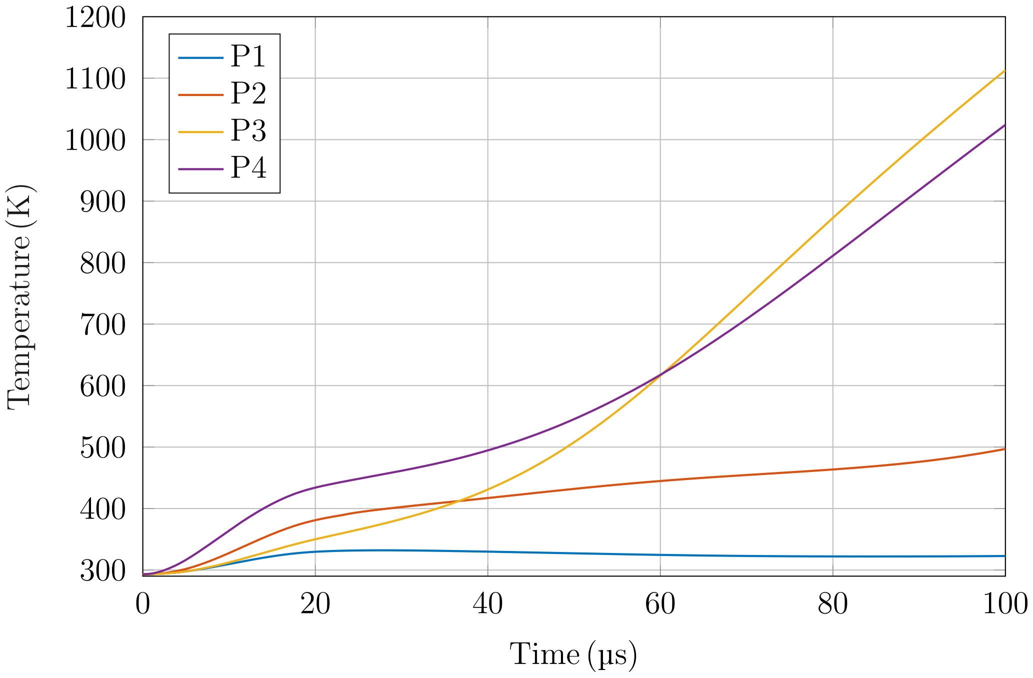

Fig. 4.35 Temporal evolution of the temperature at the evaluation points P1–P4.

Figure 4.36 shows the temperature field in the railgun at $t = 100\,\mu\text{s}$. The highest temperatures appear in the inner region of the armature tip, indicating severe localized Joule heating. As aluminum melts at approximately 933 K, partial melting may occur in this area. In the present single-use breaker, this is acceptable. However, for future multi-shot railgun actuators, materials with higher melting temperatures, such as copper (1358 K), could be used to improve thermal robustness and durability.

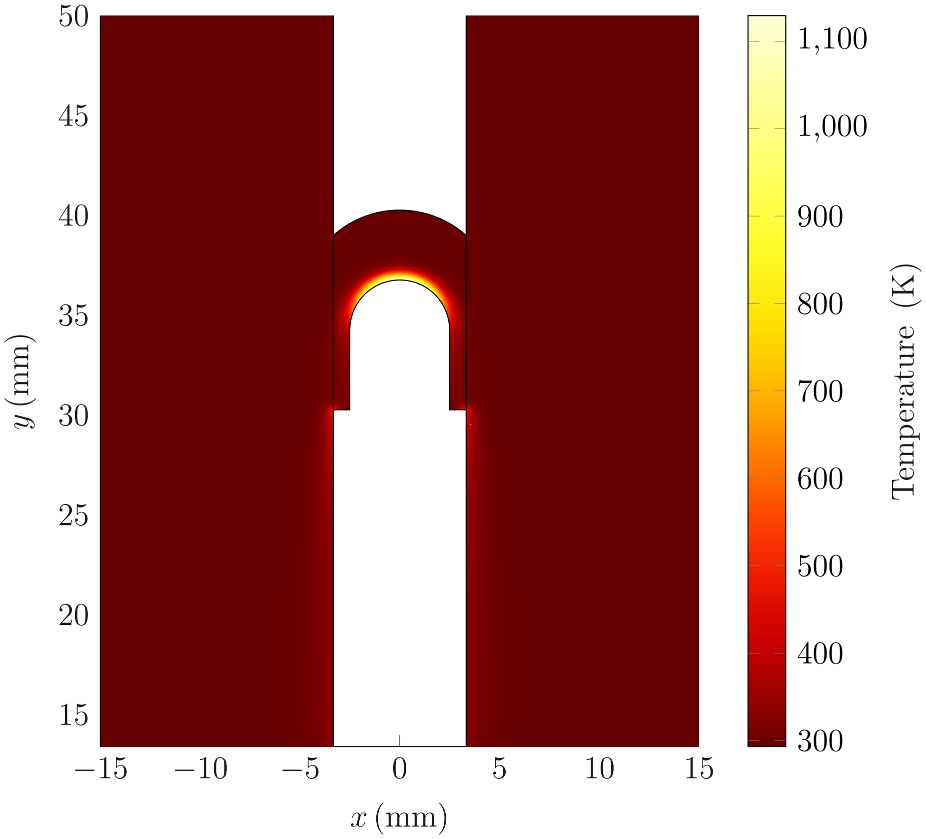

Fig. 4.36 Temperature field in the railgun at $t = 100\,\mu\text{s}$.

4.2.4 Friction Model

Because the current density $\mathbf{J}$ in the rails and armature has a significant y-component, transverse Lorentz forces arise in the railgun. These x-directed electromagnetic forces affect system performance by imposing mechanical loads on the rails and inducing armature deformation. The resulting x-components of the forces acting on the rails and armature are shown in Fig. 4.37.

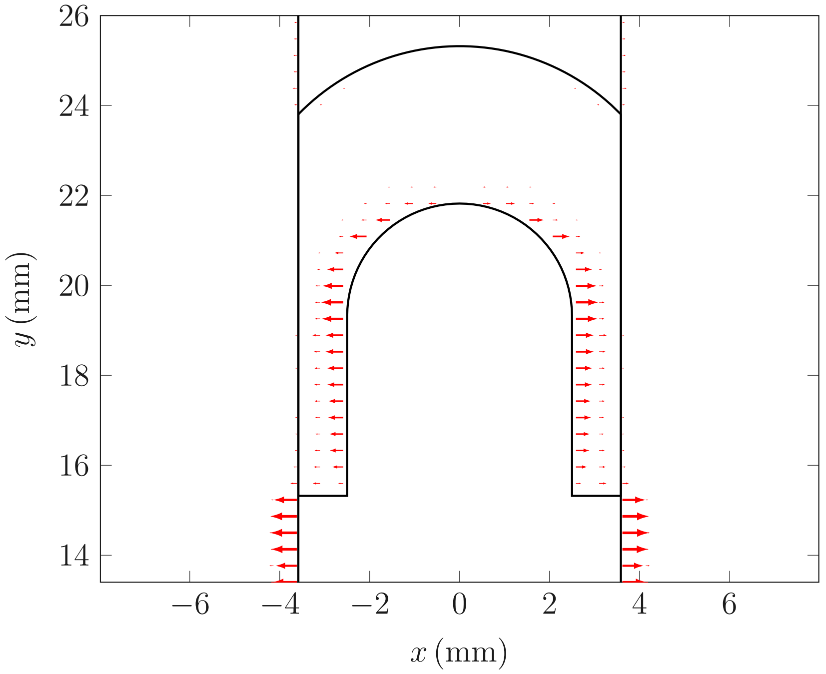

Fig. 4.37 Electromagnetic force distribution in the railgun at $t = 20\,\mu\text{s}$, showing the transverse (x-direction) force components acting on the rails and on the armature in the horizontal midplane.

At the initial instants of operation, the armature is positioned on top of the rails, such that the current enters almost directly into the armature. Under these conditions, the y-component of the current density in the rails, J_y, is nearly zero, and consequently the transverse electromagnetic forces acting on the rails are negligible. In contrast, the armature carries a considerable J_y component, as shown in Fig. 4.30, resulting in significant transverse Lorentz forces acting on the armature. Moreover, the proximity effect concentrates the current along the inner edges of the armature, reducing the effective distance between opposing current paths and thereby increasing the resulting electromagnetic forces. These forces lead to an increase in the normal contact force between the armature and the rails and, as a consequence, the friction force must be taken into account.

As the armature progresses along the rails, the total transverse force acting on the rails increases. Beyond a certain point, this rail force can exceed the corresponding armature force, which may result in a loss of electrical contact at the rail–armature interface and the onset of arcing. To prevent this scenario, the system is preloaded by means of a spring mechanism. In addition to maintaining electrical contact, the spring mechanism compensates for unavoidable manufacturing tolerances, rail non-parallelism, and surface imperfections by allowing elastic compliance of the rail assembly, thereby ensuring a more uniform and reliable contact pressure along the armature path. Fig. 4.38 shows the temporal evolution of the transverse electromagnetic force acting on the armature, $F_{x,\mathrm{a}}$, and on the rails, $F_{x,\mathrm{r}}$.

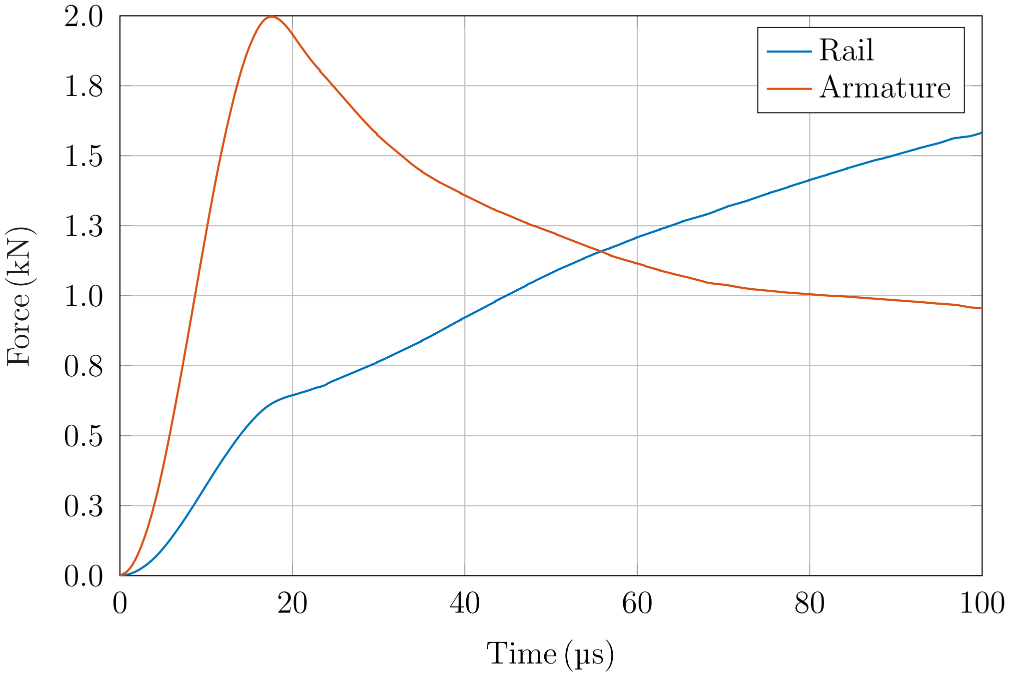

Fig. 4.38 Temporal evolution of the transverse electromagnetic force acting on the rails and armature.

It is important to note that the transverse armature force shown in Fig. 4.38 is computed as

$$F_{x,\mathrm{a}} = 4 \int_{V_\mathrm{a}} J_y B_z \, \mathrm{d}V, \tag{4.60}$$

where the integration volume V_a corresponds to one quarter of the armature, as defined in Fig. 4.37. Owing to symmetry, the net transverse electromagnetic force acting on the complete armature is zero. Nevertheless, the force obtained from the expression above represents the local transverse loading acting on the armature–rail contact regions and is therefore essential for determining the total normal contact force. This normal force directly enters the calculation of the total friction force and must be accounted for in the mechanical analysis of the railgun.

Similarly, the transverse electromagnetic force acting on the rails, $F_{x,\mathrm{r}}$, is computed using as

$$F_{x,\mathrm{r}} = 4 \int_{V_\mathrm{r}} J_y B_z \, \mathrm{d}V, \tag{4.61}$$

where V_r denotes the portion of the rail volume belonging to the deformed geometry. The remaining rail segments are excluded from the integration, as they serve only an auxiliary numerical role to separate the railgun from the magnetic insulation domain and do not exist in the physical system.

It is also important to note that, to bring the numerical model closer to the real geometry, the parameter y_{00}—which represents the distance between the armature and the non-deformed domains (see Fig. 4.25) and corresponds to the initial armature position—has been reduced from 1.6 mm to 0.5 mm. This adjustment is essential, since an excessively large y_{00} would overestimate $F_{x,\mathrm{r}}$, leading to an underestimation of the normal contact force and, consequently, of the friction force.

Figure 4.38 shows that, at the beginning of the railgun operation, the transverse force acting on the armature, $F_{x,\mathrm{a}}$, is significantly higher than that acting on the rails, $F_{x,\mathrm{r}}$, resulting in a large normal contact force and high friction. Toward the end of the simulation, $F_{x,\mathrm{r}}$ exceeds $F_{x,\mathrm{a}}$, reaching approximately 1.58 kN compared to 0.95 kN for the armature, indicating loss of electrical contact and the onset of arcing. To avoid this scenario, a minimum preload force of 629 N is required; therefore, a preload corresponding to a mass of 50 kg is applied to each rail, resulting in a total preload force of 981 N.

The friction force F_f is evaluated as

$$F_\mathrm{f} = \mu N, \tag{4.62}$$

where μ denotes the friction coefficient and N the normal force at the rail–armature interface. In the present analysis, the normal force is computed as

$$N = F_{x,\mathrm{a}} - F_{x,\mathrm{r}} + F_\mathrm{sp}, \tag{4.63}$$

where F_sp represents the preload force applied to the rails by the spring mechanism, which can be described by the linear spring relation

$$F_\mathrm{sp} = k \Delta x, \tag{4.64}$$

with k denoting the spring stiffness and Δx the spring compression.

For simplicity, F_{sp} is assumed to be constant in the model, although in reality it varies with the spring compression. Prior to the discharge, the armature is initially compressed by the preload. Once current starts flowing, the armature undergoes transverse expansion while the rails are pushed outward by the electromagnetic forces, further compressing the springs and increasing the normal contact force during operation.

The friction coefficient μ represents one of the major sources of uncertainty in the railgun model, as it depends on a wide range of interacting factors. It is strongly influenced by the surface finish of the contacting bodies, with smoother surfaces leading to lower friction coefficients. In addition, μ is characteristic of the materials in contact and depends on the relative sliding velocity, decreasing as the speed increases. The normal force also affects the friction coefficient: higher normal loads lead to larger real contact areas at the microscopic level, which in turn results in higher effective friction coefficients. In practice, the value of μ is usually determined experimentally. However, the copper–aluminum interface is not well documented in the literature and available data are scarce, in contrast to steel-based contacts, which are extensively studied. As reported in [99], the friction coefficient for aluminum–aluminum contacts lies in the range 1.05–1.35, while values close to unity are also reported for copper–copper interfaces. Based on these considerations, three constant friction coefficients, $\mu = 0.90$, 0.95, and 1.00, are assumed in the simulation model to account for this uncertainty.

The equivalent driving force acting on the armature, F_{eq}, is defined by the balance between the electromagnetic force F_{em} and the friction force F_{f}. When the electromagnetic force exceeds the friction force, the equivalent force is given by

$$F_{\mathrm{eq}} = F_{\mathrm{em}} - F_{\mathrm{f}}, \qquad \text{if } F_{\mathrm{em}} > F_{\mathrm{f}}, \tag{4.65}$$

whereas if the electromagnetic force is insufficient to overcome friction and the armature is at rest, $\dot{y} = 0$, the equivalent force is set to

$$F_{\mathrm{eq}} = 0, \qquad \text{if } F_{\mathrm{em}} < F_{\mathrm{f}} \text{ and } \dot{y} = 0. \tag{4.66}$$

Figure 4.39 shows the equivalent force acting on the armature for friction coefficients $\mu = 0.00$, 0.90, 0.95, and 1.00. In the case $\mu = 0.00$, the simulation time is limited to 100 µs, since extending the simulation leads to excessive compression of the deforming green domain (Fig. 4.25), eventually resulting in negative element volumes. The results clearly indicate that friction severely degrades the railgun performance. Without friction, the peak equivalent force reaches approximately 2.7 kN, whereas with $\mu = 0.90$ the peak force drops to about 391 N, with $\mu = 0.95$ to 341 N, and with $\mu = 1.00$ to 294 N. Furthermore, when friction is included, a delay of approximately 50 µs is observed before motion starts, as the electromagnetic force is initially insufficient to overcome the friction force. It can also be seen that around $t \approx 200$ µs the equivalent force becomes negative when friction is accounted for, indicating a deceleration of the armature. Finally, for $\mu = 1.00$ the driving force suddenly goes to zero at $t \approx 360$ µs, corresponding to a complete stop of the armature (see Fig. 4.40); a similar behavior is observed for $\mu = 0.95$ at $t \approx 397$ µs.

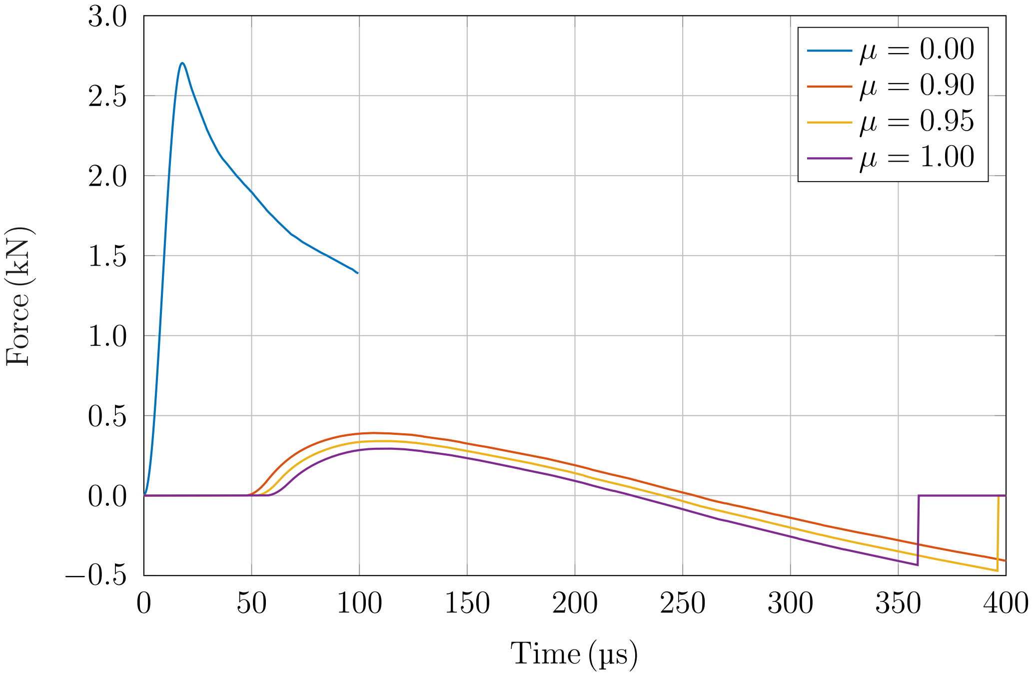

Fig. 4.39 Equivalent driving force acting on the armature for different friction coefficients, $\mu = 0.00$, 0.90, 0.95, and 1.00.

Figure 4.40 shows the armature speed for friction coefficients $\mu = 0.00$, 0.90, 0.95, and 1.00. As expected from the equivalent driving force analysis, the armature speed is strongly reduced by the presence of friction, significantly affecting the dynamic response of the system under operating conditions. In the frictionless case ($\mu = 0.00$), the armature reaches a maximum speed of approximately 297 m/s. When friction is included, the achievable speed decreases markedly: for $\mu = 0.90$, the maximum speed is about 85 m/s, with a final speed of 32 m/s at the end of the simulation. For $\mu = 0.95$, the maximum speed is reduced to 67 m/s, and the armature comes to a complete stop at $t = 397\,\mu\text{s}$. A similar behavior is observed for $\mu = 1.00$, for which the maximum speed is approximately 52 m/s, and the armature stops earlier, at $t = 360\,\mu\text{s}$.

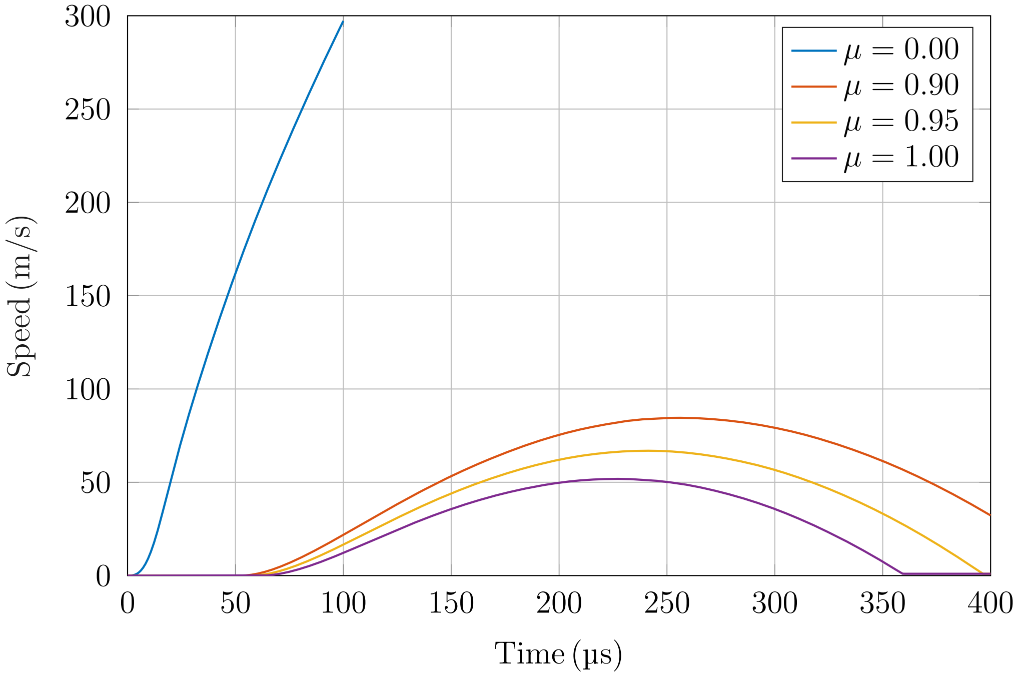

Fig. 4.40 Armature speed as a function of time for different friction coefficients, $\mu = 0.00$, 0.90, 0.95, and 1.00.

Figure 4.41 shows the armature displacement for friction coefficients $\mu = 0.00$, 0.90, 0.95, and 1.00. In the frictionless case ($\mu = 0.00$), a displacement of 15 mm is achieved within 100 µs, demonstrating the maximum achievable performance. For $\mu = 0.90$, the armature reaches a total displacement of almost 20 mm over 400 µs, while the full breaker stroke of 15 mm is completed at approximately 315 µs. When the friction coefficient is increased to $\mu = 0.95$, the maximum displacement is limited to about 14 mm, and for $\mu = 1.00$ the armature travel is further reduced, reaching a maximum displacement of approximately 10 mm.

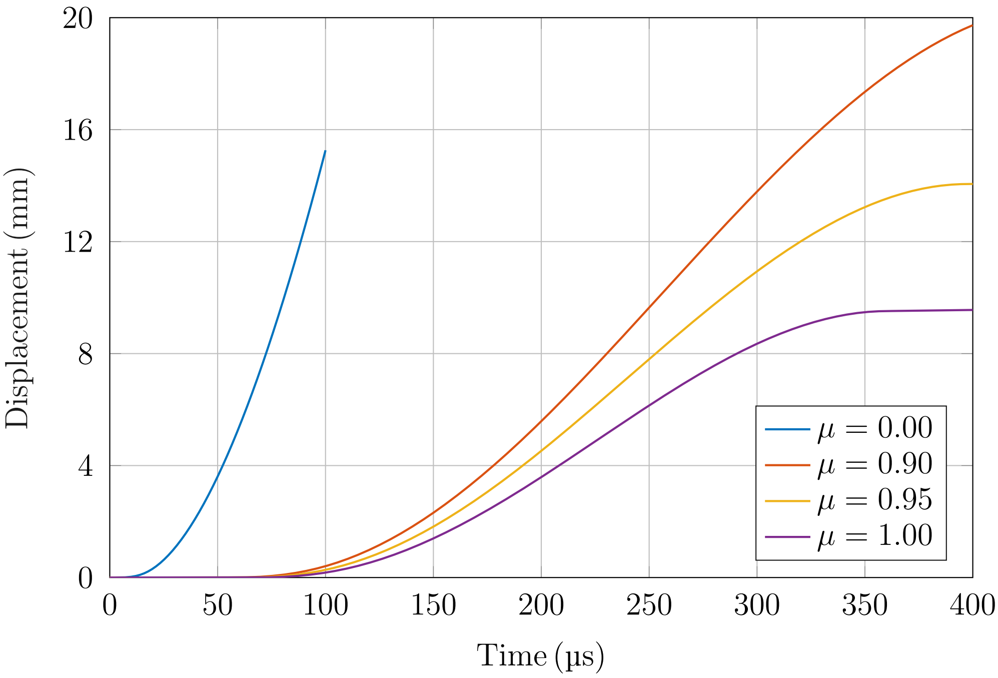

Fig. 4.41 Temporal evolution of the transverse electromagnetic force acting on the rails and armature.

From the obtained results, it can be clearly seen that friction has a strong detrimental impact on the overall performance of the railgun. One effective mitigation strategy consists in modifying the armature geometry: by changing the armature from a C-shaped configuration to a rectangular shape, the transverse electromagnetic force acting on the armature is significantly reduced, which in turn lowers the normal contact force and, consequently, the resulting friction force. In addition, increasing the separation between the rails represents another viable approach to improve performance. A larger rail spacing reduces the transverse electromagnetic forces acting on the rails, thereby decreasing the required preload force. As a result, the normal force at the rail–armature interface is reduced, leading to lower friction losses and improved railgun efficiency.

4.3 Experimental Validation

During the modeling stage, some simplifying assumptions were introduced to keep the problem tractable. In particular, the friction coefficient μ was assumed constant, neglecting its dependence on sliding speed and normal force. Moreover, the contact interface was not explicitly modeled: heat generation by friction, electrical contact resistance, and thermal contact resistance at the armature–rail interface were neglected. As a result, the predicted interface temperature cannot be considered accurate. This limitation is potentially significant, since these effects may increase the local temperature and lead to material melting. The presence of a molten layer may, in turn, act as a lubricant and reduce the effective friction coefficient. In this section, the proposed model is validated against experimental results to assess whether the adopted assumptions are acceptable under the operating conditions.

Figure 4.42 shows the prototype of the railgun actuator used for the experimental validation. The rails are painted black and the armature white to maximize optical contrast and facilitate armature tracking with the high-speed camera. Each rail includes nine rods sliding over the FR-4 blocks (yellow side blocks), constraining rail motion to the transversal direction. The FR-4 blocks are clamped to a massive stainless-steel block for structural rigidity. Although only three preloading springs per side are visible, five per side are used in the actual setup to withstand the total load. SWG10-60 springs are employed, with a maximum load of 490 N and a spring constant of 40.9 N/mm. The required spring compression to achieve the desired preload is given by

$$\Delta x = \frac{P}{k N_{\mathrm{sp}}} = 2.38\,\mathrm{mm}, \tag{4.67}$$

where $P = 490\,\mathrm{N}$ is the preload force and N_{sp} is the number of springs per rail.

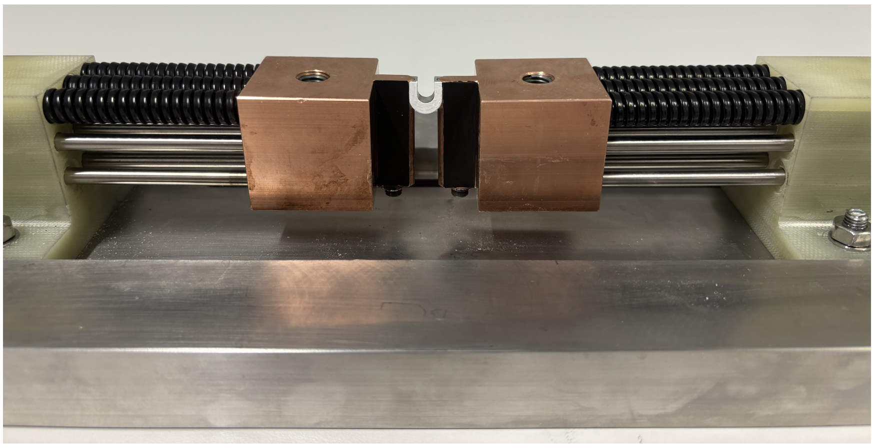

Fig. 4.42 Prototype of the railgun actuator used for experimental validation.

The experimental test setup combines synchronized electrical and optical equipment and is shown in Fig. 4.43. Electrical measurements were performed using a Tektronix DPO 7104C oscilloscope to record the muzzle voltage and railgun current. The current was measured with a PEM CWT1500R Rogowski current probe, while the muzzle voltage was acquired using a Tektronix TA042 differential voltage probe. Optical diagnostics were carried out with an i-Speed 727 Mono high-speed camera from IX Cameras, capable of a maximum frame rate of 200000 frames per second. To balance spatial resolution and temporal accuracy, recordings were performed at 100000 frames per second using a Nikon AF-S Nikkor 50 mm f/1.8G ED lens. Loss of electrical contact between the rails and the armature leads to arc formation; the intense broadband arc radiation would otherwise overexpose the sensor and prevent reliable armature tracking. This issue is mitigated by employing a MidOpt BP365 bandpass filter, which transmits only wavelengths in the 615–645 nm. Since arc radiation spans the visible spectrum, most of its optical power is rejected. Nevertheless, the remaining arc light can still be intense; therefore, an external red illumination source centered at 625 nm, with higher intensity than the arc emission, is used so that the recorded images are dominated by the controlled illumination. To avoid saturation, the lens aperture was set to f/4 and an ND8 neutral density filter was added.

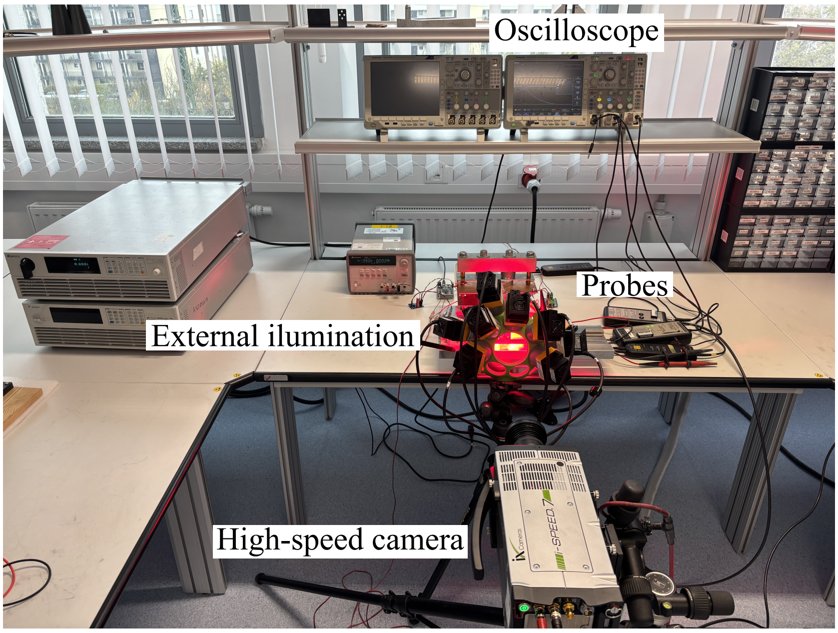

Fig. 4.43 Experimental test setup for the railgun actuator validation.

The entire experimental setup is coordinated by an Arduino Due, which acts as the central control unit. When an experiment is initiated, the Arduino generates a single trigger pulse that simultaneously performs three actions: it triggers the thyristor of the electrical drive, arms the oscilloscope, and starts the recording of the high-speed camera. Upon receiving the logic-high trigger signal, both the oscilloscope and the camera begin data acquisition, ensuring precise synchronization between the electrical measurements and the optical recordings.

The armature position was extracted using the Xcitex ProAnalyst 2023 software. Figure 4.44 compares the experimentally measured armature displacement with the results obtained from the simulation model for friction coefficients $\mu = 0.90$, $\mu = 0.95$, and $\mu = 1.00$. It can be observed that the model assuming $\mu = 0.95$ closely matches the experimental results up to approximately $t = 270\,\mu\text{s}$, with a maximum deviation of about 0.1 mm. Beyond this point, a significant discrepancy arises between the simulation and the experiment results. This deviation cannot be attributed to the transition from static to kinetic friction, as such a transition occurs at much lower speeds (around 1 m/s).

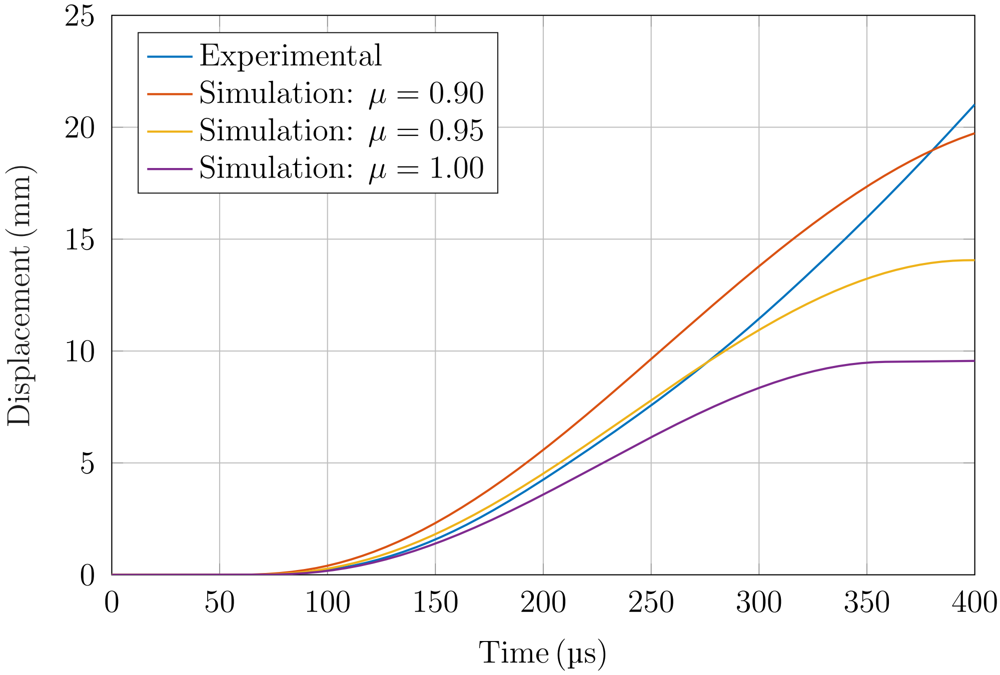

Fig. 4.44 Comparison between experimentally measured armature displacement and simulation results for different friction coefficients ($\mu = 0.90$, $\mu = 0.95$, and $\mu = 1.00$)

Evidence supporting a different mechanism is shown in Fig. 4.45(a), where aluminum deposits appear on the rails, indicating melting at the armature–rail interface. The onset of this layer occurs about 10 mm from the armature tip, corresponding to $t \approx 270\,\mu\text{s}$, which matches the divergence between experimental and simulated results. Material loss is also visible on the armature (Fig. 4.45(b)), further confirming melting. The deposited aluminum is confined to a short rail section rather than extending along its full length, likely because the high armature velocity expels most molten material. In the present application, this degradation is acceptable since the breaker is intended for single-use operation. For future multi-shot implementations, materials with higher melting points, such as steel or tungsten, should be considered to ensure reliable long-term operation. Overall, the model accurately predicts dry-friction behavior, with an error of about 0.1 mm. Once melting begins at $t \approx 270\,\mu\text{s}$, molten material reduces friction—an effect not included in the model.

(a)

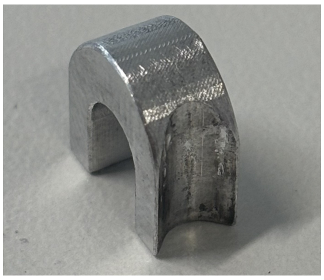

(b)

Fig. 4.45 Post-test inspection of the rail–armature interface showing (a) rails, and (b) armature.

Figure 4.45 shows that, aside from the presence of aluminum deposits on the rail surface, no significant damage to the railgun structure is observed after the shot. The rails and the armature remain mechanically intact, with no evidence of severe erosion, deformation, or cracking. This indicates that the observed melting is localized and limited to the contact interface, without compromising the overall integrity of the actuator. These results suggest that, despite the extreme operating conditions, the railgun actuator can withstand a firing event without critical degradation, thereby opening the possibility of its application in multiple-operation circuit breakers rather than being restricted to single-use devices.

The presented model could be further improved by reducing the friction coefficient once the armature starts to melt. Implementing such a refinement, however, requires an accurate estimate of the temperature at the armature contact area, which represents the main challenge. As already discussed, the electromagnetic problem must be formulated using curl-conforming elements; consequently, the interface conditions are governed by (4.40)–(4.43). Under these constraints, imposing identity-pair continuity or source–destination boundary conditions (for example, to introduce an explicit electrical contact resistance) would overconstrain the problem and potentially lead to nonphysical field distributions or numerical instability. For this reason, once curl elements are used in any of the model physics, it is not possible to employ source and destination boundaries at the interface: the domains share a single boundary, and the contact interface cannot be treated as two paired boundaries. As a result, the temperature at the armature contact area cannot be obtained in a straightforward manner within the present modeling strategy, particularly under highly transient operating conditions. Although several workarounds exist, they are beyond the scope of this thesis and would require a substantially more complex model. One possible approach is to introduce a very thin interfacial layer domain representing the contact, to which effective electrical and thermal conductivities are assigned in order to emulate the contact resistances and approximate the associated heat generation mechanisms.

Figure 4.46 shows the railgun at different operating times, namely $t = 0\,\mu\text{s}$, $t = 130\,\mu\text{s}$, $t = 260\,\mu\text{s}$, and $t = 400\,\mu\text{s}$. It can be observed that the image quality is sufficiently high to allow precise tracking of the armature position throughout the entire motion.

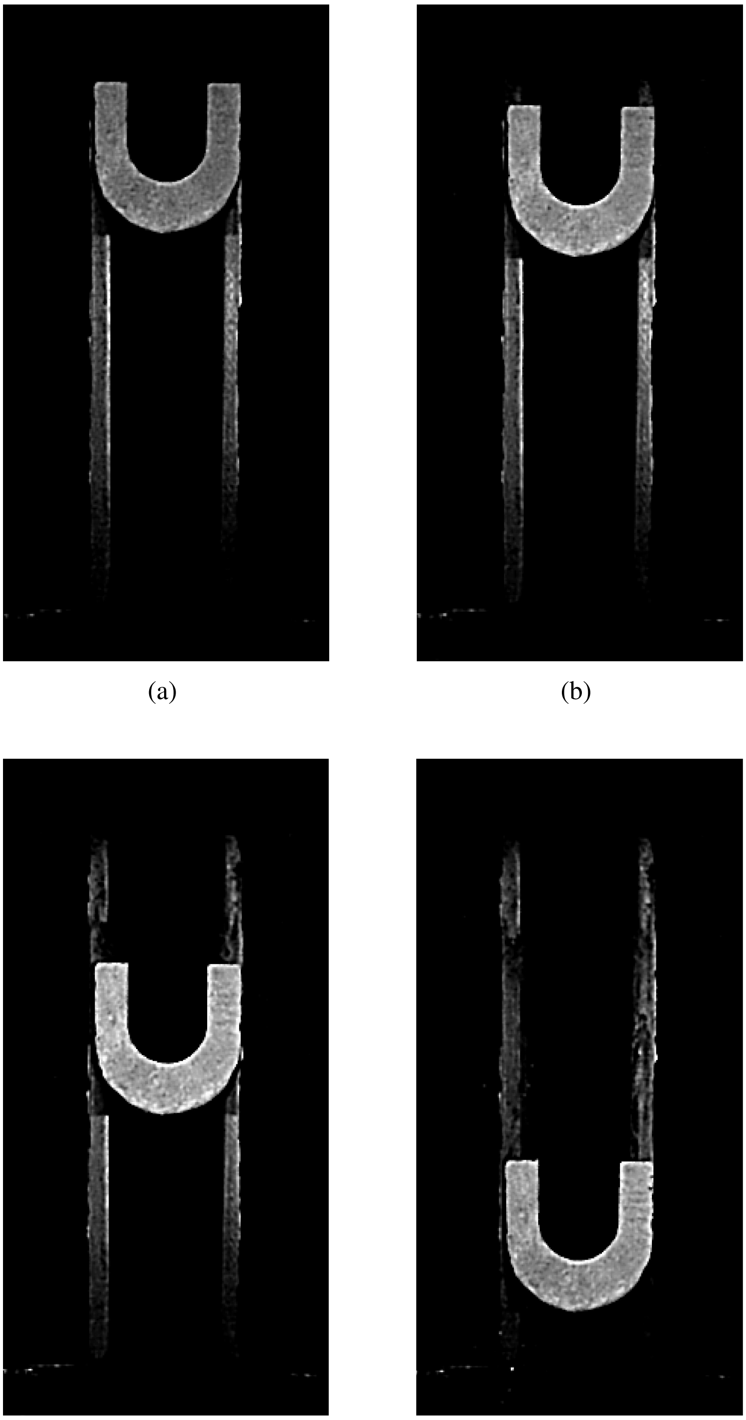

(a) (b)

(c) (d)

Fig. 4.46 High-speed camera images of the railgun at different operating times ((a) $t = 0\,\mu\text{s}$, (b) $t = 130\,\mu\text{s}$, (c) $t = 260\,\mu\text{s}$, and (d) $t = 400\,\mu\text{s}$).

The armature speed was obtained by numerical differentiation of the experimentally measured armature displacement. Because the camera frame rate provides position data only every 10 µs, a direct differentiation would lead to a strongly noise-corrupted speed waveform. To mitigate this issue, intermediate data points were first introduced by interpolation, and the resulting displacement signal was subsequently smoothed using the cubic smoothing spline function (`csaps`). This method computes a cubic spline that balances fidelity to the measured data with smoothness by minimizing a weighted combination of the squared fitting error and the spline curvature, thereby effectively filtering high-frequency noise while preserving the underlying dynamics. Figure 4.47 compares the experimentally obtained armature speed with the simulation results for the friction coefficients $\mu = 0.90$, $\mu = 0.95$, and $\mu = 1.00$. A very good agreement is observed between the experimental data and the simulation results obtained with $\mu = 0.95$ up to the point where melting effects become relevant, after which the results diverge for the reasons discussed previously. At $t = 400$ µs, the armature reaches a measured speed of approximately 106 m/s.

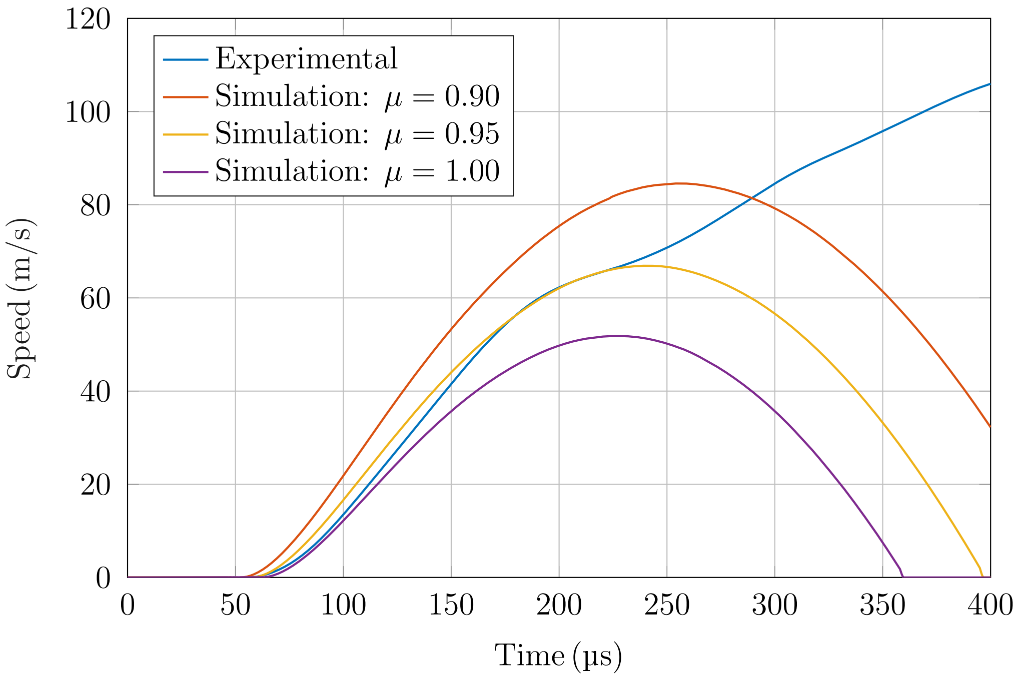

Fig. 4.47 Comparison between the experimentally obtained armature speed and simulation results for different friction coefficients ($\mu = 0.90$, $\mu = 0.95$, and $\mu = 1.00$).

From the experimentally obtained armature speed, the acceleration can be computed by numerical differentiation, and the corresponding driving force can then be estimated by multiplying the acceleration by the armature mass. Performing a second numerical differentiation is inherently challenging and is expected to introduce a non-negligible level of noise and error, particularly given the limited temporal resolution of the experimental data. As shown in Fig. 4.44, the agreement between experimental and simulated force is therefore less accurate than for displacement and velocity. Nevertheless, it can be observed that up to approximately $t = 220\,\mu\text{s}$, the experimental and simulated force waveforms follow a similar overall trend. At later times, the experimentally derived force exhibits noticeable oscillations toward the end of the motion. These oscillations may be partly attributed to numerical artifacts introduced by the differentiation process; however, they may also reflect a real physical effect, potentially associated with the presence of molten aluminum at the contact interface, which would lead to a non-constant and dynamically varying effective friction coefficient.

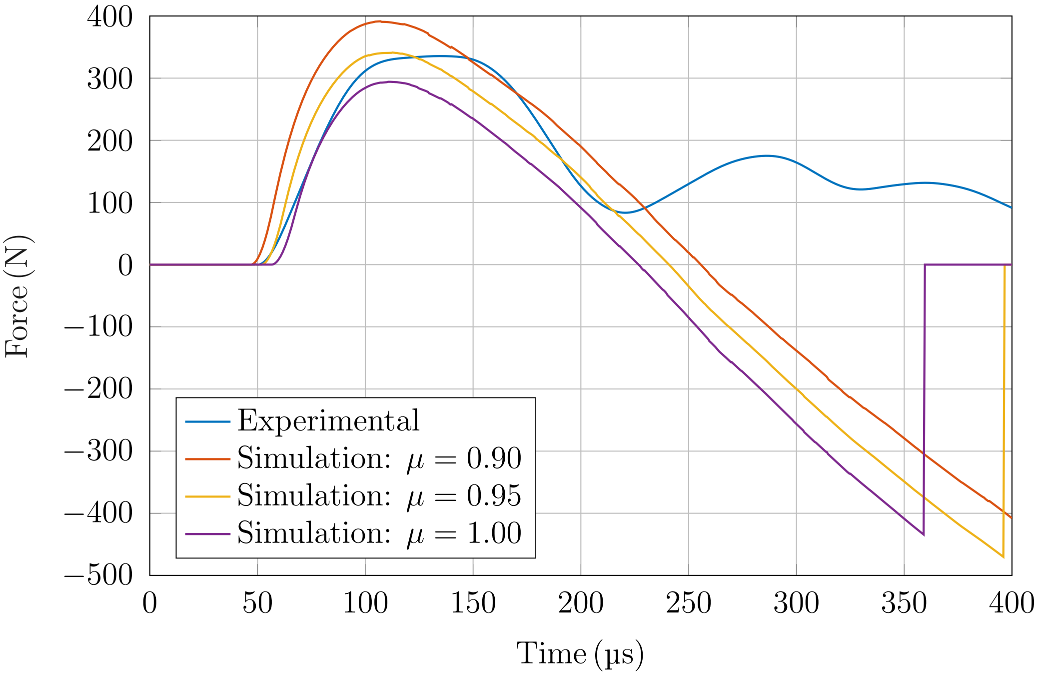

Fig. 4.48 Comparison between the experimentally obtained armature force and simulation results for different friction coefficients ($\mu = 0.90$, $\mu = 0.95$, and $\mu = 1.00$).

Since friction has a strongly detrimental effect on railgun performance, it might be tempting to reduce the preload in order to improve the dynamic response. However, this approach must be considered with caution. Reducing the preload also increases the electrical contact resistance between the rails and the armature, which leads to higher Joule losses. Moreover, an excessively low preload may result in intermittent loss of electrical contact, causing arcing at the interface and further increasing the losses within the actuator. Figure 4.49 compares the armature displacement obtained with a preload of 490 N per rail and 392 N per rail. As expected, the configuration with lower preload exhibits a higher initial acceleration. Nevertheless, the system with the higher preload overtakes the lower-preload case at approximately $t = 177\,\mu\text{s}$. At $t = 400\,\mu\text{s}$, the configuration with 490 N preload reaches an armature displacement of approximately 21 mm, whereas the configuration with 392 N preload reaches only about 17 mm.

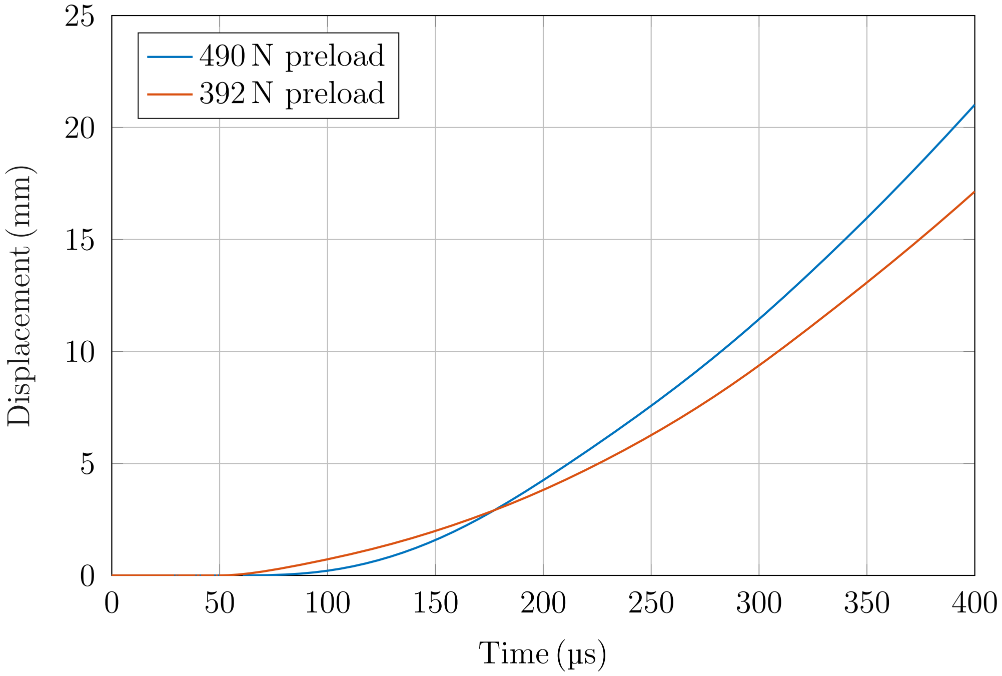

Fig. 4.49 Comparison of armature displacement for two different preload forces applied to each rail (490 N and 392 N).

By analyzing the railgun current for both preload configurations, the reasons for the superior performance of the 490 N preload case become evident. As shown in Fig. 4.50, the current profile corresponding to the 490 N preload is consistently slightly higher than that of the 392 N configuration. This directly implies a higher electromagnetic force acting on the armature and, consequently, a higher driving force. In addition, the 392 N preload configuration exhibits a sudden drop in current at approximately $t = 255\,\mu s$, followed by a further decrease around $t = 320\,\mu s$. These current reductions significantly degrade the actuator performance.

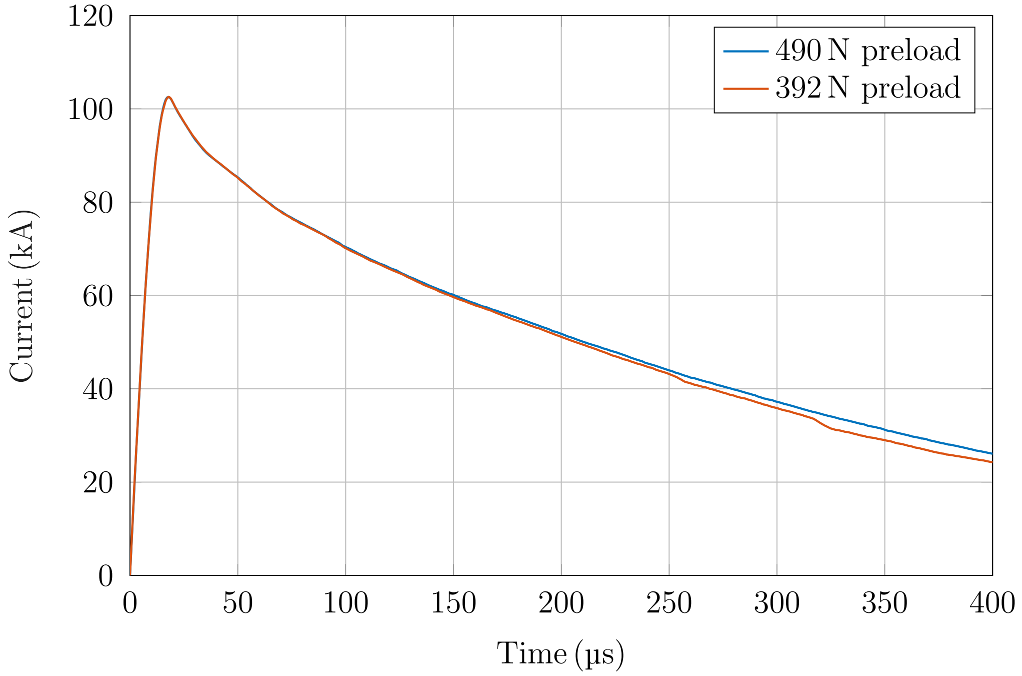

Fig. 4.50 Measured railgun current for two different preload forces applied to each rail (490 N and 392 N).

Figure 4.51 shows the muzzle voltage, defined as the voltage measured at the end of the rails. This voltage represents the combined voltage drop across the armature and the rail–armature contact interfaces. At the beginning of the discharge, a pronounced voltage spike is observed in both configurations; this spike corresponds to the inductive term $L\mathrm{d}i/\mathrm{d}t$ associated with the armature, since the current rise rate is very high at the initial stage. Subsequently, both preload configurations exhibit an almost identical muzzle voltage for a short time interval. As the discharge progresses, the muzzle voltage in the 392 N preload configuration increases more than in the 490 N case, indicating a higher effective contact resistance, which also explains the lower current levels previously observed. In addition, distinct voltage spikes appear at approximately $t = 255\,\mu s$ and $t = 320\,\mu s$ in the 392 N configuration; these spikes explain the corresponding current dips and are attributed to temporary loss of electrical contact and the consequent arc formation at the rail–armature interface, as shown in Fig. 4.52.

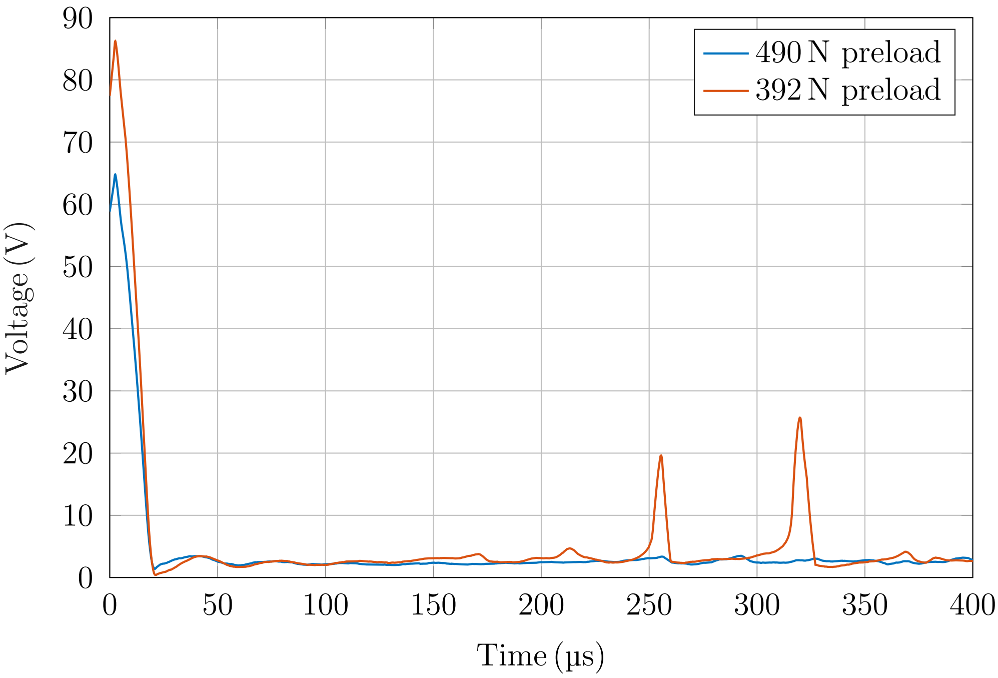

Fig. 4.51 Measured muzzle voltage for two different preload forces applied to each rail (490 N and 392 N).

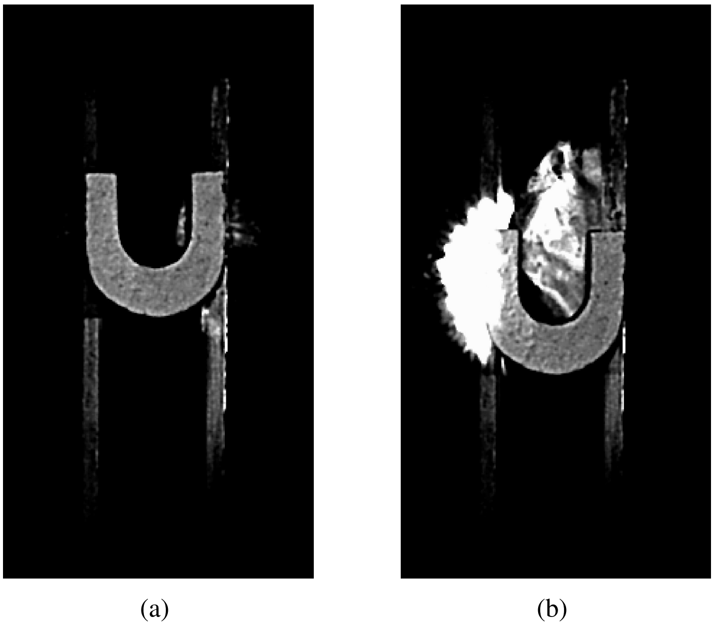
(a)

(b)

Fig. 4.52 High-speed camera images showing arc formation at the rail–armature interface during operation with reduced preload: (a) $t = 260\,\mu\text{s}$ and (b) $t = 320\,\mu\text{s}$.

In Fig. 4.51(a), the arc is more difficult to observe because its energy is lower and it occurs on the backside of the armature. As a result, the emitted light is partially obscured from the camera view, since the arc forms on the right-hand side of the armature and is not directly visible in the recorded frame.

Figure 4.53 shows the rails and the armature corresponding to the 392 N preload configuration after the shot. In contrast to the higher-preload case, a noticeably higher level of damage is observed. In particular, the rails exhibit significant surface degradation, with clear signs of abrasion caused by arc activity at the rail–armature interface. This damage is consistent with the intermittent loss of electrical contact discussed previously and further confirms that the reduced preload promotes arcing, leading to increased wear and degradation of the rail surfaces.

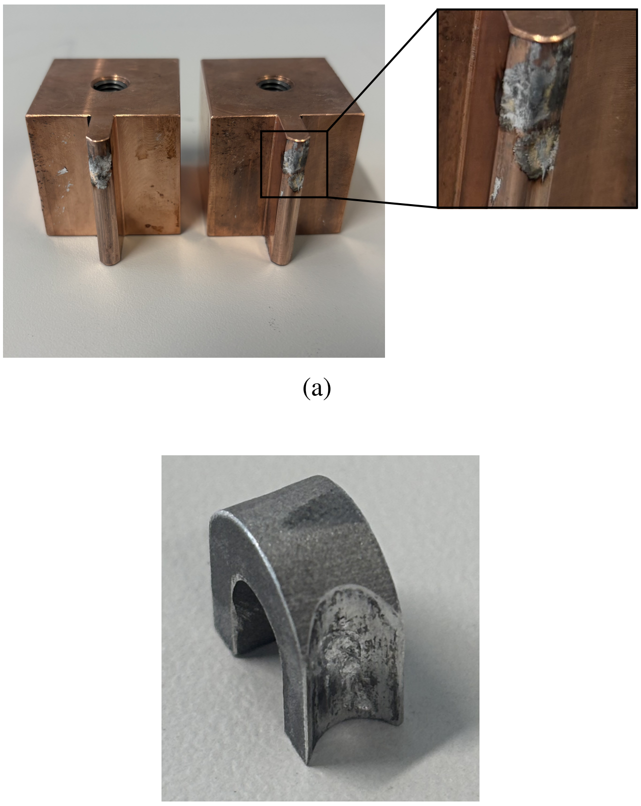

(a)

(b)

Fig. 4.53 Post-test inspection of the rail–armature interface for the 392 N preload configuration showing (a) rails, and (b) armature.

Figure 4.54 presents the system-level results obtained using the simulation framework introduced in Chapter 2. In contrast to the previous analyses, where the breaker arc voltage was computed assuming an average armature speed, the present results incorporate the experimentally measured armature displacement. Specifically, the measured displacement is used to reconstruct the instantaneous breaker contact separation, from which the time-varying arc length is obtained and directly translated into the corresponding arc voltage. In this way, the breaker voltage evolution reflects the real actuator dynamics rather than an idealized kinematic assumption. Figure 4.54 shows the resulting breaker current for three different system inductances, namely $L_s = 10\,\mu H$, $50\,\mu H$, and $100\,\mu H$ In all cases, current interruption is achieved in less than 700 µs, with interruption times of approximately 420 µs, 580 µs, and 700 µs for 10 µH, 50 µH, and 100 µH, respectively. The peak current is limited to about 11.5 kA for $L_s = 10\,\mu H$, 3.9 kA for 50 µH, and 2.6 kA for 100 µH. These results demonstrate that the proposed solution significantly outperforms state-of-the-art pyrotechnic fuses, which typically exhibit interruption times of 1 ms to 2 ms for comparable system inductances. Moreover, the achieved performance is superior to that of Thomson-coil-based actuators, which interrupts currents in approximately 800 µs for a 10 µH grid while limiting the current to about 12 kA.

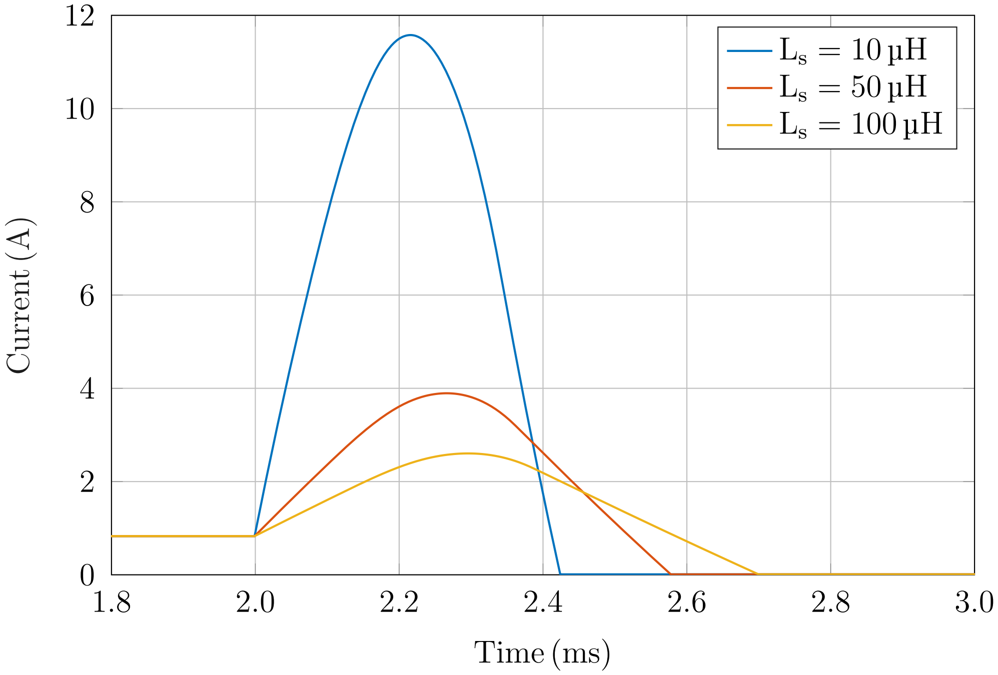

Fig. 4.54 System-level breaker current obtained using the simulation model of Chapter 2, where the experimentally measured armature displacement is used to compute the time-varying contact separation and arc voltage, for three different system inductances ($L_s = 10\,\mu H$, 50 µH, and 100 µH).

4.4 Summary and Conclusions

This chapter presented the modeling, experimental validation, and performance assessment of a railgun-based actuator for ultrafast mechanical circuit breaker applications. A hierarchical modeling strategy was adopted, progressing from analytical formulations to quasi-static and fully transient multiphysics simulations, and ultimately validated through experiments.

At the analytical level, simplified electromagnetic and mechanical models were developed to gain physical insight into the railgun actuation principle. Despite relying on idealized assumptions, these models provided useful guidance for parameter scaling, sensitivity analysis, and preliminary design choices. Building on this foundation, a quasi-static electromagnetic model was employed to evaluate current density, magnetic field, and Lorentz force distributions as a function of armature position. This enabled the extraction of position-dependent electromagnetic force profiles, which were used in a reduced-order dynamic model, offering a good balance between accuracy and computational efficiency.

The main contribution of the chapter is the development of a fully transient multiphysics model coupling three-dimensional electromagnetic fields, mechanical motion, and heat transfer. Since the electromagnetic problem is solved in a full 3D geometry, curl-conforming (edge) elements were required to correctly solve Maxwell's equations. This constraint precludes the use of classical Moving Mesh (ALE) approaches based on sliding domains, as these rely on source–destination or identity-pair boundary conditions that would overconstrain the electromagnetic formulation. Instead, a geometry-deformation-based approach was adopted to describe the armature motion while preserving inherent field continuity. Mesh quality was ensured through periodic remeshing based on element distortion criteria.

Friction was explicitly modeled as a dominant loss mechanism using a Coulomb-type law with a constant friction coefficient. The simulations showed that friction strongly limits actuator performance, significantly reducing acceleration and peak speed. The model reproduced the experimentally measured armature displacement and velocity with deviations below 0.1 mm under dry-friction conditions, with the best agreement obtained for a friction coefficient of $\mu = 0.95$. Nevertheless, a key limitation of the model is the assumption of constant friction. Experimental observations indicate that, once melting occurs at the rail–armature interface, molten aluminum acts as a self-lubricant, leading to a sharp reduction in effective friction. Although a temperature-dependent friction law could capture this behavior, the use of curl-conforming elements enforces strict interface conditions defined by Maxwell's equations, requiring the rail–armature interface to be treated as a single shared boundary. This prevents straightforward evaluation of contact temperature and local Joule heating. More advanced interface modeling strategies were therefore considered beyond the scope of this work.

Experimental validation confirmed the high performance of the actuator. The armature reached a displacement of approximately 21 mm at $t = 400\,\mu\text{s}$, while the required breaker stroke of 15 mm was achieved in about 300 µs. The experimentally derived velocity profile showed a peak speed of approximately $106\,\text{m}/\text{s}$, far exceeding that of conventional electromagnetic actuators. The influence of preload force was also investigated. Although reducing preload initially improves acceleration by lowering friction, experiments demonstrated that insufficient preload increases electrical contact resistance and leads to intermittent contact loss and arcing. As a result, the lower preload configuration (392 N per rail) exhibited inferior performance and significantly higher rail damage compared to the higher preload case (490 N per rail), highlighting the need to balance mechanical and electrical considerations.

Finally, system-level simulations incorporating the experimentally measured armature displacement were used to evaluate breaker performance under realistic grid conditions. For system inductances of $\text{L}_\text{s} = 10\,\mu\text{H}$, $\text{L}_\text{s} = 50\,\mu\text{H}$, and $\text{L}_\text{s} = 100\,\mu\text{H}$, current interruption was achieved within approximately 420 µs, 580 µs, and 700 µs, respectively, with peak currents limited to 11.5 kA, 3.9 kA, and 2.6 kA. These results significantly outperform state-of-the-art pyrofuses and exceed the performance reported for Thomson-coil-based actuators.

In summary, Chapter 4 demonstrates that the proposed railgun-based actuator is a highly effective solution for ultrafast mechanical circuit breakers. The combined modeling and experimental results confirm its feasibility, robustness, and clear performance advantage over existing technologies, while also identifying friction and contact phenomena as the primary factors limiting further improvements.

Chapter 5

Conclusions and Future Work

This chapter provides a consolidated overview of the main topics addressed throughout the thesis. In addition, it outlines potential directions for future research that could further extend and complement the present work.

5.1 Conclusions

In this thesis, the modeling and design of a railgun-driven electromagnetic actuator for ultrafast LVDC circuit breakers are addressed. It is shown that the proposed railgun-based actuation concept outperforms the fastest single-use current interruption technology reported in the state of the art, namely the pyrofuse, and provides a significantly faster dynamic response than Thomson-coil–based actuators commonly employed in ultrafast circuit breakers.

Chapter 1 established the motivation and reviewed the state of the art of circuit breaker technologies with a focus on LVDC systems. It highlighted the intrinsic difficulty of DC current interruption due to the absence of natural current zero crossings and the typically low inductance of DC networks, which leads to very high fault current rise rates. Solid-state circuit breakers were identified as the fastest solution, achieving interruption times below $10\,\mu s$, but suffering from high conduction losses, lack of galvanic isolation, and unfavorable failure modes. Hybrid breakers reduce some of these drawbacks at the cost of increased complexity, while mechanical circuit breakers remain the most robust and cost-effective solution but are fundamentally limited by actuator speed. The analysis identified ultrafast actuation as the key enabler for next-generation mechanical circuit breakers and established the pyrofuse as the performance benchmark for single-use interruption.

Chapter 2 presented a system-level simulation of an 800 V, 800 A LVDC protection scenario representative of ultrafast electric vehicle charging applications. The results demonstrated that system inductance strongly affects fault evolution: lower inductance leads to higher peak currents but shorter interruption times, placing stringent requirements on actuator dynamics. It was further shown that increasing actuator speed not only shortens interruption time and limits peak current, but also significantly reduces the energy dissipated in the breaker, enabling a reduction in arc chamber size and improving overall efficiency.

Chapter 3 focused on the pulse-power electric drive supplying the railgun actuator. The developed drive delivers up to 165 kA within 22 µs, with a maximum $\mathrm{d}i/\mathrm{d}t$ of 12 kA/µs. Distributed-gate thyristors were shown to be well suited for this application, while a standard rectifier diode is sufficient for freewheeling operation. Due to the extremely low impedance of the railgun load, parasitic resistance and inductance dominate the current waveform, making layout optimization critical. The realized drive exhibits 88 nH of stray inductance and 0.6 mΩ of parasitic resistance. In particular, the stray inductance between the capacitor bank and the freewheeling diode was identified as a major efficiency-limiting factor, as its stored magnetic energy is dissipated in the diode rather than transferred to the railgun.

Chapter 4 investigated the railgun actuator through analytical modeling, quasistatic and fully transient multiphysics simulations, and experimental validation. An energy-based analytical model provided physical insight but overestimated the electromagnetic force. A quasistatic model improved accuracy by computing the force as a function of current and armature position and coupling it to the mechanical dynamics. A three-dimensional transient multiphysics model, including electromagnetic fields, heat transfer, mechanical motion, and friction, enabled accurate prediction of current distribution, magnetic field, and temperature rise. Friction was shown to severely limit performance, with C-shaped armatures and small rail spacing exacerbating transversal forces. A mechanical preload was required to maintain electrical contact. Experimental results validated the model with an armature position error of approximately 0.1 mm. The prototype achieved 15 mm displacement in 300 µs and a peak speed of 106 m/s. System-level simulations using measured armature motion showed interruption times between 420 µs and 700 µs for system inductances from

10 µH to 100 µH, significantly outperforming pyrofuses and exceeding the response of Thomson-coil–based actuators.

Overall, this thesis demonstrates that railgun-based electromagnetic actuation is a viable and high-performance solution for ultrafast LVDC mechanical circuit breakers. By combining system-level analysis, dedicated pulse-power drive design, multiphysics modeling, and experimental validation, it is shown that actuation speed is the key factor enabling reduced interruption time and energy dissipation, while preserving the inherent advantages of mechanical breakers.

5.2 Future Work

Several directions for future research emerge from the results of this thesis and could further enhance the performance, efficiency, and practical applicability of railgun-driven ultrafast LVDC circuit breakers.

From the perspective of the electric drive, a promising improvement consists in replacing the distributed-gate thyristor with a triggered spark gap as the main switching element. Triggered spark gaps offer significantly faster turn-on times, typically below 100 ns, compared to approximately 30 µs for distributed-gate thyristors. In addition, spark gaps do not impose intrinsic $\mathrm{d}i/\mathrm{d}t$ limitations and are generally more compact and cost-effective. Their reduced physical size would allow a substantial reduction of the current loop area, leading to lower stray inductance and, consequently, higher energy transfer efficiency and improved drive performance.

Regarding modeling, the accuracy of the railgun actuator model could be further improved by incorporating a detailed description of temperature evolution in the rail–armature contact regions. An explicit thermo-electrical contact model would enable the prediction of local temperature rise and its influence on contact resistance and friction behavior. This extension would allow the transition from dry to lubricated friction regimes to be captured more realistically, improving the predictive capability of the multiphysics simulations under extreme operating conditions.

From a design standpoint, significant performance gains are expected from modifying the armature geometry. Replacing the C-shaped armature with a rectangular cross-section would reduce transversal electromagnetic forces acting on the armature, thereby lowering the normal contact force and associated friction losses. In addition, increasing the separation between the rails would further reduce repulsive transversal forces, allowing the preload force required to maintain electrical contact to be decreased. The combined effect of these design changes would be a reduction in friction losses and an increase in achievable acceleration and efficiency.

Beyond the basic railgun configuration investigated in this work, alternative railgun topologies should be explored. In particular, quadrupole and augmented railgun configurations offer the potential to improve force uniformity, reduce current crowding, and mitigate mechanical stress on the rails and armature. A comparative assessment of these topologies in the context of ultrafast actuation for circuit breakers would provide valuable insight into their suitability and scalability.

Finally, future work should focus on the complete design, construction, and experimental testing of a railgun-driven circuit breaker prototype. This includes the integration of the actuator with a realistic arc chamber, insulation system, and mechanical housing, as well as validation under representative fault conditions. Such a demonstrator would represent a crucial step toward assessing long-term reliability, manufacturability, and system-level integration in practical LVDC applications.

References

[1] D. Siderov, R. Stanev, K. Viglov, V. Efthymiou, C. Charalambous, S. Khadem, and S. Patra, "A Review of State of the Art Low Voltage Direct Current Networks Development," in *2022 14th Electrical Engineering Faculty Conference (BulEF)*, Sep. 2022, pp. 1–8, iSSN: 2831-5782. [Online]. Available: https://ieeexplore.ieee.org/document/10021199/

[2] T. Dragicevic, J. C. Vasquez, J. M. Guerrero, and D. Skrlec, "Advanced LVDC Electrical Power Architectures and Microgrids: A step toward a new generation of power distribution networks," *IEEE Electrification Magazine*, vol. 2, no. 1, pp. 54–65, Mar. 2014. [Online]. Available: https://ieeexplore.ieee.org/document/6774539/

[3] P. Nuutinen, T. Kaipia, P. Peltoniemi, A. Lana, A. Pinomaa, A. Mattsson, P. Silventoinen, J. Partanen, J. Lohjala, and M. Matikainen, "Research Site for Low-Voltage Direct Current Distribution in a Utility Network—Structure, Functions, and Operation," *IEEE Transactions on Smart Grid*, vol. 5, no. 5, pp. 2574–2582, Sep. 2014. [Online]. Available: https://ieeexplore.ieee.org/document/6777363/

[4] V. A. K. Prabhala, B. P. Baddipadiga, and M. Ferdowsi, "DC distribution systems — An overview," in *2014 International Conference on Renewable Energy Research and Application (ICRERA)*, Oct. 2014, pp. 307–312. [Online]. Available: https://ieeexplore.ieee.org/document/7016575/

[5] T. Dragičević, X. Lu, J. C. Vasquez, and J. M. Guerrero, "DC Microgrids—Part I: A Review of Control Strategies and Stabilization Techniques," *IEEE Transactions on Power Electronics*, vol. 31, no. 7, pp. 4876–4891, Jul. 2016. [Online]. Available: https://ieeexplore.ieee.org/document/7268934/

[6] H. Kakigano, Y. Miura, T. Ise, and R. Uchida, "DC micro-grid for super high quality distribution — System configuration and control of distributed generations and energy storage devices," in *2006 37th IEEE Power Electronics Specialists Conference*, Jun. 2006, pp. 1–7, iSSN: 2377-6617. [Online]. Available: https://ieeexplore.ieee.org/document/1712250/

[7] A. Sannino, G. Postiglione, and M. Bollen, "Feasibility of a DC network for commercial facilities," *IEEE Transactions on Industry*

Applications, vol. 39, no. 5, pp. 1499–1507, Sep. 2003. [Online]. Available: https://ieeexplore.ieee.org/document/1233614/

[8] K. C. Lee, A. Ukil, and Y.-M. Yeap, "Short-circuit protection for MV & LVDC grid," in *2014 IEEE PES Asia-Pacific Power and Energy Engineering Conference (APPEEC)*, Dec. 2014, pp. 1–6, iSSN: 2157-4847. [Online]. Available: https://ieeexplore.ieee.org/document/7065999/

[9] Y. Wu, T. Ma, L. Hou, T. Qi, Z. Wang, J. Yan, and H. Ma, "Research on Fault Isolation Technology and Device Development of LVDC System," in *2021 IEEE/IAS Industrial and Commercial Power System Asia (I&CPS Asia)*, Jul. 2021, pp. 1086–1091. [Online]. Available: https://ieeexplore.ieee.org/document/9621628/

[10] J. Yang, "Protection issue discussion of DC network development: Circuit breaker or fault-tolerant converter," in *11th IET International Conference on Developments in Power Systems Protection (DPSP 2012)*, Apr. 2012, pp. 1–6. [Online]. Available: https://ieeexplore.ieee.org/document/6227573/

[11] C. M. Franck, "HVDC Circuit Breakers: A Review Identifying Future Research Needs," *IEEE Transactions on Power Delivery*, vol. 26, no. 2, pp. 998–1007, Apr. 2011. [Online]. Available: https://ieeexplore.ieee.org/document/5686894/

[12] A. A. S. Emhemed and G. M. Burt, "An Advanced Protection Scheme for Enabling an LVDC Last Mile Distribution Network," *IEEE Transactions on Smart Grid*, vol. 5, no. 5, pp. 2602–2609, Sep. 2014. [Online]. Available: https://ieeexplore.ieee.org/document/6861452/

[13] A. Virdag, N. A. Khan, T. Hager, and R. W. DeDoncker, "Performance Analysis of Hybrid DC Circuit Breaker based on Counter-Current Injection Method for Low-Voltage DC Grids," in *2019 IEEE Third International Conference on DC Microgrids (ICDCM)*, May 2019, pp. 1–6. [Online]. Available: https://ieeexplore.ieee.org/document/9232682/

[14] U. Tahir, W. Abdullah, and L. Ali, "Design and Development of Solid-state DC Circuit Breaker," in *2022 International Conference on Electrical Engineering and Sustainable Technologies (ICEEST)*, Dec. 2022, pp. 1–8. [Online]. Available: https://ieeexplore.ieee.org/document/10077870/

[15] X. Pei, O. Cwikowski, D. S. Vilchis-Rodriguez, M. Barnes, A. C. Smith, and R. Shuttleworth, "A review of technologies for MVDC circuit breakers," in *IECON 2016 - 42nd Annual Conference of the IEEE Industrial Electronics Society*, Oct. 2016, pp. 3799–3805. [Online]. Available: https://ieeexplore.ieee.org/document/7793492/

[16] S. Glaser and D. Westermann, "Investigation of Operating Point Setting and Stability Behavior of LVDC Arc Flashes," in *2024 IEEE PES Innovative Smart Grid Technologies Europe (ISGT EUROPE)*, Oct. 2024, pp. 1–6. [Online]. Available: https://ieeexplore.ieee.org/document/10863658/

[17] Q. Guo, J. Zhang, and T. Chi, “Review of DC Circuit Breaker Technology,” in *2022 IEEE Sustainable Power and Energy Conference (iSPEC)*, Dec. 2022, pp. 1–5. [Online]. Available: https://ieeexplore.ieee.org/document/10033027/

[18] A. N. Greenwood and T. H. Lee, “Theory and Application of the Commutation Principle for HVDC Circuit Breakers,” *IEEE Transactions on Power Apparatus and Systems*, vol. PAS-91, no. 4, pp. 1570–1574, Jul. 1972. [Online]. Available: https://ieeexplore.ieee.org/document/4074890/

[19] T. Senda, T. Tamagawa, K. Higuchi, T. Horiuchi, and S. Yanabu, “Development of HVDC Circuit Breaker Based on Hybrid Interruption Scheme,” *IEEE Transactions on Power Apparatus and Systems*, vol. PAS-103, no. 3, pp. 545–552, Mar. 1984. [Online]. Available: https://ieeexplore.ieee.org/document/4112552/

[20] X. Leishi, S. Chao, and L. Qifu, “Research on Short-Circuit Test and Simulation of CSG First Mechanical HVDC Circuit Breaker in VSC-HVDC,” in *2018 International Conference on Power System Technology (POWERCON)*, Nov. 2018, pp. 2764–2769. [Online]. Available: https://ieeexplore.ieee.org/document/8601627/

[21] T. Schultz, B. Hammerich, L. Bort, and C. M. Franck, “Improving interruption performance of mechanical circuit breakers by controlling pre-current-zero wave shape,” *High Voltage*, vol. 4, no. 2, pp. 122–129, Jun. 2019. [Online]. Available: https://ietresearch.onlinelibrary.wiley.com/doi/10.1049/hve.2018.5103

[22] T. Schultz, P. Herzog, and C. M. Franck, “Current Injection Circuit Breakers for HVDC: Overview on Improved Injection Circuits,” in *2019 5th International Conference on Electric Power Equipment - Switching Technology (ICEPE-ST)*, Oct. 2019, pp. 253–258, iSSN: 2643-9816. [Online]. Available: https://ieeexplore.ieee.org/document/8928888/

[23] J. J. Shea, “Low voltage power distribution level DC circuit breaking,” in *2017 4th International Conference on Electric Power Equipment - Switching Technology (ICEPE-ST)*, Oct. 2017, pp. 187–194. [Online]. Available: https://ieeexplore.ieee.org/document/8188825/

[24] C. Dassanayake, N. Kularatna, A. Steyn-Ross, N. Gurusinghe, and K. Gunawardane, “Arc Characteristics in Multiple Pole DC Circuit Breakers,” in *2023 IEEE Fifth International Conference on DC Microgrids (ICDCM)*, vol. Single, Nov. 2023, pp. 1–6. [Online]. Available: https://ieeexplore.ieee.org/document/10433616/

[25] C. Xu, T. Damle, and L. Graber, “A Survey on Mechanical Switches for Hybrid Circuit Breakers,” in *2019 IEEE Power & Energy Society General Meeting (PESGM)*, Aug. 2019, pp. 1–5, iSSN: 1944-9933. [Online]. Available: https://ieeexplore.ieee.org/document/8973674/

[26] P. Weaver, K. Pechrach, and J. McBride, “Arc root mobility on piezoelectrically actuated contacts in miniature circuit breakers,” *IEEE Transactions on Components and Packaging Technologies*, vol. 28, no. 4, pp. 734–740, Dec. 2005. [Online]. Available: https://ieeexplore.ieee.org/document/1546182/

[27] W. Holaus and K. Frohlich, “Ultra-fast switches- a new element for medium voltage fault current limiting switchgear,” in *2002 IEEE Power Engineering Society Winter Meeting. Conference Proceedings (Cat. No.02CH37309)*, vol. 1, Jan. 2002, pp. 299–304 vol.1. [Online]. Available: https://ieeexplore.ieee.org/document/985002/

[28] A. Bissal, J. Magnusson, and G. Engdahl, “Comparison of Two Ultra-Fast Actuator Concepts,” *IEEE Transactions on Magnetics*, vol. 48, no. 11, pp. 3315–3318, Nov. 2012. [Online]. Available: https://ieeexplore.ieee.org/document/6332648/

[29] A. Al-Qarni and A. EL-Refaie, “Design and Analysis of Double-Sided Thomson Coil Actuator for Extra Fast Opening Operation,” in *2021 IEEE Energy Conversion Congress and Exposition (ECCE)*, Oct. 2021, pp. 4361–4368, iSSN: 2329-3748. [Online]. Available: https://ieeexplore.ieee.org/document/9595133/

[30] R. Rodrigues, Y. Du, A. Antoniazzi, and P. Cairoli, “A Review of Solid-State Circuit Breakers,” *IEEE Transactions on Power Electronics*, vol. 36, no. 1, pp. 364–377, Jan. 2021. [Online]. Available: https://ieeexplore.ieee.org/document/9120203/

[31] L. Rubino, G. Rubino, P. Marino, L. P. Di Noia, and R. Rizzo, “Universal Circuit Breaker for PV power plants,” in *2017 6th International Conference on Clean Electrical Power (ICCEP)*, Jun. 2017, pp. 750–755, iSSN: 2474-9664. [Online]. Available: https://ieeexplore.ieee.org/document/8004775/

[32] G. D. Demetriades, W. Hermansson, J. R. Svensson, K. Papastergiou, and T. Larsson, “DC-breaker for a multi-megawatt Battery Energy Storage System,” in *2014 International Power Electronics Conference (IPEC-Hiroshima 2014 - ECCE ASIA)*, May 2014, pp. 1220–1226, iSSN: 2150-6086. [Online]. Available: https://ieeexplore.ieee.org/document/6869742/

[33] D. A. Molligoda, P. Chatterjee, C. J. Gajanayake, A. K. Gupta, and K. J. Tseng, “Review of design and challenges of DC SSPC in more electric aircraft,” in *2016 IEEE 2nd Annual Southern Power Electronics Conference (SPEC)*, Dec. 2016, pp. 1–5. [Online]. Available: https://ieeexplore.ieee.org/document/7846117

[34] K. Tan, P. Liu, X. Ni, C. Peng, X. Song, and A. Q. Huang, “Performance evaluation of multiple Si and SiC solid state devices for circuit breaker application in 380VDC delivery system,” in *2016 IEEE Applied Power Electronics Conference and Exposition (APEC)*, Mar. 2016, pp. 983–989. [Online]. Available: https://ieeexplore.ieee.org/document/7467990

[35] Z. J. Shen, Z. Miao, A. M. Roshandeh, P. Moens, H. Devleeschouwer, A. Salih, B. Padmanabhan, and W. Jeon, “First experimental demonstration of solid state circuit breaker (SSCB) using 650V GaN-based monolithic bidirectional switch,” in *2016 28th International Symposium on Power Semiconductor Devices and ICs (ISPSD)*, Jun. 2016, pp. 79–82, iSSN: 1946-0201. [Online]. Available: https://ieeexplore.ieee.org/document/7520782/

[36] D. P. Urciuoli, D. Ibitayo, G. Koebke, G. Ovrebo, and R. Green, “A compact 100-A, 850-V, silicon carbide solid-state DC circuit breaker,” in *2016 IEEE Energy Conversion Congress and Exposition (ECCE)*, Sep. 2016, pp. 1–5. [Online]. Available: https://ieeexplore.ieee.org/document/7854656/

[37] M. Kempkes, I. Roth, and M. Gaudreau, “Solid-state circuit breakers for Medium Voltage DC power,” in *2011 IEEE Electric Ship Technologies Symposium*, Apr. 2011, pp. 254–257. [Online]. Available: https://ieeexplore.ieee.org/document/5770877/

[38] P. Cairoli, L. Qi, C. Tschida, V. R. Ramanan, L. Raciti, and A. Antoniazzi, “High Current Solid State Circuit Breaker for DC Shipboard Power Systems,” in *2019 IEEE Electric Ship Technologies Symposium (ESTS)*, Aug. 2019, pp. 468–476. [Online]. Available: https://ieeexplore.ieee.org/document/8847815/

[39] J.-Y. Kim, S.-S. Choi, and I.-D. Kim, “A novel reclosing and rebreaking AC thyristor circuit breaker,” in *2015 9th International Conference on Power Electronics and ECCE Asia (ICPE-ECCE Asia)*, Jun. 2015, pp. 2574–2581, iSSN: 2150-6086. [Online]. Available: https://ieeexplore.ieee.org/document/7168137/

[40] J. Hayes, K. George, P. Killeen, B. McPherson, K. J. Olejniczak, and T. R. McNutt, “Bidirectional, SiC module-based solid-state circuit breakers for 270 Vdc MEA/AEA systems,” in *2016 IEEE 4th Workshop on Wide Bandgap Power Devices and Applications (WiPDA)*, Nov. 2016, pp. 70–77. [Online]. Available: https://ieeexplore.ieee.org/document/7799912/

[41] Y. He, C. Xu, Y. Li, and F. Z. Peng, “A Survey of Hybrid Circuit Breakers: Component-Level Insights to System-Wide Integration,” *IEEE Open Journal of Power Electronics*, vol. 5, pp. 513–533, 2024. [Online]. Available: https://ieeexplore.ieee.org/document/10478126/

[42] D. Bösche, P. Vieth, F. Anspach, E. Peters, E.-D. Wilkening, and M. Kurrat, “Test Setup Design for Measuring the Conductance in the Mechanical Part of Hybrid-Circuit-Breakers Before and After Current Commutation,” *IEEE Access*, vol. 9, pp. 165 262–165 270, 2021. [Online]. Available: https://ieeexplore.ieee.org/document/9648192/

[43] P. van Gelder and J. Ferreira, “Zero volt switching hybrid DC circuit breakers,” in *Conference Record of the 2000 IEEE Industry Applications Conference. Thirty-Fifth IAS Annual Meeting and World Conference on Industrial Applications of Electrical Energy (Cat. No.00CH37129)*, vol. 5,

Oct. 2000, pp. 2923–2927 vol.5, iSSN: 0197-2618. [Online]. Available: https://ieeexplore.ieee.org/document/882581/

[44] Y. He, Q. Yang, Y. Li, S. Kim, F. Z. Peng, M. Bosworth, L. Wang, Z. Jin, Y. Shi, N. Bonaventura, M. Steurer, C. Xu, and L. Graber, "Control Development and Fault Current Commutation Test for the EDISON Hybrid Circuit Breaker," *IEEE Transactions on Power Electronics*, vol. 38, no. 7, pp. 8851–8865, Jul. 2023. [Online]. Available: https://ieeexplore.ieee.org/document/10083235/

[45] T. Nakano, R. Sasaki, W. Ohnishi, Y. Yamano, and Y. Inada, "Active Control of Pyrofuse in Circuit Breaker with State Estimation of Current-Limiting Fuse," in *IECON 2024 - 50th Annual Conference of the IEEE Industrial Electronics Society*, Nov. 2024, pp. 1–6. [Online]. Available: https://ieeexplore.ieee.org/document/10905289/

[46] T. Sakuraba, R. Ouaida, S. Chen, and T. Chailloux, "Evaluation of Novel Hybrid Protection Based on Pyroswitch and Fuse Technologies," in *2018 International Power Electronics Conference (IPEC-Niigata 2018 -ECCE Asia)*, May 2018, pp. 2153–2157. [Online]. Available: https://ieeexplore.ieee.org/document/8507793/

[47] F. Gómez de León, A. Bissal, M. Repetto, and F. Freschi, "A Novel Railgun-Based Actuation System for Ultrafast DC Circuit Breakers in EV Fast-Charging Applications," *World Electric Vehicle Journal*, vol. 16, no. 9, p. 514, Sep. 2025, publisher: Multidisciplinary Digital Publishing Institute. [Online]. Available: https://www.mdpi.com/2032-6653/16/9/514

[48] B. Li, Z. Kang, C. Su, L. Wu, S. Xiong, N. Duan, and C. Wang, "Influence of Temperature and Air Pressure on Arc Characteristics of Horizontal Air Insulated Disconnector," in *2022 IEEE International Conference on High Voltage Engineering and Applications (ICHVE)*, Sep. 2022, pp. 1–4, iSSN: 2474-3852. [Online]. Available: https://ieeexplore.ieee.org/document/9961341/

[49] Autoliv, "Pyro Safety Switch PSS-5 Datasheet," Feb. 2025. [Online]. Available: https://www.autoliv.com/sites/autoliv/files/2025-02/PSS-5_2.pdf

[50] Eaton, "Eaton Bussmann series EV pyro fuses Datasheet," Feb. 2025. [Online]. Available: https://www.eaton.com/content/dam/eaton/products/emobility/power-distribution-protection/power-distribution-unit/eaton-pyro-fuse-data-sheet.pdf

[51] Mersen, "Catalog of DC Fuse and Pyrofuse for EV/HEV Battery and Auxiliary Overcurrent Protection," Dec. 2020. [Online]. Available: https://de.mersen.com/sites/default/files/files_imported_ep/DC-Fuse-and-Pyrofuse-for-EV-HEV-Mersen-EN.pdf

[52] P. Wienkamp, N. Langenberg, S. Kimpeler, T. Ballweber, and A. Moser, "Coil Design Study of Ultrafast Thomson Coil Actuator," in *2022 IEEE 7th Southern Power Electronics Conference (SPEC)*, Dec. 2022, pp. 1–5, iSSN: 2832-2983. [Online]. Available: https://ieeexplore.ieee.org/document/10058377/

[53] A. Bissal, “Modeling and Verification of Ultra-Fast Electro-Mechanical Actuators for HVDC Breakers,” Ph.D. dissertation, KTH Royal Institute of Technology, Stockholm, Sweden, 2015.

[54] D. Vilchis-Rodriguez, R. Shuttleworth, and M. Barnes, “Finite element analysis and efficiency improvement of the Thomson coil actuator,” in *8th IET International Conference on Power Electronics, Machines and Drives (PEMD 2016)*, Apr. 2016, pp. 1–6. [Online]. Available: https://ieeexplore.ieee.org/document/7739390/

[55] D. S. Vilchis-Rodriguez, R. Shuttleworth, and M. Barnes, “Experimental validation of a finite element 2D axial thomson coil model with inductance and resistance compensation,” in *13th IET International Conference on AC and DC Power Transmission (ACDC 2017)*, Feb. 2017, pp. 1–6. [Online]. Available: https://ieeexplore.ieee.org/document/7934961/

[56] S. H. Park, H. J. Jang, J. K. Chong, and W. Y. Lee, “Dynamic analysis of Thomson coil actuator for fast switch of HVDC circuit breaker,” in *2015 3rd International Conference on Electric Power Equipment – Switching Technology (ICEPE-ST)*, Oct. 2015, pp. 425–430. [Online]. Available: https://ieeexplore.ieee.org/document/7368444/

[57] F. Song, F. Li, B. Zhang, M. Zhu, C. Li, G. Wang, H. Gong, Y. Gan, X. Jin, B. M. Novac, and I. R. Smith, “Analysis of the Optimal Operation Frequency With Lowest Time-Delay Jitter for an Electrically Triggered Field-Distortion Spark Gap,” *IEEE Transactions on Plasma Science*, vol. 47, no. 10, pp. 4708–4712, Oct. 2019. [Online]. Available: https://ieeexplore.ieee.org/document/8832195/

[58] Y. Bacqueyrisses, B. Guegan, F. Bayol, and D. Arnal, “Comparative Study of Two Types of Spark Gap Switches for Parallel Triggering,” in *2024 10th Euro-Asian Pulsed Power Conference, 25th International Conference on High-Power Particle Beams and 20th International Symposium on Electromagnetic Launch Technology (EAPPC/BEAMS/EML)*, Sep. 2024, pp. 1–2. [Online]. Available: https://ieeexplore.ieee.org/document/10748064/

[59] C. S. Reddy, A. Sharma, and K. C. Mittal, “Experimental Investigations Into Pulse-Charged Spark Gap Recovery Times and Influencing Factors,” *IEEE Transactions on Plasma Science*, vol. 44, no. 3, pp. 331–337, Mar. 2016. [Online]. Available: https://ieeexplore.ieee.org/document/7368932/

[60] H. Rahaman, J. W. Nam, S. H. Nam, and K. Frank, “Investigation of Spark-Gap Discharge in a Regime of Very High Repetition Rate,” *IEEE Transactions on Plasma Science*, vol. 38, no. 10, pp. 2752–2757, Oct. 2010. [Online]. Available: https://ieeexplore.ieee.org/document/5497195/

[61] P. Osmokrovid and K. Rasovic, “Optimization Of The Three-electrode Spark Gap Characteristics,” in *Eighth IEEE International Conference on Pulsed Power*, Jun. 1991, pp. 859–862. [Online]. Available: https://ieeexplore.ieee.org/document/733418/

[62] P. Osmokrovic, N. Arsic, and N. Kartalovic, “Triggered three-electrode spark gaps,” in *Digest of Technical Papers. Tenth IEEE International Pulsed Power Conference*, vol. 2, Jul. 1995, pp. 822–827 vol.2. [Online]. Available: https://ieeexplore.ieee.org/document/599713/

[63] B. J. Baliga, “Thyristors,” in *Fundamentals of Power Semiconductor Devices*, B. J. Baliga, Ed. Cham: Springer International Publishing, 2019, pp. 641–753. [Online]. Available: https://doi.org/10.1007/978-3-319-93988-9_8

[64] M. P. GmbH, “Distributed Gate Thyristors for Induction Power Supply Applications (Application Note),” 2000. [Online]. Available: https://www.rellpower.com/wp/wp-content/uploads/2018/03/MS-Power-GmbH-Distributed-Gate-Thyristors.pdf

[65] M. Forouzesh, Y. P. Siwakoti, S. A. Gorji, F. Blaabjerg, and B. Lehman, “Step-Up DC–DC Converters: A Comprehensive Review of Voltage-Boosting Techniques, Topologies, and Applications,” *IEEE Transactions on Power Electronics*, vol. 32, no. 12, pp. 9143–9178, Dec. 2017. [Online]. Available: https://ieeexplore.ieee.org/document/7872494/

[66] F. G. De León, K. Joshi, A. Bissal, W. Ali, and M. Repetto, “Utilization of a Snubber Capacitor in a 1 kV Flyback Converter to Optimize the Charging of a Capacitor Bank,” in *IECON 2023- 49th Annual Conference of the IEEE Industrial Electronics Society*, Oct. 2023, pp. 1–6, iSSN: 2577-1647. [Online]. Available: https://ieeexplore.ieee.org/document/10311653/

[67] C. Adragna, “AN1326 APPLICATION NOTE,” Nov. 2002. [Online]. Available: https://www.st.com/resource/en/application_note/an1326-l6565-quasiresonant-controller-stmicroelectronics.pdf

[68] K. Gwan-Bon, “Application Note AN4147 Design Guidelines for RCD Snubber of Flyback,” Jun. 2005.

[69] STMicroelectronics, “Application Note AN443 Series Operation Of Fast Rectifiers,” May 2025. [Online]. Available: https://www.st.com/resource/en/application_note/an443-series-operation-on-fast-rectifiers-stmicroelectronics.pdf

[70] J. Gallant, T. Vancaeyzeele, B. Lauwens, B. Wild, F. Alouahabi, and M. Schneider, “Design Considerations for an Electromagnetic Railgun Firing Intelligent Bursts to Be Used Against Antiship Missiles,” *IEEE Transactions on Plasma Science*, vol. 43, no. 5, pp. 1179–1184, May 2015. [Online]. Available: https://ieeexplore.ieee.org/document/7094309/

[71] J. Han, Y. Pan, and J. He, “Study of Employing Railguns in Close-in Weapon Systems,” *IEEE Transactions on Magnetics*, vol. 45, no. 1, pp. 641–644, Jan. 2009. [Online]. Available: https://ieeexplore.ieee.org/document/4774053

[72] J. Domin, “Hybrid electromagnetic launcher with pneumatic assist — Influence of coil-gun “switch on” and “switch off” time upon missile velocity,” in *2016 13th Selected Issues of Electrical Engineering and Electronics (WZEE)*, May 2016, pp. 1–4. [Online]. Available: https://ieeexplore.ieee.org/document/7800212

[73] S. Yang, M. Chagas, J. Ordonez, and J. Vargas, “Multiphysics model of a notional all-electric ship railgun — Model development and application,” in *2017 IEEE Electric Ship Technologies Symposium (ESTS)*, Aug. 2017, pp. 285–291. [Online]. Available: https://ieeexplore.ieee.org/document/8069295

[74] P. Lehmann, B. Reck, M. D. Vo, and J. Behrens, “Acceleration of a Suborbital Payload Using an Electromagnetic Railgun,” *IEEE Transactions on Magnetics*, vol. 43, no. 1, pp. 480–485, Jan. 2007. [Online]. Available: https://ieeexplore.ieee.org/document/4033071/

[75] I. R. McNab, G. V. Candler, and C. S. Barbee, “Projectile Nosetip Thermal Management for Railgun Launch to Space,” *IEEE Transactions on Magnetics*, vol. 43, no. 1, pp. 491–495, Jan. 2007. [Online]. Available: https://ieeexplore.ieee.org/document/4033079

[76] N. Kawashima, A. Yamori, M. Yanagisawa, H. Kubo, M. Kohno, and S. Teii, “Stable and reproducible production of high velocity projectile in ISAS railgun (HYPAC),” *IEEE Transactions on Magnetics*, vol. 29, no. 1, pp. 431–434, Jan. 1993. [Online]. Available: https://ieeexplore.ieee.org/document/195613

[77] Z. Wang, S. He, Y. Wen, Z. Zhan, and F. Liu, “Launch process of augmented electromagnetic railgun under nonideal condition,” in *2012 16th International Symposium on Electromagnetic Launch Technology*, May 2012, pp. 1–4. [Online]. Available: https://ieeexplore.ieee.org/document/6325133/

[78] S. Song and C. Cheng, “Measurement of Solid Armature’s In-Bore Velocity Using B-Dot Probes in a Series-Augmented Railguns,” *IEEE Transactions on Plasma Science*, vol. 43, no. 5, pp. 1310–1315, May 2015. [Online]. Available: https://ieeexplore.ieee.org/document/7073647/

[79] X. Fu, D. Zhang, W. Yuan, and P. Yan, “Design and Analysis of the 270-kJ PPS for Augmented Railgun,” *IEEE Transactions on Plasma Science*, vol. 45, no. 7, pp. 1496–1502, Jul. 2017. [Online]. Available: https://ieeexplore.ieee.org/document/7972039/

[80] A. Keshtkar, L. Gharib, M. S. Bayati, and M. Abbasi, “Simulation of a Two-Turn Railgun and Comparison Between a Conventional Railgun and a Two-Turn Railgun by 3-D FEM,” *IEEE Transactions on Plasma Science*, vol. 41, no. 5, pp. 1392–1397, May 2013. [Online]. Available: https://ieeexplore.ieee.org/document/6497647/

[81] Y. Zhang, J. Ruan, S. Liu, X. Yang, Y. Zhang, and D. Wang, “Salvo Performance Analysis of Double-Projectile Railgun,” *IEEE Transactions on*

Plasma Science, vol. 39, no. 1, pp. 203–209, Jan. 2011. [Online]. Available: https://ieeexplore.ieee.org/document/5575448/

[82] T. Watt and M. Crawford, "Experimental Results From a Two-Turn 40-mm Railgun," *IEEE Transactions on Magnetics*, vol. 45, no. 1, pp. 490–494, Jan. 2009. [Online]. Available: https://ieeexplore.ieee.org/document/4773637/

[83] Y. Zhang, M. Sun, and P. Guo, "Comparison of performances between stack and plane turn-augmented railgun," in *2011 International Conference on Electrical and Control Engineering*, Sep. 2011, pp. 121–124. [Online]. Available: https://ieeexplore.ieee.org/document/6056998/

[84] Z. Yang, G. Feng, S. Liu, and J. Shi, "Performances of a Large Scale Quadrupole Railgun," in *2017 International Conference on Computer Technology, Electronics and Communication (ICCTEC)*, Dec. 2017, pp. 853–857. [Online]. Available: https://ieeexplore.ieee.org/document/8789173

[85] K. Jamison and R. Stearns, "Electrical performance of a round bore, augmented, quadrupole railgun," *IEEE Transactions on Magnetics*, vol. 33, no. 1, pp. 560–565, Jan. 1997. [Online]. Available: https://ieeexplore.ieee.org/document/560074

[86] S. Liu, X. Du, J. Guan, and J. Shi, "Research on Transient Contact Characteristics of the Hyperbolic Rail Augmented Quadrupole Launcher," *IEEE Transactions on Plasma Science*, vol. 50, no. 10, pp. 3794–3801, Oct. 2022. [Online]. Available: https://ieeexplore.ieee.org/document/9904891

[87] K. Manohar and K. Srichandan, "Analysis of Quadrupole Magnetic Field Reluctance-Based Launcher With Different Coil Switching Patterns," *IEEE Transactions on Plasma Science*, vol. 51, no. 5, pp. 1370–1376, May 2023. [Online]. Available: https://ieeexplore.ieee.org/document/10109776

[88] S. A. Taher, M. Jafari, and M. Pakdel, "A New Approach for Modeling Electromagnetic Railguns," *IEEE Transactions on Plasma Science*, vol. 43, no. 5, pp. 1733–1741, May 2015. [Online]. Available: https://ieeexplore.ieee.org/document/7091004/

[89] F. Deadrick, R. Hawke, and J. Scudder, "MAGRAC–A railgun simulation program," *IEEE Transactions on Magnetics*, vol. 18, no. 1, pp. 94–104, Jan. 1982. [Online]. Available: https://ieeexplore.ieee.org/document/1061800/

[90] X. Yu and Z. Fan, "Simulation and Two-Objective Optimization of the Electromagnetic-Railgun Model Considering VSEC Resistance and Contact Resistance," *IEEE Transactions on Plasma Science*, vol. 39, no. 1, pp. 405–410, Jan. 2011. [Online]. Available: https://ieeexplore.ieee.org/document/5518435/

[91] C. Hodge, J. Flower, and A. Macalindin, "A comparison of co-energy and lorenz force based simulations of rail guns," in *2009 IEEE Electric Ship Technologies Symposium*, Apr. 2009, pp. 157–164. [Online]. Available: https://ieeexplore.ieee.org/document/4906509/

[92] H. H. Woodson and J. R. Melcher, *Electromechanical Dynamics*, ser. Electromechanical Dynamics. Cambridge, MA: Massachusetts Institute of Technology (MIT OpenCourseWare), 2009, vol. 3. [Online]. Available: https://ocw.mit.edu/courses/res-6-003-electromechanical-dynamics-spring-2009/pages/part-i/

[93] S. Umans, A. E. Fitzgerald, and C. Kingsley, *Fitzgerald and Kingsley's Electric machinery*, seventh edition ed. New York: McGraw-Hill, 2014.

[94] F. Gómez de León, M. Repetto, and A. Bissal, "A Novel Railgun Simulation Model Based on a Quasistatic," in *XXVIII. Symposium Electromagnetic Phenomena in Nonlinear Circuits (EPNC 2024)*. Portoroz, Slovenia: Univerzitetna založba Univerze v Mariboru, May 2025, publication Title: Univerzitetna založba Univerze v Mariboru. [Online]. Available: https://press.um.si/index.php/ump/catalog/book/963/chapter/471

[95] L. Liu, "COMSOL Blog: What Is the Curl Element (and Why Is It Used)?" Dec. 2019. [Online]. Available: https://www.comsol.com/blogs/what-is-the-curl-element-and-why-is-it-used

[96] W. Frei, "COMSOL Blog: Deformed Mesh Interfaces: Rotations and Linear Translations," Sep. 2015. [Online]. Available: https://www.comsol.com/blogs/deformed-mesh-interfaces-rotations-and-linear-translations/

[97] S. Hundertmark and M. Roch, "Transient 3-d simulation of an experimental railgun using finite element methods," in *2012 16th International Symposium on Electromagnetic Launch Technology*, May 2012, pp. 1–5. [Online]. Available: https://ieeexplore.ieee.org/document/6325117/

[98] F. Gómez de León, A. Bissal, M. Repetto, and F. Fabio, "Comparison of Multiphysics 3-D Transient and Quasistatic Models for Railgun Simulations," in *Computation of Electromagnetic Fields (COMPUMAG)*, Jun. 2025.

[99] "Wayback machine," Feb. 2019. [Online]. Available: https://web.archive.org/web/20190201171526/http://www.roymech.co.uk/Useful_Tables/Tribology/co_of_frict.htm#method